UNIVERSITY OF VERONA

DEPARTMENT OF

Diagnostic and Public Health

PhD PROGRAM in
Natural sciences and Engineering
PhD in Nanoscience and Advanced Technologies

PRESENTED BY ***MARCO GEROSA***
XXXIV CYCLE

Tunable iron-based contrast agent for efficient Magnetic Fluid Hyperthermia in Magnetic Resonance Imaging and Magnetic Particle Imaging

S.S.D. FIS/07 APPLIED PHYSICS

COORDINATOR:	Prof. Adolfo Speghini
TUTOR:	Prof. Pasquina Marzola

Ph.D. STUDENT: Marco Gerosa

Tunable iron-based contrast agent for efficient Magnetic Fluid Hyperthermia in Magnetic Resonance Imaging and Magnetic Particle Imaging– MARCO GEROSA

Tesi di dottorato

Verona, Febbraio 2022

ISBN

Acknowledgment

Financial support obtained from the Foundation for Nanotheranostics Research in Cancer Therapy RNC (Treviso, Italy) and the University of Verona (Joint Project 2019) is gratefully acknowledged. MRI experiments were performed at the Centro Piattaforme Tecnologiche (CPT, University of Verona) with the help of Dr. Elena Nicolato, University of Verona, which is gratefully acknowledged.

The advise and help during the whole Project from Dr. Forlin (MBN Nanomaterialia) and Professor Matteazzi is gratefully acknowledged.

SOMMARIO

Negli ultimi anni il nostro gruppo di ricerca si è concentrato nello studio delle applicazioni biomediche delle nanoparticelle magnetiche per scopi di terapia e diagnosi delle patologie tumorali su modelli animali.

Da un punto di vista diagnostico, di grande interesse da parte del gruppo sono state le tecniche di imaging tomografico e molecolare capaci di rilevare esigue quantità di ferro (componente essenziale delle nanoparticelle magnetiche usate per scopi biomedici) in esperimenti *in vitro* e *in vivo*. Per tali scopi le tecniche utilizzate principalmente sono state la Risonanza Magnetica Nucleare (MRI) e l'Imaging di Particelle Magnetiche (MPI), capaci di fornire una elevata risoluzione tomografica morfologica (MRI) e la capacità di osservare esigue quantità di ferro sia *in vitro* su cellule che *in vivo* su modelli murini (MPI).

Da un punto di vista terapeutico, sono state oggetto di rilevante interesse nanoparticelle magnetiche in grado di produrre ipertermia magnetica. L'ipertermia magnetica è un termine utilizzato per indicare la generazione di calore da parte di nanoparticelle una volta sottoposte all'applicazione di campi magnetici esterni alternati.

Nello specifico delle ricerche del gruppo negli ultimi quattro anni sono state studiate, caratterizzate e applicate a modelli di tumore mammario (MDA-MB-231 e 4T1) *in vitro* e *in vivo* nanoparticelle aventi peculiari caratteristiche di transizione di fase. Tali particelle si sono dimostrate capaci di subire una transizione di fase magnetica in funzione della variazione di temperatura, previa applicazione di campi magnetici esterni alternati, tale da alterare la loro capacità di generare calore. Tale classe di nanoparticelle si è rivelata un importante punto di svolta nel panorama dell'ipertermia magnetica in ambito preclinico, in quanto capace di autoregolare la variazione di temperatura prodotta dall'applicazione di campi magnetici alternati esterni prevenendo così la possibilità di danneggiare tessuti sani nell'immediato intorno dei tessuti patologici.

Una vasta varietà di tecniche di indagine è stata adottata per caratterizzare le nanoparticelle utilizzate per scopi sperimentali. In particolare, tecniche quali spettroscopia a infrarosso, diffrazione a raggi X, scattering di luce dinamico e microscopia elettronica a trasmissione hanno permesso di comprendere la natura chimico-fisica dei mediatori di ipertermia utilizzati nella successiva fase sperimentale.

L’applicazione dell’ipertermia per sperimentazione *in vitro* e *in vivo* è stata osservata poi mediante indagini di MRI e MPI confrontate successivamente con i risultati istologici ottenuti dalla colorazione dei tessuti coinvolti negli studi (tipicamente tessuti tumorali e i principali organi coinvolti nell’accumulo di nanoparticelle quali il fegato, i reni e la milza).

Nel complesso, i risultati *in vitro* e *in vivo* sono stati rilevanti al punto da essere oggetto di una pubblicazione scientifica e una ulteriore futura pubblicazione attualmente in fase di finalizzazione, a conferma della concreta possibilità di una loro futura applicazione in ambito clinico biomedico.

ABSTRACT

In recent years our research group has focused on the study of the biomedical applications of magnetic nanoparticles for therapy and diagnosis (theranostics) of tumor pathologies on animal models.

Considering diagnostics, the tomographic and molecular imaging techniques able to detect small quantities of iron (an essential component of magnetic nanoparticles used for biomedical purposes) during *in vitro* and *in vivo* experiments were of great interest to the group. For these purposes the techniques mainly used were Nuclear Magnetic Resonance (MRI) and Magnetic Particle Imaging (MPI), able to provide a high morphological tomographic resolution (MRI) and the ability to observe small quantities of iron both *in vitro* on cells and *in vivo* on murine models.

Considering therapy, magnetic nanoparticles able to produce magnetic hyperthermia were mostly studied. Magnetic hyperthermia is a term used for the generation of heat by nanoparticles once subjected to the application of alternating external magnetic fields.

Specifically, one of the main research interests of the group in the last four years was to study, characterize and apply, in breast cancer models (MDA-MB-231 and 4T1) both *in vitro* and *in vivo*, nanoparticles with a peculiar magnetic phase transition. These particles have proved able to undergo a magnetic phase transition as a function of the temperature variation, after applying external alternating magnetic fields. In this way it was possible to alter their ability to generate heat. This class of nanoparticles has demonstrated to be an important turning point in the panorama of magnetic hyperthermia in the preclinical field, as they were able to self-regulate the temperature variation produced by the application of external alternating magnetic fields thus preventing the possibility of damaging healthy tissues in the immediate surrounding of the pathological tissues.

A wide variety of investigation techniques was adopted to characterize the nanoparticles used for experimental purposes. In particular, techniques such as infrared spectroscopy, X-Ray powder diffraction, dynamic light scattering and transmission electron microscopy have made it possible to understand the physico-chemical nature of the hyperthermia mediators used in the subsequent experimental phase.

The application of hyperthermia for *in vitro* and *in vivo* experimentation was then observed by means of MRI and MPI investigations subsequently compared with the histological results obtained from the staining of the tissues involved in the studies

(typically tumor tissues and the main organs involved in the bioaccumulation of nanoparticles such as the liver, kidneys and spleen).

Overall, the *in vitro* and *in vivo* results were as relevant as being the subject of a scientific publication and a further future publication currently being finalized, confirming the concrete possibility of their future application in the biomedical clinical field.

INDEX

- Veronica Torresan, Andrea Guadagnini, Denis Badocco, Paolo Pastore, Guillermo Arturo Muñoz Medina, Marcela B. Fernàndez van Raap, Ian Postuma, Silva Bortolussi, Marina Beki´c, Miodrag Coli´c, Marco Gerosa, Alice Busato, Pasquina Marzola, and Vincenzo Amendola, *"Biocompatible Fe-B alloy nanoparticles designed for neutron capture therapy guided by magnetic resonance imaging",* Advanced Healthcare Materials,. 2020, 2001632.
- Elena Chistè, Gloria Ischia, Marco Gerosa, Pasquina Marzola, Marina Scarpa and Nicola Daldosso, *"Porous Si microparticles infiltrated with magnetic nanospheres",* Nanomaterials, 2020, 10, 463.
- Pradip Das, Lucia Salvioni, Manuela Malatesta, Federica Vurro, Silvia Mannucci, Marco Gerosa, Maria Antonietta Rizzuto, Chiara Tullio, Anna Degrassi, Miriam Colombo, Anna M. Ferretti, Alessandro Ponti, Laura Calderan, Davide Prosperi, *"Colloidal polymer-coated Zn-doped iron oxide nanoparticles with high relaxivity and specific absorption rate for efficient magnetic resonance imaging and magnetic hyperthermia"* Journal of Colloid and Interface Science, 579 (2020) 186–194
- Federica Vurro, Ylenia Jabalera, Silvia Mannucci, Giulia Glorani, Alberto Sola-Leyva, Marco Gerosa, Alessandro Romeo, Maria Grazia Romanelli, Manuela Malatesta, Laura Calderan, Guillermo R. Iglesias, María P. Carrasco-Jiménez, Concepcion Jimenez-Lopez and Massimiliano Perduca, *"Improving the Cellular Uptake of Biomimetic Magnetic Nanoparticles",* Nanomaterials, 2021, *11*, 766.
- Vincenzo Amendola, Andrea Guadagnini, Stefano Agnoli, Denis Badocco, Paolo Pastore, Giulio Fracasso, Marco Gerosa, Federica Vurro, Alice Busato, Pasquina Marzola, *"PEG-coated silver-iron nanoparticles as efficient and biodegradable MRI contrast agent",* Journal of Colloid and Interface Science, 596 (2021) 332–341

List of Figures

List of Figures from the Introduction

Figure 1. Hysteresis loop of different materials. As mentioned above the response of the different magnetic materials could determine their ability to exchange heat once stimulated from an external magnetic field. (Image reproduced from Namdeo et al., 2008).

Figure 2. Curve for a superparamagnetic material. At the intersection of axes where the magnetic field and the magnetization is equal to zero the orientation of the magnetic moment of each single particle is random. Once the magnetization reaches the saturation all the magnetic moments align to the same orientation imposed by the external magnetic field (image reproduced from Hervault et al., 2014)

Figure 3. Hysteresis loop of a magnetic material. The area of the hysteresis loop represents the energy dissipated during a magnetization cycle (image reproduced from Arora et al., 2018).

Figure 4. Arrangement of magnetic dipoles considering an externally applied magnetic field. (image reproduced from Das et al., 2019).

Figure 5. Magnetization decreases with temperature for materials with a different T_C and a theorical example of self-regulating temperature achieved during AMF exposure for materials with different T_C. (courtesy of MBN Nanomaterialia, Caronera di Treviso, Treviso, Italy)

Figure 6. These graphs were famous in the early days of MPI and still are meaningful. The left one represents an oscillating magnetic field at a frequency f_1 (green curve), the nonlinear magnetization curve (black curve) and the time-dependent magnetization (red curve) with the higher harmonics expressed by the below Fourier transform. On the right an off set is applied to the oscillating magnetic field and observing the field in the saturated region it is possible to deduce that no harmonics have been produced and so the Fourier transform has produced no signal (image reproduced from Gleich and Weizenecker, 2005).

Figure 7. An example of the theranostic platform defined by the MPI application to a case of U87MG xenograft mouse model. Iron-based nanoparticles were found both in the tumor as well as in the organ, but it was possible to isolate the tumor region and heat it up through MFH treatment performed with the MPI itself set at another frequency. In this

way, heat is localized only via FFP/FFL and the collateral damages are minimized (image reproduced from Tay et al., 2018).

Figure 8. An example of how it works the production of contrast in MRI through magnetic nanoparticles. Water molecules present in the tissue would be oriented through the induced magnetic field produced by the magnetic response of the contrast agent, in this case nanoparticles. This reorientation of the water molecules changes the signal produced by the tissue itself composing the contrast ratio change (Image reproduced from Jun et al., 2007).

List of Figures from the Results and Discussion 1

Figure 1. Characterization of M48 and G-M48 nanoparticles. a, b) TEM images of M48; c) XRPD pattern of M48: black line, experimental data; red pattern, Fe3O4 (magnetite, COD n.9002319), blue pattern, alpha-Fe2O3 (hematite, COD n.9000139); d) FTIR spectrum of G-M48 (black line); FTIR spectrum of glucose (red line), e) M48 magnetization vs temperature; f) Hydrodynamic diameter (by Dynamic Light Scattering) of G-M48.

Figure 2. *In vitro* viability of MDA-MB-231 cells and G-M48 internalization at TEM. a) MTT assay in MDA-MB-231 cells shows that G-M48 is safe up to a concentration of 150 μg/mL and up to 48 h of incubation time; the error bar represents SEM over six replicates. Transmission electron microscopy images of G-M48 uptake and distribution in MDA-MB-231 cells. b) MDA-MB-231 cells internalize G-M48 via endocytosis (arrow). c-f) G-M48 nanoparticles are compartmentalized into endosomes (arrowheads in c,d) distributed in the cytoplasm, as well as in residual bodies (asterisks in e,f). MDA-MB-231 cells show well-structured mitochondria (M) and endoplasmic reticulum cisternae, demonstrating no cell damage. N: cell nucleus.

Figure 3. Viability of MDA-MB-231 after MFH treatments and related histologies of the different groups. a) Thermograms were collected in water solutions at different concentrations of G-M48 suspension; b) MTT assay on MDA-MB-231 cells after multiple MFH treatments (each every 24 h). (c-h) Light microscopy images of H&E stained MDA-MB-231 cells: c) control cells, d) cells incubated with G-M48 without AMF application, e) f), g), h) Cells incubated with G-M48 and subjected to I, II, III, IV MFH treatments and observed 24 hours after the treatment. Scale bar: 50 μm.

Figure 4. Characterization of G-M48 as temperature sensitive MRI contrast agents. *In vivo* biodistribution and clearance verified by MRI and histological examination. a) The plot of transversal relaxation rate versus Fe concentration in water dispersed G-M48 phantoms, at 25°C. MRI images of phantoms cross section are also reported. b) SNR of G-M48 water suspension at 25 and 75°C and related magnetization curve of M48. The T2 signal variation has been observed in the related histogram. c-d) MRI images of a phantom constituted by a capillary filled with G-M48 (white arrow) and placed inside a thermostated box at 25°C and at 75 °C. MR images of a representative animal acquired using a T_2-weighted sequence before (e, h), 40 min (f, i) and 72 hours (g, l) after the injection of G-M48. The liver and the kidney are indicated by arrows in Figure 4 (e-h), respectively. After 40 min the signal intensity (S.I) in the liver dropped by 32.6% (Figure 4 (f) arrow). In the kidneys, no appreciable loss of signal could be detected 40 min post-injection, while at 72 hours the S.I decreased by 45 % (Figure 4 (l)). Prussian Blue staining of liver and kidneys 72h after administration of G-M48 (Figure 4 (m, n), respectively).

Figure 5. Schematic illustration of the *in vivo* experiment.

Figure 6. MRI monitoring of the % of tumor growth and histological examination. Representative MR images of the tumor's growth for the group administered with saline solution (a) and G-M48 + MFH (b). (c) Average tumor volume at different time points after tumor implantation (mean ± SEM). (d) % Tumor growth 3 and 6 days after the first MFH treatment (corresponding to 23 and 26 days after tumor implantation, respectively). A TWO-way ANOVA statistical test and a multiple comparison Tukey-Kramer test was used to assess the statistical significance of the % Tumor growth. (e-f) Histological slices of tumors treated with G-M48+MFH stained with Prussian Blue (e) and H&E (f). (g-h) Histological slices of tumors treated with saline and stained with Prussian Blue (g) and H&E (h).

Figure S1. Zeta Potential for G-M48 nanomaterials.

Figure S2. MTT assay in HeLa Cells incubated with G-M48 (10-150 µg/ml) for 2, 24 and 48h of internalization.

Figure S3. MTT assay in HeLa cells after MFH treatment.

Figure S4. T_2 weighted MR images of tumor mass before (a) and after (b) intratumoral injection of G-M48 (1.2mg Fe/mL) in mice. The distribution of G-M48 is clearly visible

(b) as hypointense areas (arrow and asterisks).The tumour mass was excised for histological examination with Prussian Blue staining; representative histological slices from the excised tumour tissue are reported in frames c-d: blue stained areas inside the tumour tissue (c) and at the tumour periphery (d) confirmed the presence of iron (magnification ×10).

Figure S5. a) Representative MR images of mice treated with G-M48 at Day 0 and Day 6. The tumor growth is comparable to the saline group. (b-c) Histological analysis of tumor mass at day 6. Prussian Blue staining reveals the presence of iron (b), while H&E staining shows the preservation of tumor tissue (c).

List of Figures from the Results and Discussion 2

Figure 1. **a.** XRPD graph demonstrates the predominant composition of the nanoparticle and its most common phases. **b.** IR spectroscopy was of great help to understand the surface composition before the coating procedure. **c.** ζ- potential of G-M55. As can be seen from the graph it has been monitored up to one week showing a good average colloidal stability **d.** Hydrodynamic radius at DLS. As for the previous measurement it has been observed for one week and it has demonstrated a performant consistency and a sharp peak.**e.** TEM has been used to investigate the morphology and structure of the nanoparticles. In particular there is a robust agreement between the hydrodynamic radius measured through DLS and the average dimension observed at the TEM.

Figure 2. Characterization of G-M55 as a bimodal contrast agent. **a.** Relaxometry measurement of naked (M55) and coated (G-M55) nanoparticles through RELAX module of MPI. By means of this measure the signal efficiency and the resolution given by the tracer was quantified. **b.** Plot of transversal relaxation rate (1/T2) versus Fe concentration in water dispersed G-M55 phantoms, at 25°C. The slope of the fitting straight line (53.20 mM-1s-1) represents the transversal relaxivity coefficient (r_2). c. T2w MR images of phantoms containing decreasing concentrations of G-M55.

Figure 3. **a.** Calibration curve of the tracer used for the labeling experiment. The slope of the straight line underlines the ability of the single nanoparticle to serve as a MPI contrast agent. **b.** Number of cells that can be observed considering a 1.0 mg Fe/ml of incubation. The slope of the straight line defines the ability of the tracer to serve as an

efficient cell labeling agent in MPI **c.** The whole row is composed by the different number of cells that can be observed in MPI using G-M55 as a labeling agent.

Figure 4. **a.** Characterization of in vitro viability of MDA-MB-231 through MTT assay with different concentrations of G-M55. **b.** AMF application at Nanotherics Magnetherm comparing a Control (water solution) with G-M55 water dispersed solution. C = 4.1 10^9 $Am^{-1}s^{-1}$. **c.** MTT assay to assess the efficiency of G-M55 to act as MFH mediator with different number of treatments. **d.** Internalization of G-M55 in MDA-MB-231 observed at TEM. **e.** G-M55 efficiency as MFH tracer observing the expression of HSPs in immunofluorescence.

Figure 5. **a.** T_2-weighted images of liver of mice treated with G-M55 NPs at different timepoints. **b.** Plot of T_2 signal change, expressed as signal intensity decrease (%), in liver, (spleen), kidneys at different time points up to 72h after administration of G-M55 NPs. **c.** Detail of liver tissue of the animal treated with G-M55 NPs. Tissues were treated with Prussian Blue and Fast red as counterstaining to underline nanoparticles presence. **d.** Histological analysis of tissues from animals not treated and from animals treated with G-M55 NPs. HE is reported of the main organs involved in biodistribution.

Figure 6. **a.** T_2-weighted images of a representative tumor from animals treated with G-M55 (top) and from animals treated with G-M55 and hyperthermia (bottom) at different timepoints. **b.** Tumor volume growth after the MFH treatments at different time points. The statistical analysis shows the increasing difference among the groups at different time points. **c.** Tumor volume growth expressed as % after the MFH treatments at different time points. **d. - e.** Histological analysis of tumors from animals treated with G-M55 NPs and from animals treated with G-M55 NPs and MFH. HE (magnification 4x and 10x) and iron staining (magnification 4x and 10x) are reported. The “N” letters indicate the necrotic zones of tumors. Black arrows indicate representative blue spots corresponding to iron deposits in the tissues treated with the iron staining.

List of Figures from the Results and Discussion 3

Figure 1. Two different mice at day 14 post implantation, two doses of the SynomagPEG, 24 mg/kg and 3 mg/kg. White arrows indicate the location of the tumor.

Introduction

1. *Magnetic Fluid Hyperthermia*

It is possible to define hyperthermia as the procedure of raising the temperature of a part of or the whole body of a living being above standard temperature for a certain amount of time. Fluctuations of temperature in a living organism could actively interfere with metabolism and homeostasis processes, for example hydro-saline and acid-basic homeostasis as well as energetic metabolism. Other critical areas deeply affected by temperature fluctuations are related to the regulation of a wide range of biological mechanism as the lipid and carbohydrate metabolism in which adipose tissues in general play a substantial role as regulator. A relevant increase of temperature could be responsible for the alteration in lipid metabolism and in particular could interfere with the carbohydrate-lipid metabolism as reported in Barnabucci et al., 2009. In the last decades the effect of a slight increase of temperature has been widely investigated in several papers as for example in Song et al., 2005. A modest increase up to 2.0 °C starting from physiological conditions (37.0 °C) led to a mild heat shock for the cells. More consistent temperature increase could lead to severe heat shocks that could induce physical phase changes in the phospholipidic layers of the cell membrane. Among the most common alterations produced in the cell structure, the viscosity changes related to the transition from solid to liquid of the cell membrane surface should be mentioned. These eventful physical transitions could be responsible for consequent relevant changes as in the electrical and thermal conductivity of the biological membranes with consequent fluctuations in the efficiency and speed of the signal transduction as well as alteration in the general response of the cell membranes to different stimuli. The heat shock stimulus itself and the consequent activation of the proteins involved in the recognition and response of the increasing temperature could be deeply affected as well.
As far as the anticancer therapies are concerned, the term “hyperthermia” is referred to the treatment of cancer by administering heat in different ways (Pelaz et al., 2017).

Nowadays, conventional approaches commonly used for cancer treatment include a combination of chemotherapy drugs, invasive surgery, guided focused ultrasound ablation, thermal ablation, and radiation therapy. Across all these old-fashioned and brand-new patterns of cancer therapy it could also be introduced hyperthermia. It is usually applied in combination with an already established treatment modality as one of the mentioned above (preferentially radiotherapy and/or chemotherapy) and it is exploited reaching temperatures in the range of 40-46 °C inside the tumor mass. Recent advancements in clinical studies (see for example Moyer et al., 2008 and Lee et al., 2010) have demonstrated that the success of a hyperthermia cancer treatment is strictly related to the minimum temperature rise occurring in the tumor tissue. It is easily understood that the efficiency of hyperthermia treatment against cancer disease is related to the temperature achieved during the treatment itself. However, this is not the only parameter determining the efficacy of the treatment. The length of the treatment, the time window chosen to administrate it, the chemical and physical characteristics of the tumoral tissues, the tumor microenvironment and the tumor vascularization could also be important foci of the whole analysis as reported in Hegyi et al., 2013.

Despite all the challenges faced to develop the hyperthermia treatment suitable for cancer therapy, significant steps have been done to introduce this therapeutic path into clinical trials. Nonetheless an important and tough challenge stands still, the chance to reduce damages to healthy tissues and other adverse effects. As already well known in literature in fact, high temperatures, (especially above 43 °C), can easily induce cell death stimulating different apoptosis pathways inside the cell. Even killing a huge number of tumor cells, hyperthermia applied reaching over 43.0 °C could still harm healthy tissues or at least severely injure these ones. Considering this issue, one of the main goals of the last decade was to develop an efficient hyperthermia mediator able to stabilize its increase of temperature up to 44 to 45 °C. In this way the ability to harm tumoral cells would be summed up to the chance of keeping the surrounding tissue healthy.

For this purpose, Magnetic Fluid Hyperthermia (MFH) has been developed and pushed in the last three decades. It is a non-invasive technique for cancer therapy and has several advantages compared to traditional hyperthermia therapies as reported in several papers as Kumar et al., 2011; Laurent et al., 2011; Thiesen et al., 2008 and Gneveckow et al., 2004.

As a therapeutic approach, MFH involves the administration of magnetic nanoparticles (MNPs) as heat mediators into the tumor followed by its exposure to an external alternating magnetic field (AMF). Due to the AMF application, the temperature inside the tumor mass tend to increase and the temperature inside cells reach values from 42 to

46 °C resulting in an effective and efficient thermal ablation of the tumor. The heat generation itself is clearly attributable to the heat dissipation of the magnetic energy provided by the high frequency AMF applied to the magnetic nanoparticles. Considering the magnetic single domain nanoparticles (NPs), from a physical perspective, the magnetic energy conversion into heat came from the internal Néel fluctuations and the external Brownian relaxation phenomenon (Das et al., 2019).

Among the well-known advantages of MFH respect to other therapies, as for example near-infra-red laser-based hyperthermia, its higher penetration ability of magnetic field in biological tissues and an enhanced accumulation of magnetic nanoparticles in the tumor tissues via magnetic targeting strategy for cancer treatment (Fontes et al., 2017). In addition, due to the chance of exploit MFH in combination with other therapies it could be also evaluated the synergistic effects with traditional choices as chemotherapy and radiotherapy (Ito et al., 2003; Di Corato et al., 2015; Cazares-Cortes et al., 2017).

In general, the heating power of magnetic nanoparticles strictly depends on nanocrystal size, chemical and physical composition of the material and the solvent properties (Fortin et al., 2008). Thanks to the developments of nanotechnology in the last years because of its widespread application in cancer therapy and diagnostics, various methods have been established to synthetize high-quality magnetic nanoparticles and to chemically modify their surface to allow their utilization in a biological (and so safe/toxic-free) environment. To treat cancer pathologies, nanomedicine-based modalities have already been devised (Zhang et al., 2019). The expansion of nanotechnology is already having a strong impact on biotechnology and healthcare (Zagar et al., 2010).

In the last decade a few clinical trials have taken place in different countries to test Magnetic Fluid Hyperthermia. Modern sophisticated magnetic nanoparticles have been developed and patented to be tested for clinical trials. The Nanomedicine Company, MagForce (founded in 1997 in Berlin, Germany) has currently developed NanoTherm®, a solution composed by superparamagnetic iron oxide nanoparticle that can change its polarity a hundred thousand times per second, under the proper frequency of AMF, generating the promised heat. Among the most promising clinical trials after the FDA approval in the US there is a clinical study in stage II with the enrollment of approximately 120 patients. The following centers, specialized in cancer detection and cancer therapy, are involved in the application of MFH technology: the University of Texas, San Antonio; the University of Seattle, Washington (Chandrasekharan et al., 2020); Vall d'Hebron University Hospital and Fuenlabrada University Hospital both in Spain (Rubia-Rodriguez et al., 2021).

2. *Mechanisms of heat generation*

It is now relevant to understand the physical mechanism behind the heat generation. The conversion from magnetic energy to thermal energy in magnetic nanoparticles subjected to an alternating magnetic field can be due to a wide range of mechanisms depending on different variables.

At first it is important to divide the nanoparticles in two classes, considering the magnetic domain of reference, multi-domain nanoparticles and single domain nanoparticles.

In multi-domain NPs (as the ones characterizing the ferri- or ferromagnetic material), the production of heat is simply due to hysteresis losses, i.e. the amount of energy dissipated during a whole magnetization cycle (Cherukuri et al., 2010). In physical theory it is possible to define the Weiss domain as the magnetic domain of a specific region of space of a material. Considering the multi-domain NPs, a ferromagnet is composed by Weiss domains in which the magnetic moments of atoms are aligned parallel one to each other to maintain a lower energy state, while a ferrimagnet is composed by magnetic domains with magnetic moments of different amplitudes and opposed one to each other. Once applied an external magnetic field, it is possible to observe that the magnetic domains tend to align themselves in the direction of the applied external field. Once exposed to an external magnetic field, the saturation magnetization is reached as soon as each single magnetic moment of each domain is aligned toward the same direction imposed by the magnetic field.

Once the external magnetic field is turned off, the magnetization starts to decrease even if it does not get back to zero at the end of the process. This net magnetization still present in the material is the so-called remaining magnetization. At this point, for a ferromagnetic material, the only way to reduce the magnetization to zero again is to apply a magnetic field with a defined intensity in the opposite direction.

It is possible to represent the magnetization curve of a ferromagnetic material through a simple hysteresis loop (Figure 1.). To compute and measure the efficiency of the hysteresis losses it is possible to integrate the area of the hysteresis loop itself. The phenomenon of superparamagnetism can be observed in ferromagnetic as well as in ferrimagnetic materials if the material itself is packed in the form of nanoparticles. The smaller the particles chosen the higher the probability to observe a single-domain magnetic region even in a bulk material. Usually, even nanomaterials are packaged as a bigger bulk material, so it seems very unlikely to observe a single-domain material. Nevertheless, it is possible to isolate and analyze even single regions in a whole material, reducing the infinite amount of magnetic moment associated with the atoms of the material to a precise finite amount or even so a single magnetic moment.

Indeed, small enough NPs (or small enough regions in a material) are single-domain particles, which can be regarded as a single magnetic moment composed of all magnetic moments of the atoms forming the NPs. Such nanoparticles are named superparamagnetic nanoparticles.

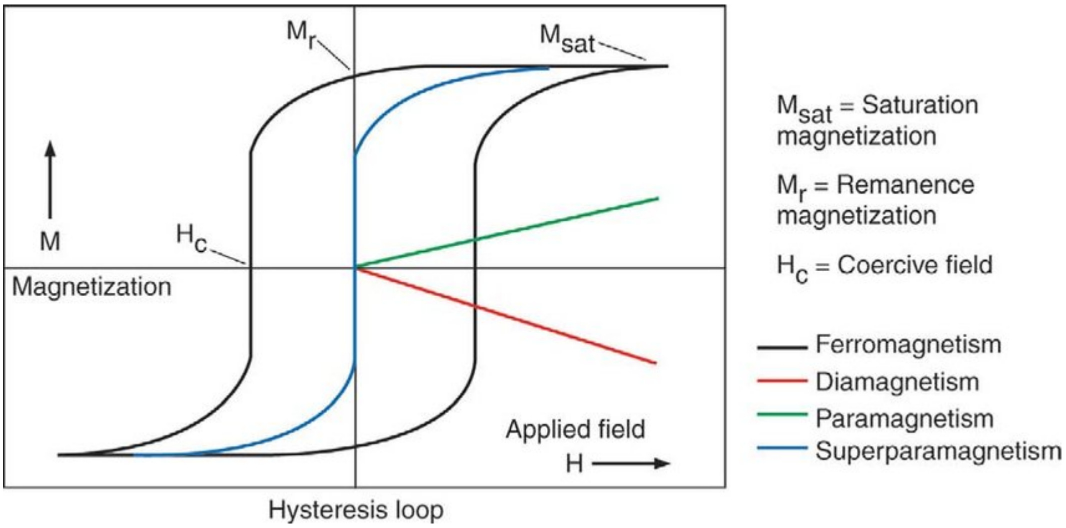

Figure 1. Hysteresis loop of different materials. As mentioned in the text, the response of the different magnetic materials determines their ability to exchange heat once stimulated by an external magnetic field. (Figure reproduced from Namdeo et al., 2008).

In the last decades, for biomedical applications, superparamagnetic NPs were preferred over ferri- and ferromagnetic NPs thanks to their ability to not retain any magnetization once the external magnetic field is removed (Figure. 2). Compared to multi-domain NPs, single-domain NPs can dissipate heat through relaxation losses, which can be described and summarized in two types: Néel relaxation and Brownian relaxation.

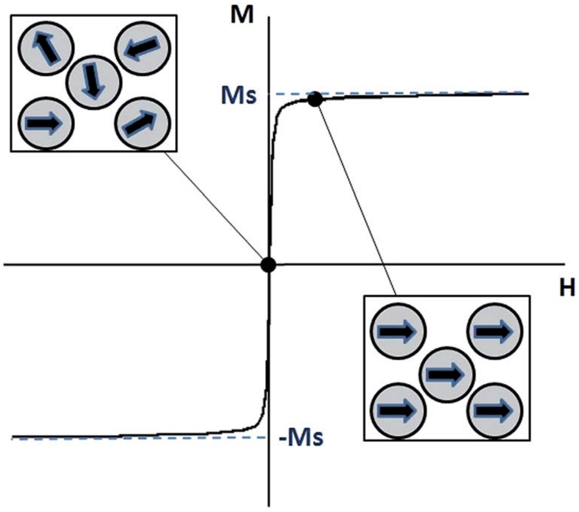

Figure 2. Curve for a superparamagnetic material. At the intersection of axes where the magnetic field and the magnetization is equal to zero the orientation of the magnetic moment of each single particle is random. Once the magnetization reaches the saturation all the magnetic moments align to the same orientation imposed by the external magnetic field (Figure reproduced from Hervault et al., 2014)

In general, in Néel relaxation, the heat generation occurs because of a fast alteration in magnetic moments direction relatively to the crystal lattice. On the other side, the Brownian relaxation occurs by the physical movement of particles within a medium and therefore can be enhanced or inhibited by the viscosity of the medium itself that tends to modify the rotation of the particles.

More specifically, the magnetic relaxation mechanism depends on several important parameters: size, shape and composition of the NPs as well as the viscosity of the compound itself and its chemical-physical stability in different dispersion media. From a physical perspective, Néel relaxation derives from the reorientation of the magnetic moment in the same direction of the external applied magnetic field with each field oscillation (Suto et al., 2009), (Kotitz et al., 1999). It is possible to estimate the Néel relaxation time τ_N by the following equation:

$$\tau_N = \tau_0 e^{\frac{KV}{K_B T}}$$

where $\tau_0 = 10^{-9}$ s, K is the anisotropy constant, V is the volume of the magnetic particle, K_B is the Boltzmann constant and T is the temperature.

The size of nanoparticles is the most important parameter to be considered in the Néel relaxation. For a bigger particle, it could be critical to establish an efficient thermal exchange because it requires a higher amount of energy, to be provided by the external magnetic field, to produce the rotation of its own magnetic moment and the consequent magnetic relaxation. Differently, a smaller particle requires less energy for the rotation of its magnetic moment.

As mentioned before, the other mechanism related to the magnetic relaxation is the Brownian relaxation that is basically induced by thermal excitation (Suto et al., 2009), (Kotitz et al., 1999). As well as the Néel relaxation time, the Brownian relaxation time τ_B is expressed by the following equation:

$$\tau_B = \frac{3\eta V_H}{K_B T}$$

where η is the viscosity of the medium, V_H is the hydrodynamic volume of the particle, K_B is the Boltzmann constant and T is the temperature.

As for the Néel mechanism, the Brownian relaxation mechanism is strongly size-dependent, shape-dependent, and viscosity-dependent (Kotitz et al., 1999). The first two features are related to the geometry of the nanoparticle itself. The bigger the size the slower would be the relaxation process itself. Also, the higher viscosity of the liquid medium will slow down the rotation of the particles. Considering only the dimensions of the nanoparticles the losses due to the Néel relaxation process will prevail in small NPs while the Brownian relaxation process will be dominant in bigger particles (or even in simple clusters of small particles strictly held together (Suto et al., 2009 and Levy et al., 2008). Considering the strong geometry-dependency of the physical relaxation process, it is easy to understand that the Brownian losses are not found only in superparamagnetic NPs as described in Hergt et al., 2006.

Focusing on magnetic fluid hyperthermia applied to cells it is important to remember the change in viscosity that can occur in the cell membrane, inside and outside the cell. Considering such changes in viscosity, it is convenient to have NPs relaxing essentially through the Néel mechanism. In this way, once internalized in the cells, a free rotation of the nanoparticle centered in one of its axes (depending on its geometry) and due to a change of viscosity in the medium could be prevented. Reducing the degree of freedom of the nanoparticle internalized in the cells could be one of the most efficient ways to actively control the rapid increase of temperature due to the magnetic relaxation mechanisms.

Due to the size and shape of the nanoparticle, it could be necessary to consider a combination of the relaxation mechanisms mentioned above. In this way it is possible to estimate a combination of the effects given by the geometry of the nanoparticle (or of the possible aggregates and clusters formed) and the viscosity of the medium. An effective computation of the combination of the two magnetic relaxation times gives the overall effective relaxation time τ of the particles:

$$\tau = \frac{\tau_B \tau_N}{(\tau_B + \tau_N)}$$

Once considered the coupling of the two relaxation mechanisms, it can be easily introduced the matching between the relaxation time of the nanoparticle itself and the oscillation of the external magnetic field applied to the nanoparticle to obtain the heating effect. If the AMF oscillates faster than the relaxation time of the MNPs, it induces the release of heat (for the conservation of energy) from the MNPs due to the delay accumulated in the relaxation of the magnetic moment (Suto et al., 2009). The effect of this delay could be studied directly measuring the power dissipation (P) and estimating the Specific Absorption Rate (SAR). In particular, P can be computed by the following equation:

$$P = \mu_0 \chi f H^2$$

where P is the power dissipation value, μ_0 is the permeability of free space, χ is the AC magnetic susceptibility, f is the frequency of the applied AC magnetic field, and H is the strength of the applied AC magnetic field.

Nowadays, nanoparticles performance as efficient heat exchange mediator is no longer evaluated by power dissipation. Instead, the Specific Adsorption Rate (SAR), is used to quantitatively describe the efficiency of the synthetized nanoparticles. In this terms, quantification of the power dissipation of magnetic nanoparticles in an AMF is provided by the specific absorption rate (SAR) expressed in Wg^{-1}. In a few papers SAR is also reported as ILP (intrinsic loss power) even if between the two there is a slight difference (Suto et al., 2009). As reported in Das et al., 2019, SAR crucially depends on a wide range of internal and external parameters such as size, size distribution in space, shape and geometry of the nanoparticle (or the nanoparticle cluster), chemical composition, possible surface modification due to functionalization or coating applied, saturation magnetization of the particles as well as external parameters as frequency and amplitude (intensity) of the applied magnetic field.

SAR can be computed exploiting the following equation:

$$SAR = C\frac{dT}{dt}\frac{m_s}{m_m}$$

where C is the specific heat capacity of the sample, the ratio dT/dt is the slope of the time-dependent heating curve interpolated in a short time window compared to the amount of time used to perform the whole measure, m_s is the mass of the solvent used to dilute NPs and m_m is the mass of the NPs.

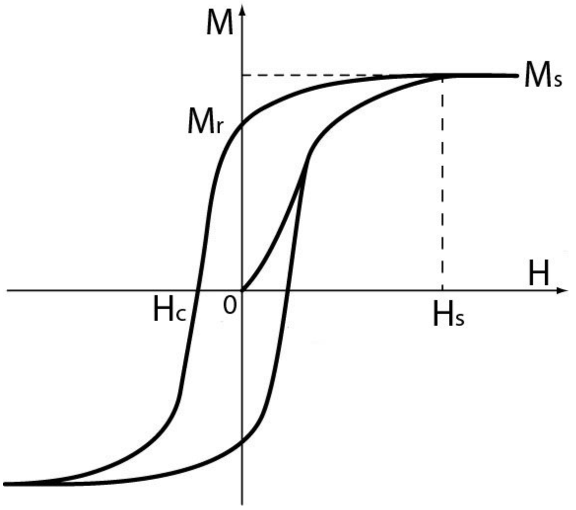

Figure 3. Hysteresis loop of a magnetic material. The area of the hysteresis loop represents the energy dissipated during a magnetization cycle (Figure reproduced from Arora et al., 2018).

The SAR is a very common and efficient parameter to determine and compare the efficiency of a compound considering its only fundamental features as mass, thermal capacity, and thermal fluctuations due to external magnetic field. Once determined the hysteresis cycle of the material (as reported in Figure 3 for example) it is possible to estimate the energy dissipated as heat during the magnetization cycle. The integral of the magnetization function is the effective power energy transformed into heat. A remarkable value as result of this integral could be of great impact for preclinical and clinical studies; in fact, high heating potential is crucial for the clinical use of MFH. The higher is the heating potential of a compound the smaller would be the amount of nanoparticles required to be injected into patients.

Toxicity is still one of the main issues related to the application of magnetic nanoparticles (combined with an external magnetic field) to serve as an intravenous drug combined with other more conventional therapies. Therefore, it is highly desirable to obtain MNPs with an exceptional SAR value as reported in Liu et al., 2012 and Sharifi et al., 2012. After the discovery of superparamagnetic NPs, research related to the application of MFH to cancer therapy was driven towards that direction. Superparamagnetic nanoparticles produce heat via Néel and Brownian relaxation mechanisms and compared to ferromagnetic NPs they can generate a larger amount of heat and a higher SAR at lower field amplitudes. The chance to apply weaker external magnetic field amplitudes could be positively reflected on patients that could experience a smaller amount of physical stress in terms of symptoms during the treatment as reported in Hergt et al., 2007.

To regulate the impact of magnetic fluid hyperthermia and to safely introduce this treatment in clinics Hergt et al., 2007 suggested a mathematical rule related to nanoparticles feature that must be attended. During the early days of magnetic hyperthermia applications for cancer therapy it was commonly used the Brezovich criterion to identify an upper limit to the magnetic field strength and the frequency applied in the treatments. This limit was calculated through the equation $C = H*f$ (H is the magnetic field intensity in Am^{-1} and f is the frequency of the related field in s^{-1}) and it is equal to $4.85\ 10^{8}\ \mathrm{Am}^{-1}\mathrm{s}^{-1}$. Nowadays it is accepted another safety criterion, the so called Hergt criterion. It is a less rigid rule that was introduced to adapt the magnetic hyperthermia procedure to different geometries and shapes of the treated body in order to safely apply hyperthermia to patients and avoid damages on healthy tissues. It can be summarized as $C = H*f \leq 5.0\ 10^{9}\ \mathrm{Am}^{-1}\mathrm{s}^{-1}$ Hergt et al., 2006.

Another critical issue fixed by Hergt et al., 2007 was related to the optimal size of the nanoparticles to obtain a high SAR value. This size is the one that is close to the physical transition from superparamagnetic to ferromagnetic behavior of the material.

From an experimental perspective there is a clear lack of standardized protocol to measure the heat dissipation produced by the magnetically excited nanoparticles. To directly measure SAR a few devices are present on the market but the ideal one would require an adiabatic setup to avoid interferences from external agents that could directly modify the bulk temperature and so the Brownian relaxation mechanism. Considering in vitro studies and possible measure of SAR inside cells it has to be considered also the possible toxicity introduced by a non-sterile environment as well as non-standard working conditions for cells (warm air stream around 37.0 °C with fluxed CO_2). Even so, most of the research groups use non-adiabatic and often home-made setups which results in more sources of inaccuracies and tend to increase variability of the SAR values (Natividad et al., 2008). Even the choice of the magnetic field intensity and the frequency applied (related also to the average dimension of the nanoparticles) greatly differ from different laboratory although the Hergt criterion for the clinical applications should be fulfilled. To be more accurate and to reduce the source of error each research group measures the nanoparticles heating abilities under different magnetic field intensities and frequencies.

Considering all the above-mentioned details related to the investigation of the heating ability of the particles it can be easily deduced that it is very difficult to compare SAR values among different nanoparticles even normalizing it with common standard conditions. Starting from the above reported difficulties, in the last decade a new parameter, more accurate than SAR, was introduced. Such parameter, named intrinsic loss of power, or simply ILP (Kallumadil et al., 2009).

ILP can be computed through the following equation:

$$ILP = \frac{SAR}{fH^2}$$

ILP is obtained by normalizing the SAR by the frequency and the squared intensity of the field amplitude and is therefore independent of the magnetic field parameters themselves. By the way, the direct consequence of this formula is that polydispersity of magnetic nanoparticles causes a decrease in ILP values. This reduction is strictly bounded to the dimension of the nanoparticles and the chance of aggregation due to their chemical composition and eventual surface coating. The heating ability of the nanoparticles is dependent on the surrounding conditions (boundary conditions of the bulk) of the medium and so of the entire cell.

Thanks to this parameter it was possible to compare way different superparamagnetic nanoparticles and understand the most efficient one in terms of heating exchange.

3. *Cellular effects of heat generation*

The application of Magnetic Fluid Hyperthermia technique at the in vitro and in vivo level can easily induce different kind of damages directly to cells. Considering hyperthermia as a valuable tool in the fight against cancer it could be of great interest to observe the damages produced by hyperthermia at the cellular level. It is well known from literature that hyperthermia may kill or at least weaken tumor cells. In the last decade, the necessity to control and limit the effects produced by thermotherapy on healthy cells composing the tumor microenvironment also emerged.

One of the most common cellular mechanisms solicited by hyperthermia is apoptosis. Once thermally stimulated over a certain temperature level, cancerous cells can undergo apoptosis in direct response to applied heat, while healthy tissues can easily maintain a normal temperature (Hegyi et al., 2013). There is a wide range of direct mechanisms related to the increasing temperature that could kill cancer cells: the most relevant include denaturation, folding, unfolding and aggregation of proteins, coagulation, immune system response produced by the over expression of the heat shock proteins on the cellular membrane, apoptosis, cell cycle arrest, autophagy, and necrosis.

Over the past years MFH has demonstrated to be a powerful tool against cancer and other diseases exploiting a different range of temperatures. In the 40-46°C temperature range MFH kills cells (even healthy cells) in a reproducible time and temperature dependent manner. As reported in Laszlo et al., 1992, at a cellular level there are a few changes induced by hyperthermia that must be due to temperature-induced alterations in molecular pathways, which usually involve inhibition of protein synthesis, DNA and RNA.

Protein synthesis is a fundamental process involved in almost all biological activities that could be easily inhibited during heating. Even milder temperature (around 43 °C, exploited for mild hyperthermia) reached through smaller steps of temperature increase could instead cause an over expression of heat shock proteins (HSP) (Kregel et al., 2002). The over expression of HSP could be easily correlated with a peculiar biological mechanism defined as thermotolerance. It is hard to say from the over expression of HSP if the heat shock has led to inactivating or activating responses. The response to a signal could led to different endings. For example, during apoptosis mechanism, also defined as programmed cell death, cells in healthy or ill tissues trigger their self-destruction in response to a specific molecular signal (Kerr et al., 1994). This kind of biological event can’t be easily unveiled, even tough, different signals related to HSP could be investigated. As far as the necrosis mechanism is concerned, there is associated inflammation induced in the surrounding microenvironment. Necrosis is induced by a huge, induced increase of temperature (approximately over 60 °C measured in the tissue and defined as thermoablation) that would lead to permanent damage to the vascular system, preventing the chance of auto repairing of the organism. Apoptosis occurs almost spontaneously in cancer cells once the tissue is exposed even to a mild increase of temperature (around 43 °C), thereby slowing tumor growth. This effect could be also enhanced through a combination of heat, irradiation, and chemotherapy. Another relevant difference between these two mechanisms of cell death is that apoptosis is a natural process while necrosis is a cellular damage that would lead to a premature death of cells in tissues and causes an inflammatory response in the surrounding environment (Golstein et al., 2007). Thermoablation (that cause necrosis) in high temperature range (above 46 °C) could not be the most suitable option to treat cancer due to the potentially relevant side effects on healthy tissues. Considering the weaker side effects, mild hyperthermia produced by externally applied magnetic fields set with proper frequencies could be more appropriate although not without flaws. Several studies over the last 20 years (Hildebrandt et al., 2002) have demonstrated that the thermal energy required to induce apoptosis in cells is close to the thermal energy needed for protein denaturation which means that the direct consequence of mild hyperthermia is based on the denaturation of the cell membrane and on the response of the cytoplasmic proteins to the thermal shock. Typical features and signs of thermal damage (and early apoptosis) caused by the application of mild hyperthermia are alteration of membrane geometry and composition, cytoskeletal and cytoplasmic damage including cell rounding, overexpression of HSP and early folding-unfolding of a wide range of proteins located mainly on the cell membrane. Such relevant alternations may cause alterations during DNA synthesis and impairment of its repairing ability, among the most important consequence of protein denaturation.

Comparing different cells, it has been observed higher sensitivity to heat and thermal stress for those undergoing mitosis phase. This crucial observation makes cancer cells more susceptible to heat than any other healthy cell thanks to their well-known ability to undergo faster cell division process. This selective feature, characteristic of the hyperthermia process, is most certainly due to the architecture and morphological structure of the cell itself that hides huge differences between healthy and pathological cells. In a normal tissue the density of the vessel, the organization of the capillaries net and their capacity is completely different from a cancerous cell. This last tissue is basically abnormal thanks to its huge and disorganized vasculature. The disorganized structure of tumor vasculature can also lead to oxygen and nutrient starvation (Siemann et al., 2011). In terms of clinical and preclinical studies it's important to distinguish between small tumors, usually characterized by high blood flow and big tumors, usually characterized by low blood flow. From this feature it is possible to define a general rule that could help to understand the aggression of the tumor: generally, blood flow decreases with increasing tumor size (Song et al., 1984).

From a physiological perspective, application of hyperthermia up to temperature of 43 °C (low-mild-hyperthermia) could induce an increase of blood flow that could facilitate tumor expansion improving its ability to supply oxygen faster from the organism. Once obtained a similar effect, MFH could be used in combination with radiotherapy or chemotherapy. Radiotherapy because, as reported in Hildebrandt et al., 2002, radio-sensitivity is increased by tissue huge oxygenation and chemotherapy because drug delivery is strongly favored by high levels of vascularization and perfusion as reported by Wust et al., 2002.

Once hyperthermia is applied at temperatures between 43 to 45 °C (mild hyperthermia) tumor blood flow tends to decrease while in normal tissue it significantly increases. This decreased blood flow led to lower heat dissipation rate and consequently the temperature in tumor tissue will rise faster than in normal tissue. This difficulty in dissipating heat could cause apoptosis while, healthy tissues, more easily maintain physiological temperatures.

In general, the conversion of magnetic energy into heat and the heat exposure would produce regions of hypoxia, acidosis, and energy deprivation. In addition to its cytotoxicity, these tumor micro-environmental factors make cancer cells more sensitive to hyperthermia and heat exposure. In fact, depending on the temperature reached and the exposure time of the tissue, the application of MFH may increase or decrease the tumor oxygenation, leading to consistently different scenarios (Song et al., 2001).

Fundamental considerations related to the application of MFH to cancerous tissues could be done also considering the main differences between a normal cell and a cancerous cell.

Biophysical differences arise quite easily considering a few chemical-physical characteristics based on the different electric properties of the normal cells respect to the pathological ones:

- Tumor cells membrane and charge distribution over the phospholipidic surface is electrochemically different.
- The lipidic composition of the phospholipidic membrane of tumor cells compared to the healthy cells, especially regarding to the sterol content.
- Production of ATP in tumoral cells is slower because of the huge demand for energy consumption due to the high proliferative rate. This fact contributes to an instability of the ionic channel exchange due to the transport of K^+ and Na^+ ions.
- Changing membrane permeability, the influx of K^+, Mg^{2+} and Ca^{2+} ions increase, while the efflux of Na^+ decreases. Consequently, cell membrane potential decreases further, and the tumor cells will be negatively polarized in average.
- The conductivity and the dielectric constant of the tumor tissue will be higher than normal.

4. Magnetic nanoparticles for magnetic fluid hyperthermia

To understand the impact of magnetic nanoparticles for hyperthermia on cancer treatment and to design optimal heat mediators it is essential to start from the laws of magnetism that allow to exploit the energy conversion from electromagnetic energy to heat via dissipation.

Considering the arrangement of magnetic dipoles in the presence or absence of an external magnetic field, magnetic materials (in this case magnetic nanomaterials), are usually classified into several categories as: diamagnetics, paramagnetics, ferromagnetics, ferrimagnetics and antiferrimagnetics.

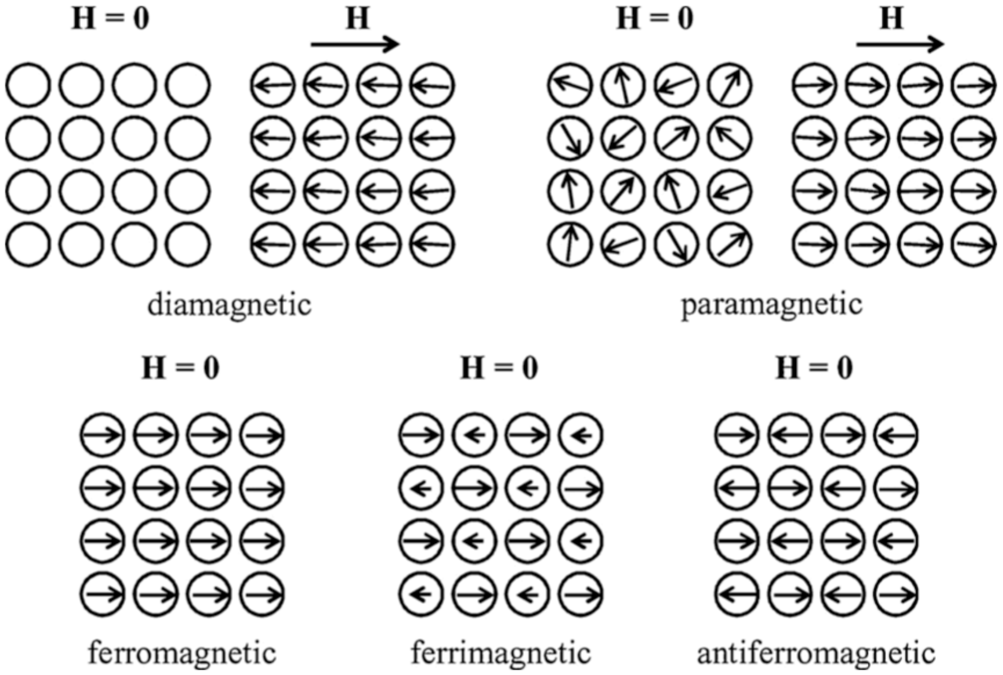

Figure 4. Arrangement of magnetic dipoles within an externally applied magnetic field. (Figure reproduced from Das et al., 2019).

- Diamagnetic nanomaterials: in absence of magnetic field, they do not have magnetic dipoles, but they start to generate them once the external magnetic field is applied.
- Paramagnetic nanomaterials: they already have existing randomly oriented dipoles in absence of external magnetic field. Those dipoles will be aligned in the same direction after an external magnetic field is applied.

- Ferromagnetic nanomaterials: they have a permanent magnetic dipole in the absence or in the presence of an external magnetic field. For ferrimagnetic material, a few random weak magnetic dipoles exist in antiparallel to neighboring stronger dipoles even in absence of magnetic field.
- Antiferromagnetic nanomaterials (or uncompensated ferrimagnetism): where the minimum energetic configuration is realized having permanent magnetic dipoles in antiparallel configuration in the absence or in the presence of an external magnetic field.

Even having an extensive knowledge of the different magnetic behavior of the nanoparticles in the past decades, for biological applications as magnetic fluid hyperthermia, researchers exploited mostly superparamagnetic and ferromagnetic nanomaterials (Chang et al., 2018; Huang et al., 2013; Kumar et al., 2011; Liu et al., 2020).

By exploring the heating properties of magnetic nanoparticles excited by alternating magnetic fields for hyperthermia applications, it was possible to clarify the influence of important parameters as magnetic anisotropy constant (K), hydrodynamic volume (derived from the hydrodynamic radius) and saturation magnetization. All these structural parameters depend on geometry, size, shape, chemical and physical composition of the nanomaterial (Laurent et al., 2011).

Size and dispersion are crucial factors in determining the saturation magnetization and in enhancing the heating capacity of nanoparticles. The bigger the nanoparticle, the highest will be the saturation magnetization. Saturation magnetization is proportional to the heating capacity itself as measured by SAR (or even using the ILP to evaluate the efficiency of the nanomaterial). In general, the iron-oxide nanoparticles with a hydrodynamic radius smaller than 10 nm display SAR value considerably lower than nanoparticles with radius in the range of 14 to 20 nm and same chemical composition. Size influences also side effects produced by the nanomaterials. The bigger the nanoparticle, the highest will be the cytotoxicity of the compound inside cells (Fortin et al., 2008).

The geometry of the nanoparticles is relevant to determine the efficiency of the nanoparticles themselves. In the last decade a lot of different shapes have been adopted and tested especially for biomedical applications. A crucial point was to obtain a low surface energy: in this way the magnetic anisotropy would be significantly reduced, and the saturation magnetization would be enhanced leading to a higher SAR and consequent more pronounced heating efficiency.

It is well known that spherical iron oxides have significantly lower value of SAR compared to cubic nanoparticles with the same chemical composition and equivalent volume (Martinez-Boubeta et al., 2013). Considering a different metal, also gold nanostars have shown higher SAR respect to their equivalent spherical nanoparticles (Guardia et al., 2012).

In conclusion, chemical and physical features of nanoparticles have been deeply investigated over the years to optimize the composition and reach a standard. Nowadays, one of the most popular methods to optimize SAR is to dope ferrite nanoparticles with different metal ions in order to increase saturation magnetization and therefore improve SAR and ILP (Jang et al., 2009).

As already explained before, in magnetic nanoparticles-based hyperthermia, heating deeply depends on particle distribution over the targeted tumor site. In general, magnetic heat generation can be associated with two different mechanism of heat generation already defined: relaxation (as Néel and Brownian relaxations) and hysteresis loss. Considering the first approach the generation of thermal loss is due to a tendency of the sources of friction to a phase lag between the applied magnetic field and the orientation of the magnetic moments of the particle distribution.

According to the ILP formula reported above, the intrinsic loss power of a nanomaterial is related to the material composition (the elements), the structural characteristics of the magnetic nanoparticle and the magnetic features. The intensity and frequency of AMF adopted also play a crucial role (Pankhurst et al., 2003). The microenvironment in which magnetic nanoparticles are embedded influences ILP because of intracellular elements that constantly inhibit the particles movement. Finally, considering the definition of Néel and Brownian relaxation, the first one is considered the main source of heat generation during intracellular magnetic fluid hyperthermia.

In the last 30 years several in vitro and in vivo studies have been conducted exploiting direct administration of magnetic nanoparticles into a tumor followed by AMF exposure. These studies have considered several endpoints of therapeutic efficacy as tumor size (and associated growth factor), metastasis rate of the primal tumor, invasiveness of the metastasis and of tumor cells, neo angiogenesis, tumor cell growth and proliferation.

As perfectly described by Lacroix et al., 2010; Dadfar et al., 2019 and Etemadi et al., 2021 a huge variety of nanoparticles were studied. Here follows a summary of the most relevant magnetic nanoparticles synthetized and their actual application related to cancer therapy.

In general, it is important to define a size range for the nanoparticles used in magnetic fluid hyperthermia. Usually, the size ranges from 1 to 200 nm. Nanoparticles can be ferromagnetic or superparamagnetic and they usually are dispersed in a non-magnetic matrix (Kharisov et al., 2014). In terms of chemical composition nanoparticles can be oxides, metallic, or metallic shell types and are prepared in laboratory by co-precipitation, microemulsion, thermal decomposition, or hydrothermal techniques. Depending on the specific application, nanoparticles can be coated with organic or inorganic coatings to enhance chemical stability, biodistribution and to prevent aggregation and cytotoxicity (Soto et al., 2007; Lewinski et al., 2008). The size of nanoparticles has crucial effect on their fate when systemically injected into living organism. Smaller nanoparticles present advantages because are characterized by longer blood half-time and lower liver uptake. In general, nanoparticles size is fixed before synthesis procedure upon considerations regarding their fate in terms of therapeutic effect. The smaller the size the easier is the diffusion and so the distribution at targeted sites (Pelaz et al., 2017).

Jordan, one of the true pioneers of magnetic fluid hyperthermia in one of his crucial papers related to MFH (Jordan et al., 1997) investigated the abilities of silane and dextran magnetite nanoparticles (3–13 nm) to induce hyperthermia in vitro, and provided evidence of intracellular hyperthermia, apoptosis mechanism and tissue necrosis.

A few years later, Hilger (Hilger et al., 2001), provided a deep analysis related to a wide range of aspects of nanoparticles. He examined the effects of magnetite nanoparticles changing the shapes, the aspect ratios (difference among the various diameters and possible configurations), and the hydrodynamic diameters. All these features were tested on a human breast tissue and in in vivo experiments with murine tumors. A relevant increase in tissue temperatures was observed both in human tissue and in mouse tumor after the AMF application. For this study Hilger started with magnetite nanoparticles and synthesized super paramagnetic iron oxide nanoparticles for the treatment of breast cancer and investigated their effects in vivo. After several experiments histological results shown that heat was released in localized spots producing necrosis inside the tumor.

By investigating different magnetic nanoparticles (especially iron-oxide nanoparticles) it has been demonstrated that a crucial role is played by the coating. One of the most tested coating over the years was the dextran coating or the glucose coating. They are cheap to produce and to bound to iron-oxide nanoparticles. Probably the main reason because glucose (or dextran) is so popular as coating is related to his ability to be internalized by tumoral cells due to the huge need of nutrients of these cells. In 2009 Cassim (Cassim et al., 2009) synthesized ferromagnetic, dextran-coated nanoparticles with an average dimension of 100 nm and observed that these particles delivered heat to tumor cells without adversely affecting surrounding cells in vitro and in vivo. This result was another milestone in preclinical research related to MFH: it suggested that MFH could be a standalone therapy, not necessarily used in combination with radio or chemotherapy.

It is hard to tell when organic or inorganic coating could be necessary, it mainly depends on the cytotoxicity of the compound, if it could be relevant to help nanoparticles to get into cells, to enhance their ability to ablate cancerous tissue (for example enhancing their SAR-ILP) or to stretch their circulation time in the organism.

In a paper of 2014, Rana (Rana et al., 2014), reported about the effect of polyaniline coating of superparamagnetic iron-oxides Fe_3O_4 nanoparticles. These coated iron-oxides showed a huge improvement in killing tumor cells in vitro compared to their naked version. Coated version of this specific NP had higher SAR value due to greater stability (given by the coating) and induces magnetic hyperthermia in tumor cells with remarkable results.

Another relevant examples of coated magnetic nanoparticles, was reported in Majid et al., 2014. They synthesized iron oxide nanospheres (with a size range from 15 to 35 nm) with tunable shell thicknesses composed by silica layers. As compared with naked nanoparticles, magnetic NPs had higher SAR and higher efficiency in killing cancer cells in vitro.

Treatment of cancer have also been tackled exploiting different approaches of synthesis and different geometrical shapes of nanoparticles. Liu et al., 2016 synthesized a new class of $Fe_{0.6}Mn_{0.4}O$ nanoparticles called nanoflowers and used them to treat cancer cells in vitro and cancer tissue in vivo. Even at the lowest concentration used of around 50 μg/mL of nanoparticles, these NPs exhibited promising results as heat exchange mediator and inhibited tumor growth both in vitro and in vivo without affecting surrounding healthy cells. Liu et al., 2021, reported efficient magnetic nanocrystals of Mn-Zn ferrite produced with an average size of 50 nm and organically coated with biocompatible phospholipids. A huge efficiency as heat exchange mediators of such nanocrystals, upon exposition to electromagnetic field in destroying cancer cells causing necrosis both in vitro and in vivo, was reported.

Doping with magnesium a common superparamagnetic nanoparticle with a tiny hydrodynamic dimension (average diameter around 23 nm for the iron-oxide Fe_3O_4 core), Jang et al., 2018 developed an interesting tool that exhibited efficient heating and enhanced antitumor activity both in vitro and in vivo compared to any other commercially available NPs.

During the years, also the magnetic structure of the compounds has been deeply explored as in Hemery et al., 2017. In this study, authors compared monocore and multicore magnetic iron oxide nanoparticles Fe_3O_4 (with an approximate average dimension of around 58 nm). They applied the same external magnetic field to the two different NPs and evaluated the MFH efficiency on an in vitro model of human glioblastoma. The efficiency of the multicore NPs was detected not only by higher SAR-ILP value but also by the better and faster cellular internalization leading to a more effective destruction of tumoral cells.

Another important chapter of biomedical application of magnetic nanoparticles to tumoral cells is related to the combined action of chemotherapy and MFH mediated by NPs. Among this branch of study, a wide variety of examples are worth to mention, especially the ones related to the use of nanoparticle as a carrier.

Mieszawska et al., 2013 developed a biocompatible and thermoresponsive polymer-based nanomaterial loaded with doxorubicin to enhance the efficiency of the NPs treatment as antitumoral agent. Due to the heating produced by magnetic NPs once exposed to an alternating magnetic field, this polymer swelled and release doxorubicin from its pores on the surface. Thanks to this combined action the NPs became a platform able to kill cancer cells more efficiently than application of MFH protocols.

Another relevant example is related to doxorubicin coated magnetic microspheres of PLGA (polylactic glycolic acid) synthesized by Fang et al., 2015. These NPs were applied for a combined chemo-thermal therapy.

Doxorubicin was encapsulated inside the cores of hollow microspheres and when exposed to an alternating magnetic field, the heat exchanged by the magnetic nanoparticle induce doxorubicin release and rapid inhibition of tumor cell growth in vivo (Fang et al., 2015).

All these investigations and much more have conferred promising outcomes after application of the magnetic fluid hyperthermia in the treatment of cancers, but a few has been done regarding the chance to limit the interactions of magnetic nanoparticles with the whole organism, especially the healthy tissues. Basically, none of these studies have clearly declared assessed the effect of magnetic nanoparticle and the hyperthermia protocol on healthy cells. Further investigations must be performed and should be clearly focused on the comprehension of interactions between NPs and healthy tissues. In particular, the risk of overheating normal tissue surrounding tumoral lesion does exist and can constitute and important limitation for application of MFH.

During my PhD I had the chance to work with a peculiar class of iron-based NPs and apply them as heat exchange mediators able to do not harm the healthy tissues thanks to their self-controlled increase of temperature.

5. *Nanoparticles exhibiting self-regulating temperature for magnetic fluid hyperthermia*

One of the most critical issues to be solved for the successful application of magnetic fluid hyperthermia is to determine the ability of the nanoparticles to be able to target only the tumoral cells and to only harm the malignancy and not the healthy tissue surrounding it. Over the years several approaches have been performed to tackle this issue but none of them seemed to be adequate.

Among the most promising ones there was the chance to develop nanoparticles as bioimaging contrast agents for Magnetic Resonance Imaging (MRI) and other imaging techniques. In general, the development of novel contrast mechanisms and labeling agents for MRI is important to better understand cell tracking by a non-invasive way and the eventual readouts of different physiological conditions both in vitro and in vivo (Ahrens et al., 2013; Shapiro et al., 2004). A huge number of synthesis attempts has been performed to define which chemical compound could be better to be used as a biomarker for magnetic fluid hyperthermia applied to tumoral tissues including usage of conventional magnetic materials for the preparation of nanoscale particles useful for MRI also (Bulte et al., 2004)

The appropriate selection of the most suitable magnetic material as contrast agent in MRI and at the same time performing MFH is based on several parameters. It is essential to choose the magnetic material which could be more adapt at physiological conditions around 37 °C (so with a working temperature around 37°C). Among these materials, a wide range of compositions has been explored as iron, iron oxides, manganese oxides, mixed materials formulation, and mixed metal formulations.

All these materials share an important feature, the Curie temperature. In Physics, the Curie Temperature (T_c) is the temperature related to the transition from ferromagnetic to paramagnetic state of matter. T_c is the value above which a ferromagnetic material switches its whole magnetic moment orientation following the orientation provided by the external magnetic field. It must be observed that most of the metals (and so of the magnetic nanoparticles) have Curie Temperatures in the order of hundreds of Celsius degrees revealing almost impossible to observe and exploit the advantage derived from this energetic transition.

To understand the ability of the magnetic material to serve as a heat mediator and at the same time as a contrast agent it is relevant to know that MRI takes place with specific DC magnetic field settings related to typical magnetic field magnitude between 0.5T and 20T where any sort of magnetic material is almost completely saturated. In this scenario it is hard to find a dependency of the net magnetization of the lattice (or of the nanoparticles cluster) that really depends upon other variables such as pH of the solution, temperature, chemical composition of the material and other common physiological parameters. Taking into account this factor, it is clear that it is not easy to design a magnetic material having relevant switchable magnetic properties useful for a safe and reliable MFH and at the same time a high contrast ratio to be observed at standard working temperature (physiological temperature) in tomographic imaging at high DC magnetic fields.

During my PhD I had the chance to focus my attention and efforts on an interesting class of magnetic materials commonly known as magnetocaloric materials. This class of materials provide a close match to the requirements depicted above related to the design of a high contrast ratio switchable and tunable MRI contrast agents (Banobre et al., 2018; Moya et al., 2014; Barbic et al., 2019).

A closer examination of the whole class of magnetocaloric materials led us to know that some of them have extremely sharp first and second order magnetic phase transitions at physiological temperatures. These phase transitions can have a positive or a negative slope of magnetization versus temperature making them interesting candidates for switchable MRI contrast agents.

It is relevant to briefly summarize what a magnetic phase transition is and why it is so important for the application of magnetic materials as imaging biomarker and heat exchange mediators (McHenry et al., 2002).

Magnetic phase transition can occur when we are in the presence of a magnetic order defined as collective magnetism. This order appears in materials characterized by a particular ordering temperature, for example the already mentioned Curie Temperature (T_C) or the Néel Temperature T_N). These temperatures are examples of a class of physical phenomena which are described as magnetic phase transitions. The physical properties and thermodynamics of these phase transitions can be described by energy functions, in terms of magnetization phase diagrams, or in terms of critical exponents that describe the variation of thermodynamic properties (as a function of the order parameter) as the ordering temperature is approached.

At a closer mathematical look: first order magnetic phase transition works at temperature $T < T_C$ where T_C is a critical parameter. H as the intensity of the magnetic field, the magnetization M has a discontinuity at $H = 0$ for $T < T_C$. Considering the Landau theory of magnetic transitions and the mean field approximation it is possible to consider magnetization as a self – consistent equation

$$M = \tanh\left(\beta(H + 2DM)\right)$$

where D is the number of spatial dimensions.

Keeping $H = 0$ and changing the temperature T, it is possible to encounter a transition at $T = T_C$. During this transition the order parameter, M, remains in the continuous domain but its derivative with respect to temperature $\partial M/\partial T$ changes discontinuously generating a second order magnetic phase transition.

In conclusion, nowadays magnetocaloric materials tuned through material science techniques, as doping or thermal treatments, are of great relevance as a new generation of magnetic fluid hyperthermia mediators.

During my PhD I have characterized and exploited an iron-based magnetocaloric material composed by different phases. Such material was endowed with the innovative self-regulating heating ability: this effect consists in a stable increase of temperature up to a certain maximum (self-regulating temperature or T_{SR}) below the T_C of the material itself once exposed to an AMF.

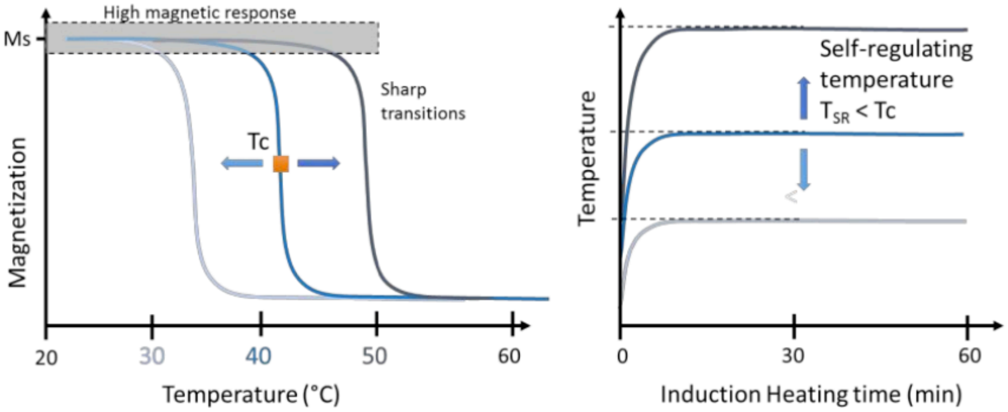

Figure 5. Magnetization decreases with temperature for materials with different T_C and a theorical example of self-regulating temperature achieved during AMF exposure for materials

with different T_C. (courtesy of MBN Nanomaterialia, Carbonera di Treviso, Treviso, Italy)

These nanoparticles have been employed as heating agents against breast cancer both for in vitro and in vivo studies. As already described, the heating of the nanoparticles can be produced through different dissipation mechanisms (Néel and Brownian relaxation). According to the explanations related to magnetic phase transitions, when the material is approaching T_c, both the magnetization and the magnetic anisotropy decrease, with a progressive lowering of the efficiency as heat exchange mediator. It is well known that Néel losses scale as magnetization saturation, therefore above T_c, once magnetization is negligible, magnetic losses tend to become negligible too, switching off the heating mechanisms. Considering local heat losses, nanoparticles start to reach an equilibrium condition at a temperature level named T_{SR}, smaller than the T_C. As a direct consequence this effect provides an intrinsic control for induction heating during the energy conversion when a sharp magnetic transition occurs.

Regarding the iron-based nanoparticles employed during my research activities, T_C corresponds to a second order magnetic transition, that can be observed at the threshold between ferromagnetism to paramagnetism. Once exceeded this temperature there is no more magnetic order. Paramagnetism takes place and so the net magnetization is equal to zero. In this way the related possible magnetic losses stimulated by the energy exchange with the external electromagnetic field have been switched off completely, erasing the ability of the NPs to transform AMF absorbed into heat. The modulation of T_C can be produced by modifying the ferromagnetic bulk lattice perturbing it with the introduction of a dopant, in this case a non-ferromagnetic material. Usually, this process can be performed in several ways: introducing a non-metal element to decrease the T_C (materials as perovskite manganates with La); introducing elements like Cu, Ag or Cr to directly modify the T_C. One of the biggest concerns about this second method is related to the existent correlation between net magnetization and T_C of each single element introduced in the ferromagnetic lattice. During the synthesis and doping procedure, it is possible to lower the global T_C diluting the chemical solution. As a downside of a similar process there is the reduction of the heating efficiency of the whole material.

To obtain a material that could be exploited for safe MFH as well as contrast agent in MRI it is essential to control the modulation of composition, the structural and chemical disorders as well as magnetic properties and magnetic anisotropy. To enhance heat exchange mediator features it is essential to exhibit hysteretic behavior considering anisotropy and size of the final compound.

Particularly for iron oxides nanoparticles it is important to identify critical diameters and sizes among different regimes: the multi magnetic domains nanoparticles, the single magnetic domain nanoparticles, and the superparamagnetic domain nanoparticles. The most influent mechanisms related to heat induction, as Néel and Brownian relaxation process, are size and temperature dependent and that is why to achieve heating efficiency it is not common to reduce too much the average size of the crystal lattice. The description of the nanoscale system tunable magnetic nanoparticles also involves many other variables that tend to complexify the heating dynamics.

Although many considerations and theories have been developed to theoretically describe the induction heating phenomenon in nanoparticles and the heat exchange with the surrounding matrix, a clear description of this phenomenon approaching the T_C is still missing as well as precise considerations on dynamical magnetic phase transitions of nanoparticles from ferromagnetic to paramagnetic behavior going through T_C. Despite the promising tuneability of magnetic properties, the potential biomedical applications of the existing magnetic materials have not been explored up to now. Several approaches have been investigated as the interaction with the external matrix under alternated magnetic fields, their size distribution and structural morphology.

My work during the PhD has been focused on magnetic induction heating of self-regulating temperature iron oxides for safe and efficient hyperthermia. In order to monitor the efficacy of the treatment and the ability of the chosen particle to act as a contrast agent it was employed magnetic resonance imaging (MRI) and magnetic particle imaging (MPI). During the last years, for therapeutic purposes, MFH as been associated with different imaging techniques to observe the heating effects tumor tissues. Often, conventional, and already commercial iron oxides have been employed, demonstrating the chance of a localized treatment but, at the same time, the need of intrinsic control of the temperature increase, to safely avoid overheating of healthy tissues composing the tumor microenvironment.

So far, the major challenges of magnetic hyperthermia treatment tackled by researchers are related to the uniform control of temperature in the malignancy area and in the surrounding neighborhood and the enhancement of the half-life of magnetic nanoparticles in the bloodstream to increase the chance of target the tumor while injected intravenously. Considering cancer diagnostics, it is of great relevance to develop not only efficient heat mediator but also powerful contrast agent able to monitor the treatment provided. The intrinsic high level of toxicity of most of the metals do not simplify this search however a wide range of chemical compounds has been clinically approved and tested to be successfully applied as theranostic agents (which means that a single tracer could provide both diagnosis and treatment of the tumor).

Specifically, during my PhD, I have worked on a peculiar iron-based nanoparticle composed by different phases of magnetic material and able to simultaneously treat and diagnose cancer that could be defined as theranostic agent. The lack of control on the MFH treatments has been overcome by this innovative material that enable the operator to push hyperthermia in cancer tissue without risking the healthy cells. To be applied for such theranostic purposes, these nanoparticles were finely characterized through a wide range of invasive techniques as InfraRed Spectroscopy, XRD spectroscopy, Transmission Electron Microscopy, Dynamic Light Scattering and Magnetic Resonance Imaging. Once coated with a biocompatible double shell of organic components as citrate and glucose (more recent tests have been performed with a chitosan variant) to provide a good suspension and colloidal stability to the compound in physiological conditions. Their self-regulating heating mechanism has been tested in a non-clinical range of temperature (from 25 to 75 degrees) and monitored through MRI to observe the switch in contrast ratio defined by the second order magnetic phase transition.

Exploiting their iron-based chemical nature it was possible also to test a relevant innovation in the field of biomedical imaging, the MPI technique coupled with MRI. It has allowed to test the efficiency of these particles as tomographic contrast agent with a temperature dependent magnetic relaxation.

All the knowledge developed so far gave rise to a finely tuning magnetic nanomaterials by design able to perform switch in contrast ratio and to provide a strong tool for MFH treatments in vitro and in vivo.

6. *Magnetic Particle Imaging and Magnetic Resonance Imaging*

During my PhD it soon raised the necessity of observing magnetic nanoparticles to monitor their biodistribution in vivo, their cytotoxicity, their ability to serve as contrast agent and their ability to play as heat exchange mediator while and after performing magnetic fluid hyperthermia treatments. Due to the chance of using the MRI routinely and considering the long history of iron-based contrast agents I have performed a consistent number of acquisitions and analysis by MRI to monitor the nanoparticles, naked, coated and during in vivo experiments. MRI is probably the most suitable tomographic technique used to observe iron-based magnetic nanoparticles due to its high contrast ratio, its sensitivity, the well-known literature and established protocols and its preclinical and clinical use.

However, during my PhD I was lucky enough to test a wide range of other imaging modalities, from advanced microscopy molecular imaging to structural imaging. But none of these seemed to be as useful, precise, and powerful as MRI up to the invention of Magnetic Particle Imaging (MPI). To better understand the revolution introduced by this tomographic technique it could be useful to make a small step behind and describe how it was developed (Gleich et al., 2005).

Contrast agents and tracers in medical imaging provide important information for diagnosis and therapy, but for a few specific applications it could be required a higher resolution, both spatial and temporal, respect to currently available medical imaging techniques as MRI (Beuf et al., 2004, Hendrick et al., 1993, Sosnovik et al., 2005). In magnetic resonance imaging the use of magnetic tracers strictly depends on background signal from the host tissue and from the microenvironment of the tissue of interest. Specific threshold has been studied over the years concerning the in vitro and in vivo (Nunn et al, 1997) detection limit setting up the overall resolution of the MRI related to the biomedical application of magnetic nanoparticles. MRI allows to observe iron-based nanoparticles starting from the magnetic relaxation induced in the tissue of interest. Magnetic nanoparticles would generate a lack of signal (void signal) in the tissue due to their magnetic components. This is what is called an indirect measure of the presence of nanoparticles because it is not based on the signal itself of the compound but on the change in relaxation (for T_1 and T_2 measures) induced by their own presence. Considering this peculiar feature of MRI, a sensitive method for detecting the magnetic particles directly was invented by Gleich and Weizenecker (Gleich et al., 2005) and it is based on the direct measure of magnetic fields generated by nanoparticles exploiting their relaxometry (Romanus et al., 2002). Collecting the data as spatial points it came out a relevant drawback about the low spatial resolution reserved for this imaging modality. The innovation of the MPI was about this direct molecular imaging modality bounded to several mathematical methods employed to achieve high-resolution images of magnetic tracers by means of the nonlinear magnetization curve of nanoparticles. Already the first experiments achieved a spatial resolution below 1 mm, defining MPI as a high spatial resolution and high sensitivity tomographic imaging technique.

MPI relies on the nonlinearity of the magnetization curves of ferromagnetic material and the fact that the particle magnetization saturates at some magnetic field strength. It is possible to apply to magnetic nanoparticles an oscillating magnetic field, called the 'modulation field', with a specific frequency f_1 and amplitude A: once applied the magnetic material will demonstrate his own magnetization as a function of time M(t). This function is composed by the so-called drive frequency f_1 and his harmonics. Through appropriate filtering the higher harmonics could be easily split from the collected signal. Once applied the modulation field it is possible to superimpose another magnetic field with a relevant large magnitude and constant in time. At this point magnetic nanoparticles saturate and once saturated there is no more harmonics generation. This physical phenomenon gives rise to the chance of spatially encoding the nanoparticles positions. But to do so it is crucial to introduce another magnetic field, the so-called selection field; a time independent magnetic field that is equal to zero and vanishes in the so-called field free point (FFP), a specific region at the center of the imaging device with a complete lack of magnetic field and increasing magnetic field magnitude close to the edge of the field. Because of the superimposition of these three magnetic fields, if there is any magnetic material at the position of the FFP it will produce a signal containing higher harmonics, but all the other magnetic material remains saturated. Once defined this mathematical and physical concept and applied to more dimensions it is possible to consider also regions of interest and even volume of interest, generating a 2D or 3D tomographic image. Even considering a generation of a 3D image (defined by a 3D spatial encoding), it is sufficient to use a single selection field because a spatial variation in one single direction of the field will generally be followed by variations on the other components in other directions. To generate the necessary movement, it would be sufficient to move the whole coil, or the object inserted inside the coil. To simplify the physical understanding of the events it could be assumed a fixed low amplitude of the magnetic field. Otherwise, the magnetic field would shift the FFP significantly.

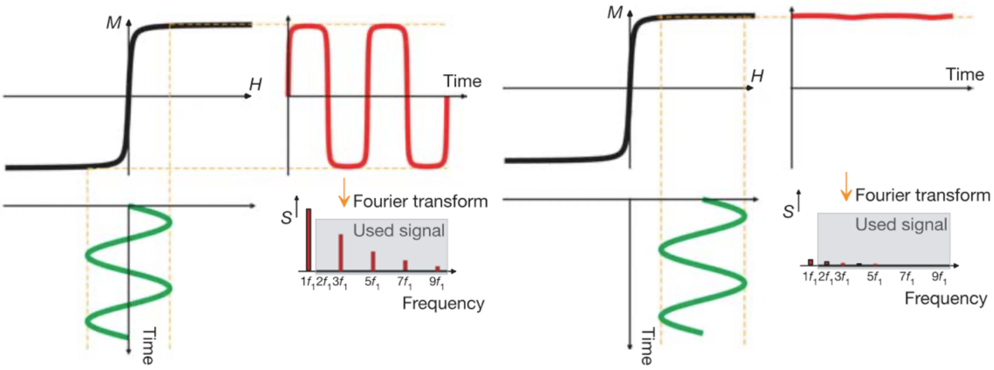

Figure 6. These graphs were famous in the early days of MPI and still are meaningful. The left one represents an oscillating magnetic field at a frequency f_1 (green curve), the nonlinear magnetization curve (black curve) and the time-dependent magnetization (red curve) with the higher harmonics expressed by the below Fourier transform. On the right an off set is applied to the oscillating magnetic field and observing the field in the saturated region it is possible to deduce that no harmonics have been produced and so the Fourier transform has produced no signal (image reproduced from Gleich and Weizenecker, 2005).

To conclude this brief introduction to physical principles of MPI, to form an image with this new tomographic modality the magnetic tracer material must be applied to the object. The object itself must be placed in the selection field with a superimposition of a modulation field. To produce the spatial encoding of the signal the object must be moved to discrete positions and during this movement the magnitudes of the harmonics have to be recorded. Mapping the magnitude of the harmonics analyzed through the Fourier transform of the harmonics signal it is possible to produce an image of the magnetic tracer directly by its own magnetic signal.

Even so the method described below lead us to the conclusion that the signal to noise ratio (SNR) is still low due to the weak modulation magnetic field introduced and to the mechanical movement that leads to a necessary low scanning speed. Due to these evidences, it was necessary to introduce the so called drive fields, three orthogonal magnetic fields provided form external sources. Thanks to the drive fields, the three components of the selection field could be erased in any spatial direction. Additionally, it is possible to generate the driving fields through a coil pair with specific design of the current waveform, in this way it would be easier to move the trajectory of the FFP over the magnetic object that has to be observed. The advantage of using the drive fields is that they could accelerate the movement of the FFP dramatically. To produce a sufficiently strong drive field, able to erase at any point in space the selection field, it is crucial to apply a sinusoidal current with a high frequency to each coil pair applied to the whole system.

Once the FFP (now fastened by the drive fields) passes on a location of the magnetic object there would be a significant change in magnetization. This change could be translated into a signal in the recording coil showing higher harmonics of the drive fields. The image reconstruction method is now based on this data, acquired in a faster and reliable way due to the drive fields. Moreover, the presence itself of the drive fields makes the presence of the low modulation field completely obsolete. Through the introduction of the drive fields in each spatial direction it is possible to overcome the lack of the image reconstruction method mentioned before, the low SNR and the low encoding speed due to the previous mechanical movements.

An alternating way to produce the spatial encoding of the image would be of mixing the two different acquisition modalities, the mechanical movement, and the presence of the FFP.

During the last decade there were built several custom scanners for the MPI and also commercial scanners, one from Bruker-Biospin (Preclinical Magnetic Particle Imaging) and the other one from Magnetic Insight (Momentum Magnetic Particle Imager). Nowadays, the existing MPI systems are limited to small animal- sized bores with bores up to up to around 1.2 m (Panagiotopoulos et al., 2015) and magnetic gradient strengths up to 7 T/m (Yu et al., 2017). The actual fastest Image acquisition times with the available scanners have been shown to be equal to 20 ms per acquisition for smaller fields of view (Panagiotopoulos et al., 2015). As underlined in Harvell-Smith et al., 2022, MPI sensitivity and contrast are competitive with MRI cell tracking and imaging applications and even so it is possible to conclude that MPI sensitivity has not yet achieved the true physics limit. This leave room for further optimization of the sensitivity through the implementation of more refined electronics that would allow to detect even smaller amount of iron up to a few picograms of iron per voxel with a reduced scan time (respect to the actual limit of around 20 seconds).

All of the scanners built have adopted a scan modality considering the system that had to be observed. In general, it is well known that there are two main modalities of acquisition. The one described before that exploit the so called FFP, which could produce 3D images and the field free line, or FFL. This second one could produce projection images that lead to consistently high-resolution images respect to FFP acquisitions. In particular, the FFL approach achieve up to orders of magnitude higher speed and SNR for image reconstruction over FFP scanning modality (Ferguson et al., 2015; Goodwill et al., 2012).

Considering the application of the MPI imaging modality to the localization of magnetic nanoparticles and to track magnetic fluid hyperthermia damages there raises several considerations.

The enormous advantage of the MPI over the other techniques is based on the complete absence of biological signal derived from the background due to the biological tissues. The only signal acquired derives from magnetic signal produced by magnetic objects with a proper relaxation. This gives rise to a high positive and direct image contrast and SNR for magnetic tracers (especially superparamagnetic tracers or SPIO) (Weizenecker et al., 2009).

The physics governing MPI is different from MRI, and it is not possible to perform MPI in an MRI scanner. The MPI signal comes from SPIO or proper magnetic tracers in general as they immediately respond to an externally applied magnetic field. Nanoparticle’s dynamics and magnetic relaxation is well defined by Langevin physics. Once activated the external magnetic fields the magnetic moments of the particles align with applied magnetic fields until they reach superparamagnetic saturation. As already explained the spatial encoding of the image itself derived from the MPI signal is based on the saturation of the SPIOs with a strong gradient field and the drive fields which move the FFP or the FFL to acquire the signal without any other background noise from other regions. It is crucial to understand that the induced signal is linearly proportional to the amount of iron present in the sample analyzed. This fact enables a linear reconstruction

process and allows to define a precise point spread function (PSF), useful to determine the relaxivity of the nanoparticles themselves (Goodwill et al., 2010; Lu et al., 2013).
As mentioned before MPI has been applied already to the monitoring of damages produced by MFH through the heat exchange of iron-based nanoparticles. In particular, in the last decade, a considerable effort has been spent to set up a proper imaging modality able to directly observe the heating exchange process. In this case MPI has demonstrated to be more efficient than conventional molecular imaging techniques (Tay et al., 2018; Du et al., 2019; Yu et al., 2017). MFH has demonstrated to be quite a challenge to be understood and detected with conventional methods over the years. First and foremost, iron-based nanoparticles delivered systemically aggregates and accumulates in off-target organs even if properly chemical coated. Without a proper spatial control of the heating mechanism a huge damage could be induced in the healthy organs while treating the malignancy. Another challenge is related to the ability of the actual imaging modalities to be quantitative over the dose of iron used as heat mediators. Up to MPI introduction on the market for research purpose there was no chance to be accurate in the estimate of the dose of iron present in a specific spatial location, especially for deeper tissues.
MPI seems to be able to address all the challenges proposed. Compared to MRI, MPI safety is bound by SAR and the stimulation itself of the magnetic nanoparticles. Considering so MPI has remarkable advantages respect to another tomographic imaging modality as MRI. First of all, MPI has demonstrated to be more sensitive respect to MRI in terms of iron dose detected. MPI goes even under picograms of iron (Graeser et al., 2017; Saritas et al, 2013). The real time imaging guaranteed by MPI also is a specific feature of this new imaging modality with a temporal resolution that goes far beyond any other imaging techniques, approximately around 46 frame per second (Ludewig et al., 2017). Unlike MRI, it is also a direct quantitative method that could precisely estimate the dose of iron present in a specific spatial area. This detection is possible thanks to MPI physics that is based on magnetic saturation of iron-based contrast agents almost everywhere except the field free region (that could be a field free point or a field free line). In this area, the unsaturated tracers can respond to small excitation (up to 20 mT) and produce spatially accurate reconstruction of the volume observed.

Among the advantages of the MPI above the other techniques applied to observe directly or not MFH there is the fact that the iron core used to generate the MPI signal could be exploited to generate heat for MFH. Heat, as well as MPI signal, is generated by rotation of magnetic moments that produces a signal in MPI. Thanks to the dipole rotation of the nanoparticles, the MPI signal could detect at the same time not only the position of the nanoparticle, but also the position of the MFH treatment itself and monitor it in real time. This detection method is based on a gradient magnetic fields-based mechanism that magnetically lock the nanoparticles in a single place through magnetic saturation and prevent rotation to generate heat or MPI signal. Only the field free region will produce a signal that would localize at the same time the nanoparticle and MFH. The only weakness of this method that is based on precise thermal dose localization with high spatial resolution is the dependency from magnetic gradient strength. Consider so, there is still plenty of room to improve the spatial resolution of this imaging technique.

To ensure heating only in magnetic hyperthermia stage and not on other frequencies (during the imaging stage) it would be possible to employ low frequency (20 kHz) for imaging purpose and higher frequency for hyperthermia purpose (around 350 kHz as suggested by preclinical and clinical trials).

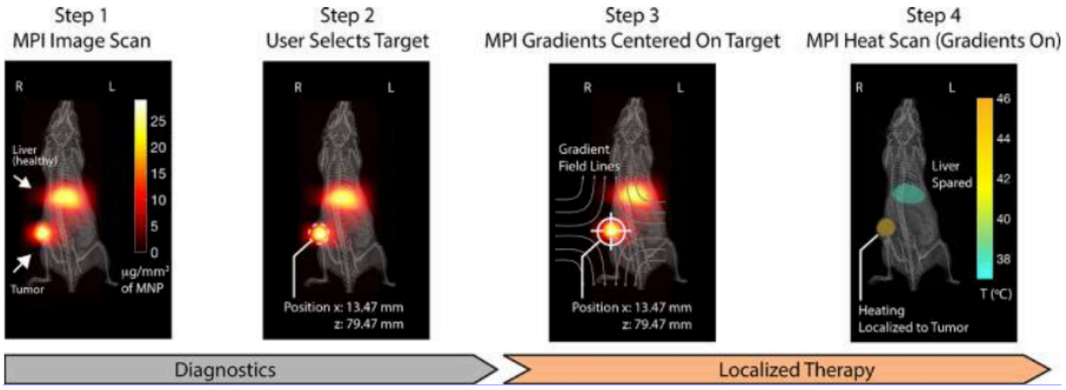

Figure 7. An example of the theranostic platform defined by the MPI application to a case of U87MG xenograft mouse model. Iron-based nanoparticles were found both in the tumor as well as in the organ, but it was possible to isolate the tumor region and heat it up through MFH treatment performed with the MPI itself set at another frequency. In this way, heat is localized only via FFP/FFL and the collateral damages are minimized (image reproduced from Tay et al., 2018).

Exploiting iron-based nanoparticles for MFH treatments I have used the most common tomographic technique to monitor nanoparticles spreading all over the organism, nanoparticles magnetic efficiency as contrast agents and as heat exchange mediator and the damages produced by MFH.

It is well known that Magnetic Resonance Imaging (MRI) is a non-invasive diagnostic technique (Shokrollahi et al., 2013; Laurent et al., 2009). Main features of MRI include imaging flexibility, it is harmless for the patient and highly accepted, it has a high spatial resolution and an optimized soft tissue contrast considering the different types of tissues that could be observed. It is also quantitative providing several physiological parameters and important clinical information (Caravan et al., 1999; Na et al., 2009; Strijkers et al., 2007). Among all the important features deeply explored in preclinical and clinical research all over the years there stands out the strong spatial resolution negatively affected by the lack of proper probes used as contrast agent or tracers with high sensitivity. In the last couple of decades, a wide range of biocompatible materials (mostly in form of nanoparticles) have been tested as positive or negative contrast agents.

Exploiting magnetic nanoparticles with a high SNR able to enhance MRI sensitivity many attempts have been made to improve sensitivity and facilitate biological and functional information. As a result, a wide range of magnetic nanoparticles like paramagnetic and superparamagnetic iron oxide-based compositions have emerged (Hofmann-Amtenbrink et al., 2010; Senpan et al., 2009; Jin et al., 2014).

Considering MRI as a molecular imaging technique compared to MPI the major lack of MRI is its lower temporal sensitivity and lower specificity for contrast agents (Figure 8) However, MRI contrast agents act by shortening T_1 (longitudinal magnetization) and T_2 (transverse magnetization) providing adequate relaxivity and susceptibility effects, biological and biomedical safety, very low toxicity, optimal stability and biodistribution as well as a proven elimination by the organism.

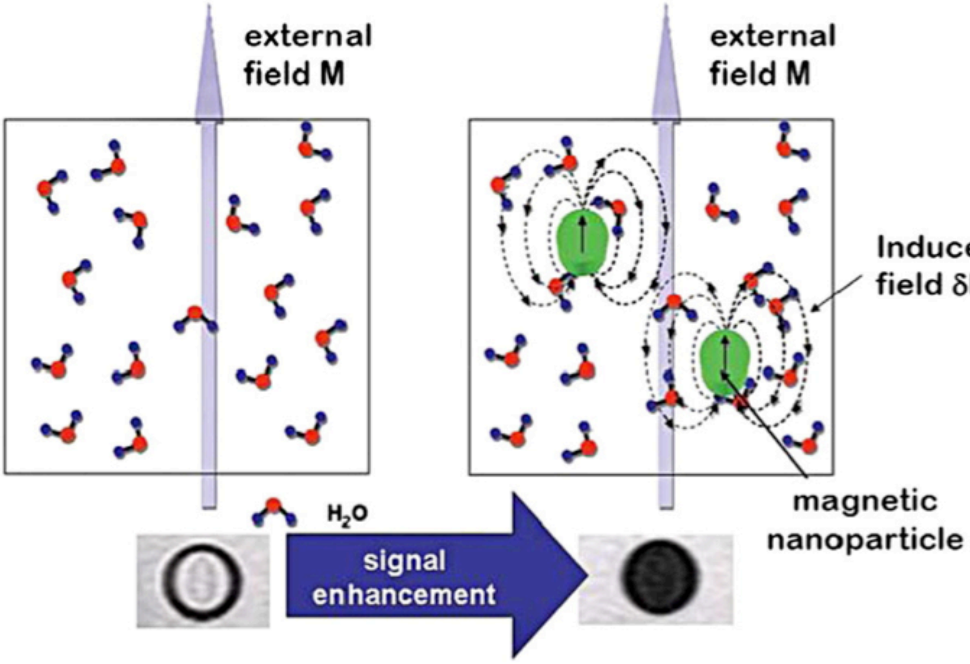

Figure 8. An example of how it works the production of contrast in MRI through magnetic nanoparticles. Water molecules present in the tissue would be oriented through the induced magnetic field produced by the magnetic response of the contrast agent, in this case nanoparticles. This reorientation of the water molecules changes the signal produced by the tissue itself composing the contrast ratio change (Image reproduced from Jun et al., 2007).

It is possible to divide MRI contrast agents following two different lines: the clinical application line or the chemical composition line. Considering the first one there are two different kinds of contrast agents: the positive contrast agents and the negative ones. The first category is basically related to extracellular agents and blood pool imaging, the second one concerns passive targeting (Yao et al., 2020). In my case of study, tumor imaging and nanoparticles applied as heat exchange mediators in the organism, I have exploited positive contrast agents.

Considering the chemical composition there are two main categories: the paramagnetic contrast agents and the superparamagnetic ones. As already explained from a physical perspective the difference is basically that superparamagnetic compounds could form a significantly larger magnetic moment and are based on an iron-oxide core composed mainly by iron. This type of contrast agent shortens T_2 relaxation times acting negligibly on T_1 relaxation times.

One of the most relevant downsides of using magnetic nanoparticles as contrast agents in MRI is that to achieve sufficient contrast for imaging purpose it is necessary to use high concentrations of nanoparticles with very high saturation magnetization. Considering this feature, it is important to choose the most suitable material to synthetize the nanoparticles. Superparamagnetic nanoparticles have a higher magnetic moment requiring lower concentrations respect to paramagnetic nanoparticles. Moreover, the average size of superparamagnetic nanoparticles is smaller than paramagnetic ones. This geometrical characteristic allows them to be cleared faster and mostly without consequences from the host organism. To produce an efficient contrast agent that could be exploited as tracer for MRI it is essential to be focused on different aspects of the nanoparticle. In particular it would be fundamental to define the precise material composition (and so the crystal structure) and the size and shape of the nanoparticle (Sharifi et al., 2012; Pankhurst et al., 2009). The size dependency crucially influences the MR signal enhancement. Smaller particles are characterized by a low r_2/r_1 ratio. In the nanoscale regime, surface magnetic spins tend to be tilted to form a magnetically disordered spin surface layer which has a significant effect on the magnetic moments and MR contrast-enhancement effects (Bodganov et al., 2011). As the particle size decreases, the surface effect becomes dominant as the particle size decreases and so the net magnetic moment. In Figure 7 it is demonstrated how the nanoparticles could affect the relaxation processes of the protons in the surrounding water molecules resulting in shortening of the spin-spin relaxation time of the proton themselves. This fact results in a void signal enhancement during the MRI acquisitions.

MR images could display all kinds of soft tissues considering different values of T_2 relaxations. Exploiting this feature, the iron-based contrast agent with a high saturation magnetization could be clearly visible in MRI because it induces a T_2 relaxation value completely different from the surrounding healthy tissues.

It is well known that iron-based nanoparticles (especially superparamagnetic ones) properly coated with organic molecules have a competitive relaxivity, a consistent blood retention time, high biocompatibility, and biodegradability due to low toxicity (Harisinghani et al., 2003; Dragar et al., 2021; Hartshorn et al., 2018). As mentioned before, due to their relevant magnetic core and to the production of an enhanced proton relaxation, iron-based nanoparticles could be used with lower doses respect to other kind of nanoparticles as MRI contrast agents. The issue related to the dose employed as imaging agent is still actual. It is one of the cardinal points that makes MPI so important. As already explained, Magnetic Particle Imaging can observe ultralow amount of iron (up to a few picograms of iron) with a poor spatial resolution but a consistent temporal resolution. On the other hand, MRI can observe bigger amounts of iron with a high spatial resolution but with a poor temporal resolution.

The need of an efficient contrast agent could be also explained considering that the typical receptors are present in the organism with a very low concentration (approximately around 10^{-11} $molg^{-1}$. To observe such sparse biomarkers, it is necessary to apply different strategies. For example, it could be increased the effective relaxivity per particle containing the potential high level of cytotoxicity during the synthesis procedure. Nowadays an entire class of materials is applied and devoted to this purpose: magnetite, maghemite, ferrite, nickel, cobalt, cobalt ferrite and so on and so forth.

In the last decade the search for an efficient T_2 contrast agent for MRI was focused on iron-based nanoparticles (from ferromagnetic to superparamagnetic ones). Lack of cytotoxicity, chemical and physical stability over time and biodegradability were the main issues considered and tackled. On the top of these issues there was also the difficulty related to the artifacts produced by the iron-based nanoparticle due to magnetic susceptibility. To answer all these expectations different synthesis procedures were tested over the years and almost an infinite set of coatings were proven. The most common ones were dextran and glucose coatings, citrate, or other organic molecules, polyethyleneglycol (PEG) and chitosan. All these coatings have high biocompatibility and the enhanced chemical and physical stability over time. Regarding this issue, Mailander et al., 2008, and Wang et al., 2017 provided a comprehensive update of the stabilization procedure and availability on the market of commonly used magnetic nanoparticles.

The issue related to chemical stability and biocompatibility will never be stressed enough: it is one of the major problems associated with magnetic nanoparticles that tend to aggregate in the blood stream leading to the blocking of the blood flow and their stocking in the liver instead of reaching the desired target. In MRI this issue could be easily observed through nanoparticles biodistribution once injected intravenously in a mouse model (for preclinical studies).

During my PhD I had the chance to test a wide range of contrast agents produced with different synthesis procedures and employed for various aims, from blood pool contrast agents, to tumoral target specific tracers and heat exchange theranostic mediators. For my main working activity, I have tested iron-based contrast agents able to perform MFH treatments with a consistent T_2 relaxation able to be observed in MRI with the most common imaging sequences.

7. Nanoparticle delivery to the tumor site: present and further steps

Treating tumors with nanoparticles allows to have a clear view about the biodistribution of magnetic compounds once injected intravenously or intratumorally. The physiological pathways as well as the efficiency of the contrast and heating agent is completely different and is heavily affected by the injection path chosen. In the intratumoral injection it is possible to observe the behavior of the particles related to the high intratumoral pressure and the huge angiogenesis locally present in the tumor surroundings. The efficiency of the magnetic agent is maximized considering that there is almost no waste of the nanoparticles that are collected by the tumor itself. The intravenous injection is completely different. It is crucial to fix and define several parameters of the nanoparticles as their chemical stability, their ability to bound the plasma and serum proteins, their ability to reach the desired target, their biocompatibility, their half-life in the blood stream, the ability of the nanoparticles to evade the liver endothelial reticulum and so on and so forth. A part from these two mainstream line of nanoparticles administration there is also the magnetic targeting. This technique allows to improve the accumulation of nanoparticles in the tumoral area exploiting external magnetic fields used as guides to attract nanoparticles in a specific site. It has been already tested with interesting results (Angelakeris et al., 2017). During my PhD I have performed several in vivo studies to observe the efficiency of the nanoparticles as heat mediators against tumors. Considering the huge number of difficulties hided by the intravenous injections, almost all these studies have been performed exploiting local intratumoral injection of the contrast agent. Although a few in vivo trials have been finally performed to study new treatment protocols to maximize the efficacy of MFH on tumors by using specific macrophages to evade the ability of the RES to block the nanoparticles in the liver. The macrophages have the specific function to saturate the RES before the intravenous nanoparticles injection in order to help them reach the target by the blood stream before being cleaned by the physiological pathway.

It is well known that magnetic nanoparticles must be delivered to the target body site and should be kept inside the tumor to reach a sufficient concentration to act as hyperthermic agent. As already mentioned, there are two different approaches for the delivery of nanoparticles.

Intratumoral injection, that is the easiest way to administer nanoparticles in the tumor. Different clinical trials for MFH have already tested this physiological pathway (Johannsen et al., 2010). Via this way it is clearly easy to achieve a high concentration of nanoparticles in the tumor site. However, this method has several downsides. First, it is suitable only for certain type of tumors, especially the most superficial and accessible ones. Second it guarantees a non-homogeneous distribution of nanoparticles because once injected inside the tumor it is hard to obtain a plain and homogeneous distribution of the nanoparticles. Moreover, the high concentration of nanomaterial does not consider the toxicity fluctuations. Tumoral cells could start dying not only because of the treatment but also because of the high cytotoxicity of the nanoparticle's aggregates (Huang et al., 2013).

Intravenous injection mainly exploits the so-called enhanced permeability and retention effect (EPR effect) (Acharya et al., 2011). This effect is based on the pathophysiological characteristics of tumors in comparison to healthy tissues. In these last ones, small molecules or drugs could easily extravasate from blood vessels. This chance is neglected to nanoparticles considering their typical size. Otherwise in the tumors, the wide-open fenestrations in the blood vessels membrane allow the extravasation of materials with sizes up to several hundreds of nanometers, including so the nanoparticles. The EPR effect seems to be one of the main (if not the main) contributors to the accumulation of nanoparticles in the tumoral tissue. It is crucial to understand that each tumor has his own EPR effect considering the mass of the tumor, the angiogenesis, the growth rate in time and many other parameters related to the tumor itself. Considering so, the EPR effect is highly heterogeneous and could change over time quite easily, that is why it is considered a passive targeting mechanism and it could not be considered the one and only target mechanism for the intravenous injections.

To critically exploit EPR effect, magnetic nanoparticles should be able to have a long enough half-life in the blood stream. Considering so, nanoparticles should have a hydrodynamic size of around 200 nm at most to evade the liver clearance due to the presence of RES and at least a dimeter around 50 nm to avoid kidneys clearance. (Krishnan et al., 2010; Das et al., 2019).

Another critical parameter related to the circulation of nanoparticles in the blood stream is the chemical coating (organic or inorganic). Coating plays a crucial role in the permeability of the nanoparticles in cancer cells as well as in healthy cells. It mainly contributes to stability over time of the compound in the blood stream and contributes to generate stability to the whole solution; it prevents aggregation and keep the hydrodynamic radius under defined dimensions. The chemical coating could also be part of the mechanism of active delivery improving the specificity of the nanoparticles for the tumor. Once properly coated with a first shell, nanoparticles could undergo a process of functionalization of their surface with targeting agents as antibodies, antibodies fragments, receptors, peptides, and many other alternatives. All these biological factors could actively contribute to the targeting purpose of the nanoparticles once injected systemically.

In conclusion, the systematic delivery of nanoparticles via the EPR effect results in a homogeneous distribution of the nanomaterial in the tumor in comparison to an intratumoural injection. However, the main downside of this delivery method lies in the difficulty to reach a substantial concentration of nanoparticles in the tumor site able to perform efficient MFH treatments.

8. *Aim of the work*

During my PhD program I have investigated different aspects of magnetic nanoparticles to exploit them as contrast agent for tomographic imaging in MPI and MRI as well as heat mediators for MFH treatments. I have focused my attention on iron-based nanoparticles and several aspects related to them:

- the characterization process with a wide range of techniques;
- the coating procedure to improve the biocompatibility and the stability in time as well as the internalization procedure;
- the biomedical application of nanoparticles as heating agents during MFH treatments;
- the biomedical application of nanoparticles as contrast agents for MPI and MRI;
- the testing of the ability to switch contrast ratio varying the Curie Temperature.

For my work as first author (Gerosa et al., 2021, Nanotheranostics) I have tested an innovative, promising nanomaterial, developed by M.B.N. Nanomaterialia (Carbonera di Treviso, Treviso, Italy) and named M48. The aim of this work was to generate a robust theranostic platform able to be exploited as heat exchange mediator and contrast agent in MRI to tackle breast cancer. M48 is composed of iron oxide-based phases and shows self-regulating temperature due to the observable second order magnetic phase transition from ferromagnetic to paramagnetic state. A double shell organic and hydrophilic coating based on citrate ions and glucose molecules allows biocompatibility and chemical stability of the nanomaterial in biological matrices and makes them suitable for *in vivo* use. A wide range of qualitative and quantitative techniques is used to characterize this material, exploiting morphological imaging as Transmission Electron Microscopy to define their shape; X-Ray Powder Diffraction to observe the different iron phases of the core; Infrared Spectroscopy to observe the bonding among the different coatings and the nanoparticle core and Dynamic Light Scattering to test their chemical stability in time and their hydrodynamic radius. Heat mediator efficiency for MFH treatments is demonstrated *in vitro* and *in vivo* in breast cancer cells and tumors, confirming excellent features for biomedical application. In this study M48 is administered locally via intratumor injection. It was chosen the MDA-MB-231 breast cancer cell line to test these particles. The temperature increase, up to the Curie temperature, gives rise to a phase transition from ferromagnetic to paramagnetic state, promoting a shortage of the r_2 transversal relaxivity that allows a switch in the contrast in Magnetic Resonance Imaging (MRI). Due to the limitation of the experimental apparatus used and to the synthesis condition applied it was not possible to test this feature at working temperature around the ones used for MFH treatments, but the effect was clearly observed at higher temperatures by MR imaging. Combining this feature with a competitive transversal (spin-spin) relaxivity, M48 paves the way for a new class of temperature sensitive T_2 relaxing contrast agents.

For the second work (still not published) as first name author I have focused my attention on a new iron-based nanoparticle synthesized by M.B.N. Nanomaterialia (Carbonera di Treviso, Treviso, Italy) named M55, more performant respect to M48 in terms of magnetic features and heat exchange ability. The aim of this last work (still ongoing in the Lab) was to understand the behavior of a nanoparticle able to be observed both in MRI and MPI and exploited as heat exchange mediator for MFH treatments on breast cancer tumor not only via conventional techniques as the ones used for M48 but also exploiting a new hyperthermia device applied to MPI and named HYPER module (Magnetic Insight Inc., Alameda, California, USA). This innovative device has a peculiar characteristic of being able to magnetically excite and heat the nanoparticle with the same frequency and without harming the healthy tissue surrounding the tumor. In this way it is possible to set up an innovative, non-invasive, and safe theranostic platform able to deeply exploit all the magnetic feature of a nanoparticle.

The final work as first author is a brief paper published as a Conference Paper on the International Journal of Magnetic Particle Imaging (Gerosa et al., 2020, International Journal of Magnetic Particle Imaging)and released during the International Workshop on Magnetic Particle Imaging held in Wurzburg, Germany, March 2021. For this work I have focused my attention on how to exploit Magnetic Particle Imaging to observe magnetic nanoparticles and localize a tumor in a mouse model by a systemic injection. I have studied the tumor microenvironment composed by tumor-associated-macrophages (TAMs). They are thought to be protumoral enhancing cancer progression. Often the presence of TAMs has been correlated with the metastasis of tumor and their ability to inhibit the immune responses mediated by T cells. MPI is applied in combination with computed tomography (CT) to detect passively targeted TAMs homing to a breast cancer model. The magnetic nanoparticles employed to target TAMs for this study is a PEG-coated magnetic nanoparticle (commercially available). The main aim of this work was to understand the behavior of MPI in an in vivo study under variable conditions as different concentrations of tracer and sensitivity of the imaging technique (different acquisition mode) to observe the signal in the tumor even administering systemically the nanoparticles.

Results and Discussion:

1. Investigation of M-48, as temperature sensitive MRI contrast agent and MFH agent in breast cancer cells and murine model

a. Introduction

Cancer is a serious health issue due to a large number of cancer-related human deaths worldwide. Nowadays, conventional approaches commonly used for cancer treatment include a combination of chemotherapy drugs, invasive surgery, guided focused ultrasound ablation, thermal ablation, and radiation therapy. However, none of these techniques is free from risks due to the possible high level of toxicity and invasiveness. Nanotechnology has provided valuable tools in the war against cancer during the last few years, including systems for selective drug and gene delivery or innovative diagnostic agents (Accardo et al, 2019; Calcagno et al., 2019; Pelaz et al., 2017). Nanotechnology advancements have also made possible developing a therapeutic approach named Magnetic Fluid Hyperthermia (MFH) based on local heating of tumor cells. MFH is considered a promising cancer treatment method, known as green therapy due to the limited effect on the tumor surroundings and relatively low toxicity (Court et al., 2017). MFH is currently under testing both in preclinical studies (Court et al., 2017; Mannucci et al., 2014; Mannucci et al., 2018) and clinical trials, especially for the treatment of gliomas and prostate cancer (Johannsen et al., 2010). This method delivers thermal energy to the target region exploiting magnetic nanoparticles (NPs) as mediators of heating exchange and exposing the tumor to an alternating magnetic field (AMF). When magnetic NPs are injected in the tumor, and an AMF is applied, tumor cells may reach the temperature of 42-46 °C. Such a temperature increase is due to the generation of heat from magnetic NPs. Magnetic energy is indeed dissipated into heat via two different mechanisms depending on the size of the magnetic domain of the NPs. For a multi-magnetic domains NP, the heating effect is due to hysteresis losses. For a single-domain NP, it is due to the Brownian-Nèel relaxation mechanism. It involves the rapid rotation (reorientation) of the magnetic moments within the domain of the nanoparticles in the case of Nèel relaxation and physical rotation of nanoparticle within the fluid in the case of Brownian relaxation process in the presence of AMF resulting in an extremely selective thermal ablation of the tumor (Ito et al., 2005). The increase of temperature causes the activation of various mechanisms inside the cell such as unfolding and denaturation of proteins, necrosis, aggregation, apoptosis, and immune response (Laurent et al., 2011), promoted by the activation of heat shock proteins and by the polarization of tumor-associated macrophages gathered by the inflammatory response of the surroundings (Ito et al., 2003).

In the last years, numerous research groups studied magnetic NPs, such as iron oxides, and ferrous fluids that could play a substantial role in treating tumors by MFH (Mondal et al., 2017; Fantechi et al., 2014; Kobayashi et al., 2011; Kandasamy et al., 2018; Jia et al., 2018; Lu et al., 2018). A widely recognized limitation of this technique is represented by the risk of overheating tumor tissue that may jeopardize surrounding healthy tissues (Hervault et al., 2014).

This work aims to test an innovative, self-regulating temperature nanomaterial synthesized in the form of nanoparticles, hereafter denoted as M48. M48 belongs to a class of innovative nanomaterials developed by MBN Nanomaterialia S.p.A. (Treviso, Italy) that show self-regulating temperature (Matteazzi, European Patent EP 2961429B1 Pr. 28.02.2014). The self-regulating heating effect consists of a stable temperature increase of the magnetic nanomaterial when exposed to AMF up to a maximum value (T_{SR}, Self-Regulating Temperature) below the Curie Temperature (T_c). This effect provides an intrinsic control for induction heating and exploits an efficient energy conversion – from electromagnetic energy to heat – regulated by a sharp magnetic transition. The values of T_c can be modulated by adjusting the composition of the nanomaterial itself. The Curie Temperature is observed in correspondence to a second-order magnetic transition threshold between ferromagnetism and paramagnetism. Above T_c, the magnetization is negligible and consequently, magnetic losses do not occur, switching off the heating mechanisms under AMF. The overheating phenomenon and the related dangerous effects on the healthy surrounding tissues can therefore be avoided thanks to the self-regulating properties of the maximum temperature level. Such properties are of paramount utility when the nanomaterial is integrated into biological matrices.

Moreover, thanks to its magnetic properties, M48 is a promising contrast agent for Magnetic Resonance Imaging (MRI) allowing in principle for simple monitoring of hyperthermia treatment and reliable control of local temperature distribution in the treated tissue. Indeed, considerable interest has been recently devoted to temperature-sensitive contrast agents for guiding thermal therapies (Hervault et al., 2014; Barbic et al., 2019). However, safer and more reliable compounds for *in vivo* theranostic methods with low toxicity and tunable temperature are highly desirable.

According to the American Cancer Society, breast cancer is the second most common cancer worldwide after lung cancer, the fifth most common cause of cancer death and the leading cause of cancer death in women. Current therapeutic approaches include surgery followed by chemotherapy/ radiotherapy, an invasive and debilitating approach. Novel therapy methods, minimally invasive, and devoid of negative impacts, are needed to reduce mortality rates in breast cancer patients. In this respect, MFH has been proposed as an innovative approach to breast cancer treatment Miaskowski et al., 2019.

In this paper, M48 was tested both *in vitro* and *in vivo* in breast cancer cells and experimental model as an efficient MFH heat mediator. An organic coating was applied to the prepared iron-based nanomaterials to guarantee biocompatibility and stability in physiological fluids. The capability to act as temperature-sensitive contrast agent for MRI was also demonstrated *in vitro*.

b. Materials and Methods

Synthesis of the iron-based NPs

M48 is synthesized by MBN Nanomaterialia S.p.A (Treviso, Italy) using a proprietary mechanochemical process (Matteazzi, European Patent EP 2961429B1 Pr. 28.02.2014). Briefly, M48 was prepared from MgO, Fe_2O_3 and TiO_2 powders in proportion 2:4:1, performing High Energy Ball Milling (Predescu et al., 2018; Matteazzi et al., 2000) in stainless steel equipment for 6h followed by thermal treatment in air at 1200°C for 4h. The resulting powder is finely ground by a second ball milling step of 1h, then homogeneously dispersed in propan-2-ol and processed by ultrasonication to promote de-aggregation. Centrifugal classification allowed us to extract smaller particles < 200 nm. The detailed processing parameters are courtesy of MBN.

Structural characterization

For phase analysis, an X-Ray Powder Diffractometer (Thermo ARLX'TRA) equipped with a Cu-anode X-ray source with a Peltier Si (Li) cooled solid state detector was used. The XRPD patterns were collected with a scan rate of 0.04°/s, with a measurement time of 1.0 s/step. The samples were prepared by careful homogenization in a mortar with few drops of ethanol. After evaporation of the solvent, the sample was deposited on a low background sample stage.

Morphological analysis

The size and morphology of M48 were investigated using Transmission Electron Microscopy (TEM, FEI TECNAI G2). For TEM analysis M48 was added to the copper grid and desiccated for one day before TEM imaging.

Coating of the iron-based NPs

The iron-based NPs were coated with citrate moieties (using Trisodium Citrate dihydrate 99% Alfa Aesar as reagent) and then with glucose (using D-(+)-Glucose SigmaUltra 99.5% Sigma as reagent). For the coating procedure, a microwave assisted synthesis was exploited to significantly reduce the reaction time. One mL of M48 suspension (concentration of 9.6 mg/mL) and 3.0 mL of sodium citrate solution (concentration of 1 M) were added in a 10 mL glass vial for the microwave assisted reaction, using an Anton Paar Monowave 400 microwave reactor. The heat treatment followed a general literature protocol with some optimizations (Santos-Marques et al., 2006) (heat treatment at 90°C for 7 min). The obtained nanoparticles were collected by centrifugation at 8000 rpm for 5 min. The whole procedure was repeated for the glucose capping (concentration of the glucose starting solution of 1M). At the end of the coating procedure, the NPs suspension was dialyzed overnight (Spectra/Por 3 Dialysis Membrane Standard RC Tubing MWCO: 3.5 kD). Hereafter, the citrate and glucose capped NPs will be referred to as G-M48.

Dynamic Light Scattering measurements

The hydrodynamic size and the zeta potential for G-M48 were determined with a Malvern Zetasizer Nano instrument. The sample was prepared diluting G-M48 water suspension with water (1:5 in volume) in a proper plastic cuvette.

Infrared Spectroscopy

The organic capping on the M48 surface was analyzed by using FTIR spectroscopy, with a JASCO FT/IR-660 plus. The sample was prepared by dispersing G-M48 in a KBr pellet (3 mg of NPs in 100 mg of KBr).

Cytotoxicity assay

The cytotoxicity of G-M48 was evaluated in two cell lines: HeLa and MDA-MB-231 cells, cervix and breast cancer cell line respectively (purchased by ATCC Manassas, VA). Cells were cultured in Dulbecco's Minimum Essential Medium (DMEM) with 10% of

Fetal Bovine Serum (FBS), 1% of a mix of penicillin/streptomycin 1:1 and 1% of L-glutamine 200 mM, seeded onto 96-well plates (2500 cells/well) and incubated at 37°C in humidified air with 5% CO_2 for 24h. After 24 h, the medium was replaced with fresh medium containing 10, 50, 100, 150 ug/ml of G-M48.

The MTT (3-(4,5-dimethylthiazol-2-yl)-2,5- diphenyltetrazolium bromide cytotoxicity assay was performed after 2, 24, and 48 h of incubation: 100 µl of MTT (at 5 mg/ml concentration, purchased from Sigma, Italy) were added to each well and incubated for additional 4 h (37°C, 5% CO_2). Formazan crystals were dissolved in 100 µl of DMSO, and the absorbance was read at a wavelength of 570 nm using a microplate reader (HTX Microplate Reader BioTek Instruments, Winooski, VT, USA). Four measurements of optical density (OD) were recorded for each sample, and cell viability (%) was calculated with the following equation: CV% = (ODsample/ ODcontrol) × 100.

Nanoparticles Internalization in cells: TEM analysis

HeLa and MDA-MB-231 cells were grown as monolayers on glass coverslips, treated with 150 µg/ml of G-M48 for 2, 24 and 48 h at 37 °C, and then fixed with 2.5% (v/v) glutaraldehyde and 2% (v/v) paraformaldehyde in 0.1 M phosphate buffer, pH 7.4, at 4 °C for 1 h. Afterward, cells were post-fixed with 1% osmium tetroxide and 1.5% potassium ferrocyanide for 1 h, dehydrated with acetone and embedded in Epon resin. Ultrathin sections were stained with lead citrate for 2 min and observed in a TECNAI G2 transmission electron microscope (FEI Company Italia Srl, Milan, Italy) operating at 80 kV and equipped with a Megaview III camera for digital image acquisition.

Magnetic Fluid Hyperthermia

MFH was performed by using a Nanotherics MagneTherm system (Warrington, United Kingdom) in water. The heat dissipation value strictly depends on the frequency and amplitude of the applied alternating magnetic field (AMF). The transformation of magnetic energy into thermal energy mediated by magnetic nanoparticles in the presence of an external AMF is quantified from the value of specific absorption rate (SAR). The SAR value of nanoparticles in solution is calculated by using the following equation:

$$SAR = \frac{C}{m_{Fe}} \frac{\Delta T}{\Delta t}$$

Where C is the specific heat capacity of the solvent per g, ΔT is the temperature variation in time, m_{Fe} is the mass of iron in the compound per g (Predescu et al., 2018; Cotin et al., 2019).

The AMF apparatus yields a maximum magnetic field intensity of 23 kA/m (≈29 mT). A multichannel thermometer equipped with optical fiber probes (FOTEMP4, Optocon AG, Germany) was used to assess temperature variation within the sample every 10.0 s. For MFH characterization of G-M48, in order to satisfy the Hergt criterion (less rigid than the previously published Brezovich one) for the clinical translatability of the compound, a frequency f = 473.1 kHz (0.473 MHz) was coupled with a field strength H = 8.75 kA/m (Muela et al., 2016; Brero et al., 2000; Obaidat et al., 2015; Kita et al., 2010; Hergt et al., 2006). These parameters were tested as the most efficient and clinically safe among the ones provided by the Magnetherm device, providing a coupled $H*f = 4.1\ 10^9\ Am^{-1}s^{-1}$ (between 0.110 and 0.970 MHz and between 1.0 and 23 kA/m).

Thermograms of G-M48 were acquired for different concentrations (2.5, 3.75, 5, 7.5 and 10 mg/mL). The multichannel thermometer was placed inside the sample during the 20 min acquisition time. The time window of 20 min for the effective treatment was chosen considering preliminary results and experimental conditions suitable for possible translatability to the clinics. Preliminary results showed that about 15 min were necessary to reach the temperature plateau and therefore the total treatment time amounted to about 35 min (MFH protocol).

To maintain cell cultures at 37°C a homemade device constituted by a closed box with a thermostated air stream was used.

To avoid contamination of cell cultures, the temperature was calibrated before the measurement in a disposable sample for each single acquisition. For MTT assay, cells were plated on 96 well plates. Cells were incubated for 24 hours with 150 µg/mL of G-M48 and treated for 35 min with MFH protocol. Untreated cells, untreated cells subjected to MFH and cells treated with 150 µg/mL of G-M48 but not exposed to MFH were used as controls. Twenty-four hours after MFH treatment, MTT cytotoxicity assay and Hematoxylin and Eosin (H&E) staining were performed. For H&E, after the incubation time, cells were fixed with 4% buffered formalin solution for 15 min, rinsed with PBS and then stained with Mayer’s hematoxylin (nucleus) and eosin (cytoplasm). Six images of each sample were taken at 10X using a BX-URA2 Olympus microscope (Olympus

Optical, GMBH, Hamburg, Germany) equipped with a digital camera. MDA-MB-231 cells viability was evaluated after one, two, three and four hyperthermia treatments and normalized to that of the respective control cells.

Characterization of G-M48 as temperature sensitive MRI contrast agent

MRI was performed using a Bruker Biospin 7T, 72 mm bore (Bruker Biospin, Ettlingen, Germany) scanner to evaluate the in vitro transversal relaxation rate (r_2 coefficient), the switching contrast ratio property and the in vivo biodistribution of G-M48.

The transversal relaxation times and the switching contrast ratio property were measured using a standard Spin-Echo Multi-Echo sequence with the following parameters: TR = 2000 ms, TE = from 6.5 to 170.43 ms, FOV=55x55mm, matrixsize = 128 x 128, slice thickness = 1 mm, number of echoes = 25. Transversal relaxation rates ($1/T_2$) were plotted as a function of the Fe concentration and r_2 relaxivity was obtained by the slope of the fitting straight line. To characterize the switching contrast ratio property, a magnetic field compatible system for the control of temperature, from 5°C up to 80 °C, was designed. A phantom was prepared with a capillary filled with G-M48 (1.9 mg/ml) solution immersed in water and settled inside the temperature-controlled box. To completely avoid the thermal stretching of the box itself, the temperature was slowly increased by 5°C every 15 min starting from 25°C.

To unveil the biodistribution of G-M48 in vivo, Balb/c, male mice (n = 3, 6–8 weeks old, Envigo) were used. Animals were anesthetized with gas anesthesia (a mixture of O_2 and air containing 1–1.5% of isofluorane), placed in a heated animal bed and inserted in a 7.2 cm internal diameter bird-cage coil. G-M48 was injected at a dosage of 2 mg Fe/kg. T2-weighted images of the mice body were acquired using a Rapid Acquisition with Relaxation Enhancement (RARE) sequence with the following parameters: FOV = 60 x 40 mm, MTX = 256 x 256, slice thickness=1mm, TE = 33ms and TR = 2.500 ms. The images were acquired before, 40 min, 24 and 72 h after G-M48 injection.

Characterization of G-M48 nanoparticles as hyperthermia mediators in vivo

N = 30 nude homozygote female mice (Harlan Laboratories, Udine, Italy) were maintained under standard environmental conditions (temperature, humidity, and 12 h/12 h light/dark cycle, with water and food ad libitum) and veterinarian control in the animal facility of the University of Verona. Animal experiments were conducted following Italian law (D.L. 4 March 2014 no. 26) and the European Union normative (2010/63/EU).

Two million MDA-MB-231 cells (human breast adenocarcinoma) were injected subcutaneously in the flank of nude mice (n = 27). Starting from 15 days after cells inoculation, the size of the tumor mass was measured every three days by MRI. Three mice did not develop tumor and were excluded from the study. Twenty-one days post tumor implantation (when tumor volume reached about 200 µl) mice were divided into three groups according to the treatment. Animals in the first group (n = 8, CTRL) received saline intratumorally. Animals in the second group (n = 8, G-M48) received G-M48 [1.2mg Fe/mL]. Animals in the third group (n = 8, G-M48 + MFH) received G-M48 [1.2mg Fe/mL] and were exposed to four MFH cycles immediately, 24h, 72h and 96h after G-M48 injection. In order to improve the homogeneity of the distribution of G-M48 within the tumor tissue, the total injected volume (100 µl) was divided in 5 aliquots and injected in different areas of the tumor. Each MFH treatment consisted of 35 min application (in agreement to the MFH protocol adopted for the in vitro study) of an oscillating magnetic field with a maximum intensity of 23 kA/m (≈29 mT) and a frequency of 473 kHz. In particular, it was chosen the same field strength and frequency used for the in vitro studies (H = 8.75 kA/m and f = 473.1 kHz). During MFH treatments, animals were maintained at 37°C using a homemade device constituted by a closed box with a thermostated air stream.

All mice were monitored by MRI before (day 1), 3 days (day 3) and 6 days (day 6) after the injection of G-M48 to monitor the efficacy of treatments. T_2 weighted images were acquired in the axial plane usingaRARE3DsequencewithTR=1200ms,TEeff= 47.5ms, NEX=1,f ield of view = 25 × 25 × 25 cm^3, matrix size (MTX) = 256 × 128 × 32, slice thickness = 0.8 mm, flip angle = 90°, RARE factor = 16. To measure the volume of tumors, MR images were processed with Paravision software and a custom-made MATLAB (MathWorks, Natick, USA) script. The tumor area was manually selected slice by slice and tumor volume was calculated as $(\sum^{n}{}_{i=1}\ pu_i) * image\ resolution$, where pu_i represents the number of pixels manually selected. The percentage increase in tumor volume was calculated at each time point as 100* $(V_t\text{-}V_0)/V_0$, where V_t is the tumor volume at time t and V_0 is the initial volume.

Histology

Mice were sacrificed and tumor, liver, kidneys were dissected out, washed with PBS 0.1 M and fixed in 10% formalin for 4 hours. Tissues were embedded in paraffin, cut in 5 µm thick sections with a microtome and dried at 37°C for 24 h. To evaluate the presence of iron in the tissue, Prussian Blue (PB) staining was performed: sections were incubated with PB solution (5% hydrochloric acid and 5% potassium ferrocyanide) for 40 min and counterstained with nuclear fast red (Bioptica) for 10 min. Sections were examined under a light microscope (Olympus BXS1) equipped with a charge-coupled device camera. Finally, to evaluate tissue damage in tumor tissue, sections were stained with Hematoxylin and Eosin (H&E).

Statistical Analysis

Statistical analysis was performed using Prism software (8.1.1, GraphPad Inc., La Jolla, CA, USA) and confirmed by a custom script for statistical analysis realized in MATLAB (Mathworks, Natick, MA, USA). All the data are expressed as mean ± standard deviation of the mean (Mean ± SEM). Statistically significant differences were evaluated by TWO-way ANOV A with multiple comparisons using the Tukey-Kramer method. Differences were considered statistically significant when the p-value < 0.05.

c. Results and Discussion

Morphological and structural characterization

TEM allowed investigation of M48 morphology. TEM images, reported in Figure 1 (a,b), reveal that M48 nanoparticles have a large size dispersion and are present as single nanoparticles or aggregates with size ranging from around 10 nm to more than 100 nm. A decreased particle size distribution could positively affect the *in vivo* application of M48 nanoparticles. For example, reduction of size could affect the biodistribution with decreased liver uptake that is desirable in the prospective of systemic administration. Decreasing particles size could however also affect their magnetic properties. When the size of the NPs is of the order of the size of magnetic domain, there will be a switch to superparamagnetic single domain NPs with no transition. The optimization of size distribution of the magnetic core of the NPs is a very important future development of our work and will be the objective of further investigations.

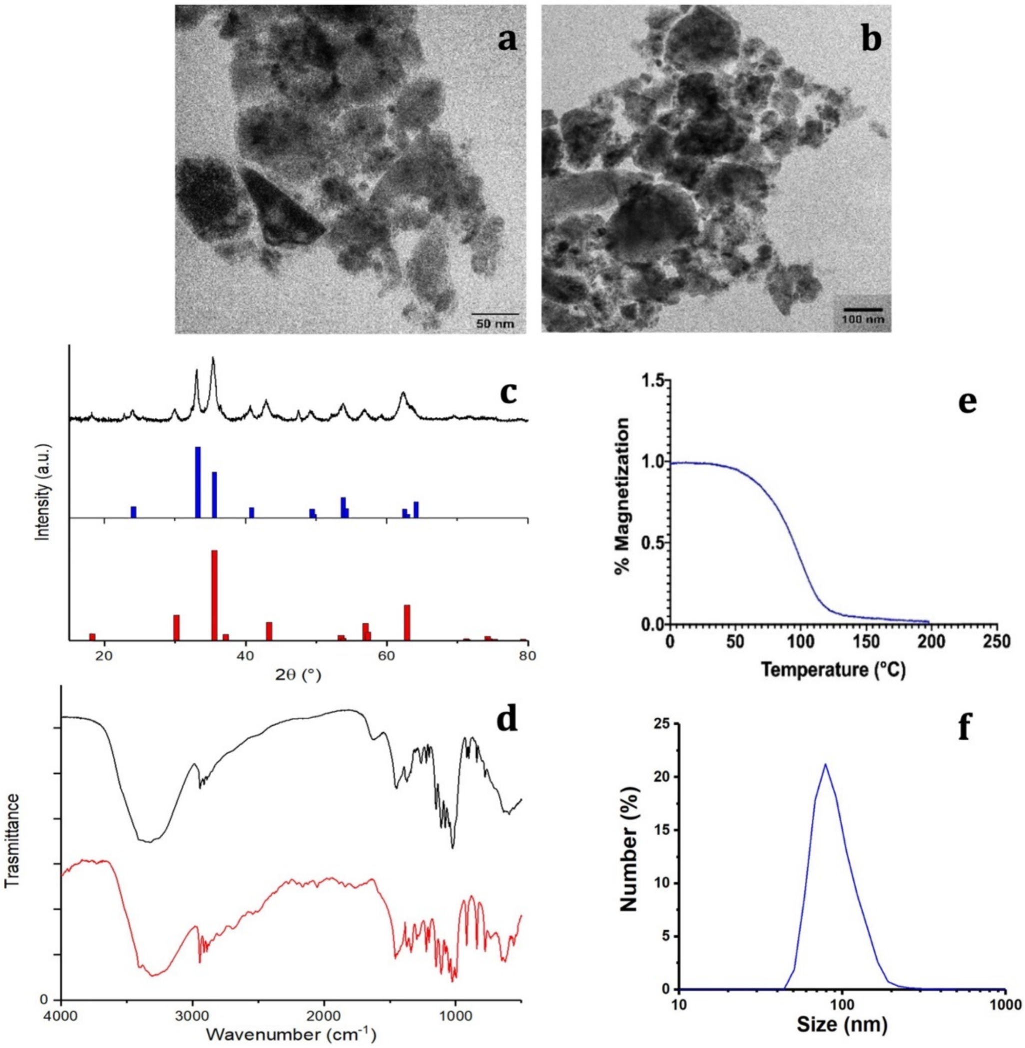

Figure 1. Characterization of M48 and G-M48 nanoparticles. a, b) TEM images of M48; c) XRPD pattern of M48: black line, experimental data; red pattern, Fe3O4 (magnetite, COD n.9002319), blue pattern, alpha-Fe2O3 (hematite, COD n.9000139); d) FTIR spectrum of G-M48 (black line); FTIR spectrum of glucose (red line), e) M48 magnetization vs temperature; f) Hydrodynamic diameter (by Dynamic Light Scattering) of G-M48.

The composition (both phase and structural characterization) of M48 was investigated by the XRPD technique. The measured XRPD pattern obtained for the M48 sample is shown in Figure 1 (c) (black line). A detailed analysis of the experimental XRPD pattern revealed that the M48 sample is composed by more than one iron oxide compounds. This behavior can be observed in Figure 1 (c), where the XRPD patterns of α-Fe_2O_3 (hematite, Crystallography Open Database (COD) n. 9000139) and Fe_3O_4 (magnetite, COD n. 9002319) are shown in blue and red patterns, respectively. From an EDX analysis of the

M48 sample, also Mg and Ti metals were found, and a relative molar ratio Fe:Mg:Ti = 1:1:0.3 was evaluated. This evidence indicates that other iron-containing compounds, as magnesium ferrites or iron titanates, that have XRPD patterns compatible with the experimental one, can be present in the sample.

Coating of M48 nanoparticles

To use the sample in biological systems, M48 NPs were surface coated with glucose molecules and citrate ions moieties. The idea of using two hydrophilic coating agents was pursued to provide high colloidal stability and good biocompatibility of the NPs.

As described in the experimental section, the NPs were capped with citrate ions and glucose moieties. Citrate capping was chosen as this capping enhances the stability of inorganic NPs in water (Cortelletti et al., 2017). On the other hand, glucose coating was chosen considering the pronounced glucose greed of tumor cells. Indeed, malignant tumors exhibit a high rate of glucose uptake compared to normal cells. Glucose molecules are internalized via GLUT transporters, highly expressed on the cancer cell surface (Calvo et al., 2010). For this reason, glucose coating is an effective way to facilitate the entry of NPs into tumor cells.

The surface coating was characterized using FTIR spectroscopy. Figure 1 (d) shows the FTIR spectrum of the citrate and glucose coated M48 sample (hereafter denoted G-M48) compared with the glucose molecule's FTIR spectrum. Several features in the FTIR spectrum of G-M48 are due to the glucose molecule, confirming that glucose is present on the nanoparticles surface. On the other hand, it was impossible to distinguish any characteristic band of the citrate ions, most probably due to a higher amount of glucose than the citrate ions on the nanoparticle surface. Figure 1 (d) shows one broadband around 3300 cm^{-1} due to -OH stretching of glucose or citrate ions and a narrow band around 2900 cm^{-1} due to -CH stretching of the organic backbone. In the region between 1600 and 500 cm^{-1}, many vibrations due to the glucose molecular skeleton are observed, in substantial agreement with those observed for the FTIR spectrum of the glucose molecule (red line in Figure 1(d)), in the fingerprint region. Besides, an absorption band around 570 cm^{-1} can be assigned to a Fe-O vibration of the inorganic phase.

Colloidal and magnetic properties of water dispersion of G-M48

Dynamic Light Scattering (DLS) was exploited to investigate the colloidal stability of water dispersion of G-M48 through the measurement of the zeta potential. The obtained zeta potential value of –23.2 ± 10.7 mV, reported in Figure S1, confirms good colloidal stability (Kovàr et al., 2017).

The thermomagnetic analysis was performed on dry M48 nanoparticles, measuring magnetic susceptibility variation with temperature, on-heating between -85 and 200 °C, and on-cooling down to 40°C, in inert Argon atmosphere, applying a 10 Oe magnetic field at 502 Hz. A Curie temperature (T_C) of 95 °C was determined as the temperature of susceptibility at half height of the curves normalized at the maximum peak before susceptibility drop. Indeed, thanks to their innovative design and synthesis approach, M48 at low temperature is in an ordered state with low entropy, a so-called ferromagnetic state, and can undergo a second-order phase transition into a paramagnetic state at a specific temperature T_C (T_C = 95°C).

Cytotoxicity and cell internalization

An important feature for the biomedical application of nanoparticles in MFH is the absence of cytotoxicity when used without AMF. Cell viability was therefore assessed after 2, 24, and 48h of incubation with G-M48 in MDA-MB-231 (Figure 2 (a)) and HeLa cells (results in supplementary information). MTT assay reveals that G-M48 is safe up to the concentration of 150 μg/mL for long incubation times (48 h, Figure 2 (a)). The electron-dense chemical composition of G-M48 allowed to unveil the intracellular distribution and the internalization process of the nanoparticles in MDA-MB-231 cells (Figure 2 (b-f)) at different incubation times. In the cytoplasm, G-M48 nanoparticles were always found enclosed into endosomes (Figure 2 (c-d), arrowheads) and, following the lytic pathways, secondary lysosomes/residual bodies (Figure 2 (e), 2 (f), asterisks). G-M48 nanoparticles were thus always entrapped in vesicular structures and never free in the cytoplasm or in contact with any organelle, confirming that endocytosis can be identified as the primary internalization process in MDA-MB-231 cells. Mitochondria, endoplasmic reticulum and Golgi complexes preserved their morphology, confirming the absence of cell damage or death up to 48 h of incubation time.

In vitro Magnetic Fluid Hyperthermia characterization

Figure 3 (a) reports the thermograms up to the plateau collected in aqueous suspensions of G-M48 at different concentrations. As expected, an increase in NPs concentration (and so in the iron content) increases temperature variation. Thermograms were collected starting from a specific bulk temperature, in this case, 37.0 °C. This starting condition was chosen to simulate the condition of *in vivo* experiments. As reported in Figure 3 (a), the most concentrated sample reveals a promising increase of temperature of 5.5 ± 0.5 °C that paves the way to more exciting results *in vitro* and *in vivo*. For each sample the temperature plateau was reached approximately after 15 minutes. The SAR of G-M48 was determined in aqueous solution from the acquired thermograms, and a value of 47.0 ± 8.0 Wg^{-1} was obtained. SAR depends on various parameters such as size, shape, and magnetic properties of nanoparticles, frequency, and intensity of the applied external AMF (Kekalo et al., 2015). The result agrees with typical SAR values reported in the literature for iron oxide nanoparticles (ranging from 20 to 400 Wg^{-1}) (Kekalo et al., 2015; Das et al., 2019).

As reported in Das et al., 2019 (Das et al., 2019), cancer cells are more sensitive to temperature enhancement than non-tumoral cells, and usually, temperature around 46 °C can induce death in tumor cells. According to literature, MFH involves cancer treatment in a temperature range of 40–46 °C, at which denaturation and aggregation of intracellular proteins induce cell death (Hildebrandt et al., 2002).

During the early days of magnetic hyperthermia applications for cancer therapy it was commonly used the Brezovich criterion in order to identify an upper limit to the magnetic field strength and the frequency applied in the treatments. This limit was calculated through the equation $C = H*f$ (H is the magnetic field intensity in Am^{-1} and f is the frequency of the related field in s^{-1}) and it is equal to $4.85\ 10^{8}\ Am^{-1}s^{-1}$. Nowadays it is accepted another safety criterion, the so called Hergt criterion. It is a less rigid rule that was introduced to adapt the magnetic hyperthermia procedure to different geometries and shapes of the treated body. It can be summarized as $C = H*f \leq 5.0\ 10^{9}\ Am^{-1}s^{-1}$. Considering this rule, the frequency and the magnetic field strength were chosen according to the Hergt criterion with a final value of $C = 4.1\ 10^{9}\ Am^{-1}s^{-1}$, perfectly fitting the above condition (Hergt et al., 2006).

G-M48 was tested as hyperthermia mediator on MDA-MB-231 cells at the concentration of 150 µg/mL, verified to be the highest non-toxic concentration (Figure 3 (b)). MDA-MB-231 cells were incubated with G-M48 for 24h and exposed to four cycles of AMF spaced 24h one each other.

Every effective cycle lasted 20 min (following the initial 15 minutes, necessary to reach the temperature plateau). Then, cell viability was determined 24h after the last hyperthermia treatment and normalized to the related control cells, as shown in Figure 3 (b). The percentage of cell viability was significantly affected by MFH treatment compared to control conditions (untreated cells, untreated cells subjected to MFH, and cells treated only with G-M48 but not exposed to MFH). MDA-MB-231 cells treated only with G-M48 but not exposed to MFH showed a percentage of viability of 95.3 ± 4.3%, while cells treated with G-M48 and exposed to MFH showed a percentage of viability of 73.0 ± 2.5% and 52.0 ± 4.3% after the first and the second hyperthermia treatment, respectively. After the third and the fourth treatment, the viability recovers up to 73.0 ± 5.2% and 88.0 ± 18.0%.

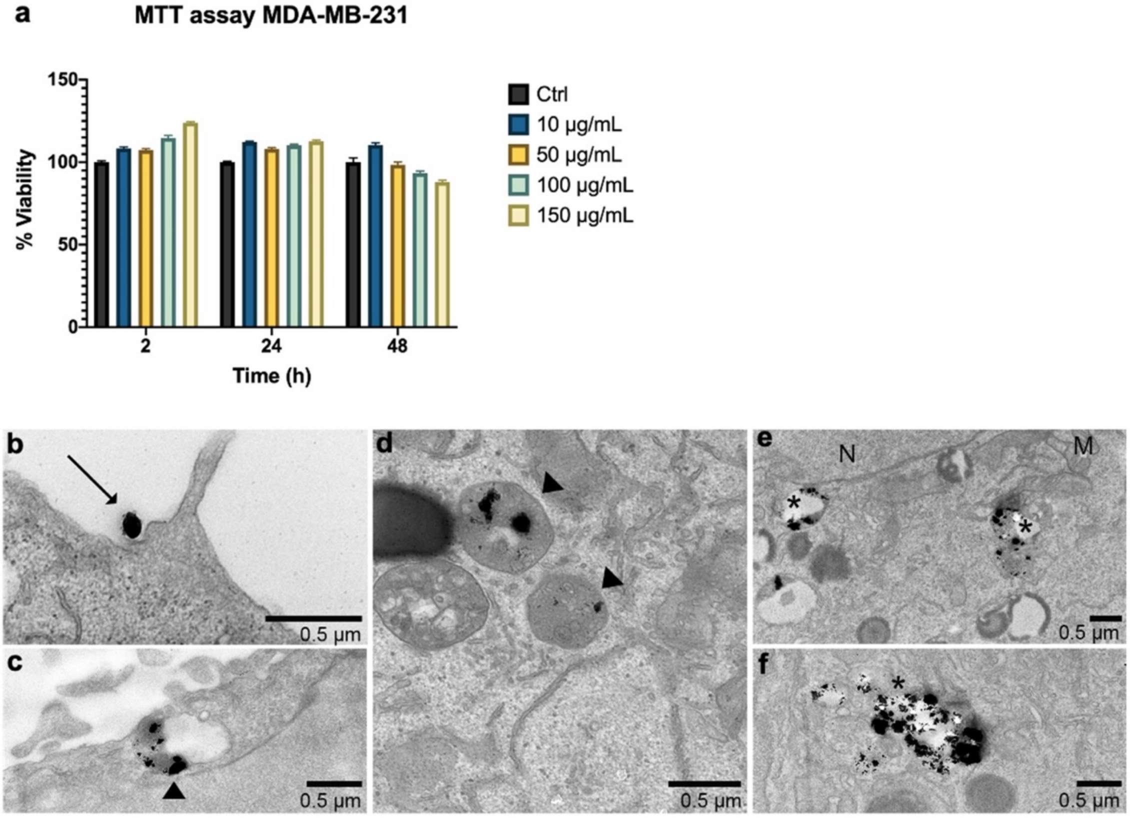

Figure 2. *In vitro* viability of MDA-MB-231 cells and G-M48 internalization at TEM. a) MTT assay in MDA-MB-231 cells shows that G-M48 is safe up to a concentration of 150 µg/mL and up to 48 h of incubation time; the error bar represents SEM over six replicates. Transmission electron microscopy images of G-M48 uptake and distribution in MDA-MB-231 cells. b) MDA-MB-231 cells internalize G-M48 via endocytosis (arrow). c-f) G-M48 nanoparticles are compartmentalized into endosomes (arrowheads in c,d) distributed in the cytoplasm, as well as in

residual bodies (asterisks in e,f). MDA-MB-231 cells show well-structured mitochondria (M) and endoplasmic reticulum cisternae, demonstrating no cell damage. N: cell nucleus.

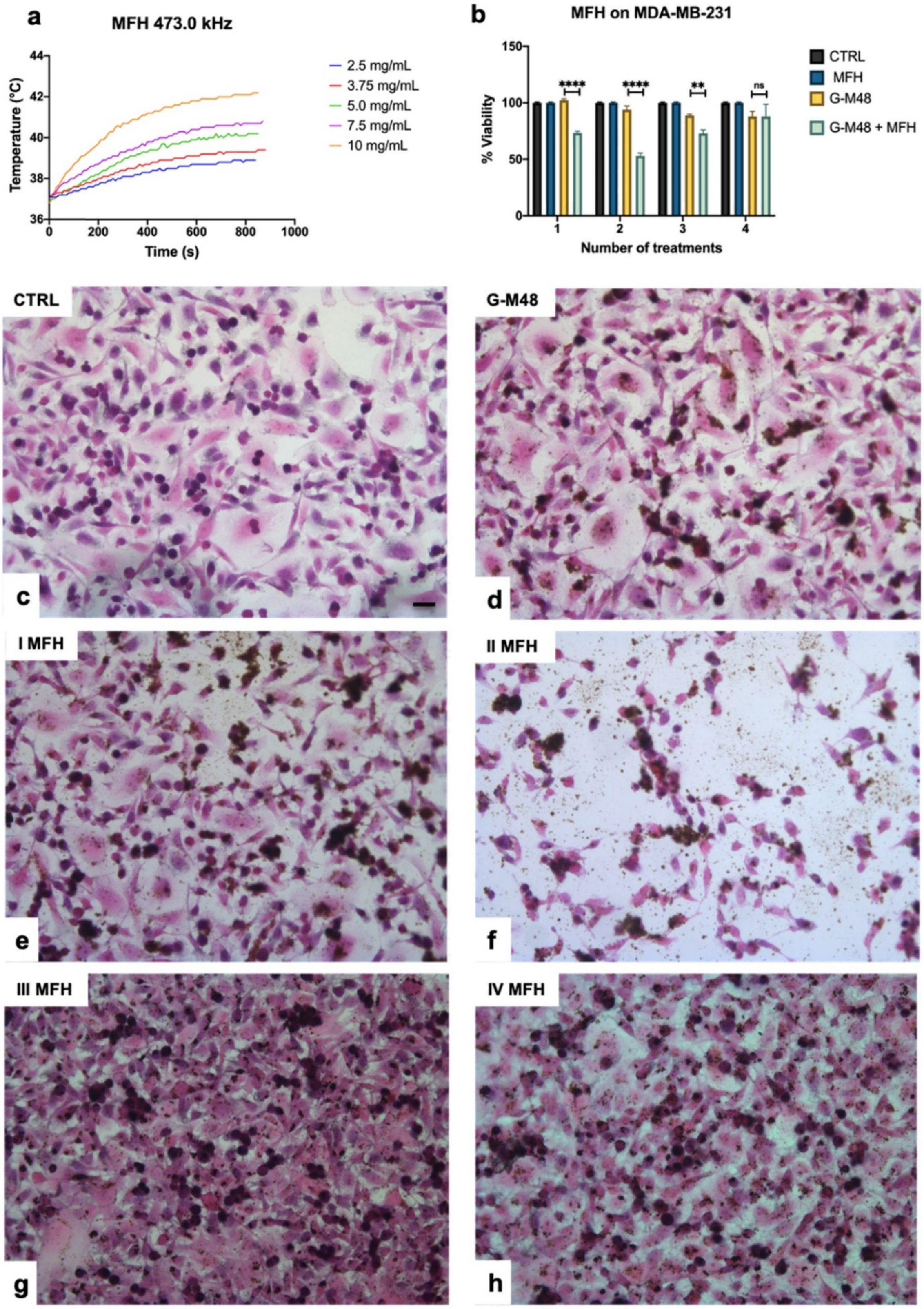
a
MFH 473.0 kHz
Temperature (°C)
Time (s)
36
38
40
42
44
0
200
400
600
800
1000
2.5 mg/mL
3.75 mg/mL
5.0 mg/mL
7.5 mg/mL
10 mg/mL
b
MFH on MDA-MB-231
% Viability
Number of treatments
0
50
100
150
1
2
3
4
****
****
**
ns
CTRL
MFH
G-M48
G-M48 + MFH
CTRL
c
G-M48
d
I MFH
e
II MFH
f
III MFH
g
IV MFH
h

Figure 3. Viability of MDA-MB-231 after MFH treatments and related histologies of the different groups. a) Thermograms were collected in water solutions at different concentrations of G-M48 suspension; b) MTT assay on MDA-MB-231 cells after multiple MFH treatments (each every 24 h). (c-h) Light microscopy images of H&E stained MDA-MB-231 cells: c) control cells, d) cells incubated with G-M48 without AMF application, e) f), g), h) Cells incubated with G-M48 and subjected to I, II, III, IV MFH treatments and observed 24 hours after the treatment. Scale bar: 50 μm.

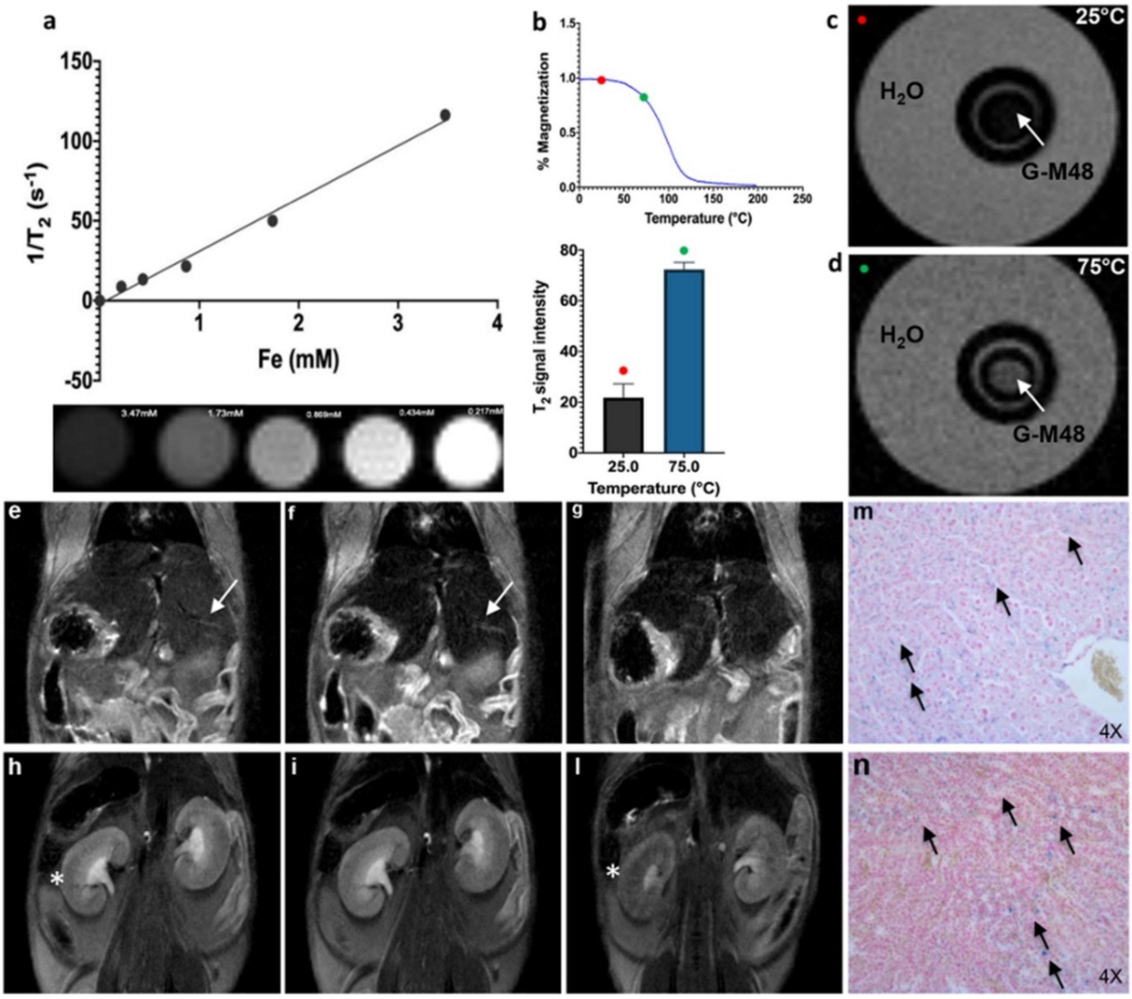

Figure 4. Characterization of G-M48 as temperature sensitive MRI contrast agents. *In vivo* biodistribution and clearance verified by MRI and histological examination. a) The plot of transversal relaxation rate versus Fe concentration in water dispersed G-M48 phantoms, at 25°C. MRI images of phantoms cross section are also reported. b) SNR of G-M48 water suspension at 25 and 75°C and related magnetization curve of M48. The T2 signal variation has been observed in the related histogram. c-d) MRI images of a phantom constituted by a capillary filled with G-M48 (white arrow) and placed inside a thermostated box at 25°C and at 75 °C. MR images of a

representative animal acquired using a T_2-weighted sequence before (e, h), 40 min (f, i) and 72 hours (g, l) after the injection of G-M48. The liver and the kidney are indicated by arrows in Figure 4 (e-h), respectively. After 40 min the signal intensity (S.I) in the liver dropped by 32.6% (Figure 4 (f) arrow). In the kidneys, no appreciable loss of signal could be detected 40 min post-injection, while at 72 hours the S.I decreased by 45 % (Figure 4 (l)). Prussian Blue staining of liver and kidneys 72h after administration of G-M48 (Figure 4 (m, n), respectively).

Histological examination of MDA-MB-231 cells stained with H&E confirmed the results obtained by MTT (Figure 3 (c-h)). Cells incubated with G-M48 and subjected to AMF demonstrated a more pronounced cell death effect after the first (e) and the second (f) MFH treatment in comparison with control cells (c) or to cells incubated with G-M48 without AMF application (d). In agreement with the MTT data, after the third and fourth treatment, cell viability recovered. The observed recovery effect can be partially attributed to cell replication and consequent G-M48 dilution. Moreover, it is well-known that hyperthermia stress induces the synthesis of a class of proteins named ‘heat shock proteins’ (Hsps) (Calderwood et al., 2002), which may induce thermoresistance with a consequent decrease of the efficacy of the last two treatments (Sapareto et al., 1984; Hall et al., 1984; Khoei et al., 2004).

Characterization of G-M48 as MRI temperature sensitive contrast agent

The transversal (spin-spin) relaxation time of water dispersion containing G-M48 was measured at 7T in a series of phantoms with variable iron concentration (from 0.21mM to 3.47 mM). Values of $1/T_2$ vs. Fe concentration were interpolated using a straight line whose slope determines the transversal relaxivity of the NPs under investigation (Figure 4 (a)). As shown in the same figure, the T_2-weighted MR images of G-M48 phantoms tend to become darker with increasing iron concentration showing that G-M48 can effectively reduce the spin-spin relaxation time of water protons as a T_2 contrast agent. Transversal relaxivity (r_2) of 32.10 $mM^{-1}s^{-1}$ was obtained, comparable to the value of a commercial iron oxide MRI contrast agent, like Endorem (Hidebrandt et al., 2002; Calderwood et al., 2002) confirming the potential of G-M48 as a contrast agent for MRI. As reported in Figure 1 (c), the magnetization of M48 strongly depends on temperature through a second-order magnetic phase transition occurring at 95°C (T_C). Therefore, a relevant decrease in the transversal relaxivity is expected as temperature increases. Figure 4 (c, d) shows MR images of a phantom containing a G-M48 filled capillary embedded in water acquired at 25°C (i.e., well below T_C) and at 75°C (i.e., not far from T_C), corresponding to the red and green dots respectively in Figure 4 (b). A substantial increase in the signal of the G-M48 filled capillary is visible. The histogram shows the quantitative signal to noise ratio (SNR) of G-M48 capillary that increases from 21.8 ± 5.4 (T = 25 °C) to 72.3 ± 2.0 (T = 75°C). This property allows G-M48 to be a temperature-sensitive contrast agent. The SNR increase could be more relevant if observed at 95°C, but the available experimental apparatus could not be used at temperatures higher than 75 °C. However, as an iron-based contrast agent, it has to be considered the well-known issue related to the susceptibility artifacts that produces in MRI images "signal voids" in large areas surrounding the iron core. High local concentrations of NPs, as those used in MFH, may therefore destroy the signal of tumor tissue and prevent the observation of tumor anatomical details.

The currently used nanoparticle has a ferromagnetic-paramagnetic transition at 95°C, while a substantially lower transition temperature (around 42-45°C) should be necessary for safe and effective translation to the clinic. However, the present nanoparticle belongs to a class of nanomaterials whose transition temperature can be modulated by adjusting the composition of the nanomaterial itself. The present is a proof-of-concept of the usefulness of such materials as temperature sensitive contrast agent and future investigations will be devoted to preparation and characterization of nanoparticles with ferromagnetic-paramagnetic transition occurring at lower temperature.

Finally, the biodistribution and clearance of M48 nanoparticles were investigated *in vivo*. G-M48 was intravenously injected in healthy mice and monitored up to 72h. In Figure 4, MR images of a representative mouse acquired using a T_2-weighted sequence before (e, h), 40 min (f, i), and 72 (g, l) hours after the injection of G-M48 are shown. A dosage of 2 mg Fe/kg was administered. The signal intensity (S.I) in the liver decreased by 32.6 ± 5.2% (Figure 4 (f) arrow) and by 46.8 ± 3.9% 40 min and 24 h after injection, respectively, indicating early hepatic accumulation of the nanoparticles. Seventy-two hours after G-M48 injection, the S.I in the liver dropped by 58.13±4.5% (Figure 4 (g)). In the kidney, no appreciable loss of signal could be detected 40 min post-injection (p.i.), while 72 h p.i. the S.I decreased by 45 ±7.3% as it is visible in Figure 4 (l) (asterisk). The loss of S.I in both cortex and medulla of the kidney observed 72h p.i. may indicate renal clearance of G-M48. No loss of signal was detected in the spleen.

To validate MRI results, histological examination was performed. Prussian Blue staining of liver and kidneys (see Figure 4 (m, n)) showed several blue spots homogeneously distributed in the tissues indicating the presence of iron. Of note, the tissues exhibit no relevant modifications in the parenchyma with good preservation of cellular morphology, as shown in Figure 4 (m, n) for liver and kidney, respectively, indicating that G-M48 has a good biocompatibility.

Characterization of G-M48 as hyperthermia mediators *in vivo* in an experimental model of breast cancer

The experimental plan illustrated in Figure 5 was implemented to test the efficacy of G-M48 as an MFH mediator *in vivo*.

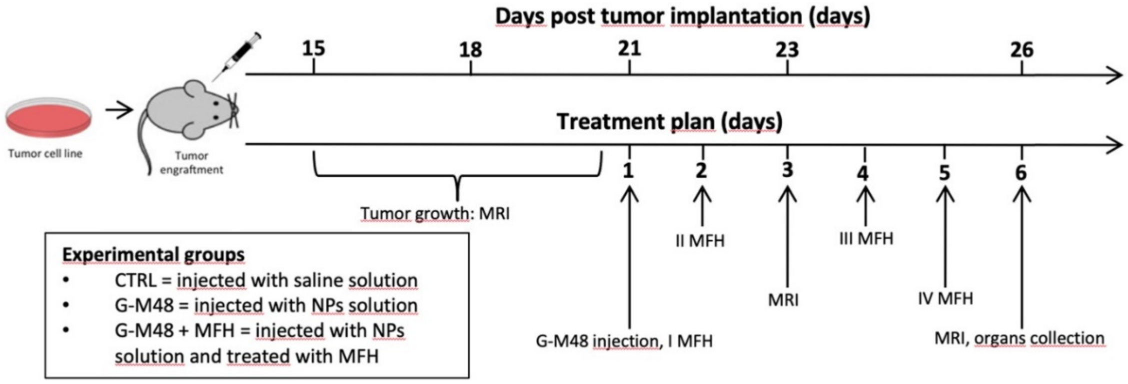

Figure 5. Schematic illustration of the *in vivo* experiment.

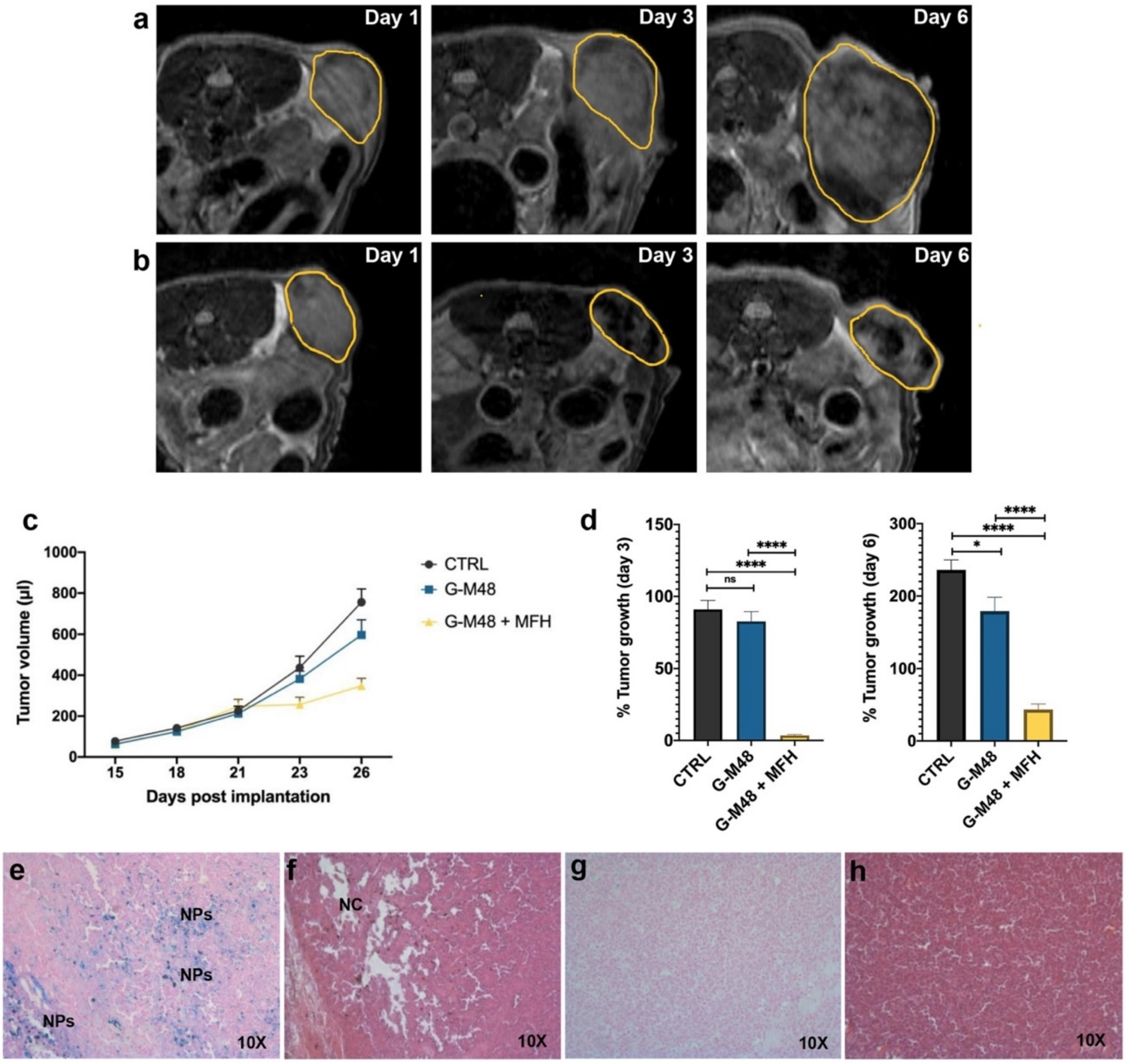

Figure 6. MRI monitoring of the % of tumor growth and histological examination. Representative MR images of the tumor's growth for the group administered with saline solution (a) and G-M48 + MFH (b). (c) Average tumor volume at different time points after tumor implantation (mean ± SEM). (d) % Tumor growth 3 and 6 days after the first MFH treatment (corresponding to 23 and 26 days after tumor implantation, respectively). A TWO-way ANOVA statistical test and a multiple comparison Tukey-Kramer test was used to assess the statistical significance of the % Tumor growth. (e-f) Histological slices of tumors treated with G-M48+MFH stained with Prussian Blue (e) and H&E (f). (g-h) Histological slices of tumors treated with saline and stained with Prussian Blue (g) and H&E (h).

Twenty-one days after cell implantation (tumor volume approximately 200 ul), G-M48 nanoparticles were intratumorally injected in mice. Four MFH treatments consisting of 20 min of exposure to AMF were applied (following the initial 15 minutes, necessary to reach the temperature plateau). Figure 6 (a-b) shows representative MRI images acquired in two mice belonging to the CTRL group and the G-M48 + MFH group. MRI images clearly show that tumor growth is considerably faster in the CTRL group than in the treated group. Moreover, the presence of G-M48 in the tumor tissue is detectable by MRI as signal voids, according to its ability to behave as a negative contrast agent (Figure S4, supplementary information, shows additional images). The tumor volume progression for the three experimental groups is reported in Figure 6 (c). The tumor volume does not differ among the three groups until day 21st after tumor cell implantation, which corresponds to day 1 of the treatment. After the second MFH cycle (24 hours after the first treatment), the tumor volume in G-M48 + MFH mice remains substantially lower than in control groups (saline solution and G-M48) (Figure 6 (c)). The percentage increase of the tumor volume for the experimental groups on day 3 and day 6 is shown in Figure 6 (d). Values are expressed as percentages of the initial size, measured at day 1 of the treatment plan (Figure 5). Data are reported as mean ± SEM. On day 3, while the tumor volume of group G-M48 + MFH is stable (3.45% ± 1.59) compared to the initial volume, the tumor volume of CTRL and G-M48 groups strongly increases by 91.11% ± 13.50 and 82.67% ± 16.68, respectively. At day 6, the tumor volume in the group G-M48 + MFH remains significantly smaller (43.47% ± 17.20) than either the CTRL group (236.09% ± 30.99) or the G-M48 group (179.51% ± 46.23), showing that G-M48 strongly inhibits tumor growth when applied as MFH mediator. It is noteworthy that a small difference in % tumor growth was also detected between CTRL and G-M48 groups. This may indicate marginal toxicity of the nanoparticles themselves that was not evidenced *in vitro*. It has to be considered that *in vivo* fate of injected nanoparticles could differ from *in vitro*: as apparent from MRI, upon intratumoral injection, nanoparticles accumulate heterogeneously in the tumor mass and, therefore, may give rise to local areas of very high concentration and toxicity. Future efforts will be devoted to minimizing such heterogeneous distribution in tumor tissues to optimize toxicity and efficacy.

The progress of tumor volume reported in Figure 6 (c) shows that the highest efficiency (no increase of tumor volume) is reached after the second MFH treatment in agreement with *in vitro* cell culture studies. Single heat treatment could induce irreversible protein damage and result in protein aggregation or inhibition of cellular functions. Moreover, it is well known that mild hyperthermia treatments can induce and regulate apoptosis and heat shock proteins (Hsps) expression. The tissue level effects include pH changes, alterations in perfusion, and oxygenation of the tumor micro- environment. To get more insight into cell death mechanisms and their dynamics, further studies will be needed to identify expression of different biomarkers related to necrosis and apoptosis. The effectiveness of any hyperthermia treatment greatly depends on the temperature generated at the targeted sites of action, duration of exposure, and specific cancer cells (Santos-Marques et al., 2006, Hildebrandt et al., 2002; Goldstein et al., 2003; Suto et al., 1995).

At day 6 of the treatment, mice were sacrificed, and the tumor masses excised for histological analysis. Figure 6 (e-h) shows histological slices of tumors treated with G-M48 + MFH and CTRL. Prussian Blue staining confirmed the presence of iron inside the tumor mass (see blue spots indicated by 'NPs') in the G-M48 + MFH group (e). H&E staining revealed damaged regions characterized by a paucity of cells distributed in different portions of the tumor (Figure 6 (f)) in the G-M48 + MFH group. The saline group resulted negative for Prussian Blue staining and did not exhibit apparent modifications in the parenchyma with good preservation of cellular morphology in the core and in the peripheral area of the mass (Figure 6 (g-h)). Good preservation of tumor tissue with the absence of necrotic areas was detected in the G-M48 group whose H&E histological slices closely resembled those of the CTRL group (see Figure S5).

Conclusion

This study characterized an innovative nanomaterial, M48, as a theranostic agent, combining diagnostic imaging with local treatment of cancerous tissues. The results show that a double shell coating process makes M48 water-soluble, biocompatible, and safe both *in vitro* and *in vivo*. T2 weighted MR images of G-M48 phantoms performed at 25°C and 75°C demonstrate the nanomaterial switching contrast property, opening new scenarios in MFH treatments controlled by MRI imaging. The biodistribution of G-M48 was investigated by MRI: clear and early loss of signal was detectable in the liver (40 min p.i.) while late loss of signal was detectable in kidneys (72h p.i.).

Finally, MFH experiments confirm the ability of G-M48 to act as a hyperthermia mediator both *in vitro* and *in vivo*. Results obtained *in vivo* are particularly interesting: after the first two MFH treatments, G-M48 nanoparticles strongly inhibit tumor growth (% tumor growth 3.45% ± 1.59 vs.91.11% ± 13.50 in the CTRL group).

Overall, our results pave the way for efficient and minimally invasive cancer therapy and diagnosis by applying a single NP as a hyperthermia heating agent and MRI contrast agent with self-regulating temperature properties.

Supplementary Information

Zeta Potential measurement of G-M48

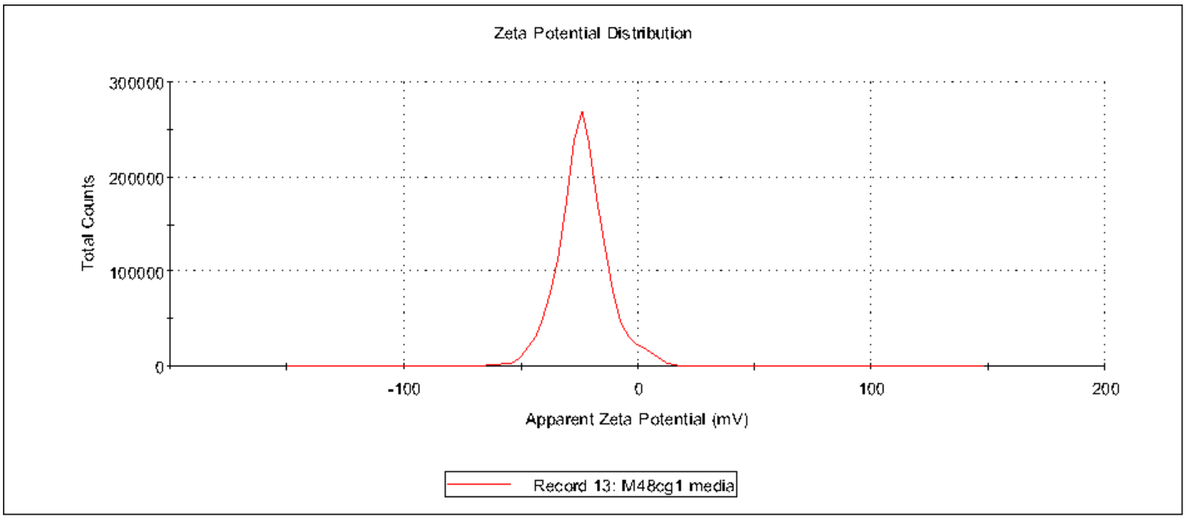

Figure S1. Zeta Potential for G-M48 nanomaterials.

Cytotoxicity in HeLa Cells

Cytotoxicity of G-M48 was evaluated on HeLa cells treated with increasing concentration of NPs (10, 50, 100 and 150 µg/ml) and incubated for 2, 24 and 48h. Results of toxicity tests are reported in Figure S2. MTT assay reveals that G-M48 does not affect in a statistically significant manner HeLa cells viability until 48h.

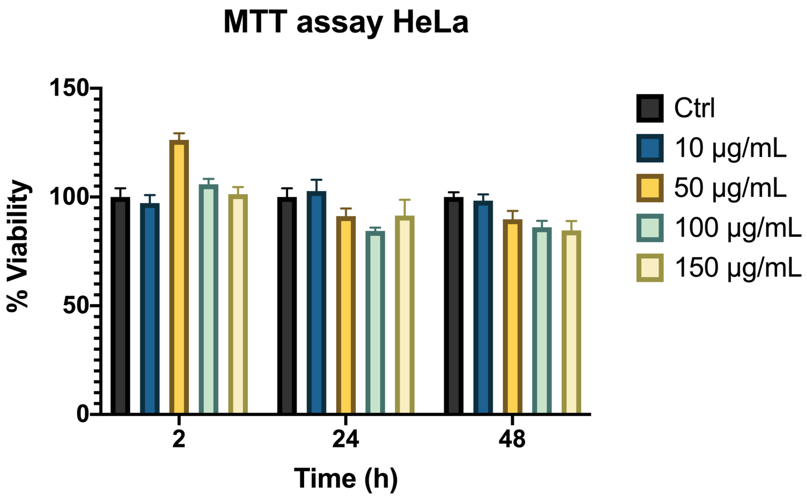

Figure S2. MTT assay in HeLa Cells incubated with G-M48 (10-150 µg/ml) for 2, 24 and 48h of internalization.

In vitro Magnetic Fluid Hyperthermia in HeLa cells

HeLa cells were incubated with G-M48 and subjected to MFH treatment for 20 minutes. Cell viability was determined by MTT assay, 24h after the hyperthermia treatment, and normalized respect to the related control cells. Different concentration of G-M48 (100, 300 and 700 µg/ml) were evaluated and the efficacy of the hyperthermia treatment on HeLa cells was obtained with 700 µg/ml of NPs (Figure S3). MTT assay on cells treated only with G-M48, but not exposed to MFH, showed viability of 95.56% while cells treated with 700 µg/mL NPs and exposed to MFH showed a viability of 72.57%.

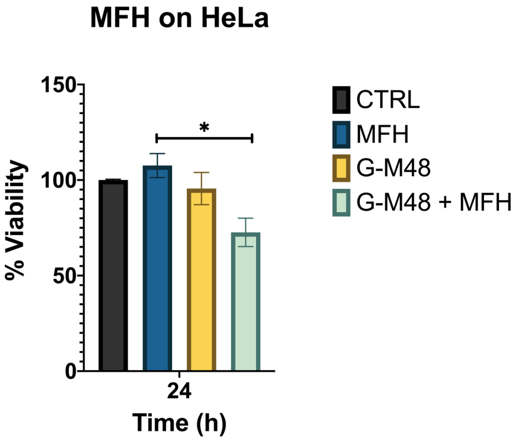

Figure S3. MTT assay in HeLa cells after MFH treatment.

Intratumoral localization of G-M48

In order to observe the distribution of NPs inside the tumor, T_2 weighted MR images were acquired before and after intratumoral injection of 50 µl G-M48 (1.2 mg Fe/ml) in mice. Representative images are reported in Figure S4 (a-b). Areas of signal drop were detected within the tumor mass (arrow in Figure S4 (b)) and in the subcutaneous region (asterisks in Figure S4 (b)). After MRI, the presence of G-M48 in the tumor tissues was confirmed by histological analysis. Prussian Blue staining of tumor tissue showed the presence of iron: several blue spots were detected inside the mass (Figure S4 (c)) and at the periphery of the tumour (Figure S4 (d)), corresponding to the dark areas detected in MRI.

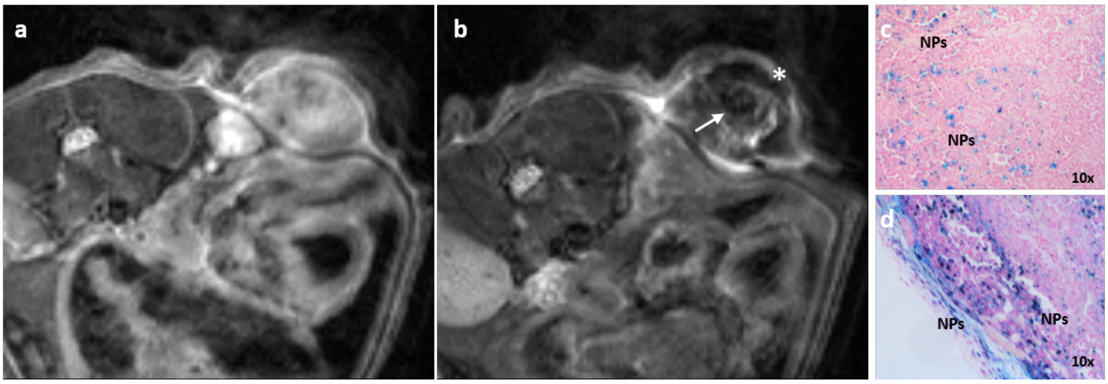

Figure S4. T_2 weighted MR images of tumor mass before (a) and after (b) intratumoral injection of G-M48 (1.2mg Fe/mL) in mice. The distribution of G-M48 is clearly visible (b) as hypointense areas (arrow and asterisks).The tumour mass was excised for histological examination with Prussian Blue staining; representative histological slices from the excised tumour tissue are reported in frames c-d: blue stained areas inside the tumour tissue (c) and at the tumour periphery (d) confirmed the presence of iron (magnification ×10).

Histological examination of tumor mass treated with G-M48

Six days after G-M48 intratumoral injection the tumor volume of mice treated with G-M48 increases of 179.51% ± 46.23 respect to the day of NPs injection. Representative MR images of mice treated with G-M48 at Day 0 and Day 6 is reported in Figure S6a. Histological analysis reveals the presence of NPs (b) and the preservation of tumor tissue (c). At day 6, the tumour masses were excised for histological examination. Figure S5 shows the Prussian Blue (b) and H&E (c) staining of the tumour tissue. Prussian Blue staining reveals several blue spots inside the tumor, proving the presence of iron inside the mass (Figure S5 (b)). Finally, mice treated with G-M48 don't exhibit evident modifications in the tumour tissue with a good preservation of cellular morphology, as shown in Figure S5 (c).

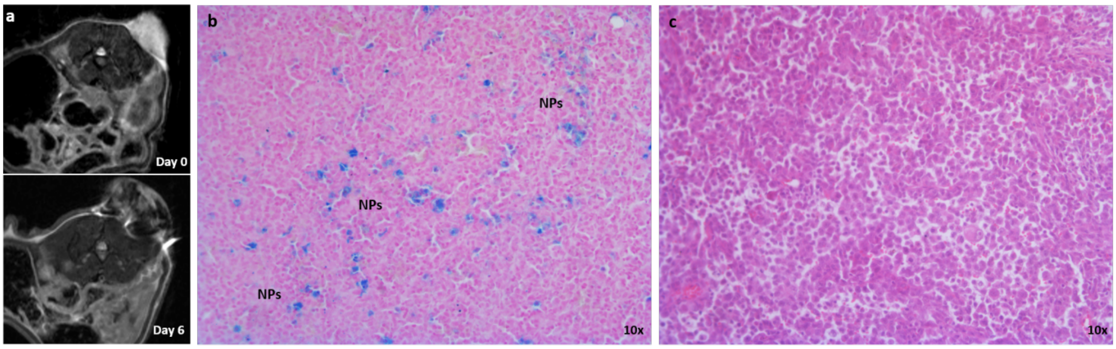

Figure S5. a) Representative MR images of mice treated with G-M48 at Day 0 and Day 6. The tumor growth is comparable to the saline group. (b-c) Histological analysis of tumor mass at day 6. Prussian Blue staining reveals the presence of iron (b), while H&E staining shows the preservation of tumor tissue (c).

2. Investigation of M55 as theranostic agent for MRI/MPI imging and MFH in breast cancer.

a. Introduction

Breast cancer is one of the leading causes of cancer morbidity and mortality. A recent review reported that breast cancer is the second most diagnosed malignancy, accounting for more than 11.6% of female cancers (Huang et al., 2021) and that it is the fifth commonest cause of cancer deaths, leading to 6.6% of all cancer mortality worldwide. The same review reports that breast cancer induces a substantial public health burden, leading to a loss of 14.8 million Disability Adjusted Life Years (DALYs). Despite progresses in early diagnosis of the disease and the availability of a variety of therapeutic approaches, its mortality rate remained the highest in the female population, representing the most reported cause of female cancer deaths.

Nowdays, the primary mammary tumors can be treated by surgery followed by chemotherapy or radiotherapy, this is an invasive and debilitating approach, contributing to the above mentioned DALYs losses. Chemotherapy and radiotherapy can damage healthy tissues, and surgery has risks of infection and bleeding and is not always curative for metastatic tumors. Novel therapy methods, minimally invasive, devoid of negative impacts, are desirable to reduce mortality rates and morbidity in breast cancer patients. Hyperthermia has been proposed to minimize morbidity and mortality of more invasive treatments. Hyperthermia can be generated in many ways, including ultrasound, RF waves and lasers (Egea-Benavente et al., 2021; Lu Y, et al. 2020.). Nanotechnology advancement has recently paved the way to Magnetic Fluid Hyperthermia (MFH) in which increase of temperature is reached by coupling magnetic nanoparticles with alternating magnetic fields. MFH has shown great promise in cancer research with the potential to overcome many of the limitations presented by other hyperthermia techniques (Kozsinnik et al., 2013).

Known limitations and challenges of MFH are represented by the need to deliver high quantity of MNPs to the tumor tissue and by the risk of overheating healthy tissues surrounding the tumors (Gerosa et al., 2021). In the currently applied preclinical and clinical protocols, MNPs are directly injected in the tumor tissue. When tumors are located in anatomical regions not easily accessible by injection, the need to deliver MNPs to tumor may result in an invasive procedure requiring surgery and anaesthesia. This is not the case of breast tumors: given that image-guided breast biopsy is routinely performed in breast cancer, the intratumor injection of MNPs required in MFH treatments could be easily performed in outpatient by trained surgeons, therefore avoiding invasive surgery.

For treatment of tumors located deep in the body, systemic administration of MNPs could be envisaged, although strongly limited by nonspecific uptake of MNPs to the liver and spleen, which typically exceeds the specific uptake to the tumor. In this respect, the application of Magnetic Particle Imaging to excite MNPs in specific regions of the body has been reported (Lu et al., 2020, Tay et al., 2018). The Field Free Region of MPI instrumentation, that can be localized over the tumor to millimeter-scale resolution, allows space selective irradiation of the tumor region.

The risk of overheating normal tissues in the close neighbouring of tumor tissue has been previously addressed by us and by other groups (Gerosa et al., 2021; Bhardwaj et al., 2020) using self-regulating temperature MNPs (Matteazzi, European Patent EP 2961429B1 Pr. 28.02.2014). In Gerosa et al. we have reported an extensive investigation of a self-regulating temperature nanomaterial synthesized in the form of nanoparticles by MBN Nanomaterialia S.p.A. (Treviso, Italy). The self-regulating heating effect consists of a stable temperature increase of the magnetic nanomaterial when exposed to Alternating Magnetic Field (AMF) up to a maximum value (TSR, Self-Regulating Temperature) below the Curie Temperature (Tc). The values of Tc can be modulated by adjusting the composition of the nanomaterial itself and is observed in correspondence to a second-order magnetic transition threshold between ferromagnetism and paramagnetism. Above Tc, the magnetization is negligible and consequently, magnetic losses do not occur, switching off the heating mechanisms under AMF. Interestingly the transition between ferromagnetism to paramagnetism is also coupled with a sharp decrease in transversal MRI relaxivity, making such MNPs temperature sensitive contrast agents (Gerosa et al., 2021). In principle, such properties are of paramount utility when the nanomaterial is integrated into biological matrices, allowing to limit the maximum temperature and at the same time to monitor the temperature reached by the change in MRI contrast. In Gerosa et al., we characterized an innovative nanomaterial, M48, as a theranostic agent, combining diagnostic MRI with local treatment of cancerous tissues. In the present paper, we have furtherly investigated such class of materials also considering (and focusing our attention on) their properties as contrast agents for MPI, in view of forthcoming application of MPI in MFH (Lu et al., 2020, Tay et al., 2018). The MNP investigated in the present paper, named M55, displays a higher Tc compared to M48. We investigated its properties as theranostic agent: namely its efficiency as therapeutic agent in MFH and its features as contrast agent for bimodal Imaging (MRI/MPI).

Our investigation has great potential to impact the future approach to the treatment of breast cancer, making it an outpatient, minimally invasive procedure with dramatic benefits for the patients and relevant economic advantages for the national health systems.

b. Materials and Methods

Synthesis of the iron-based NPs

The M55 sample is constituted by doped ferrites, prepared by MBN Nanomaterialia S.p.A (Treviso, Italy) with a proprietary mechanochemical process. The doped ferrite was synthesized from MgO, Fe_2O_3 and TiO_2 powders in proportion 2:4:1, using High Energy Ball Milling (Matteazzi, European Patent EP 2961429B1 Pr. 28.02.2014) in stainless steel equipment for a reaction time of 6 hours followed by a thermal treatment in air at 1200°C for 4 h. The resulting powder was finely ground by a ball milling step of 1h, then homogeneously dispersed in iso-propanol and ultrasonicated to promote de-aggregation. Centrifugal classification was used to extract nano-sized particles (< 200 nm). The processing was optimized with respect to the previous one (Gerosa et al., 2021), and the detailed processing parameters are courtesy of MBN.

Structural characterization

An X-Ray Powder Diffractometer (Thermo ARLX’TRA) equipped with a Cu-anode X-ray source with a Peltier Si (Li) cooled solid state detector was used to measure XRPD patterns. The XRPD pattern~~s~~ was collected with a scan rate of 0.094°/min~~s~~, with a measurement time of 6.5 s/step. The sample was prepared by homogenization using an agate mortar with few drops of ethanol. After evaporation of the solvent, the sample was deposited on a low background sample stage. The phase analysis was carried out using the ICSD database.

Morphological analysis and dimensional characterization

The size and morphology of M55 were investigated using Transmission Electron Microscopy (TEM, FEI TECNAI G2). For TEM analysis M55 was added to the copper grid and desiccated for one day before TEM imaging. Images of single particles as well as particle aggregates were acquired.

The hydrodynamic size and the zeta potential of the coated nanoparticles were determined with a Malvern Zetasizer Nano instrument. The sample was prepared in a proper plastic cuvette and the size and ζ- potential measures were repeated for the following 4 days to assess the stability of the coating.

Coating of the iron-based NPs

The doped ferrite NPs were coated with citrate moieties (using Trisodium Citrate dihydrate 99% Alfa Aesar as reagent) and then with glucose (using D-(+)-Glucose SigmaUltra 99.5% as reagent). The coating procedure strictly followed that reported in (Gerosa et al., 2021). Hereafter, the citrate, and glucose capped NPs will be referred to as G-M55.

IR Spectroscopy

The organic coating of M55 surface was determined and analyzed through FT-IR spectroscopy, with a JASCO FT/IR-660 plus. The sample was prepared by dispersing G-M55 in a KBr pellet (3 mg of NPs in 300 mg of KBr).

Cytotoxicity assay

The cytotoxicity of G-M55 was evaluated in MDA-MB-231 human mammary carcinoma cell line (purchased from ATCC Manassas, VA). Cells were cultured in Dulbecco's Minimum Essential Medium (DMEM) with 10% of Fetal Bovine Serum (FBS), 1% of a mix of penicillin/streptomycin 1:1 and 1% of L-glutamine 200 mM, seeded onto 96-well plates (3000 cells/well) and incubated at 37°C in humidified air with 5% CO2 for 24h. After 24 h, the medium was replaced with fresh medium containing 10, 50, 100, 150 and 300 µg/ml of G-M55.

The MTT (3-(4,5-dimethylthiazol-2-yl)-2,5-diphenyltetrazolium bromide) cytotoxicity assay was performed after 2, 24, and 48 h of incubation: 100 µl of MTT (at 5 mg/ml concentration, purchased from Sigma, Italy) were added to each well and incubated for additional 4 h (37°C, 5% CO2). Formazan crystals were dissolved in 100 µl of DMSO, and the absorbance was read at a wavelength of 570 nm using a microplate reader (HTX Microplate Reader BioTek Instruments, Winooski, VT, USA). Four measurements of optical density (OD) were recorded for each sample, and cell viability (%) was calculated with the following equation: CV% = (ODsample/ODcontrol) × 100.

Magnetic characterization and in vitro Magnetic Particle Imaging

The efficiency of G-M55 as multimodal contrast agent was assessed in MPI by using a RELAX module (Magnetic Insight Inc., Alameda, California, USA) and in MRI by using a 7T Bruker Biospec System. In MPI, two components of the measure were performed: the signal efficiency was measured through the MPI signal per mass of iron (high signal efficiency results in improved SNR and lower detection limits) and full-width at half-maximum (FWHM), which is related to the imaging resolution (lower FWHM results in less signal spread and improved imaging resolution). In particular, a sample containing G-M55 with a concentration of 5.5 µg of Fe in 10.0 µl volume was vortexed for 5 minutes and sonicated in a room temperature water bath sonicator for 5 minutes before testing. Relaxometry measurements were performed using the RELAX module on naked and coated nanoparticles at the same concentration and compared to VivoTrax (Ferucarbotran, Magnetic Insight Inc., Alameda, California, USA). The 1D signal acquisition mode was used for relaxometry measurements. A 2D projection images was used to test the nanoparticles with the following imaging parameters: standard mode, coronal acquisition,2-channel, FOV = 6 x 6 cm.

To measure the transversal relaxivity (spin-spin relaxation process) in MRI, the transversal relaxation time T_2 of water containing different amounts of G-M55 was measured acquiring a MSME (multi-slice multi-echo) pulse sequence. It consists of a 90° excitation RF pulse, followed by repeated 180° refocusing pulses interspersed by a fixed echo time (TE). The signals coming from each phantom at different TEs were averaged to obtain the relaxation curve decay, that was fitted with a single exponential decay function to obtain the T_2 value. Afterwards, the transversal relaxivity r_2 was obtained by measuring the modified relaxation time of water by the presence of G-M55 at different NPs concentration and then extrapolated via linear fit using the following equation: $\frac{1}{T_2} = \frac{1}{T_{2,0}} + r_2 c$.

Being $T_{2,0}$ the relaxation time of pure water, c the concentration of G-M55 (expressed as mM of Fe) and T_2 the modified relaxation time of water.

To assess the ability of the MPI to track cells MDA-MB-231 cells were seeded and cultured in Dulbecco's Minimum Essential Medium (DMEM) with 10% of Fetal Bovine Serum (FBS), 1% of a mix of penicillin/streptomycin 1:1 and 1% of L-glutamine 200 mM in a T-75 flask (5 x 10^6 cells) and accommodated for 24 hours. MDA-MB-231 cells were incubated with 1.0 mg Fe of G-M55 (two flasks) for 3 and 24 hours to observe the iron uptake. After the incubation time cells were washed 3 times with 5.0 ml of phosphate buffered saline solution (PBS) and then detached with 1.5 ml of 0.25% Trypsin, harvested and centrifuged (1200 rpm for 3 minutes). Once collected and tossed the supernatant the pellet was resuspended into 1.0 ml of PBS. The sample was divided into a triplicate of 4 x 10^6 cells in 0.1 ml PBS each in order to be imaged by MPI.

Images of the pellets were acquired using a Momentum MPI scanner (Magnetic Insight Inc., Alameda, CA, USA). It was adopted a 2D projection mode scan with the Default Mode setting (5.7 T/m gradient). The imaging parameters adopted were Field of View (FOV) = 4 x 12 cm^2, 1 average, acquisition time 10.0 s for each projection and reconstruction time 4.0 minutes.

Magnetic Fluid Hyperthermia and Magnetic Particle Imaging HYPER module

The transformation of magnetic energy into thermal energy mediated by magnetic nanoparticles in the presence of an external AMF is quantified from the value of specific absorption rate (SAR). The SAR value of nanoparticles in solution is calculated by using the following equation:

$$SAR = \frac{\Delta T}{\Delta t}\frac{C}{m_{Fe}}$$

Where C is the specific heat capacity of the solvent per g, ΔT is the temperature variation in time, m_{Fe} is the mass of iron in the compound per g. SAR was measured using a Nanotherics MagneTherm system (Warrington, United Kingdom) with samples diluted in water. The heat dissipation value strictly depends on the frequency and amplitude of the applied alternating magnetic field (AMF). The AMF apparatus yields a maximum magnetic field intensity of 23.0 kA/m (approximately 29.0 mT). A multichannel thermometer equipped with optical fiber probes (FOTEMP4, Optocon AG, Germany) was used to assess temperature variation within the sample every 10.0 s.

The multichannel thermometer was placed inside the sample during the whole acquisition time. Different concentrations of the nanoparticles were tested ranging from 2.0 mg/ml to 10.0 mg/ml of nanoparticles concentration per sample. The specific time window was chosen considering previous results obtained with G-M48 (see Gerosa et al., 2021) as well as translatability to clinics. The characteristic parameters of AMF were chosen in order to satisfy the Hergt criterion for the clinical translatability, in particular the magnetic field intensity was chosen as H = 8.75 kA/m and the frequency was selected equal to 473.1 kHz

MFH was performed in cell cultures, as well. A homemade device constituted by a closed box with a thermostated air stream-maintained cell cultures at 37°C. To avoid contamination of cell cultures, the temperature was calibrated before the measurement in a disposable sample constituted by the exact concentration of NPs used for the experiment diluted in Dulbecco's Minimum Essential Medium (DMEM) with 10% of Fetal Bovine Serum (FBS), 1% of a mix of penicillin/streptomycin 1:1 and 1% of L-glutamine 200 mM.

The SAR was also measured by using the HYPER module of the Magnetic Particle Imager Momentum Scanner (Magnetic Insight Inc., Alameda, California, USA). The change in temperature over time was recorded for both coated and naked nanoparticles for 300 seconds (necessary time window to evaluate SAR, established considering the results achieved with G-M48 as well as a minimum exposure time to AMF equal to at least 35 minutes) from thermostated room temperature with a magnetic field excitation of 12.75 kA/m at 1600 kA/m^2 gradient. Samples used were composed by 100 µl volume with the same nanoparticles concentration adopted for the measurement performed with Nanotherics.

The efficiency of the MFH treatment in cell cultures was demonstrated through a MTT assay. Cells were plated on 96 well plates, incubated for 24 hours with 150 µg/mL of G-M55 and treated for 35 minutes with MFH protocol (15 minutes to reach the temperature plateau and 20 minutes of treatment). Untreated cells and cells treated with 150 µg/mL of G-M55 but not exposed to MFH were used as controls. After twenty-four hours, MTT cytotoxicity assay was performed. The viability of MDA-MB-231 cells was evaluated after one and two hyperthermia treatments and normalized to that of the respective controls

In vivo studies

The biodistribution of G-M55 was investigated in normal nude homozygote female mice (n = 4) and in same type of mouse but bearing MDA-MB-231 subcutaneous tumor (n =

4). Nude homozygote female mice (6–8 weeks old, Envigo, Italy) were used. MRI was performed using a Bruker Biospin 7T (Bruker Biospin, Ettlingen, Germany) scanner. Animals were anesthetized with gas anesthesia (a mixture of O2 and air containing 1.5% of isofluorane), placed in a heated animal bed and inserted in a 7.2 cm internal diameter bird-cage coil. G-M55 was injected at a dosage of 4.0 mgFe/kg through the tail vein. Images of the mice body were acquired before and 10 min–30 min–60 min–24 h–72 h post G-M55 i.v injection in order to monitor the bioaccumulation inside the tumor respect to other organs uptake. The sequences adopted were the following: T_2 RARE sequence with TR = 1200 ms, TE_{eff} = 36 ms, FOV= 35×35 mm^3, MTX= 128×128, slice thickness = 1.0 mm. T_2 MAP sequence with TR = 1556.906 ms, TE_{eff} = 7.469 ms, NEX = 1, FOV= 30 × 30 mm^3, MTX= 256×128, slice thickness = 1.0 mm, Echo images = 10, Echo space = 7.47 ms.

The efficacy of G-M55 as MFH agent was investigated in N = 18 nude homozygote female mice (Harlan Laboratories, Udine, Italy). Two million MDA-MB-231 cells were injected subcutaneously in the flank of nude mice. Starting from 15 days after cells inoculation, the size of the tumor mass was measured every three days through MRI. Twenty-one days post tumor implantation (when tumor volume reached about 200 μl) mice were divided into three groups according to the treatment. Animals in the first group (CTRL) received saline intratumorally. Animals in the second group (G-M55) received G-M55 [1.2mg Fe/mL] intratumorally. Animals in the third group (G-M55 + MFH) received G-M55 [1.2mg Fe/mL] intratumorally and were exposed to four MFH cycles immediately, 24h, 48h, and 96h after G-M55 injection. Each MFH treatment consisted of 2100 s application of an AMF with an intensity of 23 kA/m and a frequency of 473.1 kHz. The number of hyperthermia cycles differs from in vitro evaluation considering the positive results obtained with G-M48 and were meant to replicate them.

All mice were monitored by MRI before (day 1), 3 days (day 4) and 5 days (day 6) post G-M55 injection to measure the time evolution of tumor size. T_2 weighted images were acquired in the axial plane using a RARE 3D sequence with TR = 1200 ms, T_{Eeff} = 47.5 ms, NEX = 1, field of view = 25 × 25 × 25 cm^3, MTX = 256 × 128 × 32, slice thickness = 0.8 mm, FA = 90°, RARE factor = 16. To measure the volume of tumors, MR images were processed with Paravision software and a MATLAB (MathWorks, Natick, USA) script. The tumor area was manually selected slice by slice and tumor volume was calculated as $(\sum_{i=1}^{n} pu_i) * image\ resolution$, where pu_i represents the number of pixel manually selected. The percentage increase in tumor volume was calculated at each time point as $100*(V_t-V_0)/V_0$, where V_t is the tumor volume at time t and V_0 is the initial volume.

Mice used in in vivo experiments were maintained under standard environmental conditions (temperature, humidity, and 12 h/12 h light/dark cycle, with water and food ad libitum) and veterinarian control in the animal facility of the University of Verona. Animal experiments were conducted following Italian law (D.L. 4 March 2014 no. 26) and the European Union normative (2010/63/EU).

Histology

Once the in vivo experiments were completed, mice were sacrificed and relevant organs (tumor, liver, kidneys, spleen, lungs, stomach, intestine and heart) were dissected out for histology. Excised samples were washed with PBS 0.1 M and fixed in Carnoy solution for 2.5 hours. Tissues were embedded in paraffin, cut in 8 μm thick sections with a microtome and dried at 37°C for 24 h. Prussian Blue staining was performed was performed to evaluate the presence of iron in the tissues: sections were incubated with PB solution (5% hydrochloric acid and 5% potassium ferrocyanide) for 20 min and counterstained with nuclear fast red (Bioptica) for 2 min. To evaluate tissue damage and morphology, sections were stained with Hematoxylin and Eosin. Sections were examined under a light microscope (Olympus BXS1) equipped with a charge-coupled device camera.

Fluorescent Immunohistochemistry

Immunofluorescence allowed to observe the overexpression of HSP70 within the cell colture (MDA-MB-231). After I, II and IV MFH treatments cells were fixed with 4% PFA solution at room temperature and then fixed with 70% ethanol at -20 °C overnight. After fixation cells were permeabilized with 0.1% Tryton X-100 in PBS for 10 minutes at room temperature. Later on incubated in blocking solution for 30 minutes and immunostained with the following primary antibodies: Rabbit Anti Caspase-3 (Abcam 1:20), Rabbit Anti HSP70 (Abcam 1:50) overnight at 4 °C. Secondary antibody against rabbit (Alexa Fluor® 488) ab150077 was used at 1:100 dilution. Then, cells were washed with PBS, counterstained with Trypan (GIBCO 1:10) for 15 seconds, washed with PBS, stained for 5 min with 1 μg/ml of Hoechst 33342 (Sigma) in PBS and finally mounted in

PBS:glycerol (1:1) to be observed at confocal microscope. Observation of HSP70 levels was accomplished with LEICA TCS-SP5 Inverted Confocal Microscope. A diode laser was employed for Hoechst 33342 with λ = 405 nm, a visible laser for HSP70 with λ = 496 nm a He/Ne laser for Trypan Blue with λ = 543 nm.

Statistical Analysis

Statistical and data analysis were realized in MatLab (Mathworks, Natick, MA, USA), then confirmed and plotted using Prism software (8.1.1, GraphPad Inc., La Jolla, CA, USA). All the data are expressed as mean ± standard deviation of the mean (Mean ± SEM). Statistically significant differences were evaluated by TWO-way ANOVA with multiple comparisons using the Tukey-Kramer method. Differences were considered statistically significant when the $p\text{-value} < 0.05$.

c. Results

Structural characterization and stability of G-M55

Phase and structural composition were investigated by X-Ray Powder Diffraction (XRPD). The obtained experimental pattern is shown in Figure 1 (a). The comparison between XRPD pattern for M55 and the single crystal patterns in the ICSD database revealed that the sample under investigation is compatible with a mixture of several metal oxides. In Figure 1 (a), the experimental pattern is compared with the singe crystal patterns of the ICSD database that better matched it. As a further confirm, EDX analysis of the M55 sample revealed the presence of Fe, Mg and Ti, indicating that other iron-containing compounds, as magnesium ferrite or iron titanate, can be present in the sample. Given the complexity of the system, it is difficult to determine the precise composition of the sample.

FTIR spectra of the G-M55 sample underline the presence of both citrate ions and glucose molecules on the surface of the M55 as capping agents. Figure 1 b shows a broad band around 3300 cm^{-1} due to -OH stretching of glucose and citrate and another band around 2900 cm^{-1} due to -CH stretching of both molecules. The presence of citrate ions is highlighted by the features around 1600-1700 cm^{-1} corresponding to the C=O stretching of carboxylate groups (Silverstein et al., 2005). The maxima of the bands are shifted for the nanoparticles with respect to the free citrate moiety because of the interaction between carboxylate groups and nanoparticle surface. It is also possible to observe bands due to other vibrations of the glucose molecular skeleton in the region between 1200 and 900 cm^{-1} in agreement with those observed for the FTIR spectrum of the glucose molecule alone (red line in Figure 1 b) (Silverstein et al., 2005). The intense absorption band around 570 cm^{-1} is assigned to Fe-O, Mg-O and Ti-O vibrations of the inorganic phase (Kiani et al., 2019).

Dynamic Light Scattering (DLS) was exploited to investigate the colloidal stability of water dispersion of G-M55 through ζ- potential and size measurements. The average ζ-potential of -32.1 ± 8.2 mV and the average hydrodynamic diameter of 113.1 ± 30 nm confirmed good colloidal stability in aqueous environments. The stability and the dimensions were investigated as a function of time throughout an entire week. The ζ-potential and the size of the nanoparticles remained substantially unvaried during the entire week, confirming an excellent colloidal stability, and demonstrating the stability of the coating. (Figure 1 c,d)

Transmission electron microscopy (TEM) allowed the investigation of M55 morphology. TEM image, reported in Figure 1 (e), reveals that M55 nanoparticles have a large size dispersion and are present as single nanoparticles or aggregates with size ranging from around 10 nm to more than 150 nm.

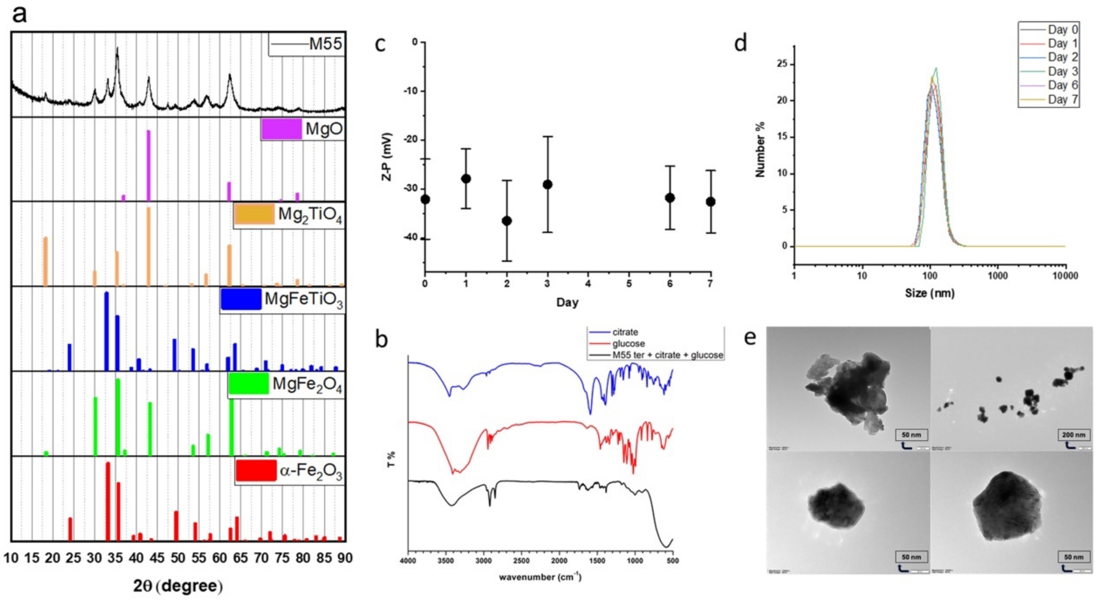

Figure 1. **a.** XRPD graph demonstrates the predominant composition of the nanoparticle and its most common phases. **b.** IR spectroscopy was of great help to understand the surface composition before the coating procedure. **c.** ζ- potential of G-M55. As can be seen from the graph it has been monitored up to one week showing a good average colloidal stability **d.** Hydrodynamic radius at DLS. As for the previous measurement it has been observed for one week and it has demonstrated a performant consistency and a sharp peak.**e.** TEM has been used to investigate the morphology and structure of the nanoparticles. There is a robust agreement between the hydrodynamic radius measured through DLS and the average dimension observed at the TEM.

Magnetic properties of G-M55

To define the ability of G-M55 to serve as multimodal contrast agent exploitable for both MPI and MRI two different magnetic characterizations were performed. At first it was assessed the MPI performance of G-M55 and it was compared to its naked version (M55) and to a commercially available MPI tracer, VivoTrax (Magnetic Insight Inc., Alameda, California, USA). The signal efficiency (i.e. the signal per ng of iron), the full width half maximum (FWHM) and the approximate resolution were measured through the RELAX module of Magnetic Particle Imager Momentum Scanner (Magnetic Insight Inc., Alameda, California, USA). Fig. 2a, shows the relaxometry measurement of naked (M55) and coated (G-M55) nanoparticles. This measurement allows quantification of the signal efficiency and the space resolution given by the tracer (see Tab. I). In MPI signal resolution is computed considering the FWHM through the formula Resolution (mm) = FWHM (mT)/Gradient(T/m) where the resolution is defined as the distance for two objects separated at 50% of their distance.

Table I. Signal Efficiency, FWHM and approximate resolution for M55 and G-M55, compared to VivoTrax

Nanoparticle	Signal Efficiency (Signal per ng/Fe)	FWHM	Approximate Resolution (mm)
M55 (isopropyl)	1.8	7.5	0.7
G-M55 (water)	1.3	16.4	1.5
Ferucarbotran (VivoTrax)	16.4	11.8	1.1

As can be observed from Table I, even if the signal efficiency is approximately 89% (for M55) and 92% (for G-M55) lower than VivoTrax, the resolution, computed from the FWHM, is better than VivoTrax for M55 and comparable to VivoTrax for G-M55.

Although M55 and G-M55 have lower signal efficiency than commercially available VivoTrax, they are able to provide similar resolution. These observations led us to define M55 and G-M55 good tracers for MPI. Further developments in the synthesis procedure will be needed to sharpen and intensify the signal efficiency of M55 and its coated version G-M55.

The transversal (spin-spin) relaxation time of water dispersion containing G-M55 was measured at 7T Bruker Biospin MRI scanner through a series of phantoms with scalable nanoparticles concentration, ranging from 0.318 mM to 1.591 mM. In Fig. 2c T2w images of above mentioned phantoms are reported. As expected, the T_2-weighted MR images of G-M55 phantoms tend to become darker with increasing iron concentration showing that G-M55 can effectively reduce the spin-spin relaxation time of water protons as a T_2 contrast agent. Values of $1/T_2$ vs Fe concentration were interpolated using a straight line whose slope determines the transversal relaxivity of the nanoparticles under investigation (Figure 2b). It was obtained a transversal relaxivity (r_2) of 53.20 $mM^{-1}s^{-1}$, comparable to the value of a commercial iron oxide MRI contrast agent, like Endorem® (Valero et al., 2014) confirming the potential of G-M55 as a contrast agent for MRI. In particular r_2 coefficient is increased by 40% respect to the r_2 coefficient shown by G-M48 (Gerosa et al., 2021).

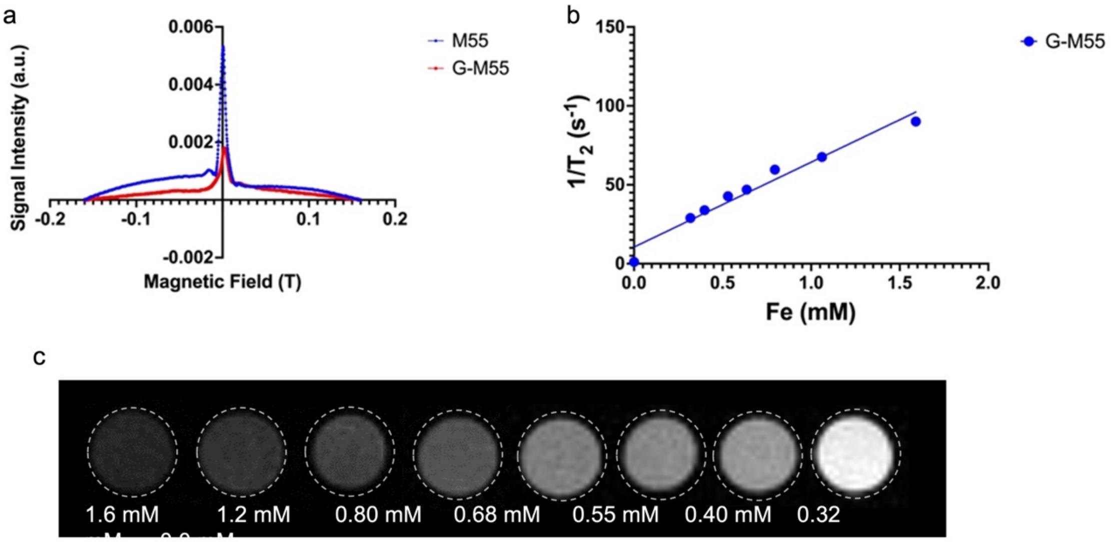

Figure 2. Characterization of G-M55 as a bimodal contrast agent. **a.** Relaxometry measurement of naked (M55) and coated (G-M55) nanoparticles through RELAX module of MPI. By means of this measure the signal efficiency and the resolution given by the tracer was quantified. **b.** Plot of transversal relaxation rate (1/T2) versus Fe concentration in water dispersed G-M55 phantoms,

at 25°C. The slope of the fitting straight line (53.20 mM-1s-1) represents the transversal relaxivity coefficient (r_2). **c.** T2w MR images of phantoms containing decreasing concentrations of G-M55.

In order to test the efficiency of G-M55 as MPI contrast agent in a biologically significant context, it was used in a cellular imaging experiment aimed at demonstrating the ability of G-M55 to label and detect MDA-MB-231 cells by MPI. The incubation protocol as well as MPI images collection and analysis have been widely described in the previous related subsection. Results are reported in Figure 3. For any MPI experiment it is essential to set up a calibration curve of the tracer that needs to be used. The linear trend of the signal intensity per mm^2 vs the iron mass per ml used is crucial to establish the feasibility of the measurement. A calibration curve of the tracer was set up by scanning in 2D different concentrations of NPs, expressed as iron content (as shown in Figure 3b). The calibration curve was then used as a reference to assess the number of cells observable in a sample. Figure 3a reports quantitatively the MPI signal intensity per mm^2 obtained scanning different amount of cells in the same volume (10 ul). The series of images shown in Figure 3 c shows the ability of G-M55 to label cells with and keep them observable up to approximately 30000 cells.

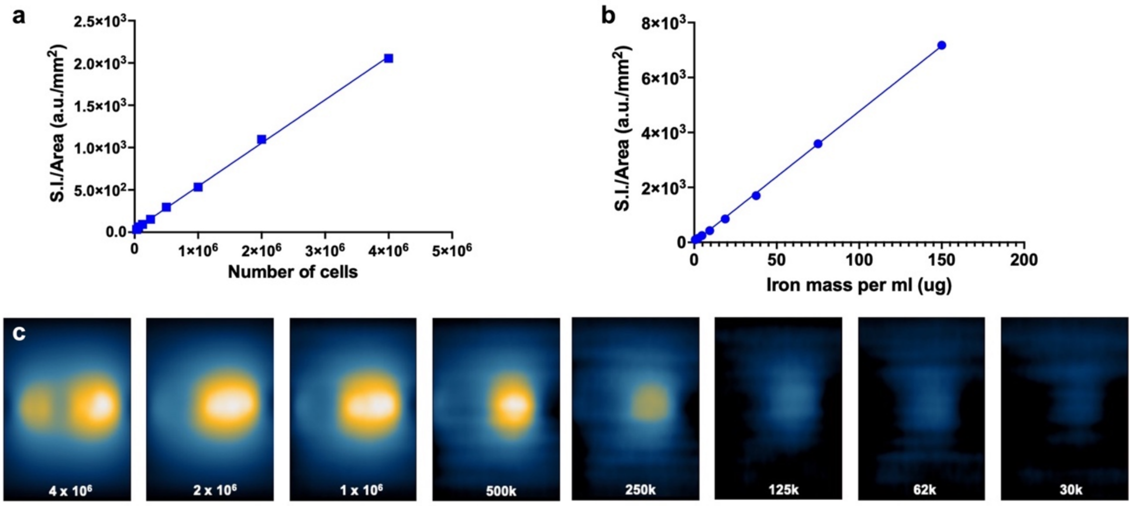

Figure 3. **a.** Calibration curve of the tracer used for the labeling experiment. The slope of the straight line underlines the ability of the single nanoparticle to serve as a MPI contrast agent. **b.** Number of cells that can be observed considering a 1.0 mg Fe/ml of incubation. The slope of the straight line defines the ability of the tracer to serve as an efficient cell labeling agent in MPI **c.** The whole row is composed by the different number of cells that can be observed in MPI using G-M55 as a labeling agent.

Cytotoxicity, internalization mechanism and in vitro MFH

Before using nanoparticles as hyperthermia mediators, it is fundamental to evaluate the biocompatibility with an *in vitro* cytotoxicity assay. The toxicity of G-M55 was therefore assessed after 2, 24, and 48h of incubation with MDA-MB-231 cells at different concentrations. MTT assay reveals that G-M55 is safe up to the concentration of 150 µg/mL for long incubation times (48 h), as shown in Fig. 4 (a). No statistically significant difference was found for the concentrations adopted. Considering these results, the highest non-toxic concentration of 150 µg/mL was chosen to perform MFH *in vitro* experiments relevant for magnetic fluid hyperthermia. TEM images performed in MDA-MB-231 cells demonstrated that G-M55 are internalized mainly via endocytosis and compartmentalized into endosomes (see Fig. 4d) in agreement with previously reported findings for a similar NPs (see Gerosa et al., 2021).

In the perspective of biomedical application as heat exchange mediator, the Specific Absorption Rate (SAR) of G-M55 was evaluated. SAR was evaluated in two different ways considering future clinical applications: first it was assessed through Nanotherics Magnetherm following a procedure comparable to the one described in Gerosa et al., 2021; second it was tested by means of the HYPER module of the MPI. In both measurements, thermograms were collected starting from a specific bulk temperature, about 36.0 °C. This starting condition was chosen to simulate the condition of *in vivo* experiments. Once observed a good heating ability of the naked nanoparticle (M55), the measures were carried out on its coated version G-M55. The same iron concentration was adopted to estimate SAR in aqueous solution with the two methods. Fig. 4 (b upper and lower) reports the thermograms collected in aqueous suspensions of G-M55 at concentration of 6mg/ml, using Nanotherics Magnetherm and the HYPER module of the MPI, respectively. As shown in Figure 4(b), an increase of 2.5 °C of temperature was detected at the used concentration. SAR estimated with Nanotherics Magnetherm resulted to be equal to 11.1 ± 1.0 Wg^{-1} and SAR estimated with RELAX module in MPI was equal to 9.5 ± 1.4 Wg^{-1}. The result seems to be slightly below typical SAR values reported in the literature for iron oxide nanoparticles (ranging from 20 to 400 Wg^{-1}) and below the value reported for G-M48 in our previous work (Gerosa et al., 2021). Considering that similar SAR values were obtained through the two different methods, we have chosen to develop our magnetic hyperthermia strategy exploiting Nanotherics

Magnetherm because the safety criterion evaluated by means of the *C* parameter (see discussion section) was significantly lower and paves the way for a more reliable and scalable solution for the clinics. Moreover, the experimental set up of the Nanotherics Magnetherm was easily exploitable for both *in vitro* and *in vivo* treatments.

G-M55 was tested as hyperthermia mediator on a triple negative mammary carcinoma cell line, MDA-MB-231, at a concentration of 150 µg/mL, verified to be the highest non-toxic concentration (Figure 4c). MDA-MB-231 cells were incubated with G-M55 for 24h and exposed to two cycles of AMF spaced 24h one each other. Cell viability data after MFH are shown in Fig. 4c. Cell viability was significantly affected by AMF application compared to control conditions (untreated cells and cells treated only with G-M55 but not exposed to MFH). At the time point of the first MFH treatment, MDA-MB-231 cells treated with G-M55 but not exposed to AMF showed a percentage of viability of 101.76 ± 3.66 %, while cells treated with G-M55 and exposed to AMF showed a percentage of viability of 84.45 ± 1.67 %. At the time point of the second MFH treatment, MDA-MB-231 cells treated with G-M55 but not exposed to AMF showed a percentage of viability of 114.91 ± 7.79 %, while cells treated with G-M55 and exposed to AMF showed a percentage of viability of 63.15 ± 3.44 %.

To have an insight into the mechanism of cell death induced by MFH treatment, after two and four MFH treatments, cells were processed for immunofluorescence protocol to evaluate the expression of HSP70, as indicators of cellular stress, including the rise of temperature. As shown in Figure 4e, the expression of HSP70 is more evident in the samples treated with hyperthermia (G-M55 + MFH) than in the control ones (G-M55 and CTRL), especially after two MFH treatments. This finding is compatible with an increase of temperature in the samples during MFH treatments, as expected. Surprisingly, the expression of HSP70 in the sample treated with G-M55 and exposed to four MFH treatments is lower than that observed in the sample exposed to two treatments, possibly indicating an effect of thermotolerance induced by multiple AMF exposures.

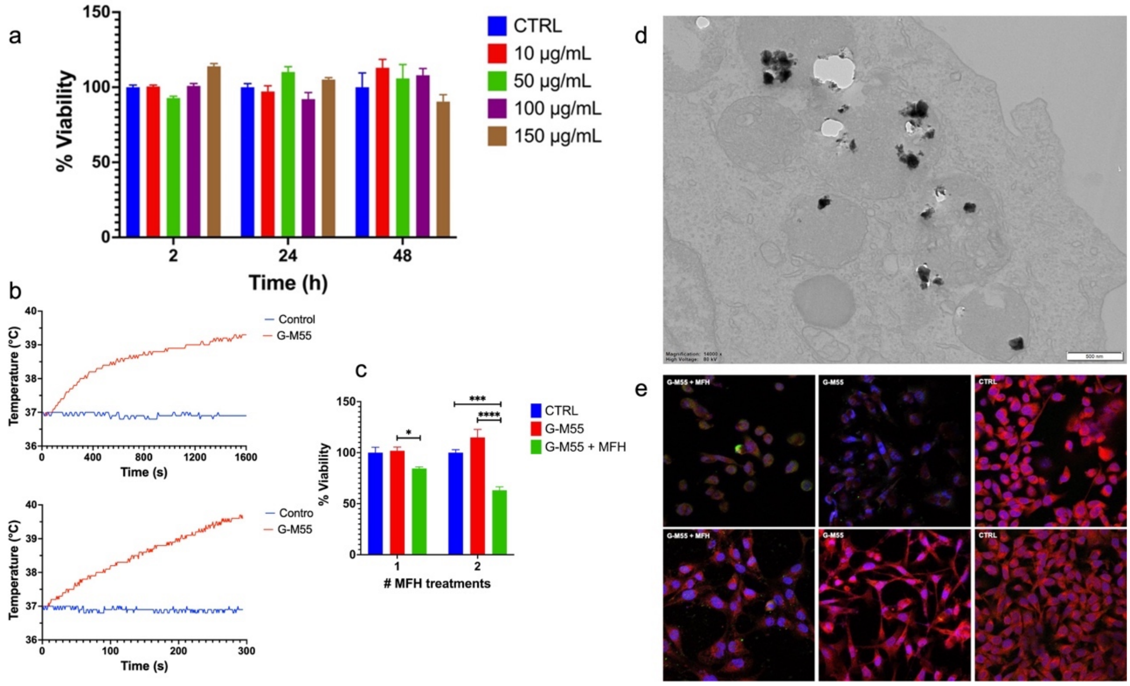

Figure 4. **a.** Characterization of in vitro viability of MDA-MB-231 through MTT assay with different concentrations of G-M55. **b.** AMF application at Nanotherics Magnetherm comparing a Control (water solution) with G-M55 water dispersed solution. C = 4.1 10^9 $Am^{-1}s^{-1}$. **c.** MTT assay to assess the efficiency of G-M55 to act as MFH mediator with different number of treatments. **d.** Internalization of G-M55 in MDA-MB-231 observed at TEM. **e.** Representative fields for G-M55 efficiency as MFH tracer observing the expression of HSPs in immunofluorescence.

In vivo biomedical application of G-M55 as Magnetic Fluid Hyperthermia mediator

The biodistribution and clearance of G-M55 was investigated in vivo. In Figure 5a, MR images of a representative mouse acquired using a T2-weighted sequence before, 10 min, 60 min and 72 hours after the injection of G-M55 are show. The signal intensity (S.I) in the liver decreased by 32.6 ± 5.2% (Figure 5 (b)) 10 min after injection, and by 20 % from 30 min onwards, indicating early hepatic accumulation of the nanoparticles followed by clearance. At difference, the percentage SI decrease in the kidney showed an increasing trend that may indicate renal clearance of G-M55. No loss of signal was detected in the spleen.

Histology of the main organs involved in the biodistribution of the tracer were performed and shown in Figure 5c and 5d. It has to be observed that none of the organs involved in the biodistribution has been harmed, injured or affected by the presence of G-M55 as can be seen from H&E staining. As expected, in Figure 5c it is possible to observe that nanoparticles presence can be observed closer to veins and vessels due to the extravasation phenomenon that mainly contributes to spread nanoparticles all over the organism.

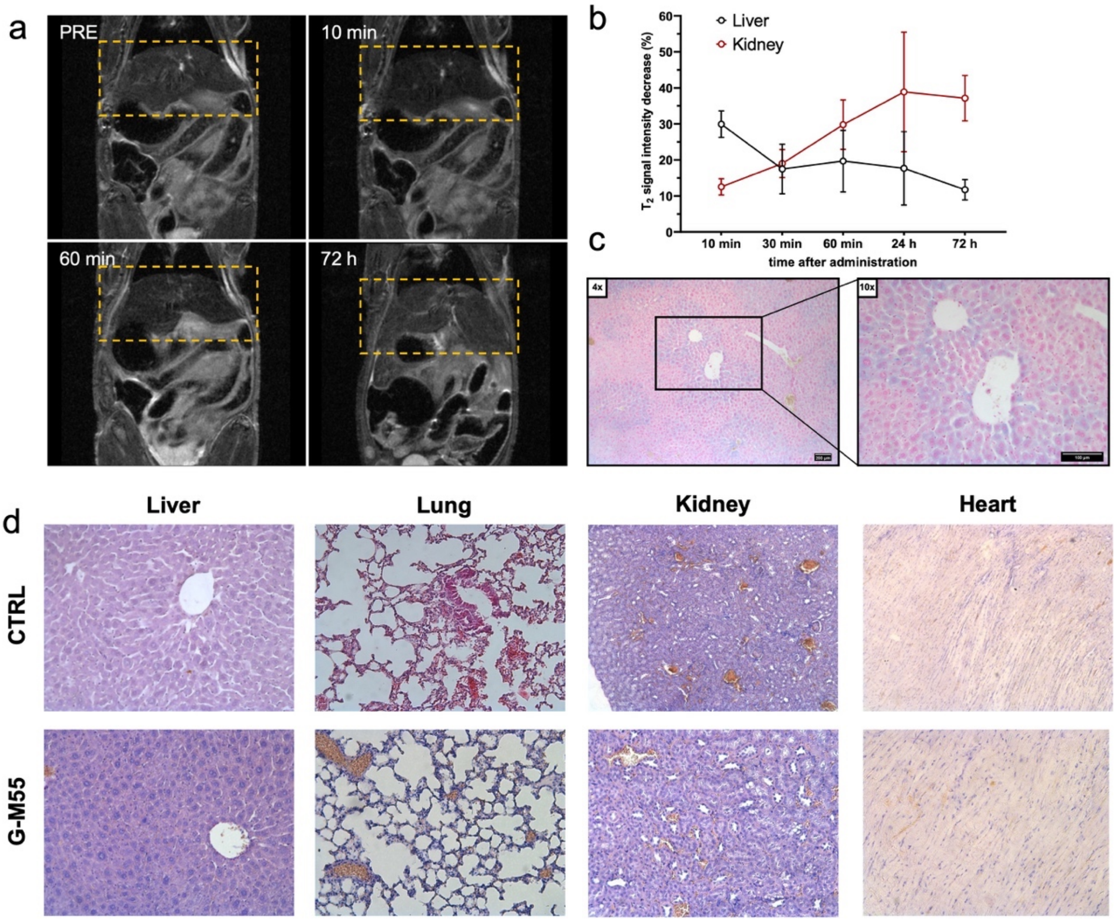

Figure 5. **a.** T$_2$-weighted images of liver of mice treated with G-M55 NPs at different timepoints. **b.** Plot of T$_2$ signal change, expressed as signal intensity decrease (%), in liver, (spleen), kidneys at different time points up to 72h after administration of G-M55 NPs. **c.** Detail of liver tissue of the animal treated with G-M55 NPs. Tissues were treated with Prussian Blue and Fast red as counterstaining to underline nanoparticles presence. **d.** Histological analysis of tissues from animals not treated and from animals treated with G-M55 NPs. HE is reported of the main organs involved in biodistribution.

The in vivo MFH experiment was performed considering the protocol described in Materials and Methods.

In Fig 6a, images of tumor in representative mice belonging to the G-M55 and G-M55+MFH are reported. The presence of G-M55 in the tumor tissue is detectable by MRI as signal voids, according to its ability to behave as a negative contrast agent. In Figure 6b and 6c, the tumor volume progression of the three groups is reported.

The graphs reported in Figure 6b and 6c correspond to the MRI measurement of the tumor volume. In particular, the tumor volume on day 4 (after 4 MFH treatments), on day 6 and on day 9.

The tumor volume does not differ among the three groups until day 21st after tumor cell implantation, which corresponds to day 1 of the treatment. After the fourth MFH cycle (72hours after the first treatment), the tumor volume in G-M55 + MFH mice remains substantially lower than in control groups (saline solution and G-M55) (Figure 6b, 6c). The percentage increase of the tumor volume for the experimental groups on day 4, day 6 and day 9 is shown in Figure 6c. Values are expressed as percentages of the initial size, measured at day 1 of the treatment plan. Data are reported as mean ± SEM.

On day 6, while the tumor volume of group G-M55 + MFH is stable (14,52%) compared to the initial volume, the tumor volume of CTRL and G-M55 groups strongly increases by 238,06% ± 23,21% and 184,25% ± 7,37%, respectively. At day 9, the tumor volume in the group G-M55 + MFH remains significantly smaller (83,37% ± 9,17%) than either the CTRL group (432,23% ± 23,76%) or the G-M55 group (378,37% ± 22,66%), showing that G-M55 strongly inhibits tumor growth when applied as MFH mediator. For this study, mice were monitored up to day 9 to analyze the tumor growth trend. 6 days after the last MFH treatment the tumor volume was significantly smaller than the control groups. At day 9, mice were sacrificed, and the tumor masses excised for histological analysis. Figure 6d shows histological slices of tumors treated with G-M55 and G-M55+ MFH. Prussian Blue staining confirmed the presence of iron inside the tumor mass. H&E staining revealed damaged regions in different portions of the tumor (Figure 6e) in the G-M55 + MFH group. Good preservation of tumor tissue with the absence of necrotic areas was detected in the G-M55 group whose H&E histological slices closely resembled those of the CTRL group.

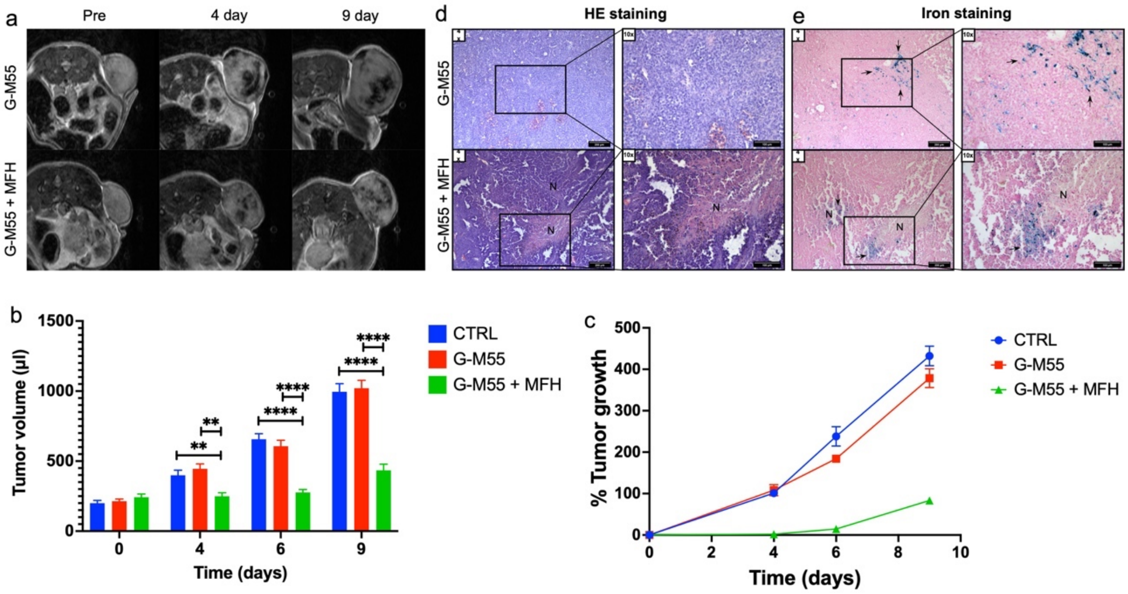

Figure 6. **a.** T_2-weighted images of a representative tumor from animals treated with G-M55 (top) and from animals treated with G-M55 and hyperthermia (bottom) at different timepoints. **b.** Tumor volume growth after the MFH treatments at different time points. The statistical analysis shows the increasing difference among the groups at different time points. **c.** Tumor volume growth expressed as % after the MFH treatments at different time points. **d. - e.** Histological analysis of tumors from animals treated with G-M55 NPs and from animals treated with G-M55 NPs and MFH. HE (magnification 4x and 10x) and iron staining (magnification 4x and 10x) are reported. The "N" letters indicate the necrotic zones of tumors. Black arrows indicate representative blue spots corresponding to iron deposits in the tissues treated with the iron staining.

d. Discussion

Considering the results obtained so far in this work (still under investigation in our lab) the development of the G-M55 has shown promising results both as contrast agent for MRI and MPI and as a MFH mediator for in vitro and in vivo applications. All the results are still under discussion but even so a few important considerations could be raised.

Through a robust characterization pipeline, it raised the efficiency of G-M55 as a magnetic tracer useful for MPI and MRI imaging. The competitive biocompatibility at high nanoparticles concentration and the ability to satisfy the Hergt criterion for the clinical translatability of the mediator recognise this magnetic nanoparticle as a challenging player among the other well-known to market nanoparticles.

MPI and MRI unveiled also peculiar features of this material as a non negligible SAR value for the MFH in vitro and in vivo applications and also its ability to serve as a contrast agent in tomographic imaging modalities exploiting a non-negligible relaxivity (in MRI) and a robust relaxometry (in MPI).

The most relevant result achieved in this work is related to the in vivo application of G-M55. As can be observed in Figure 6 the ability of this nanoparticle to act as a local MFH mediator in a murine model of breast cancer (MDA-MB-231) is consistent. More mice will definitively assess this important result.

Other topics of interest that will soon be tackled with other and more extensive experiments in our lab are related to the ability of switching contrast ratio and the observation of the mechanisms involved in cell death during and after the MFH treatments.

Switching contrast ratio ability is considerably difficult to observe through MRI or other tomographic techniques. However, Gerosa et al., 2021 have demonstrated the feasibility of this measurement on a less refined version of the same nanomaterial named G-M48. The possibility to use self-regulating temperature materials, that could increase temperature only up to the Curie temperature, is regarded as an undoubted advantage of this technique since it may represent an intrinsic safety mechanism allowing to avoid the risk of overheating surrounding tissues of inducing necrosis. One of the most relevant constraints related to this more refined version of the same nanomaterial named G-M55 is the higher Curie Temperature T_c compared to G-M48. For the experimental set up present in our lab it is quite difficult to achieve consistent results in this application considering that the Curie Temperature of G-M55 is higher than 100°C, quite hard to reach through a heating water circuit placed inside MRI. At this stage, slight changes in the chemical synthesis procedure must be applied to achieve more sustainable T_c exploitable for switching contrast ratio ability of this material.

Considering the death mechanisms induced by the application of several MFH treatments, we still need to investigate more experiments. The therapeutic application of heat is very effective in cancer treatment. Both hyperthermia, i.e. heating to 39–45°C to induce sensitization to radiotherapy and chemotherapy, and thermal ablation, where temperatures beyond 50°C destroy tumor cells directly, are frequently applied in the clinic (Kok et al., 2020). MFH is regarded as a minimally invasive thermal therapy able to provide localized heating in tumor tissues. MFH is based on a limited increase of the temperature (42-46°) of tumor tissue that can lead to apoptosis, avoiding extensive necrosis of tumor. (Gerosa et al., 2021; Bhardwaj et al., 2020). The chance of activating these mechanisms could be upregulated or downregulated by a huge variety of molecular factors that could be observed through the immunofluorescence of specific fluorescent dyes bounded to cell receptors defined as heat shock proteins (HSP). The over expression of this class of proteins is well-known to be related with application of external direct or indirect thermal stimuli.

The over expression of HSP could be correlated with thermotolerance also. It is hard to say from the over expression of HSP if the heat shock caused by MFH treatments through G-M55 as mediator has led to inactivating or activating responses. The response to a signal could led to different endings. This kind of biological event can’t be easily unveiled, even tough, different signals related to HSP could be investigated by means of other indications as the associated inflammation induced in the surrounding microenvironment.

All of these findings have to be deeply investigated in the future to set up a robust theranostic platform based on G-M55 nanoparticle, tomographic imaging techniques as MRI and MPI and MFH application.

4. Preliminary results: iron oxide nanoparticles as contrast agents for cellular imaging in MPI

a. Introduction

Tumor-associated macrophages (TAMs) are thought to be protumoral, enhancing and contributing to cancer progression. The presence of TAMs has been correlated with the metastasis of tumor cells and the inhibition of the antitumoral immune responses mediated by T cells. In this brief paper, we used Magnetic Particle Imaging (MPI) to detect passively targeted TAMs homing to a breast cancer model. TAMs were passively targeted using PEG-coated Magnetic Nanoparticles (PEG-MNPs). Escalating doses of PEG-MNPs were tested to evaluate TAM uptake at different time points. An MPI signal was detected in liver and tumor for all the groups except at the lowest dose. A novel quantitation workflow has also been proposed to calculate the quantity of iron inside the different tissues.

Magnetic Particle Imaging (MPI) is a promising tool for tracking cells tagged with Magnetic Nanoparticles (MNPs). Of great interest is tracking the behavior of cells associated with the immune system. One cell type, Tu- mor Associated Macrophages (TAMs), may act as a potential biomarker for both cancer detection and prognosis. In this study, we tag TAMs in situ with MNPs, and track their location using MPI co-registered with X-ray/CT. Immune cells (e.g. leukocytes), together with fibroblasts and endothelial cells, form the tumor microenvironment. These immune cells interact with tumor cells to influence tumor growth. One type of immune cell, macrophages, are part of the mononuclear phagocyte system that is responsible for the clearance for foreign matter from the body. Consequently, nanoparticles that interact with macrophages will be recognized and internalized (Binnemars-Postma et al., 2017). When a macrophage is recruited to a tumor site by a tumor, it is known as a Tumor Associated Macrophage, or TAM. TAMs can promote proliferation, promote metastasis, and stimulate tumor angiogenesis while inhibiting the antitumor immune response mediated by T cells (Yang and Zhang, 2017) Due to their role, TAMs are being recognized as potential biomarkers for diagnosis and prognosis of cancer. In this study, we explore a non-invasive, in vivo imaging approach using MPI for evaluating TAM recruitment to a mouse breast tumor.

MPI is an emerging imaging modality that exploits time-varying magnetic fields to directly detect Magnetic Nanoparticles (MNPs) (Gleich et al., 2005). MPI has unique capabilities when imaging MNPs. Specifically, MPI enables linear MNP quantitation with excellent dynamic range, positive contrast, deep tissue depth penetration capability, no use of ionization radiation, and no background signal. In contrast, Magnetic Resonance Imaging (MRI) detects MNPs as difficult-to-quantitate T2* signal dropouts. Of note, MPI does not see anatomy, and so we often co-register the technology with an anatomic imaging modality such as MRI and X-ray/CT. In recent years, MPI has been reported for the tracking of superparamagnetic iron-oxide (SPIO) MNPs in stem cells, for imaging of brain injuries and xenografted tumors in animals (Goodwill et al., 2012; Zheng et al., 2015 and Yu et al., 2017). Here we propose to use MPI co-registered with X-ray/CT to evaluate TAM recruitment in a mouse model of mammary carcinoma.

b. Materials and Methods

Animal Procedures

All animal procedures were conducted according to the National Research Council Guide for the Care and Use of Laboratory Animals and approved by the Animal Care and Use Committee at Stanford University. Mouse 4T1 mammary carcinoma were grown in the 4th pair (inguinal) mammary fat pad of 6-8 weeks old female Balb/c mice. The tumors became palpable 6-8 days after inoculation. A single dose of tracer (1, 3, 6, 12, 24 mg/kg) of Synomag-D® PEG (Micromod, Germany) was intravenously injected 7 days after implantation of the tumor (N = 5 mice for each dose). MPI images were ac- quired 8, 11, 14 and 17 days after tumor implantation. Mice were sacrificed on day 17.

Imaging and histology

Mice were imaged longitudinally using the Momentum™ MPI system (Magnetic Insight, Inc. Alameda, CA, USA). Animals were anesthetized with isoflurane during the duration of their scans. Projection images were taken 3 with a field of view (FOV) of 4 x 4 x 12 cm^3. Tomographic acquisition was taken using 35 projections, with each projection taking ⇠10 seconds, for a total scan time of 40 minutes including pauses for system temperature and image reconstruction. Mice were imaged with an X-ray/CT (Trifoil Imaging CT120, Northridge, CA, USA) under isoflurane anesthesia at occasional timepoints during the study. Following sacrifice, the liver, spleen and tumor were dissected and collected.

Tumors were sectioned and stained with Hematoxylin and Eosin and Prussian Blue. The stained sections were scanned, visualized, and documented with a Nanozoomer (Hamamatsu, Japan). The remaining tissue was analyzed using inducive coupled plasma (ICP) spectroscopy.

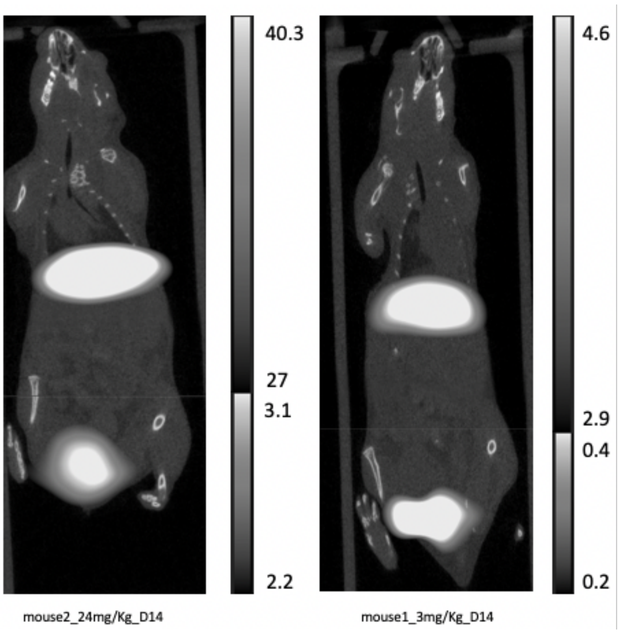

Figure 1. Two different mice at day 14 post implantation, two doses of the SynomagPEG, 24 mg/kg and 3 mg/kg. The upper white region indicate the location of the liver saturated with nanoparticles and the lower white region indicates the location of the tumor.

Data Analysis

MPI and CT were co-registered using VivoQuant (Invicro, MA, USA). For MPI quantification, the MPI signal is defined as the sum of pixel values within the Region of Interest (ROI) normalized by the ROI's volume. The up- take of Synomag-D® PEG in tumors and in livers respect to the dose injected via tail vein has been calculated normalizing the MPI signal collected from the tissue with the MPI signal collected from the tracer. The signal from the tracer was evaluated by a calibration curve obtained by images of a series of dilution which correspond to the dose adopted in the study

c. Results

In this pilot study we demonstrated MPI imaging of in situ labeled tumor associated macrophages. In a typical imaging result (Figure 1) escalating doses of Synomag-D® PEG showed consistent labeling of the tumor. The MPI tumor signal increased with the escalating dose. Signal was detected at all levels except the lowest dose (1 mg/kg). Increases in dose correlated with concentrations of iron in the tumor and liver.

From our results, we determined that, for this tumor model, the MPI signal can be detected as early as 8 days post implantation, just after the tumor becomes palpable. Tumor and liver signals peaked around day 11-14, and then gradually declined due to the clearance of the MNPs by physiological pathways.

Prussian Blue staining confirmed iron presence in the tumors of injected mice. Iron staining patterns were different from control mice. These results must be confirmed by ICP Spectroscopy.

Appendix

During my PhD program, besides my research on hyperthermic nanoparticles for biomedical applications, I gave my contribution to five collaborative studies. As a result of these collaborative research, five scientific articles were published (the articles have been reproduced with the permission of the journals'Publishers).

- In the frame of a collaboration with Prof. Amendola (University of Padova, Padova, Italy) highly biocompatible nanoparticles were synthesized and tested to enhance MRI guided therapy. My task was to test magnetic efficiency of these particles through in vitro tests and MRI magnetic characterization at different time points.

  Veronica Torresan, Andrea Guadagnini, Denis Badocco, Paolo Pastore, Guillermo Arturo Muñoz Medina, Marcela B. Fernàndez van Raap, Ian Postuma, Silva Bortolussi, Marina Beki´c, Miodrag Coli´c, **Marco Gerosa**, Alice Busato, Pasquina Marzola, and Vincenzo Amendola, *"Biocompatible Fe-B alloy nanoparticles designed for neutron capture therapy guided by magnetic resonance imaging",* Advanced Healthcare Materials, 2020, 2001632.

- In the frame of a collaboration with Prof. Daldosso (University of Verona, Verona, Italy), a novel method of production for efficiency MRI tracers has been tested to produce Si microparticles infiltrated with magnetic nanospheres. My task was to support Dr. Chistè in MRI testing of the different solutions of microparticles produced. We have tested both T_1 relaxation and T_2 relaxation of the Si microparticles infiltrated with magnetic particles respect to magnetic particles alone.

  Elena Chistè, Gloria Ischia, **Marco Gerosa**, Pasquina Marzola, Marina Scarpa and Nicola Daldosso, *"Porous Si microparticles infiltrated with magnetic nanospheres",* Nanomaterials, 2020, 10, 463.

- In the frame of a collaboration with Prof. Prosperi (University of Milano-Bicocca, Milano, Italy) it was synthesized a highly efficient polymer coated iron-oxide nanoparticle exploited as an efficient MRI tracer as well as heat mediator for MFH treatments of different cancer cell lines. My task was to magnetically characterize the material and to test it in different conditions (varying concentrations of tracer) in order to compute its specific absorption rate. Once defined the SAR, with the help and guidance of Dr. Vurro I have tested these nanoparticles as heat mediators in vitro on different healthy and cancerous cell lines.

  Pradip Das, Lucia Salvioni, Manuela Malatesta, Federica Vurro, Silvia Mannucci, **Marco Gerosa**, Maria Antonietta Rizzuto, Chiara Tullio, Anna Degrassi, Miriam Colombo, Anna M. Ferretti, Alessandro Ponti, Laura Calderan, Davide Prosperi, *"Colloidal polymer-coated Zn-doped iron oxide nanoparticles with high relaxivity and specific absorption rate for efficient magnetic resonance imaging and magnetic hyperthermia"* Journal of Colloid and Interface Science, 579 (2020) 186–194

- In the frame of a collaboration with Prof. Perduca (University of Verona, Verona, Italy) it has been synthesized a novel biomimetic nanoparticle coated with different polymers to enhance its circulation time in the bloodstream. Interesting results were achieved testing TAT and PLGA coating. My task was to test MFH efficiency of the different nanoparticles. In particular I have performed measures related to the computation of SAR/ILP and the heat mediator efficiency in vitro on different cancerous cell lines.

  Federica Vurro, Ylenia Jabalera, Silvia Mannucci, Giulia Glorani, Alberto Sola-Leyva, **Marco Gerosa**, Alessandro Romeo, Maria Grazia Romanelli, Manuela Malatesta, Laura Calderan, Guillermo R. Iglesias, María P. Carrasco-Jiménez, Concepcion Jimenez-Lopez and Massimiliano Perduca, *"Improving the Cellular Uptake of Biomimetic Magnetic Nanoparticles",* Nanomaterials, 2021, *11*, 766.

- In the frame of a collaboration with Prof. Amendola (University of Padova, Padova, Italy) it has been developed a new version of silver-iron nanoparticles coated with PEG to enhance stability in solution, biocompatibility for in vitro and in vivo experiments and contrast ratio in MRI. I was responsible for the testing of T1 and T2 MRI sequences to define the efficiency of the NPs as contrast agent. Also, I have performed histological examination and coloring of the slices to highlight the results obtained on a mouse model.

  Vincenzo Amendola, Andrea Guadagnini, Stefano Agnoli, Denis Badocco, Paolo Pastore, Giulio Fracasso, **Marco Gerosa**, Federica Vurro, Alice Busato, Pasquina Marzola, *"PEG-coated silver-iron nanoparticles as efficient and biodegradable MRI contrast agent",* Journal of Colloid and Interface Science, 596 (2021) 332–341

ADVANCED HEALTHCARE MATERIALS
www.advhealthmat.de

Biocompatible Iron–Boron Nanoparticles Designed for Neutron Capture Therapy Guided by Magnetic Resonance Imaging

*Veronica Torresan, Andrea Guadagnini, Denis Badocco, Paolo Pastore, Guillermo Arturo Muñoz Medina, Marcela B. Fernàndez van Raap, Ian Postuma, Silva Bortolussi, Marina Bekić, Miodrag Čolić, Marco Gerosa, Alice Busato, Pasquina Marzola, and Vincenzo Amendola**

The combination of multiple functions in a single nanoparticle (NP) represents a key advantage of nanomedicine compared to traditional medical approaches. This is well represented by radiotherapy in which the dose of ionizing radiation should be calibrated on sensitizers biodistribution. Ideally, this is possible when the drug acts both as radiation enhancer and imaging contrast agent. Here, an easy, one-step, laser-assisted synthetic procedure is used to generate iron–boron (Fe–B) NPs featuring the set of functions required to assist neutron capture therapy (NCT) with magnetic resonance imaging. The Fe–B NPs exceed by three orders of magnitude the payload of boron isotopes contained in clinical sensitizers. The Fe–B NPs have magnetic properties of interest also for magnetophoretic accumulation in tissues and magnetic hyperthermia to assist drug permeation in tissues. Besides, Fe–B NPs are biocompatible and undergo slow degradation in the lysosomal environment that facilitates in vivo clearance through the liver–spleen–kidneys pathway. Overall, the Fe–B NPs represent a new promising tool for future exploitation in magnetic resonance imaging-guided boron NCT at higher levels of efficacy and tolerability.

1. Introduction

Sensible improvements are expected in healthcare treatments by the introduction of new nanomedicines with high efficacy and low side effects.[1] A key advantage of nanosized medicines is the possibility to have multiple functionalities, allowing, for instance, multimodal imaging, combined therapeutic protocols, or imaging-guided therapy.[2–4] A promising, yet scarcely investigated, way to achieve multifunctional nanomedicines is the realization of bimetallic nanoparticles (NPs) designed such that each element brings the physical–chemical properties desired for a specific medical treatment. For instance, magneto-plasmonic Au–Fe alloy NPs have been proposed as multimodal contrast agents for X-ray computed tomography, magnetic resonance imaging (MRI), and Raman imaging.[5] Pt–Cu NPs were successfully tested as sensitizers for photothermal therapy of cancer, photoacoustic imaging, and

---

V. Torresan, A. Guadagnini, Prof. D. Badocco, Prof. P. Pastore,
Prof. V. Amendola
Department of Chemical Sciences
University of Padova
Via Marzolo 1, Padova I-35131, Italy
E-mail: vincenzo.amendola@unipd.it

G. A. Muñoz Medina, Prof. M. B. Fernàndez van Raap
Physics Institute of La Plata (IFLP-CONICET)
Physics Department, Faculty of Exact Sciences
National University of La Plata
La Plata 1900, Argentina

The ORCID identification number(s) for the author(s) of this article can be found under https://doi.org/10.1002/adhm.202001632

DOI: 10.1002/adhm.202001632

Dr. I. Postuma, Prof. S. Bortolussi
INFN (National Institute of Nuclear Physics) Pavia
Via Bassi 6, Pavia 27100, Italy

Prof. S. Bortolussi
Department of Physics
University of Pavia
Pavia 27100, Italy

M. Bekić, Prof. M. Čolić
Institute for the Application of Nuclear Energy
University of Belgrade
Belgrade 11080, Serbia

Prof. M. Čolić
Medical Faculty Foča
University of East Sarajevo
Republika Srpska, Foča 73300, Bosnia and Herzegovina

M. Gerosa, Dr. A. Busato, Prof. P. Marzola
Department of Computer Science
University of Verona
Verona 37134, Italy

drug release.[6] Significant tumor reduction activity has been reported in Au–Ag NPs.[7] Co–Pt NPs have been studied for magnetic resonance and photoacoustic dual-modal imaging-guided photothermal therapy.[8] Sometimes, alloying may also introduce new functions that are not found in single element nanomaterials and are exploitable for biomedical applications. This is the case, for instance, of transformable nanoalloys of Au–Fe[9] or liquid Ga eutectics[10] that have the ability to spontaneously dissolve in physiological environments, as required to solve the crucial issue of the in vivo biopersistence of inorganic and organic nanomedicines.[11–14] In particular, composition, shape, and surface coating of alloys dramatically influence their resistance to corrosion in body fluids[15] that can change from high durability to rapid degradation.[9,16,17]

To date, however, the use of bimetallic NPs with the properties required to improve the efficacy of neutron capture therapy (NCT) with the support of tomographic imaging ability remains almost unexplored. NCT relies on the accumulation of boron in tumors, followed by the irradiation with low-energy neutrons.[18–20] Given the high capture cross section of the ^{10}B isotope (19.9% natural abundance), neutron irradiation activates a nuclear reaction that releases two charged particles (an alpha particle and a lithium ion, ^{7}Li) with high linear energy transfer (LET) and a traveling range of 10–15 µm in the tissue, which is comparable to the dimensions of the cells.[18,21] Hence, NCT is a binary hadrontherapy in which all the energy of the two types of radiation is deposited inside the tumor, possibly achieving its regression and sparing healthy tissues. Once that boron is selectively accumulated in malignant tissues, NCT becomes especially promising for the treatment of several types of cancer with negative prognosis such as gliomas,[22] head and neck tumors,[23] melanoma,[24] liver cancer,[25] lung malignancies, and pleural mesothelioma[26,27] (the cancer provoked by asbestos fibers, for which the mortality peak is expected between the years 2015 and 2024 in several countries[28,29]). Nonetheless, one of the principal issues limiting clinical applicability of NCT is the difficulty of quantifying boron accumulation in the tissues that is indispensable for the identification of the appropriate neutron flux for therapy.[30–32] In several clinical trials, boron concentration is measured in blood and, after infusion of the boronated drug, the treatment plan is calculated assuming that boron concentration in the healthy tissues is the same as in blood and concentration in tumor is assumed as 3.5 times that in blood.[31,32] This empirical assumption is based on several preclinical experiments performed in animals with boronophenylalanine (BPA) as the boron carrier, indicating that the boronated drug on average gives a 3.5 tumor-to-normal tissue boron concentration ratio.[31,32] In other trials, the concentration ratio is measured by positron emission tomography, only after labeling the sensitizer with radioactive isotopes (^{18}F) and performing a prescreening of patients some days before boron NCT (BNCT). However, this expensive and time-consuming method is performed with a significantly reduced dose of labeled sensitizer to limit the cost and the side effects from the β^+ radiation of ^{18}F nuclei in the whole body. Thus, the extrapolation of the boron uptake for the clinical treatment is affected by significant uncertainties, resulting in the observation of high variability in the outcome of different patients treated within the same BNCT trial.[33–36] The development of new ^{10}B delivery systems, which are detectable in real time with noninvasive and clinically accessible total body imaging and quantification techniques, is thus crucial to trigger future improvements in NCT.[18,37,38]

MRI is a powerful and widely used clinical imaging modality.[39,40] It is based on the spin properties of the proton when it is excited with a radiofrequency (RF) pulse in the presence of an external magnetic field.[39,41] MRI provides high spatial and temporal resolution, and excellent intrinsic contrast of "soft" or low-density tissues.[39,40,42,43] In addition, MRI does not use ionizing or radiotracer radiation. To improve image quality, contrast agents such as magnetic NPs are used to significantly aid the detection and differentiation of lesions from healthy tissues.[5,39,41,44,45]

Magnetic NPs in general offer additional opportunities to assist the therapeutic action, because they can be accumulated in a specific region with appreciable precision by the magnetic field of external permanent magnets.[3,46] This procedure has no side effects and allows up to fivefold deeper penetration and threefold higher concentration in tumors.[46,47] Besides, RF alternating current (AC) magnetic fields promote heating of the NPs,[48–50] which enhances drug permeation and diffusion inside the tissues allowing better efficacy with a lower dose of total administered medicines.[51,52]

Here, we used an innovative one-step synthetic approach based on laser ablation in liquid (LAL) to realize a nanomedicine agent composed of Fe–B NPs enveloped in a shell of biocompatible polymer (polyvinyl pyrrolidone, PVP). LAL proved to be a powerful method for the achievement of bimetallic NPs, also in case of thermodynamically prohibited compounds or elements with markedly different chemical reactivity and oxidation potential.[53] Noteworthy, this synthetic approach is easy,[54,55] cost-effective,[56] amenable to scale-up with full automation,[57] and does not require the introduction of undesired chemical contaminants,[58] starting only from bulk metal components and a solution of the biocompatible polymer in a pure solvent. The resulting Fe–B NPs combine the magnetic properties of iron with the high neutron capture cross section of boron, thus providing a desirable set of functions for advanced BNCT treatments, such as MRI localization of the B-containing compound, possibility of magnetophoretic accumulation to increase the loading of B in the malignant tissue, and temperature increase in the site of accumulation by magnetic hyperthermia to improve the permeation of nanomedicine in tissues.

2. Results and Discussion

2.1. Synthesis of NPs

Fe–B NPs were obtained by LAL with 1064 nm (6 ns) laser pulses focused on a bulk Fe–B plate dipped in a cell containing a 0.1 mg mL^{-1} PVP solution in acetone (**Figure 1**A). To prevent oxidation of Fe and B, LAL was performed under Ar atmosphere in anhydrous acetone. The resulting NPs dispersion was concentrated with a Rotavapor at 30 °C, mixed 1/9 v/v with an aqueous solution of citrate buffer (pH 4.7), and incubated overnight at 20 °C. Then, the NPs were collected with a permanent magnet (Figure 1B) and washed multiple times with deionized water, before redispersion in an aqueous solution of PVP (0.1 mg mL^{-1}).

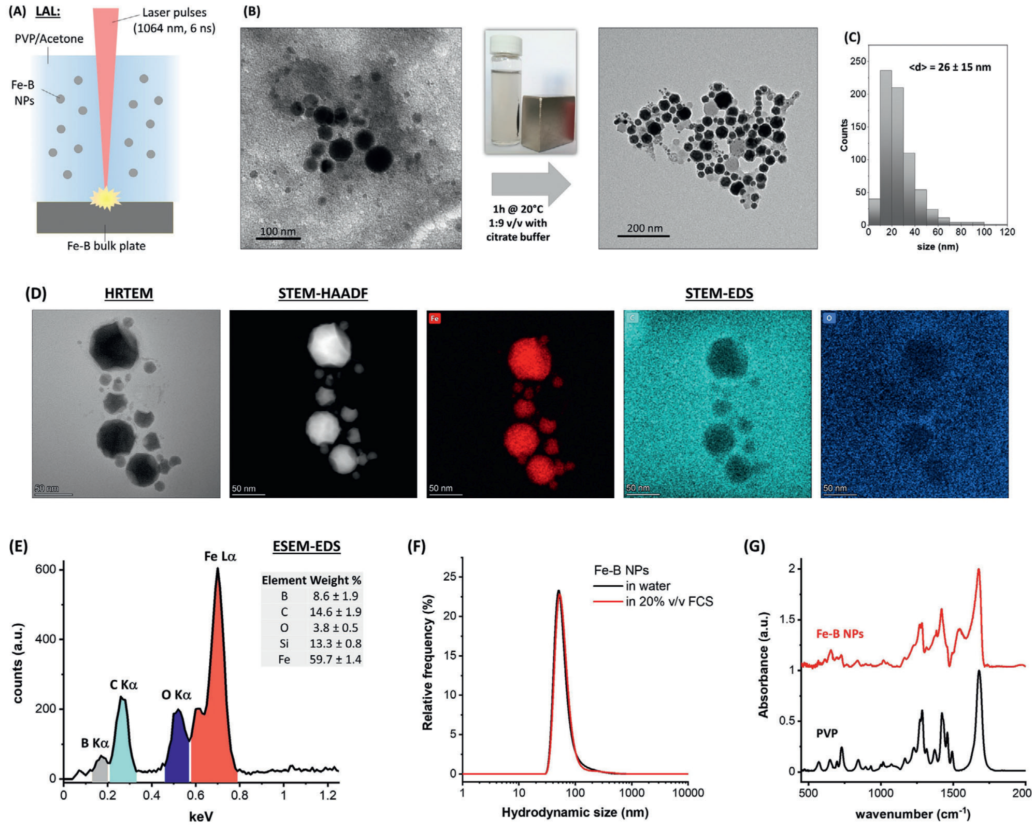

Figure 1. A) Sketch of LAL: 1064 nm (6 ns) laser pulses are focused on a Fe–B target dipped in a PVP solution in acetone under Ar atmosphere to generate Fe–B NPs. B) TEM images of Fe–B NPs just obtained from LAL (left) and after the purification with citrate buffer and collection with a permanent magnet (right). C) Size histogram of final Fe–B NPs (*n* > 500). D) STEM analysis on Fe–B NPs showing Fe (red), C (cyan), and O (blue) EDS maps. E) EDS spectrum collected on Fe–B NPs deposited on a Si substrate with an ESEM. Inset shows the quantitative composition of the deposit extracted from the fit of the EDS spectrum. F) Hydrodynamic size distribution measured by DLS on Fe–B NPs dispersed in water or in 20% v/v FCS. G) FTIR spectra of Fe–B NPs and a reference PVP powder.

2.2. Structural Characterization

The final NPs are composed of Fe/B in 1.0:0.4 atomic ratio as assessed by inductively coupled plasma-assisted mass spectrometry (ICP-MS). Incubation with citrate buffer was pursued to remove the synthesis by-products that are shown in the transmission electron microscopy (TEM) images (Figure 1B) as the low-density homogeneous matrix surrounding the NPs. This matrix is effectively removed after the treatment with citrate (Figure 1B), and the resulting Fe–B NPs have spherical shape and an average size of 26 ± 15 nm (Figure 1C).

We performed a bidimensional energy-dispersive spectroscopy (EDS) scanning TEM (STEM) analysis on the NPs to obtain additional structural and chemical information (Figure 1D). The O map indicates the absence of oxygen inside the NPs, thus confirming that Fe–B NPs are metallic. The C map also confirms that this element is not present inside the NPs, whereas the Fe map exactly matches the geometrical shape of the NPs. B is a weak emitter of characteristic X-rays, with its Kα-line (0.183 keV) partly overlapping with the tail of Kα-line of the carbon film coating the TEM grid, in a region where the response curve of the EDS detectors drops to 0. Therefore, B was clearly detected with EDS in a more convenient experimental condition, that is, an environmental scanning electron microscope (ESEM), just by depositing the NPs on a silicon substrate (Figure 1E), i.e., without the signal background originated by carbon film coating the TEM grid. Besides, ESEM analysis does not require the coating of the sample with a conductive thin film of carbon or gold. The oxygen peak in the EDS spectrum is weak (see the semiquantitative analysis reported in the inset in Figure 1E), and should be ascribed to the oxidized Si substrate, in agreement with STEM-EDS analysis.

The hydrodynamic size of Fe–B NPs measured by dynamic light scattering (DLS) in the as-obtained aqueous solution and

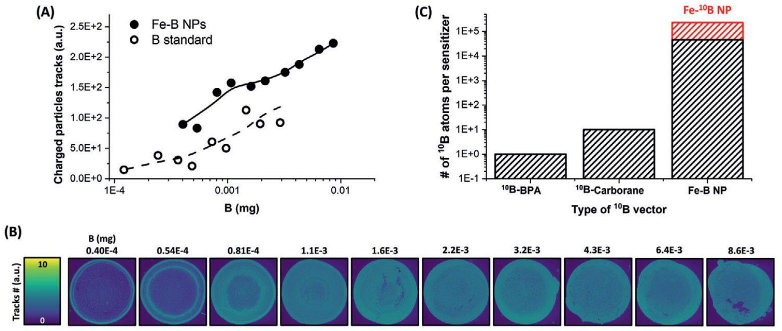

Figure 2. A) Plot of charged particles tracks versus boron concentration for Fe–B NPs (black circles) and a boron standard (H_3BO_3, hollow circles), measured by neutron autoradiography. B) Images of charged particles density in the deposits of Fe–B NPs obtained by qualitative neutron autoradiography. C) Comparison of the number of ^{10}B atoms (logarithmic scale) in clinical sensitizers (^{10}B-enriched BPA and carborane) and in a single Fe–B NP of 26 nm. The red bar represents the theoretical value achievable with a ^{10}B-enriched Fe–B target and the same LAL procedure.

after 20% v/v dispersion in fetal calf serum (FCS) is nearly identical (Figure 1F). In fact, the use of PVP as a biocompatible coating is well consolidated in literature[59,60] because of its ability to confer appreciable colloidal stability to inorganic nanomedicines. DLS indicated a hydrodynamic size of 64 ± 40 nm (66 ± 45 nm in FCS) that is larger than the TEM measured value because of the presence of the polymeric chains wrapping the NPs and the possible clusterization of NPs during the laser synthesis. Effective coating of Fe–B NPs with PVP was further confirmed by Fourier transformed infrared (FTIR) spectroscopy on a dried powder of the sample (Figure 1G), where the vibrational fingerprint of the polymer is clearly identified.

2.3. Neutron Capture Experiments

Since boron is present with high abundance in the bimetallic NPs, their ability in capturing thermal neutrons and producing charged particles with high LET, as required for their application as sensitizers for NCT, was tested by neutron autoradiography of drop samples deposited on a LET-sensitive film (CR39) functioning as solid-state charged particle track detector.[61] In fact, the charged particles emerging from the neutron capture in ^{10}B atoms of the samples generate a distribution of tracks in the LET-sensitive film. **Figure 2**A reports the results obtained for the Fe–B NPs irradiated in the thermal column of a TRIGA Mark II reactor with a thermal neutron fluence of $(2.0 \pm 0.1) \times 10^{10}$ cm^{-2} for quantitative track counting and a thermal neutron fluence of $(9.8 \pm 0.5) \times 10^{12}$ cm^{-2} for qualitative imaging. The plot of Figure 2A shows that the number of charged particle tracks generated by the Fe–B NPs is comparable to that of a standard of boron (H_3BO_3).[62] The increasing amount of charged particles generated during neutron irradiation, while increasing the amount of Fe–B NPs deposed on the CR39 film, is also qualitatively shown in Figure 2B. The slightly larger radiation density measured for the Fe–B NPs compared to the boron salt standard is ascribable to the more homogeneous deposition of the nanomaterials on the CR39 film. From the TEM-measured average NP size and the composition assessed by ICP-MS, it is estimated a number of ^{10}B atoms for single NP as high as 4.6 10^4 (Figure 2C). This number exceeds by more than three orders of magnitude the ^{10}B atoms contained in the carborane (B_{10}) derivatives reported in literature as sensitizers for BNCT, such as sodium borocaptate,[37,63–68] and it is more than four orders of magnitude larger than the ^{10}B atoms contained in ^{10}B-phenylalanine, the most used molecular drug for BNCT.[37] Noticeably, the density of ^{10}B atoms per single Fe–B NPs is amenable to a further fivefold increase by performing LAL with a ^{10}B-enriched Fe–B metal target.

2.4. Magnetic Properties

The magnetic response of the Fe–B NPs is well appreciable from the picture and the UV–vis spectra before and after magnetic attraction of the sample reported in **Figure 3**A. The magnetism of Fe–B NPs was quantitatively assessed by vibrating sample magnetometry (VSM) at room temperature, resulting in a superparamagnetic hysteresis loop (Figure 3B) consistent with a magnetic moment of 8241.8 ± 4.4 μ_B per NP and a saturation magnetization of 70 emu per g-Fe. The saturation magnetization is in agreement with that expected for Fe–B NPs,[69–71] where the magnetic ordering of Fe is weakened by spin canting states at grain interfaces and iron oxidation at particles surface,[72] as well as by dilution with a nonmagnetic element like B.[71,73]

The magnetic hyperthermia ability of the Fe–B NPs was tested in aqueous solution (Figure 3C) by applying a RF AC magnetic field of 260 kHz and amplitude of 51 kA m^{-1} and measuring a temperature increase of the aqueous solution containing the NPs on a timescale of few minutes, with a ΔT(600 s) of 22.6 °C for the Fe–B NPs versus the 3.8 °C for pure water. The specific absorption rate (SAR) was also quantified (Figure 3D), evidencing a linear dependence versus the magnetic field intensity ($R^2 = 0.99798$), with a slope of 5.5 ± 0.1 W mg-Fe^{-1} kA^{-1}.

Since magnetic NPs are renowned for the ability to shorten the transverse relaxation time T_2 of nearby water protons during MRI,[39,40] the contrast ability versus concentration of the Fe–B NPs was measured in phantoms (Figure 3E). Results confirmed that the Fe–B NPs provide a remarkable contrast, with a

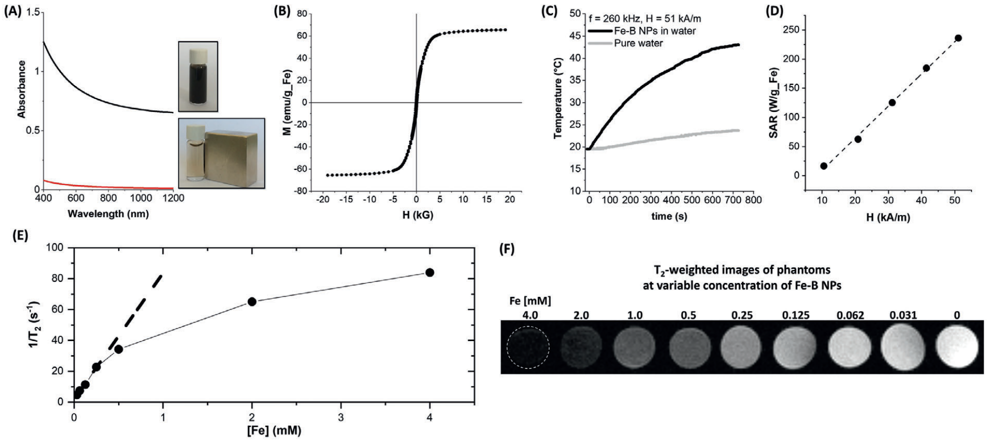

Figure 3. A) UV–vis spectra and image of Fe–B NPs solution before (black line) and after (red line) attraction of the particles with a permanent magnet. B) Magnetization curve of Fe–B NPs. C) Plot of temperature versus time in a Fe–B NPs solution in water under application of a RF (260 kHz) magnetic field (51 kA m^{-1}). The result for pure water is also reported. D) SAR measured on the Fe–B NPs at various magnetic field intensities. E) Transverse relaxivity versus Fe–B NPs concentration F) measured in phantoms.

transverse relaxivity r_2 of 82 ± 4 × 10^{-3} м Fe^{-1} s^{-1} in the linear portion of the plot of $1/T_2$ versus iron concentration. This value is close to that of benchmark contrast agents like Endorem.[5] Besides, the correlation between $1/T_2$ and the amount of NPs increases monotonously in the whole range of Fe concentration tested, which is of more than two orders of magnitude (0.031 × 10^{-3}–4.0 × 10^{-3} м). This is required to localize and quantify the boron-containing NPs directly inside the body with noninvasive clinical MRI.

2.5. In Vitro Biocompatibility Study

Biocompatibility of the Fe–B NPs was investigated in vitro with cytotoxicity and uptake experiments. Cytocompatibility of Fe–B NPs was assessed on three mouse cell lines (L929 fibroblasts, 4T1 mammary carcinoma, and B16 melanoma) and human peripheral blood mononuclear cells (PBMCs). The measure of the metabolic activity of cells (3-[4,5 dimethyl-thiazol-2lyl]-2.5 diphenyl tetrazolium bromide (MTT) assay) after 48 h of cultivation in presence of Fe–B NPs at 1–100 µg mL^{-1} of concentration showed no cytotoxic response (**Figure** 4A). These findings were further confirmed by the absence of apoptosis/necrosis (Figure 4B) and of reactive oxygen species (ROS) production (Figure 4C). Furthermore, the internalization of Fe–B NPs showed a dose-dependent uptake by all examined cells, with the monocytes/macrophages from PBMC cultures showing the highest internalization index, as expected from phagocytes, whereas B16 cells underwent to the lowest uptake of Fe–B NPs (**Figure** 5D,E). These results agree with previous pieces of evidence that Fe–B-based NPs are non-cytotoxic up to concentrations of 50–250 µg mL^{-1}, whereas only at higher concentrations, they induced cell death by apoptosis due to overproduction of ROS.[74,75] Other reports also evidenced that B-containing NPs are non-cytotoxic up to very high concentrations (40 mg mL^{-1}).[76] The presence of stabilization agents significantly influences the cytotoxicity of NPs,[77] including Fe oxide NPs,[75] but the amount of organic stabilizers in the Fe–B NPs is such to avoid negative effects on cell viability.[77]

2.6. In Vivo Biodistribution Study

The relatively high uptake by tumor cells is a generally desirable feature for Fe–B NPs that are designed as a potential candidate for NCT. However, high uptake of Fe–B NPs by the cells of mononuclear phagocytic system in vivo also deserves attention.[78] Therefore, further investigations related to the biodistribution of Fe–B NPs in vivo have been pursued. In vivo experiments were performed on healthy mice models by the administration of Fe–B NPs or benchmark Endorem iron oxides NPs, both at the same concentration of 5 mg-Fe per kg-mouse. The biodistribution was monitored by measuring the T_2% decrease in various organs and at different time points up to 30 days (Figure 5A,B), which is possible thanks to the MRI contrast agent ability of the particles. In animals treated with Fe–B NPs, the signal in liver changed to 30% after the first hour and then it slowly increased up to 60% over 30 days (Figure 5A). Instead, spleen and kidneys signals remain nearly unchanged in the first 6 h, after that they start changing continuously over the experiment duration, up to 59% (spleen) and 51% (kidneys). This change is responsible for the different contrast observed in the T_2-weighted images of the liver and kidneys 30 days after particle administration (Figure 5C). Signal evolution in animals treated with Endorem is different (Figure 5B), featuring already after 1 h a drastic change of 83% (liver), 46% (spleen), and 35% (kidneys) that become 53% (liver), 58% (spleen), and 23% (kidneys) after 30 days.

The results suggest that Fe–B NPs have longer circulation time than Endorem that is beneficial when NPs accumulation in tumors by enhanced permeation and retention is desired and to

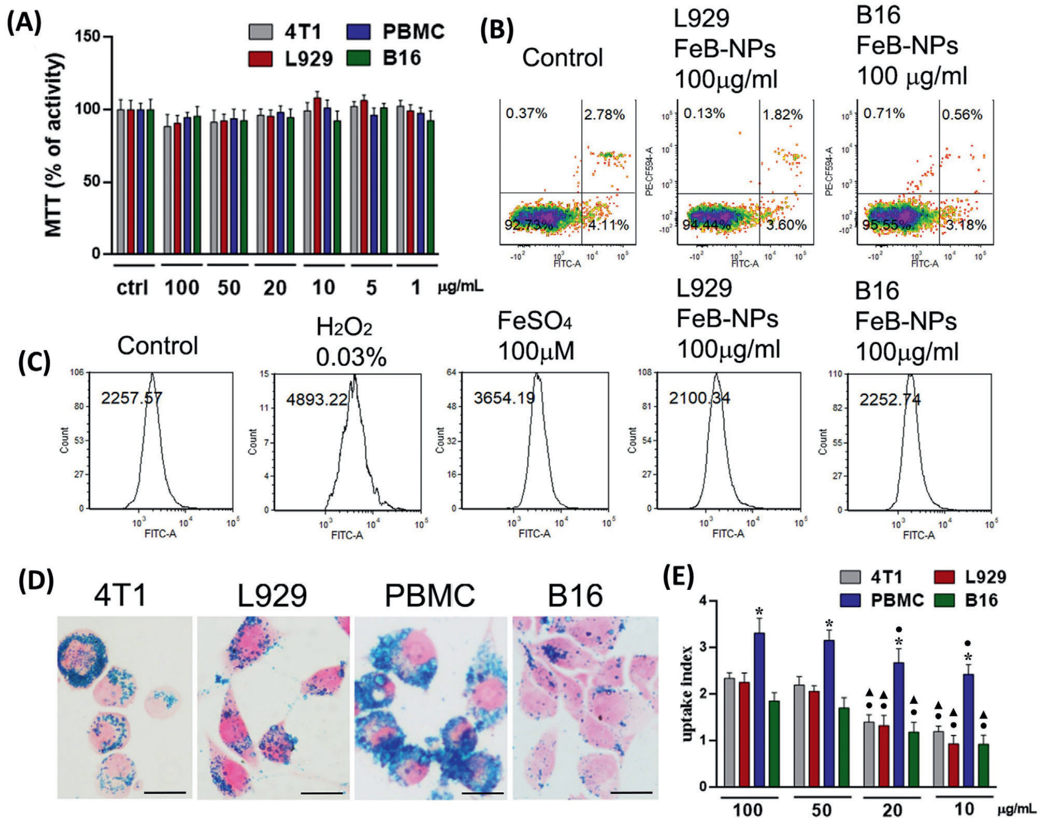

Figure 4. Cytocompatibility, ROS production, and uptake of Fe–B NPs. A) MTT activity showed no changes in mitochondrial activity in cultures of all cells independently of applied NPs concentration. B) Fe–B NPs neither induce necrosis nor apoptosis of examined cells. C) Fe–B NPs did not stimulate ROS production in comparison with positive controls (H_2O_2 and $FeSO_4$). Only results for the highest concentration on L929 and B16 cells (mean fluorescence intensity) are presented in (B) and (C) as one representative out of three independent experiments. Uptake assay (50 µg mL^{-1} of Fe–B NPs) shows highest internalization of Fe–B NPs by a cluster of monocytes/macrophages in PBMC cultures and lowest internalization of NPs by B16 cells (D, scale bar 50 µm). E) Uptake of Fe–B NPs was concentration-dependent. Results are presented as mean ± SD of internalization index. $^*p < 0.05$ of PBMC versus 4T1 (or vs 4T1, B16, and L929) for the same dose of Fe–B NPs. ●, $r < 0.05$ versus 100 and 50 µg mL^{-1}, respectively, for the same cell type (two-way ANOVA with Tukey's multiple comparisons tests).

avoid immediate clogging of spleen and kidneys, with the risk of relevant side effects. Importantly, the evolution over 30 days points out a remarkable difference in the clearance pathways of the particles that in case of the Fe–B sample is compatible with a relevant flux through the spleen (the linear trend in the linear-log plot of Figure 5A) and, successively, to the kidneys (the exponential trend in the linear-log plot of Figure 5A). In case of Endorem, the trend of T_2 indicates that these NPs start abandoning the liver (signal recovery) and move to the spleen (signal increment) but there the NPs are accumulated, because in the same period, the signal in kidneys slightly decreased. This suggests that Fe–B NPs undergo to sensible size reduction over time, going from liver to spleen and, finally, into kidneys, in a time interval in which Endorem particles remain nearly integer.[79]

In order to validate MRI results, iron content in liver, spleen, and kidneys was measured by ICP-MS analysis (Table S1, Supporting Information). Fe concentration in liver, spleen, and kidney of Fe–B NPs-treated animals resulted, respectively, 0.3, 1.3, and 2.7 times that of same organs from the Endorem-treated animals. This confirmed that Endorem NPs accumulated more in liver than the Fe–B NPs, which instead take the way of clearance through kidneys.

2.7. Histological Analysis

Histological examination at 30 days was also performed (Figure 5D). Prussian blue (PB) staining of liver administrated with Endorem showed the cytosolic deposition of blue crystals

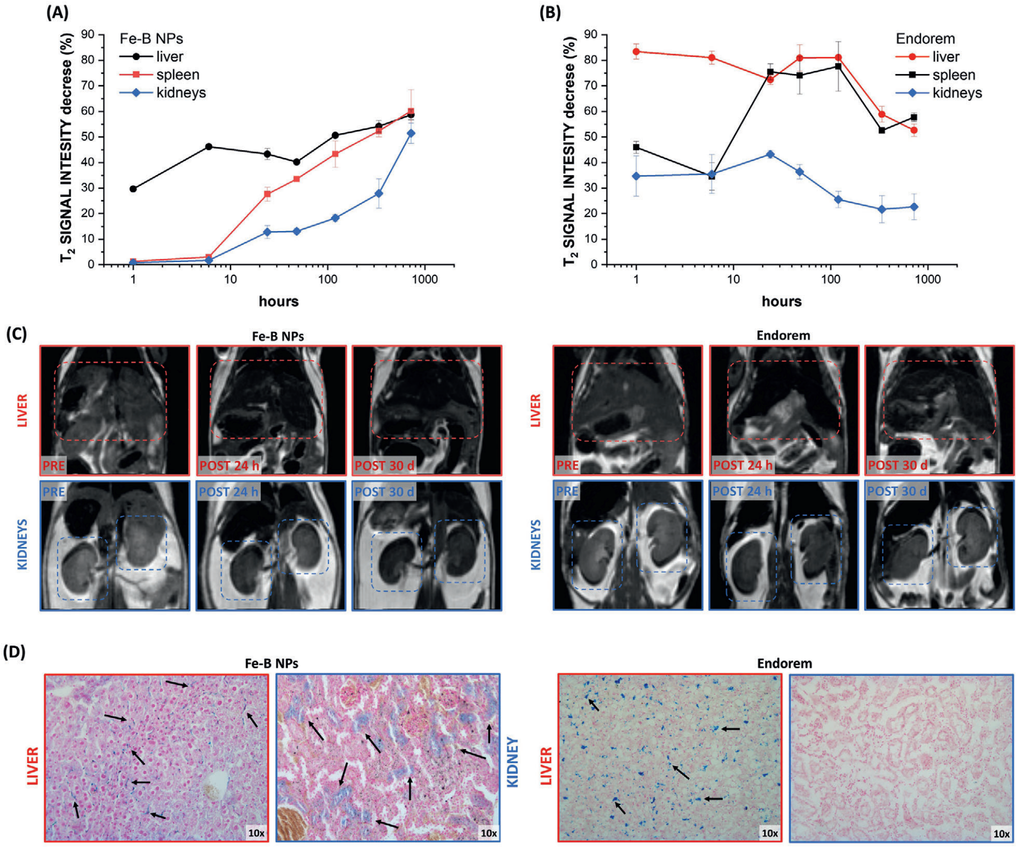

Figure 5. Plot of T_2 signal intensity decrease (%) in liver, spleen, and kidneys at different time points up to 30 days after administration of A) Fe–B NPs or B) Endorem NPs. In (A), the contrast increases in liver already after 1 day, while in spleen and kidneys, it is larger after 30 days, in the stage of particles clearance. In (B), a sudden signal change is measured, indicating the immediate clogging of all organs with these NPs. The signal is slowly restored in liver and kidneys, while increasing in the spleen, indicating that these NPs are not cleared through kidneys but remain in liver and spleen after 30 days. C) T_2-weighted images collected on the liver and kidneys of healthy mice before, 24 h, and 30 days after administration of Fe–B or Endorem NPs. D) Histological analysis of liver and kidney stained with PB (magnification 10×). Black arrows indicate representative blue spots corresponding to iron deposits.

(arrows), indicating the presence of iron in the tissue. Histological study of liver administrated with Fe–B NPs showed iron positive spots located at the hepatic sinusoid (see arrows), an area rich in Kupffer's cells. PB staining of kidney tissue clearly indicated the presence of blue spots distributed homogenously in the animal treated with Fe–B NPs. On the contrary, with Endorem, no positivity for the staining was obtained in kidneys. Finally, in order to evaluate the biocompatibility of NPs, the main organs (including liver, kidney, heart, and lung) were extracted and stained with hematoxylin and eosin. All the organs exhibit no relevant structural alterations with a good preservation of cellular morphology, as shown in Figure S1, Supporting Information. Moreover, during the observation period, the weight of all the animals was measured and no weight loss was observed (Figure S2, Supporting Information).

2.8. Fe–B Degradation Study

To further verify the long-term structural evolution in a physiological environment, the Fe–B NPs were dispersed at 0.035 mg mL^{-1} concentration in either deionized water, 20% v/v FCS at physiological pH (7.4), or at lysosomal pH (4.7), incubated at 37 °C and analyzed by TEM at different time points up to 60 days. This experiment confirmed that Fe–B NPs undergo a size reduction in the physiological environment, that is not observed in the inert aqueous solution (**Figure 6**A). The size reduction is appreciable already after 1 week at both pH conditions, although the change is more evident in the acidic lysosomal environment. Besides, only at pH 4.7, the size reduction proceeded further, reaching a value (12 nm) that is half that of the initial Fe–B NPs. The size distribution and TEM images of the samples incubated

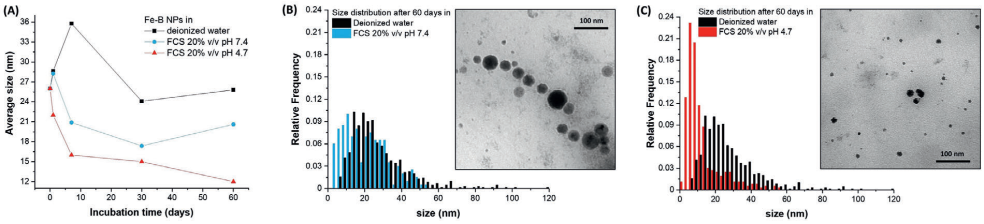

Figure 6. A) Average size of Fe–B NPs incubated at 37 °C in pure water (black squares), FCS 20% v/v at pH 7.4 (blue circles) or pH 4.7 (red triangles). B) Size histograms ($n > 500$) of Fe–B NPs before (black) and after 60 days FCS 20% v/v at pH 7.4 (blue, a representative TEM image is also shown). C) Size histograms ($n > 500$) of Fe–B NPs before (black) and after 60 days FCS 20% v/v at pH 4.7 (red, a representative TEM image is also shown).

at pH 7.4 (Figure 6B) or 4.7 (Figure 6C) for 60 days both show that a larger number of NPs with size <10 nm (i.e., below the glomerular pore size threshold in kidneys) is present compared to the pristine sample. Although a tail of larger NPs is still present in the size distribution of the sample incubated at lysosomal pH, the population of NPs smaller than 10 nm accounts for the 63% of the total.

To evaluate the mass of Fe–B NPs that undergo dissolution over time, ICP-MS analysis was performed on the residual fraction of magnetic NPs collected by a permanent magnet 60 days after incubation at 37 °C in 20% v/v FCS at pH 7.4 or 4.7. Fe–B NPs mass was reduced to 44% and 19% of its initial value at pH 7.4 and 4.7, respectively, thus confirming the slow degradation of particles in the physiological environment.

3. Conclusion

In summary, we reported on Fe–B multifunctional NPs with the range of physical and chemical properties required to assist NCT with personalized boron concentration imaging based on MRI, without the need to employ empirical models and radioactive isotopes. The Fe–B NPs were obtained by a facile, one-step, laser-assisted synthetic procedure and exceed by three orders of magnitude the ^{10}B payload of clinical boron sensitizers. The possibility to obtain a 3D image of boron distribution before the neutron irradiation is crucial for gaining in the precision of dose assessment and in the prediction of therapeutic outcome, ultimately transforming BNCT in a more personalized therapy, in which the treatment planning can be assessed based on the actual boron distribution of each patient. Besides, the Fe–B NPs open the possibility to implement other medical protocols relying on particles magnetism like magnetic accumulation or hyperthermia. Fe–B NPs also show desirable biocompatibility and degradation in the lysosomal environment that contributes to their clearance through the liver–spleen–kidneys pathway as evidenced with in vivo experiments. Thus, the Fe–B NPs represent a new promising tool for future exploitation in MR- guided boron NCT at higher levels of efficacy and tolerability and deserve further studies to assess the therapeutic potential in vivo.

4. Experimental Section

Synthesis: LAL was performed with 1064 nm (6 ns, 50 Hz) laser pulses focused to 21 J cm^{-2} with f = 10 cm lens on a bulk Fe(65 at%)B(35 at%) plate (MaTeck GmbH) dipped in a cell containing a 0.1 mg mL^{-1} PVP solution (40 kDa, Sigma-Aldrich) in anhydrous acetone (VWR) under Ar atmosphere. Then, the colloid was concentrated with a Rotavapor at 30 °C, mixed 1:9 v/v with an aqueous solution of citrate buffer (pH 4.7), and incubated overnight at 20 °C. Subsequently, the NPs were collected with a permanent NdFeB magnet, washed multiple times with deionized water, and redispersed in an aqueous solution of PVP 0.1 mg mL^{-1}.

Characterization: ICP-MS analysis for the determination of the B and Fe content was carried out with an Agilent Technologies 7700x ICP-MS (Agilent Technologies International Japan, Ltd., Tokyo, Japan) at operating conditions and data acquisition parameters as previously described.[80] The instrument was equipped with an octupole collision cell operating in kinetic energy discrimination mode used for the removal of polyatomic interferences and argon-based interferences. Optimal performance was attained by using the collision cell in He mode. For sample digestion, 0.5 g of solution was accurately weighted and digested with 0.8 g of HNO$_3$ 69% at 100 °C for 2 h. The resulting solution was diluted with the same solvent used for calibrations. Each digested solution is diluted on two concentration levels and each solution is measured thrice with the ICP-MS.

For the experiment of biodegradation monitored with ICP-MS, the Fe–B NPs were dispersed at 0.035 mg mL^{-1} concentration in either 20% v/v FCS at pH 7.4 or 4.7 and incubated at 37 °C for 60 days. Then, the Fe–B NPs were concentrated to 100 µL with a permanent NdFeB magnet (overnight exposure) and quantified with ICP-MS. The same procedure was applied to the initial solution to quantify the starting mass of magnetic Fe–B NPs.

UV–vis absorption spectra were recorded with a Jasco V770 spectrophotometer using 2 mm optical path quartz cells. DLS was performed with a Malvern Zetasizer Nano ZS in DTS1070 cells. The size was calculated from the size histograms as the arithmetic average accompanied by the standard deviation (SD). FTIR spectra of the powder samples deposed on a KBr window were collected with a PerkinElmer 1720X spectrometer.

Microanalysis was performed with an ESEM model FEI Quanta 200 on a sample of Fe–B NPs drop cast on a silicon substrate, without further metallization.

TEM analysis was performed with a FEI Tecnai G2 12 transmission electron microscope operating at 100 kV and equipped with a TVIPS CCD camera. STEM analysis was performed with a TEM Talos F200S G2. The samples for TEM analysis were prepared by evaporating NP suspensions on a copper grid coated with an amorphous carbon holey film. For the aging experiment, the Fe–B NPs were dispersed at 0.035 mg mL^{-1} concentration in either deionized water, 20% v/v FCS at pH 7.4 or 20% v/v FCS at pH 4.7 (by adding citrate buffer), and then incubated at 37 °C and analyzed at different time points (0, 1, 7, 30, and 60 days). Each time, a drop of the solution was deposed on a copper grid coated with an amorphous carbon film. ImageJ software was used to measure the geometrical size in size distributions. Statistics considered more than n = 500 NPs for each sample.

The neutron capture by ^{10}B atoms was evaluated by neutron autoradiography, according to the procedure described by Postuma et al.[61] Briefly, aqueous solutions of either Fe–B NPs or H$_3$BO$_3$ were deposited by serial drop-casting on CR39 films and drying at room temperature, to obtain spots in the 8.6 × 10^{-3}–4.0 × 10^{-4} mg-B (Fe–B NPs) or

2.9×10^{-3}–1.2×10^{-4} mg-B (H_3BO_3) range. The CR39 films were irradiated in the thermal column of the TRIGA Mark II reactor operating at 2 kW for 30 min, with a neutron fluence of $(2 \pm 0.1) \times 10^{10}$ cm^{-2} for the track counting analysis, while for qualitative imaging of the sample the reactor was operated for 2 h at 250 kW, obtaining a neutron fluence of $(9.8 \pm 0.5) \times 10^{12}$ cm^{-2}. Quantification of the generated charged particles was obtained by etching the CR39 films with PEW40 solution, imaging the tracks generated by the charged particles emitted from the ^{10}B atoms with a LEICA M205 FA stereo microscope, and counting the number of tracks per drop by means of the Scikit-Image blob detection algorithm.[61] Qualitative images of the dried drops were obtained by etching with sodium hydroxide the CR39s irradiated at the highest neutron fluence and collecting the images with the same microscope.

DC magnetometry measurements were performed at room temperature with a Lakeshore 7404 VSM, at an oscillation frequency of 82 Hz and amplitude of 5 mm, respectively. Airgap was set at 20 mm and the applied field was varied between −1.8 and 1.8 T. For measurements, the Fe–B NPs suspension was lyophilized overnight and the dried powder samples were placed in gelatine capsules.

The heating ability of the Fe–B NPs suspended in MQ water was calorimetrically evaluated by exposing 400 µL of the magnetic suspension, held in a clear glass Dewar, to RF fields of 260 kHz and field amplitudes of 11, 21, 31, 42, and 51 kA m^{-1}. Magnetocalorimetric experiments were carried out using a Hüttinger (2.5/300) field generator, which consists of a resonant RLC circuit holding a water-refrigerated five-turn coil of 5 cm inner diameter. The temperature was probed during the whole treatment with a fiber optic sensor placed at the center of the sample. The sensor was connected to a calibrated signal conditioner (Neoptix) with an accuracy of ±0.1 °C. The experiment was interrupted before reaching 50 °C to minimize solvent evaporation and prevent its destabilization. SAR parameter was calculated for each field condition from the initial slope of the temperature versus time curve with the expression $\text{SAR} = \frac{C}{[X]} \frac{\vartheta T}{\vartheta t}$ where C is the volumetric heat capacity of the solvent ($C = 4.18$ kJ cm^{-3}), and $[X] = 1.2$ mg-Fe mL^{-1} is the Fe concentration in the suspension.

Cytocompatibility, ROS Production, and Uptake Studies: In vitro cytotoxicity and uptake studies were performed on three mouse cell lines (L929 fibroblasts, 4T1 mammary carcinoma, and B16 melanoma) that were obtained from ATCC (Rockwell, MD, USA) and human PBMCs. PBMCs were obtained from blood volunteers upon signing an informed consent and approval of the study by the Ethical Committee of INEP, Belgrade, Serbia. PBMCs were isolated by centrifugation of citrated blood over the Hystopaque gradient. In all assays, the cells were cultured in RPMI 1640 medium, supplemented with 10% FCS (Sigma, Munich, Germany), 2×10^{-3} м ʟ-glutamine (Sigma), 100 U mL^{-1} penicillin, 100 mg mL^{-1} streptomycin (all antibiotics from ICN, Costa Mesa, CA, USA), and 50×10^{-6} м 2-mercaptoethanol (Sigma). The cells were cultured with six different concentrations of Fe–B NPs from 1 to 100 µg mL^{-1} in 96-well plates (Sarstedt, Numbrecht, Germany), at 1×10^4 cells per well (each in triplicates), or without NPs (negative control). The cell lines were allowed to adhere overnight at 37 °C, before the addition of ultrasonically treated Fe–B NPs.

Cytotoxicity was evaluated by MTT test and apoptosis/necrosis assay. MTT assay was used to evaluate the metabolic activity of cells in cultures, as a measure of the number of live cells. After cultivation of cells for 48 h at 37 °C, 20 µL of MTT (Sigma) solution (5 mg mL^{-1} in PBS) was added to each well and the plates were incubated for additional 4 h. Wells with a MTT solution without the cells served as blank controls. The formazan crystals were dissolved overnight by the addition of 150 µL of 0.01 N HCl/10% sodium dodecyl sulfate (SDS) (Merck, Darmstadt, Germany). The next day, the optical density (OD) value was read at 570 nm (ELISA reader, Behring II). The results were presented as the relative metabolic activity compared to the negative control, used as 100%. Fe–B NPs without cells did not interfere with the assay. For the apoptosis/necrosis assay, an annexin-V-fluorescein isothiocyanate (FITC)/propidium iodide (PI) kit (Invitrogen, Carlsbad, CA, USA) was used according to the manufacturer's protocol, followed by flow cytometry analysis (CyFlow Cube 6, Partec GmbH, Munster, Germany). The cell lines were seeded in 24-well plates (Sarstedt) (1×10^5 cells per well) and allowed to adhere at 37 °C. For comparison, the same procedure was applied for PBMCs. After 2 h, cells were treated with different concentrations of Fe–B NPs or culture medium alone (negative control) for 24 h at 37 °C. After cultivation, media were removed and the cell lines were washed three times with PBS and trypsinized. PBMCs were collected by a stronger pipetting. The collected and washed cells were stained and analyzed. The assay enables identification of necrotic (annexin-V-FITC−/PI+) cells, living (annexin-V-FITC−/PI−) cells, early apoptotic (annexin-V- FITC+/PI−) cells, and late apoptotic/secondary necrotic (annexin-V-FITC+/PI+) cells.

ROS production was detected by staining the cells using dihydrorhodamine (DHR) 123 dye following the manufacturer's protocol (Sigma-Aldrich, St. Louis, MO, USA). The cells were cultivated and proceeded as for apoptosis/necrosis assay. After 12 h of cultivation, the cells were incubated with 5×10^{-6} м DHR123 in PBS for an additional 30 min at 37 °C. Subsequently, after washing in PBS, the fluorescence intensity (fi) was analyzed in a LSRII flow cytometer (Becton Dickinson). For comparison, blank samples with the cells without DHR123 loading (with and without Fe–B NPs) were used. Appropriate positive controls were cells treated with 100×10^{-6} м ferrous ammonium sulphate ($Fe(NH_4)_2(SO_4)_2$) (Thermo Fisher Scientific, Pittsburgh, PA, USA), and with 0.3% hydrogen peroxide (H_2O_2) (Sigma-Aldrich). Results are presented as mean fi or percentage of DHR123-positive cells, from three independent experiments.

For uptake experiments, the cells (5×10^4 per well) were seeded onto 13 mm glass coverslips (Sarstedt), placed in 24-well plates (Sarstedt) and incubated in cell culture medium for 2 h at 37 °C to adhere. The cells were then incubated with Fe–B NPs overnight at 37 °C. Coverslips were removed from the plates, washed thoroughly in PBS, air-dried, and fixed with methanol (Merck). Cytospins were also prepared from some cultures by using a cytocentrifuge and fixed with methanol. After fixation and drying, coverslips and cytospins were stained with PB by immersing the specimens in a solution obtained by mixing equal amounts of 4% potassium ferrocyanide (aqueous, Merck) and 4% hydrochloric acid (aqueous, Sigma) for 20 min, rinsing in distilled water and counterstaining with nuclear fast red solution (Sigma) for 4 min. Air-dried specimens were mounted with Canada balsam (Merck) and analyzed with a light microscope (Nikon Eclipse 5i equipped with a Nikon DXM1200C camera, Tokyo, Japan). Internalization of NPs (blue-stained intracellular granules) was checked using a semiquantitative method as described in previous article.[44]

Magnetic Resonance Imaging: Magnetic resonance images were acquired with a Bruker system operating at 7 T (Bruker BioSpin, Ettlingen, Germany). The samples were dispersed in water by serial dilution starting from a solution with Fe concentration of 4×10^{-3} м. The transversal relaxation times (r_2 value) were calculated from the slopes of the best fit lines of relaxation rates ($1/T_2$) versus iron concentration. The T_2 map in phantoms was acquired using a multi-slice multi-echo sequence with the following parameters: TR = 2000 ms, TE from 6.5 to 170.43 ms, FOV = 55 × 55 mm, matrix size = 128 × 128, slice thickness = 1 mm, and number of echoes = 25.

In vivo experiments were performed in $n = 5$ Balb/c male mice (6–8 weeks old, Envigo). Mice were intravenously injected with NPs at a dosage of 5 mg-Fe kg^{-1}. For MRI acquisitions, animals were anesthetized with a mixture of O_2 and air containing 1–1.5% of isoflurane, placed in a heated animal bed and inserted in a 7.2 cm internal diameter birdcage coil. T_2-weighted images of the mice body were acquired using a rapid acquisition with relaxation enhancement sequence with the following parameters: FOV = 60 × 40 mm, MTX = 256 × 256, slice thickness = 1 mm, TE = 33 ms, and TR = 2.500 ms. The images were acquired before and 1, 6, 24, 48 h, 5, 14, and 30 days after NPs injection. T_2 signal intensity was calculated by region of interest (ROI) and normalized by the ROI defined on the white signal produced from the fat tissue. All mice were weighed before (day 0), 14, and 30 days after the NPs injection. In vivo experiments were carried out with the authorization of the Italian Ministry of Health and the Committee for Research on Laboratory Animals of the University of Verona.

Histopathology Analysis: After 30 days from NPs injection, mice were sacrificed and liver, kidneys, lung, and heart were dissected out for histopathology and ICP-MS analysis. The organs were washed with PBS

0.1 м and fixed in 10% formalin for 4 h. Tissues were embedded in paraffin and cut in 5 µm thick sections with a microtome and dried at 37 °C for 24 h. In order to evaluate the presence of Fe in the tissue, PB staining was performed on liver and kidney: sections were incubated with PB solution (5% hydrochloric acid and 5% potassium ferrocyanide) for 40 min and counterstained with nuclear fast red (Bioptica) for 10 min. To morphologically evaluate tissue damage, sections of liver, kidney, lung, and heart were stained with hematoxylin and eosin. Sections were examined under a light microscope (Olympus BXS1) equipped with a charge-coupled device camera.

Finally, to assess iron content by ICP-MS analysis in organs explanted 30 days after administration of Fe–B NPs or Endorem-treated animals, the dissections were weighted and digested with HNO_3 (ten times the organ mass) at 95 °C for 3 h.

Statistical Analysis: For the biocompatibility study in vitro, the results are presented as representative data (one or three independent experiments) or as mean ± SD values of three independent experiments. The differences between the treatments/concentrations were analyzed by repeated measures ANOVA with Tukey's multiple comparison test using the GraphPad Prism software (GraphPad, La Jolla, CA, USA). All tests were two-sided with the significance level of $p < 0.05$.

Statistical analysis of MRI measurements on $n = 5$ mice was performed using Prism software (8.1.1, GraphPad) and confirmed by a custom script for statistical analysis realized in MATLAB (MathWorks, Natick, MA, USA). All the data are expressed as mean ± SD and the statistical test performed was one-way ANOVA with multiple comparisons using Tukey–Kramer method. When the p-value < 0.05, the differences were considered statistically significant.

Supporting Information

Supporting Information is available from the Wiley Online Library or from the author.

Acknowledgements

This research was funded by the University of Padova STARS grant "4NANOMED" and the Italian Ministry of Foreign Affairs and International Cooperation "great relevance project" with protocol number 0191594. MRI experiments were performed at Centro Piattaforme Tecnologiche (CPT, University of Verona), which is gratefully acknowledged.

Conflict of Interest

The authors declare no conflict of interest.

Keywords

bimetallic nanoparticles, boron neutron capture therapy, laser ablation, magnetic nanoparticles, magnetic resonance imaging

Received: September 13, 2020
Revised: November 4, 2020

---

[1] J. Shi, P. W. Kantoff, R. Wooster, O. C. Farokhzad, *Nat. Rev. Cancer* **2017**, *17*, 20.
[2] Q. Sun, Z. Zhou, N. Qiu, Y. Shen, *Adv. Mater.* **2017**, *29*, 1606628.
[3] A. Farzin, S. A. Etesami, J. Quint, A. Memic, A. Tamayol, *Adv. Healthcare Mater.* **2020**, *9*, 1901058.
[4] Z. T. Rosenkrans, C. A. Ferreira, D. Ni, W. Cai, *Adv. Healthcare Mater* **2020**, 2000690.
[5] V. Amendola, S. Scaramuzza, L. Litti, M. Meneghetti, G. Zuccolotto, A. Rosato, E. Nicolato, P. Marzola, G. Fracasso, C. Anselmi, M. Pinto, M. Colombatti, *Small* **2014**, *10*, 2476.
[6] Z. Zhou, K. Hu, R. Ma, Y. Yan, B. Ni, Y. Zhang, L. Wen, Q. Zhang, Y. Cheng, *Adv. Funct. Mater.* **2016**, *26*, 5971.
[7] T. Shanmugasundaram, M. Radhakrishnan, V. Gopikrishnan, K. Kadirvelu, R. Balagurunathan, *Nanoscale* **2017**, *9*, 16773.
[8] X.-R. Song, S.-X. Yu, G.-X. Jin, X. Wang, J. Chen, J. Li, G. Liu, H.-H. Yang, *Small* **2016**, *12*, 1506.
[9] V. Torresan, D. Forrer, D. Badocco, P. Pastore, M. Casarin, A. Selloni, D. Coral, M. Ceolin, M. B. Fernandez van Raap, A. Busato, P. Marzola, A. E. Spinelli, V. Amendola, *ACS Nano* **2020**, *14*, 12840.
[10] X. Wang, W. Yao, R. Guo, X. Yang, J. Tang, J. Zhang, W. Gao, V. Timchenko, J. Liu, *Adv. Healthcare Mater.* **2018**, *7*, 1800318.
[11] E. B. Ehlerding, F. Chen, W. Cai, *Adv. Sci.* **2016**, *3*, 1500223.
[12] G. Yang, S. Z. F. Phua, A. K. Bindra, Y. Zhao, *Adv. Mater.* **2019**, *31*, 1805730.
[13] D. M. Valcourt, C. H. Kapadia, M. A. Scully, M. N. Dang, E. S. Day, *Adv. Healthcare Mater.* **2020**, *9*, 2000110.
[14] G. Pasparakis, T. Manouras, M. Vamvakaki, P. Argitis, *Nat. Commun.* **2014**, *5*, 3623.
[15] A. Vorobjova, D. Tishkevich, D. Shimanovich, M. Zdorovets, A. Kozlovskiy, T. Zubar, D. Vinnik, M. Dong, S. Trukhanov, A. Trukhanov, V. Fedosyuk, *Nanomaterials* **2020**, *10*, 173.
[16] D. I. Tishkevich, A. I. Vorobjova, D. A. Vinnik, *Solid State Phenom.* **2020**, *299*, 100.
[17] D. I. Tishkevich, A. I. Vorobjova, A. V. Trukhanov, *Solid State Phenom.* **2020**, *299*, 281.
[18] R. L. Moss, *Appl. Radiat. Isot.* **2014**, *88*, 2.
[19] M. A. Dymova, S. Y. Taskaev, V. A. Richter, E. V. Kuligina, *Cancer Commun.* **2020**, *40*, 406.
[20] K. Hu, Z. Yang, L. Zhang, L. Xie, L. Wang, H. Xu, L. Josephson, S. H. Liang, M.-R. Zhang, *Coord. Chem. Rev.* **2020**, *405*, 213139.
[21] Z. Gao, Y. Horiguchi, K. Nakai, A. Matsumura, M. Suzuki, K. Ono, Y. Nagasaki, *Biomaterials* **2016**, *104*, 201.
[22] H. Koivunoro, S. González, L. Provenzano, G. Santa Cruz, L. Kankaanranta, S. Savolainen, H. Joensuu, *Radiother. Oncol.* **2016**, *118*, S58.
[23] L.-W. Wang, Y.-W. H. Liu, F.-I. Chou, S.-H. Jiang, *Cancer Commun.* **2018**, *38*, 37.
[24] P. R. Menéndez, B. M. C. Roth, M. D. Pereira, M. R. Casal, S. J. González, D. B. Feld, G. A. Santa Cruz, J. Kessler, J. Longhino, H. Blaumann, R. Jiménez Rebagliati, O. A. Calzetta Larrieu, C. Fernández, S. I. Nievas, S. J. Liberman, *Appl. Radiat. Isot.* **2009**, *67*, S50.
[25] A. Zonta, T. Pinelli, U. Prati, L. Roveda, C. Ferrari, A. M. Clerici, C. Zonta, G. Mazzini, P. Dionigi, S. Altieri, S. Bortolussi, P. Bruschi, F. Fossati, *Appl. Radiat. Isot.* **2009**, *67*, S67.
[26] M. Sasai, H. Nakamura, N. Sougawa, Y. Sakurai, M. Suzuki, C. M. Lee, *Anticancer Res.* **2016**, *36*, 907.
[27] M. Suzuki, O. Suzuki, Y. Sakurai, H. Tanaka, N. Kondo, Y. Kinashi, S.-I. Masunaga, A. Maruhashi, K. Ono, *Int. Cancer Conf. J.* **2012**, *1*, 235.
[28] A. Marinaccio, F. Montanaro, M. Mastrantonio, R. Uccelli, P. Altavista, M. Nesti, A. S. Costantini, G. Gorini, *Int. J. Cancer* **2005**, *115*, 142.
[29] A. Gasparrini, A. M. Pizzo, G. Gorini, A. Seniori Costantini, S. Silvestri, C. Ciapini, A. Innocenti, G. Berry, *Eur. J. Epidemiol.* **2008**, *23*, 541.
[30] T. Nomoto, N. Nishiyama, *Biomaterials* **2018**, *178*, 583.
[31] W. A. G. Sauerwein, A. Wittig, R. Moss, Y. Nakagawa, *Neutron Capture Therapy: Principles and Applications*, Springer, Berlin **2012**.
[32] S. Savolainen, M. Kortesniemi, M. Timonen, V. Reijonen, L. Kuusela, J. Uusi-Simola, E. Salli, H. Koivunoro, T. Seppälä, N. Lönnroth, P. Välimäki, H. Hyvönen, P. Kotiluoto, T. Serén, A. Kuronen, S. Heikkinen, A. Kosunen, I. Auterinen, *Phys. Med.* **2013**, *29*, 233.

[33] I. Kato, K. Ono, Y. Sakurai, M. Ohmae, A. Maruhashi, Y. Imahori, M. Kirihata, M. Nakazawa, Y. Yura, *Appl. Radiat. Isot.* **2004**, *61*, 1069.
[34] S.-I. Miyatake, S. Kawabata, R. Hiramatsu, T. Kuroiwa, M. Suzuki, N. Kondo, K. Ono, *Neurol. Med. Chir.* **2016**, *56*, 361.
[35] Y. Ariyoshi, M. Shimahara, Y. Kimura, Y. Ito, T. Shimahara, S.-I. Miyatake, S. Kawabata, *Oncol. Lett.* **2011**, *2*, 423.
[36] T. Morita, H. Kurihara, K. Hiroi, N. Honda, H. Igaki, J. Hatazawa, Y. Arai, J. Itami, *Radiat. Oncol.* **2018**, *13*, 4.
[37] R. F. Barth, *J. Neuro-Oncol.* **2003**, *62*, 1.
[38] R. F. Barth, J. C. Grecula, *Appl. Radiat. Isot.* **2020**, *160*, 109029.
[39] D. Kim, J. Kim, Y. I. Park, N. Lee, T. Hyeon, *ACS Cent. Sci.* **2018**, *4*, 324.
[40] X. Han, K. Xu, O. Taratula, K. Farsad, *Nanoscale* **2019**, *11*, 799.
[41] N. Lee, T. Hyeon, *Chem. Soc. Rev.* **2012**, *41*, 2575.
[42] Y. Sun, H. S. Kim, S. Kang, Y. J. Piao, S. Jon, W. K. Moon, *Adv. Healthcare Mater.* **2018**, *7*, 1800266.
[43] T. Hao, Q. Chen, Y. Qi, P. Sun, D. Chen, W. Jiang, K. Liu, H. Sun, L. Li, J. Ding, Z. Li, *Adv. Healthcare Mater.* **2019**, *8*, 1901005.
[44] G. Fracasso, P. Ghigna, L. Nodari, S. Agnoli, D. Badocco, P. Pastore, E. Nicolato, P. Marzola, D. Mihajlović, M. Markovic, M. Čolić, V. Amendola, *J. Colloid Interface Sci.* **2018**, *522*, 208.
[45] C. Tapeinos, F. Tomatis, M. Battaglini, A. Larrañaga, A. Marino, I. A. Telleria, M. Angelakeris, D. Debellis, F. Drago, F. Brero, P. Arosio, A. Lascialfari, A. Petretto, E. Sinibaldi, G. Ciofani, *Adv. Healthcare Mater.* **2019**, *8*, 1900612.
[46] J. F. Liu, Z. Lan, C. Ferrari, J. M. Stein, E. Higbee-Dempsey, L. Yan, A. Amirshaghaghi, Z. Cheng, D. Issadore, A. Tsourkas, *ACS Nano* **2020**, *14*, 142.
[47] Z. Zhou, Z. Shen, X. Chen, *ACS Nano* **2020**, *14*, 7.
[48] D. F. Coral, P. Mendoza Zélis, M. Marciello, M. D. P. Morales, A. Craievich, F. H. Sánchez, M. B. Fernández Van Raap, *Langmuir* **2016**, *32*, 1201.
[49] D. F. Coral, P. A. Soto, V. Blank, A. Veiga, E. Spinelli, S. Gonzalez, G. P. Saracco, M. A. Bab, D. Muraca, P. C. Setton-Avruj, A. Roig, L. Roguin, M. B. Fernández Van Raap, *Nanoscale* **2018**, *10*, 21262.
[50] C. Papadopoulos, E. K. Efthimiadou, M. Pissas, D. Fuentes, N. Boukos, V. Psycharis, G. Kordas, V. C. Loukopoulos, G. C. Kagadis, *Phys. Med.* **2020**, *71*, 39.
[51] F. Perton, M. Tasso, G. A. Muñoz Medina, M. Ménard, C. Blanco-Andujar, E. Portiansky, M. B. F. Van Raap, D. Bégin, F. Meyer, S. Begin-Colin, D. Mertz, *Appl. Mater. Today* **2019**, *16*, 301.
[52] W. Liu, L. Chen, M. Chen, W. Wang, X. Li, H. Yang, S. Yang, Z. Zhou, *Adv. Healthcare Mater.* **2020**, *9*, 2000202.
[53] V. Amendola, D. Amans, Y. Ishikawa, N. Koshizaki, S. Scirè, G. Compagnini, S. Reichenberger, S. Barcikowski, *Chem. - Eur. J.* **2020**, *26*, 9206.
[54] J. Zhang, J. Claverie, M. Chaker, D. Ma, *ChemPhysChem* **2017**, *18*, 986.
[55] J. Xiao, P. Liu, C. X. Wang, G. W. Yang, *Prog. Mater. Sci.* **2017**, *87*, 140.
[56] S. Jendrzej, B. Gökce, M. Epple, S. Barcikowski, *ChemPhysChem* **2017**, *18*, 1012.
[57] S. Crivellaro, A. Guadagnini, D. M. Arboleda, D. Schinca, V. Amendola, *Rev. Sci. Instrum.* **2019**, *90*, 033902.
[58] V. Amendola, L. Litti, M. Meneghetti, *Anal. Chem.* **2013**, *85*, 11747.
[59] O. Rabin, J. Manuel Perez, J. Grimm, G. Wojtkiewicz, R. Weissleder, *Nat. Mater.* **2006**, *5*, 118.
[60] C. Dai, C. Wang, R. Hu, H. Lin, Z. Liu, L. Yu, Y. Chen, B. Zhang, *Biomaterials* **2019**, *219*, 119374.
[61] I. Postuma, S. Bortolussi, N. Protti, F. Ballarini, P. Bruschi, L. Ciani, S. Ristori, L. Panza, C. Ferrari, L. Cansolino, S. Altieri, *Rep. Pract. Oncol. Radiother.* **2016**, *21*, 123.
[62] S. Altieri, S. Bortolussi, P. Bruschi, P. Chiari, F. Fossati, S. Stella, U. Prati, L. Roveda, A. Zonta, C. Zonta, C. Ferrari, A. Clerici, R. Nano, T. Pinelli, *Appl. Radiat. Isot.* **2008**, *66*, 1850.
[63] C.-H. Lai, N.-C. Lai, Y.-J. Chuang, F.-I. Chou, C.-M. Yang, C.-C. Lin, *Nanoscale* **2013**, *5*, 9412.
[64] L. Ciani, S. Bortolussi, I. Postuma, L. Cansolino, C. Ferrari, L. Panza, S. Altieri, S. Ristori, *Int. J. Pharm.* **2013**, *458*, 340.
[65] D. I. Tishkevich, I. V. Korolkov, A. L. Kozlovskiy, M. Anisovich, D. A. Vinnik, A. E. Ermekova, A. I. Vorobjova, E. E. Shumskaya, T. I. Zubar, S. V. Trukhanov, M. V. Zdorovets, A. V. Trukhanov, *J. Alloys Compd.* **2019**, *797*, 573.
[66] M. R. Lutz, S. Flieger, A. Colorina, J. Wozny, N. S. Hosmane, D. P. Becker, *ChemMedChem* **2020**, *15*, 1897.
[67] I. V. J. Feiner, K. R. Pulagam, V. Gómez-Vallejo, K. Zamacola, Z. Baz, M. M. Caffarel, C. H. Lawrie, A. Ruiz-de-Angulo, M. Carril, J. Llop, *Part. Part. Syst. Charact.* **2020**, 2000200.
[68] I. Nakase, A. Aoki, Y. Sakai, S. Hirase, M. Ishimura, T. Takatani-Nakase, Y. Hattori, M. Kirihata, *ACS Omega* **2020**, *5*, 22731.
[69] M. A. Hamayun, M. Abramchuk, H. Alnasir, M. Khan, C. Pak, S. Lenhert, L. Ghazanfari, M. Shatruk, S. Manzoor, *J. Magn. Magn. Mater.* **2018**, *451*, 407.
[70] S. Ma, P. Z. Si, Y. Zhang, B. Wu, Y. B. Li, J. J. Liu, W. J. Feng, X. L. Ma, Z. D. Zhang, *Scr. Mater.* **2007**, *57*, 265.
[71] M. Amir, M. Geleri, S. Güner, A. Baykal, H. Sözeri, *J. Inorg. Organomet. Polym. Mater.* **2015**, *25*, 1111.
[72] D. Zhang, K. J. Klabunde, C. M. Sorensen, G. C. Hadjipanayis, *Phys. Rev. B* **1998**, *58*, 14167.
[73] L. Yu, K. Dong, C. Yang, Q. Wang, Y. Hou, *Mater. Lett.* **2014**, *132*, 4.
[74] S. Naqvi, M. Samim, M. Abdin, F. J. Ahmad, A. Maitra, C. Prashant, A. K. Dinda, *Int. J. Nanomed.* **2010**, *5*, 983.
[75] Q. Feng, Y. Liu, J. Huang, K. Chen, J. Huang, K. Xiao, *Sci. Rep.* **2018**, *8*, 2082.
[76] H. Türkez, M. E. Arslan, E. Sönmez, M. Açikyildiz, A. Tatar, F. Geyikoğlu, *Cytotechnology* **2019**, *71*, 351.
[77] M. Bekić, S. Tomić, R. Rudolf, M. Milanović, D. Vučević, I. Anžel, M. Čolić, *Materials* **2019**, *12*, 4121.
[78] P. Shou, Z. Yu, Y. Wu, Q. Feng, B. Zhou, J. Xing, C. Liu, J. Tu, O. U. Akakuru, Z. Ye, X. Zhang, Z. Lu, L. Zhang, A. Wu, *Adv. Healthcare Mater.* **2020**, *9*, 1900948.
[79] E. Valero, S. Fiorini, S. Tambalo, H. Busquier, J. Callejas-Fernández, P. Marzola, N. Gálvez, J. M. Domínguez-Vera, *J. Med. Chem.* **2014**, *57*, 5686.
[80] D. Badocco, I. Lavagnini, A. Mondin, G. Favaro, P. Pastore, *Spectrochim. Acta, Part B* **2015**, *114*, 81.

Journal of Colloid and Interface Science 579 (2020) 186–194

Contents lists available at ScienceDirect

Journal of Colloid and Interface Science

journal homepage: www.elsevier.com/locate/jcis

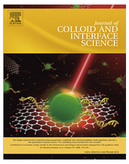

Colloidal polymer-coated Zn-doped iron oxide nanoparticles with high relaxivity and specific absorption rate for efficient magnetic resonance imaging and magnetic hyperthermia

Pradip Das [a,b], Lucia Salvioni [a], Manuela Malatesta [c], Federica Vurro [d], Silvia Mannucci [c], Marco Gerosa [d], Maria Antonietta Rizzuto [a], Chiara Tullio [a], Anna Degrassi [e], Miriam Colombo [a,*], Anna M. Ferretti [f], Alessandro Ponti [f], Laura Calderan [c], Davide Prosperi [a,g,*]

[a] NanoBioLab, Dipartimento di Biotecnologie e Bioscienze, Università di Milano-Bicocca, piazza della Scienza 2, 20126 Milano, Italy
[b] Istituto Italiano di Tecnologia, Via Morego 30, 16163 Genova, Italy
[c] Neurosciences, Biomedicine and Movement Dept., School of Medicine, University of Verona, Strada le grazie 8, 37134 Verona, Italy
[d] Computer Sciences Dept., University of Verona, Strada le grazie 7, Verona, Italy
[e] Toxicology, Accelera S.R.L. – NMS Group S.p.A., Viale Pasteur 10, 20014 Nerviano, MI, Italy
[f] Istituto di Scienze e Tecnologie Chimiche "Giulio Natta" (SCITEC), Consiglio Nazionale delle Ricerche, via G, Fantoli 16/15, 20138 Milano, Italy
[g] Nanomedicine Laboratory, ICS Maugeri S.p.A. SB, via S. Maugeri 10, 27100 Pavia, Italy

HIGHLIGHTS

- Successful preparation of highly colloidal stable polymer-coated doped magnetic nanoparticles.
- Achievement of relatively higher transverse relaxivity and specific absorption rate via doping technique.
- Effective demonstration of *in vitro* magnetic resonance imaging and magnetic hyperthermia of glioblastoma.

GRAPHICAL ABSTRACT

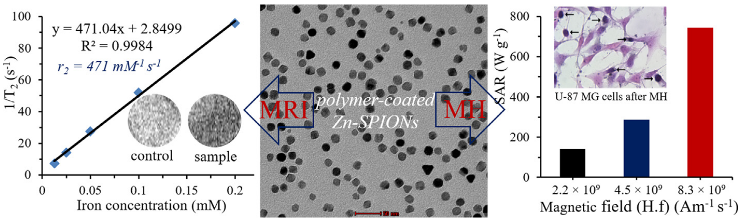

ARTICLE INFO

Article history:
Received 6 February 2020
Revised 29 May 2020
Accepted 30 May 2020
Available online 6 June 2020

Keywords:
Iron oxide nanoparticle
Zinc doping
Superparamagnetism
Polymer coating
High relaxivity
High specific absorption rate
Cancer theranostic

ABSTRACT

Colloidally stable nanoparticles-based magnetic agents endowed with very high relaxivity and specific absorption rate are extremely desirable for efficient magnetic resonance imaging and magnetic hyperthermia, respectively. Here, we report a water dispersible magnetic agent consisting of zinc-doped superparamagnetic iron oxide nanoparticles (i.e., Zn-SPIONs) of 15 nm size with high saturation magnetization coated with an amphiphilic polymer for effective magnetic resonance imaging and magnetic hyperthermia of glioblastoma cells. These biocompatible polymer-coated Zn-SPIONs had 24 nm hydrodynamic diameter and exhibited high colloidal stability in various aqueous media, very high transverse relaxivity of 471 mM^{-1} s^{-1}, and specific absorption rate up to 743.8 W g^{-1}, which perform better than most iron oxide nanoparticles reported in the literature, including commercially available agents. Therefore, using these polymer-coated Zn-SPIONs even at low concentrations, T_2-weighted magnetic resonance imaging and moderate magnetic hyperthermia of glioblastoma cells under clinically relevant magnetic field were successfully implemented. In addition, the results of this *in vitro* study suggest the superior potential of Zn-SPIONs as a theranostic nanosystem for brain cancer treatment, simultaneously acting as a contrast agent for magnetic resonance imaging and a heat mediator for localized magnetic hyperthermia.

---

* Corresponding authors.
E-mail addresses: miriam.colombo@unimib.it (M. Colombo), davide.prosperi@unimib.it (D. Prosperi).

https://doi.org/10.1016/j.jcis.2020.05.119
0021-9797/

1. Introduction

Several types of colloidal magnetic nanoparticles have been designed and successfully developed over the past decades [1–3]. Therefore, they have attracted tremendous attention in recent years for different biomedical applications – including bioimaging, drug delivery, biosensing, and therapy – because of their unique intrinsic magnetic as well as physicochemical properties [1–5]. Among them, superparamagnetic iron oxide nanoparticles (SPIONs) in the form of magnetite or maghemite nanocrystals have demonstrated promising performance as contrast agents for magnetic resonance imaging (MRI) and as heat mediators for magnetic hyperthermia (MH) [3–6].

MRI is a non-invasive, real time medical imaging technique able to generate images of the tissues at any depth of the body with excellent spatial and temporal resolution [7,8]. In addition, MRI does not require harmful agents such as radioisotopes and radiations similar to X-ray [7,8]. SPIONs have been largely proposed as negative contrast agents due to their capability to shorten the transverse (T_2) relaxation time [9] and, as a result, a number of SPIONs-based contrast agents including Resovist® and Feridex® were clinically approved [3,6,10]. However, the low transverse relaxivity (r_2) of these contrast agents consisting of polydisperse and poorly crystalline nanoparticles could not provide sufficient sensitivity in clinical application [6,11]. Furthermore, the slow body clearance of SPIONs causes several long-term side effects [6]. Therefore, almost all the clinically approved T_2 contrast agents were withdrawn or discontinued from the market [6,10].

On the other hand, MH is a promising non-invasive therapeutic modality for cancer treatment based on the production of heat from magnetic nanoparticles under an applied alternating magnetic field [4,12,13]. This strategy relies on the use of magnetic heat mediators to increase the temperature within the tumor tissue typically in the range of 41–46 ^{o}C, where cancer cells are selectively killed preserving healthy tissues. Notably, the apoptosis and/or necrosis of cancer cells occurs via several mechanisms including protein denaturation and aggregation, impairment of DNA repair processes as well as activation of the immune system promoted by over-expression of heat shock proteins [4,12]. The most commonly investigated magnetic heat mediators are superparamagnetic SPIONs, which convert magnetic energy to thermal energy through Brownian-Néel relaxations and hysteresis losses [4,12]. Nowadays, SPIONs-based MH is clinically approved in Europe as an adjuvant therapy for recurrent glioblastoma multiforme and several clinical trials are still ongoing for other cancer types [14,15]. However, the low magnetic properties of nanoparticles available for preclinical and clinical studies cause poor heating efficiency, that leads to a low specific absorption rate (SAR) [4,12,14,15]. As a result, very high dosages (in the scale of mg mL^{-1}) of SPIONs are needed to accomplish high performances in cancer therapy [14]. Furthermore, their low colloidal stability in biological media promotes the nanoparticles aggregation, further decreasing their SAR value [16].

With the aim to contribute to overcome the clinical limitations reported both for MRI and MH, the objective of the present study was to develop an efficient SPIONs-based theranostic nanosystem with superior magnetic properties and improved colloidal stability for glioblastoma cell treatment. For this purpose, among the several strategies proposed for enhancing the SPIONs magnetism (*e.g.*, optimization of nanoparticles size, use of anisotropic nanoparticles, metal ions doping, and the formation of nanoclusters), we have adopted the most promising doping approach. The controlled zinc ions substitution is highly able to enhance the magnetic properties of ferrite nanoparticles and subsequently improved their performance as contrast agents and heat mediators [17,18]. Thus, we have employed the zinc doing in Fe_3O_4 nanoparticles to attain higher relaxivity and specific absorption rate. In this approach, iron(III) ions in the tetrahedral sites of inverse spinel structure of Fe_3O_4 were partially replaced by non-magnetic zinc (II) ions [19,20]. In addition, the surface modification of hydrophobic magnetic nanoparticles is very important for their biomedical applications [1,3,4]. To make highly water dispersible nanoparticles, the polymer coating methods are more appropriate for providing long-term high colloidal stability of larger magnetic nanoparticles in different biological environments [1,3,4]. Moreover, the exposed reactive functional groups (such as primary amine and carboxyl) of the polymer-coated nanoparticles are supportive for further conjugation of therapeutic agents and targeting ligands [1,3,4]. Therefore, the synthesized non-spherical zinc-doped superparamagnetic iron oxide nanoparticles (Zn-SPIONs) were successfully coated with an amphiphilic polymer producing water dispersible nanoparticles that exhibited high colloidal stability in biological media. The polymer-coated Zn-SPIONs also showed very high transverse relaxivity (r_2) of 471 mM^{-1} s^{-1} as well as specific absorption rate (SAR) up to 743.8 W g^{-1} that was more suitable for the development of an efficient theranostic agent. Consequently, this biocompatible nanoconstruct was designed to efficiently interact with glioblastoma cells, demonstrating both contrast agent as well as heat mediator capabilities.

2. Experimental

2.1. Materials

Iron(III) acetylacetonate [$Fe(acac)_3$], iron(II) acetylacetonate [$Fe(acac)_2$], zinc chloride ($ZnCl_2$), oleic acid, oleylamine, dioctyl ether, poly(isobutene-*alt*-maleic anhydride) (MW ~ 6000 Da), dodecylamine, and anhydrous tetrahydrofuran were obtained from Sigma Aldrich. Nitric acid (67–69%) for trace metal analysis was purchased from Thermo Fisher Scientific. Eagle's minimum essential medium (EMEM), fetal bovine serum (FBS), and trypsin-EDTA solution were obtained from Euroclone.

2.2. Synthesis of hydrophobic zinc-doped superparamagnetic iron oxide nanoparticles (Zn-SPIONs)

Hydrophobic Zn-SPIONs were synthesized via a previously reported high-temperature thermal decomposition method with minor modification [21]. Briefly, $Fe(acac)_3$ (1 mmol), $ZnCl_2$ (0.2 mmol), and $Fe(acac)_2$ (0.3 mmol) were placed in a 250 mL three-neck round-bottom flask in the presence of dioctyl ether (20 mL). The mixture was stirred under vacuum at 100 ^{o}C for 30 min. Then oleic acid (0.5 mmol) and oleylamine (0.5 mmol) were injected at 100 ^{o}C under an inert atmosphere. The reaction mixture was rapidly heated to 300 ^{o}C under reflux condition and maintained at that temperature for 60 min. Next, the solution was allowed to cool to room temperature and the Zn-SPIONs were precipitated using ethanol and separated via centrifugation. The Zn-SPIONs were redispersed in hexane in presence of oleic acid and precipitated again with ethanol for further purification and then the black-brown precipitate was collected by centrifugation. Finally, pure Zn-SPIONs were stored in chloroform for characterization and polymer coating.

2.3. Synthesis of water dispersible polymer-coated Zn-SPIONs

Hydrophobic long alkyl chain capped Zn-SPIONs were transformed to be water dispersible via a polymer coating approach using pre-synthesized amphiphilic polymer, dodecyl grafted poly (isobutene-*alt*-maleic anhydride) [22,23]. Briefly, 5 mL chloroform solution of Zn-SPIONs (1 mg mL^{-1}) was mixed with 100 μL of dodecyl grafted poly(isobutene-*alt*-maleic anhydride) polymer in chloroform (0.5 M monomer concentration). Then the organic solvent was completely evaporated using rotary evaporator and the solid thin film of polymer-coated Zn-SPIONs were dispersed in Milli-Q water (9 mL) in presence of 1 mL KOH solution (0.5 M). The polymer-coated Zn-SPIONs were purified via washing several times with Milli-Q water using 50 kDa centrifugal filter. Finally, an aqueous solution of polymer-coated Zn-SPIONs was stored for further use.

2.4. ICP analysis of Zn-SPIONs

To quantify the level of zinc and iron in as-synthesized hydrophobic Zn-SPIONs and also to measure the concentration of iron in polymer-coated Zn-SPIONs, Zn-SPIONs before and after polymer coating were analyzed by inductively coupled plasma-optical emission spectroscopy (ICP-OES) after their complete digestion in 2% aqueous nitric acid solution.

2.5. Magnetic measurement

Magnetization measurements of as-synthesized and polymer-coated Zn-SPIONs were carried out by a Quantum Design MPMS XL-5 SQUID magnetometer. Weighted amounts of each sample were sealed in Teflon tape. Field-cooled (FC) and zero-field-cooled (ZFC) magnetization curves were recorded in the 5–300 K range. After cooling the sample from 300 to 5 K in zero field, the ZFC magnetization was recorded on heating to 300 K using a measuring field H_{meas} = 100 Oe. Next, the FC magnetization was measured (H_{meas} = 100 Oe) while cooling the sample from 300 to 5 K under field H_{cool} = 100 Oe. Magnetization isotherms (hysteresis loops) were recorded between + 50 kOe and −50 kOe at 300 K. All data were corrected for the diamagnetism of the sample holder and scaled to the sample mass.

2.6. Relaxivity and MRI phantom studies

The value of longitudinal (T_1) and transverse (T_2) relaxation times of several aqueous solutions of polymer-coated Zn-SPIONs at different molar concentrations of iron from 0.0125 mM to 0.2 mM were measured using 0.47 T Time-Domain NMR Benchtop Systems of Minispec mq series from Bruker. The samples were analyzed using 400 μL aqueous solutions of polymer-coated Zn-SPIONs in NMR tubes at 300 K. The value of T_1 and T_2 relaxation times were calculated using *t1_sr_mb* and *t2_cp_mb* sequence, respectively. Then the longitudinal relaxivity (r_1) and transverse relaxivity (r_2) were obtained from the slope of the regression line of $1/T_1$ and $1/T_2$ in s^{-1} against iron concentration in mM, respectively. The T_2-weighted phantom images of polymer-coated Zn-SPIONs were recorded using 400 μL aqueous solutions of nanoparticles at different molar concentrations of iron (from 0.0125 to 0.2 mM) in an Eppendorf tube. For this measurement, a MSME (multi slice multi echo) sequence with a repetition time (TR) of 4 *sec* and 16 echo time (TE), ranging from 10 to 160 ms, field of view (FOV) of 2.5 × 2.5 cm, with a matrix 256 × 128 pixels, and a slice thickness of 2 mm were used.

2.7. SAR measurement

The heating efficiency of polymer-coated Zn-SPIONs in the presence of an external alternating magnetic field was evaluated via calculation of its specific absorption rate (SAR) values at numerous strengths and frequencies. To verify and quantify the thermal profile, aqueous solutions of polymer-coated Zn-SPIONs at many nanoparticles weight concentration (1, 3, 5, and 7 mg mL^{-1}) were placed in the alternating magnetic field apparatus (Magnetherm, nanoTherics Ltd, UK), in an induction coil and exposed to an alternated magnetic field (AMF). To assess temperature variation (ΔT) in the nanoparticle solution, a multichannel thermometer equipped with optical fiber probes (FOTEMP4, Optocon AG, Germany) was used. The SAR values of Zn-SPIONs were calculated using the following formula [4].

$$SAR = C\left(\frac{dT}{dt}\right)\left(\frac{m_s}{m_m}\right)$$

Here C is the specific heat capacity of water, dT/dt is the initial slope of the time-dependent heating curve, m_s is the mass of water, and m_m is the mass of Zn-SPIONs.

2.8. Cell culture

U-87 MG glioblastoma cells, (purchased from ATCC Manassas, VA), were cultured in Eagle's minimum essential medium (EMEM) supplemented with 10% fetal bovine serum (FBS), 2 mM L-glutamine, penicillin (50 U mL^{-1}) and streptomycin (50 mg mL^{-1}). Cells were maintained at 37 °C in a humidified atmosphere containing 5% CO_2 and sub-cultured prior to confluence using trypsin-EDTA solution.

2.9. In vitro cytotoxicity assay

The toxicity of polymer-coated Zn-SPIONs on cancer cells was measured by colorimetric MTS assay. In brief, U-87 MG cells were seeded on a 96-well cell culture plate at a density of 1×10^4 cells/well. The cells were incubated with different weight concentrations of Zn-SPIONs (1, 10, 25, 50, and 100 μg mL^{-1}) for 12 and 24 h at 37 °C. Untreated cells were used as controls. After incubation, 20 μL of MTS reagent (CellTiter 96®AQueous One Solution Cell Proliferation Assay; Promega) were added, and cells were incubated for 3 h at 37 °C. Then absorbance was measured by EnSight™ multimode plate reader (Perkin Elmer, Waltham, MA, USA) setting absorbance wavelength at 490 nm. Results were normalized with respect to the viability of untreated cells and expressed as means ± std. dev.

2.10. Intracellular uptake study

The qualitative and quantitative cellular uptakes of polymer-coated Zn-SPIONs were examined using transmission electron microscopy (TEM) and inductively coupled plasma-optical emission spectroscopy (ICP-OES) analysis, respectively. For TEM analysis, U-87 MG cells were grown as monolayers on glass coverslips, treated with 10 μg mL^{-1} of Zn-SPIONs for 24 h at 37 °C, and then fixed with 2.5% (v/v) glutaraldehyde and 2% (v/v) paraformaldehyde in 0.1 M phosphate buffer (pH 7.4) at 4 °C for 1 h, post-fixed with 1% osmium tetroxide and 1.5% potassium ferrocyanide for 1 h, dehydrated with acetone and embedded as monolayers in Epon resin [24]. Ultrathin sections were observed in a Philips Morgagni transmission electron microscope (FEI Company Italia Srl, Milan, Italy) equipped with a Megaview II camera for digital image acquisition.

To determine the iron uptake in cancer cells by ICP measurement, U-87 MG cells (2.5×10^5 cells/well) were seeded on a 12-well cell culture plate. The cells were then incubated with polymer-coated Zn-SPIONs solution at the concentration of 0.1 mM iron for 8 h at 37 °C. Next, the cells were washed with PBS solution followed by cell detachment from the plate using trypsin-EDTA solution and centrifuged at 200 RCF for 5 min. Then the cells plate was suspended in 200 μL PBS and then cells were completely digested using 10% aqueous nitric acid solution. Untreated cells were used as control.

2.11. In vitro magnetic resonance imaging (MRI) analysis

U-87 MG cancer cells were first seeded on a 12-well cell culture plate at a density of 2.5×10^5 cells/well. The cells were grown for overnight and then incubated with polymer-coated Zn-SPIONs at a concentration of 0.1 mM iron for 8 h at 37 °C. Alternatively, untreated U-87 MG cells were used as a control. After incubation, the medium containing excess nanoparticles was removed and the cells were washed with phosphate-buffered saline (PBS) solution. Next, the cells were detached and centrifuged at 200 RCF for 5 min. The supernatant was removed, and cells were suspended in 200 μL PBS solution. Finally, untreated U-87 MG cells and nanoparticles labeled U-87 MG cells were embedded into 400 μL of 1% agarose gel. The samples were analyzed using spin echo sequence with a repetition time (TR) of 4 *sec* and an echo time (TE) of 80 ms; field of view (FOV): 2.5 × 2.5 cm, matrix: 256 × 128 pixels, slice thickness: 2 mm.

2.12. In vitro magnetic fluid hyperthermia (MFH) study

U-87 MG cell line was cultured in Eagle's minimum essential medium (EMEM) with 10% (v/v) fetal bovine serum (FBS), 1% (w/v) glutamine, 0.5% (v/v) amphotericin B, 100 units/mL of penicillin–streptomycin (Gibco, MA, USA), at 37 °C in a 5% CO_2 humidified atmosphere. Cells were trypsinized when subconfluent (about 80%) and then 1×10^4 cells were seeded on glass coverslips in 24-multiwell microplates. After 24 h, cells were incubated with polymer-coated Zn-SPIONs (100 μg mL^{-1}) for 2 h and then placed in the induction coil and exposed for 20 min to an AMF of 334 kHz frequency and 17 mT field amplitude. As control, some cell samples were placed in the induction coil without exposure to magnetic field. Next, the U-87 MG cells were processed after either immediate treatment or 24 h of treatment to estimate the efficiency of magnetic hyperthermia. For this purpose, cells were fixed with 4% buffered formalin solution for 15 min, rinsed with PBS and then stained with Mayer's hematoxylin (nucleus) and eosin (cytoplasm). In order to evaluate the effect of hyperthermia on cell death, ten images of each sample were taken at 20X using a BX-URA2 Olympus microscope (Olympus optical, GMBH, Hamburg, Germany) equipped with a digital camera. The percentage of dead cells was evaluated in each image, means ± standard error values were calculated for control and treated samples, and a statistical comparison was performed (one-way Anova test).

2.13. Instrumentation

The hydrodynamic sizes and zeta potential of Zn-SPIONs were determined by dynamic light scattering (DLS) measurements using a Malvern Zetasizer Nano ZS instrument. Transmission electron microscopy (TEM) image of hydrophobic Zn-SPIONs and their corresponding selected area electron diffraction (SAED) pattern and energy dispersive X-ray (EDX) spectrum were performed by a JEOL JEM-2010 microscope with an accelerating voltage of 200 kV. A TEM image of polymer-coated Zn-SPIONs was captured by FEI 120 kV Tecnai G2 Spirit BioTWIN. The magnetic properties of as-synthesized and polymer-coated Zn-SPIONs were measured using Quantum Design MPMS XL-5 SQUID magnetometer. The amount of zinc and iron in Zn-SPIONs were quantified using Optima 7000 DV inductively coupled plasma-optical emission spectroscopy (ICP-OES) system. The relaxivities of polymer-coated Zn-SPIONs were measured by 0.47 T Time-Domain NMR Benchtop Systems of minispec mq series (Bruker). T_2-weighted phantom images of polymer-coated Zn-SPIONs in aqueous solution and cancer cells were acquired by 7.0 T MRI imaging instrument (Pharmascan®, Bruker BioSpin) with samples inserted in the radiofrequency coil (38 mm, i.d.) inside the magnet. ParaVision 4.0 software from Bruker (Billerica, MA) was used for image visualization. The hyperthermic property of polymer-coated Zn-SPIONs was measured and also magnetic hyperthermia of cancer was performed using Magnetherm, nanoTherics Ltd, UK. U-87 MG cells were observed using an optical Olympus microscope (BX-URA2, Olympus optical, GMBH, Hamburg, Germany) equipped with Image ProPlus software (Media Cybernetics, Rockville, USA). U-87 MG cells were observed also using a Philips Morgagni transmission electron microscope (FEI Company Italia Srl, Milan, Italy) operating at 80 kV and equipped with a Megaview II camera (EMSIS GmbH, Muenster, Germany) for digital image acquisition.

3. Results and discussion

Hydrophobic Zn-SPIONs capped with a mixture of oleic acid and oleylamine were prepared via thermal decomposition of iron acetylacetonate in the presence of zinc chloride in dioctyl ether at elevated temperature to attain high-quality nanoparticles [21]. As determined by the analysis of transmission electron microscopy (TEM) images, the synthesized hydrophobic Zn-SPIONs displayed a non-spherical shape along with an average size of 15 ± 2 nm (Fig. S1a). The selected area electron diffraction (SAED) pattern of these nanoparticles exhibited excellent crystallinity as revealed by several strong diffraction rings, attributable to the (2 2 0), (3 1 1), (4 0 0), (4 2 2), (5 1 1) and (4 4 0) crystal planes characteristic of the face-centered cubic inverse spinel structure of magnetite (Fig. S1b) [25,26]. The successful doping of zinc ions was confirmed by energy-dispersive X-ray (EDX) analysis (Fig. S2), where the estimated amount of zinc was 1.54 wt% based on the total amount of iron and zinc (Table S1). To further support this result, the levels of zinc and iron in Zn-SPIONs were quantitatively determined by inductively coupled plasma-optical emission spectroscopy (ICP-OES) (Table S1). Notably, the resulting zinc concentration of 0.118 ppm corresponded to 1.99 wt%, which is close to the approximate value calculated from EDX analysis. The chemical formula of Zn-SPIONs calculated from ICP analysis was $Zn_{0.06}Fe_{2.94}O_4$. Taken together, such non-spherical Zn-SPIONs with narrow size distribution and remarkable crystallinity were expected to possess higher magnetic properties compared with non-doped SPIONs, boosting the competence of both MRI and MH [25,26].

Next, the hydrophobic Zn-SPIONs dispersed in chloroform were successfully phase transferred into an aqueous medium by polymer coating with the amphiphilic dodecyl-grafted poly (isobutylene-*alt*-maleic anhydride) polymer [22,23]. As determined by dynamic light scattering (DLS) analysis, water dispersible Zn-SPIONs showed a mean diameter of 24 ± 1 nm, with significant increase compared to the as-synthesized hydrophobic nanoparticles (16 ± 1 nm) (Fig. 1a). Colloidal stability was first confirmed by DLS: no significant change in hydrodynamic size of Zn-SPIONs dispersed in aqueous solution was observed over four weeks (Fig. S3).

The TEM image of polymer-coated Zn-SPIONs (Fig. 1b) revealed that each individual nanoparticle was covered by the polymer shell with no apparent aggregation. Stability of hydrophilic Zn-SPIONs in a biocompatible environment was further validated observing that these nanoparticles did not aggregate when dispersed in buffer solutions of various pH, 1 M NaCl, and DMEM medium supplemented with serum, within one week (Fig. S4). Such superior colloidal stability was also consistent with their highly negative surface charge of −70.4 ± 1.5 mV in aqueous solution as determined by zeta potential measurement, due to the presence of a large number of free carboxyl groups on the nanoparticles surface

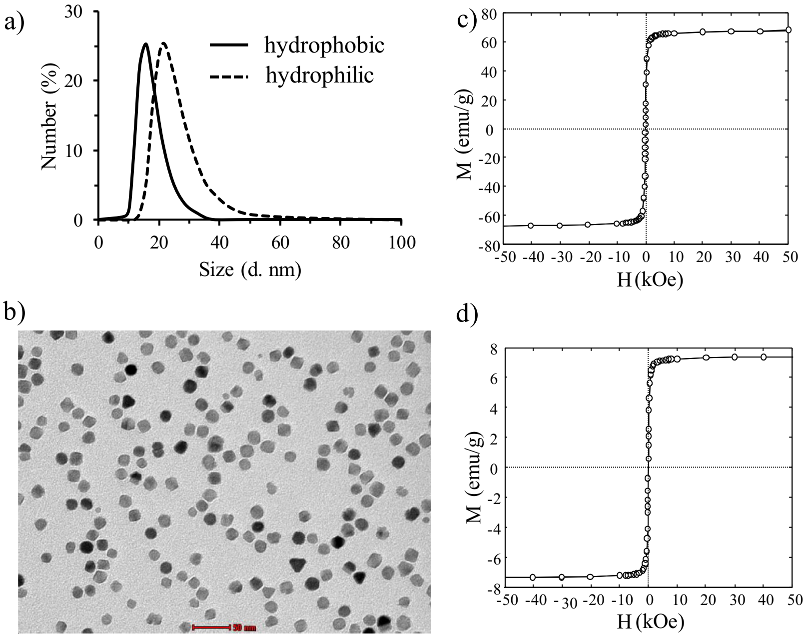

Fig. 1. (a) DLS-based sizes of hydrophobic as-synthesized Zn-SPIONs in chloroform solution and hydrophilic polymer-coated Zn-SPIONs in aqueous solution. (b) TEM image of polymer-coated Zn-SPIONs. The scale bar corresponds to 50 nm. (c, d) Field dependent magnetization curves at 300 K of as-synthesized and polymer-coated Zn-SPIONs, respectively.

(Fig. S5). Such excellent colloidal stability of polymer-coated Zn-SPIONs in a variety of biological environments is a crucial aspect for efficient biomedical applications of advanced magnetic nanoparticles.

Then, we investigated the magnetic properties of Zn-SPIONs by a superconducting quantum interference device (SQUID) magnetometer. Magnetization curves of Zn-SPIONs before and after polymer coating (Fig. 1c and 1d, respectively) exhibited superparamagnetic behavior without magnetic hysteresis at 300 K (Fig. S6). The saturation magnetization (M_s) of as-synthesized hydrophobic Zn-SPIONs was about 68 emu/g, which is larger than the M_s of undoped SPIONs of similar size obtained by thermal decomposition method [27] and similar to that of previously reported zinc-doped magnetite nanoparticles [26,28]. The enhanced magnetization observed in Zn-SPIONs is mainly attributed to their highly crystalline nature and non-spherical shape, and predominantly to the limited replacement of iron(III) ions by zinc (II) ions in the tetrahedral sites of pure SPIONs [21,25]. In addition, the M_s value was reduced to 7.4 emu/g after polymer coating. This is likely due to the presence of a large amount of polymer on the surface of the nanoparticles (i.e., contribution of polymer weight to the sample mass) [29].

The zero-field cooled (ZFC) and field-cooled (FC) magnetization further demonstrated that both Zn-SPION types were superparamagnetic at room temperature (Fig. S7). For both Zn-SPIONs, the superparamagnetic reversible regime extended down to the blocking temperature $T_B \approx 200$ K. As a measure of T_B, we used the irreversibility temperature, defined as the temperature where the ZFC and FC magnetizations differ by less than 3%. Thus, such superparamagnetic character of polymer-coated Zn-SPIONs demonstrated their capability to have high relaxivity and specific absorption rate, which will make them a potential magnetic agent for both magnetic resonance imaging and magnetic hyperthermia.

In order to evaluate the contrast enhancement abilities of polymer-coated Zn-SPIONs for MRI, the longitudinal (r_1) and transverse (r_2) relaxivities were calculated via measuring the longitudinal (T_1) and transverse (T_2) relaxation times of water protons as a function of iron molar concentration with a 0.47 T NMR relaxometer. The results demonstrated that our nanoformulations efficiently reduced both T_1 and T_2 (Fig. 2a and Fig. S8) and the calculated r_1 and r_2 values were 63.8 and 471 mM^{-1} s^{-1}, respectively. The r_2/r_1 ratio corresponded to 7.4, indicating the potential application as a T_2 contrast agent [6]. Furthermore, the observed r_2 value is larger compared to previously reported SPION-based constrast agents, including commercially available Resovist® [6,11,30]. This superior performance is presumably due to the high saturation magnetization and the unique surface chemistry of polymer-coated Zn-SPIONs [31,32,33]. These results were further supported by T_2-weighted phantom images acquired by 7.0 T MRI instrument (Fig. 2b): indeed, the phantom images became darker as a function of polymer-coated Zn-SPIONs concentration in aqueous solution and this effect was also detectable at very low iron concentrations (*e.g.*, 0.0125 mM). Overall, these findings suggested that these nanoparticles could be proposed as an effective and sensitive T_2 contrast agent for MRI purposes.

In order to evaluate the heating efficiency of polymer-coated Zn-SPIONs, the calorimetric measurements were performed at different nanoparticles weight concentrations (1–7 mg mL^{-1}) using an external alternating magnetic field. The heating profiles reported in Fig. 3a and Fig. S9 demonstrated that the solution temperature rapidly increased proportionally to the polymer-coated Zn-SPIONs concentration. Additionally, even at low concentrations (1 mg mL^{-1}), our Zn-SPIONs exhibited the capability to increase the solution temperature by 4–7 °C within 120 s exposure, which is sufficient for MH. Furthermore, the essential temperature (41–46 °C) for moderate hyperthermia was easily achieved using highly

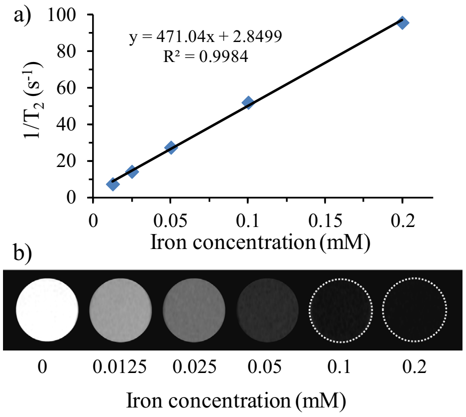

Fig. 2. (a) The analysis of T_2 relaxation rate ($1/T_2$) of aqueous solutions of polymer-coated Zn-SPIONs with different concentrations of iron from 0.0125 to 0.2 mM using 0.47 T NMR relaxometer for the measurement of transverse relaxivity (r_2). (b) T_2-weighted magnetic resonance images of aqueous solutions of polymer-coated Zn-SPIONs at various iron concentrations on 7.0 T MRI instrument, indicating higher negative contrast ability of polymer-coated Zn-SPIONs.

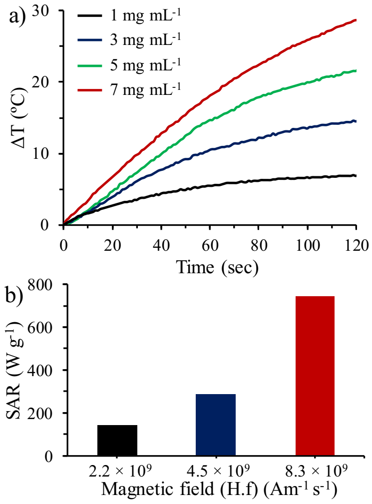

Fig. 3. (a) Time-dependent temperature curves of polymer-coated Zn-SPIONs at different nanoparticles concentrations in water in presence of an external alternating magnetic field with magnetic field strength (H) of 20 mT and frequency (f) of 522 kHz. (b) The calculated specific absorption rate (SAR) of polymer-coated Zn-SPIONs as a function of the applied magnetic field.

concentrated Zn-SPIONs solutions (*e.g.*, 7 mg mL^{-1}) in a very short time (few seconds), depending on the nanoparticle concentration and magnetic field strength (H) and frequency (f) (Fig. S10). Such an excellent hyperthermic effect was observed as a result of the superior superparamagnetic property of the highly colloidal stable non-spherical Zn-SPIONs coated with an amphiphilic polymer [2,4,21].

Besides nanoparticle concentrations, the heating capacity was demonstrated to be dependent on the properties of the magnetic field, such as its strength and frequency (Fig. S10). Then the heating efficiency of polymer-coated Zn-SPIONs was quantitatively evaluated by its specific absorption rate (SAR). Since strength and frequency of the applied magnetic field have an impact on the heating performance, different SAR values were calculated: notably, polymer-coated Zn-SPIONs displayed 141.8, 285.8 and 743.8 W g^{-1} SAR values when exposed to an external magnetic field (*H.f*) of 2.2×10^9, 4.5×10^9 and 8.3×10^9 Am^{-1} s^{-1}, respectively (Fig. 3b). This enhancement could be attributed to the additional heating contribution from hysteresis losses along with the main heating *via* Nèel and Brownian relaxations, as expected for superparamagnetic nanoparticles [20]. In addition, these SAR values were higher than the ones previously reported for most SPIONs [4,34,35], suggesting that our non-spherical Zn-SPIONs with improved heating efficiency may lower the dosage required for MH purposes.

To check the feasibility of polymer-coated Zn-SPIONs for MRI and moderate MH applications in glioblastoma, the cytotoxicity and the cellular internalization were assessed in human U-87 MG glioblastoma cell line. First, the toxic effect of polymer-coated Zn-SPIONs on cell viability was monitored by the highly sensitive colorimetric MTS assay. The cell viability was determined at 12 and 24 h upon incubation with different nanoparticles concentrations (1–100 μg mL^{-1}). The results (Fig. 4) demonstrated that after 12 h, this water dispersible Zn-SPIONs did not affect the cell viability in any of the tested concentrations, while at 24 h, a 30% *in vitro* cytotoxicity was observed only at the highest concentration. Therefore, we concluded that polymer-coated Zn-SPIONs were safe within the concentration range tested useful for MRI and MH studies in glioblastoma cancer cells.

Once established the nanoparticles biocompatibility, an ultrastructural analysis by TEM was performed to monitor the internalization and intracellular localization of polymer-coated Zn-SPIONs. After 24 h of incubation, the nanoparticles were found in cell surface invaginations as well as in endosomes and secondary lysosomes, suggesting an uptake *via* endocytic pathways (Fig. 5a). The cellular uptake was also quantitatively confirmed by ICP measurements of cell lysates: in particular, the intracellular iron level of the cells incubated with the nanoparticles was 2.3 times higher than that of untreated sample (Fig. S11).

Next, the ability of polymer-coated Zn-SPIONs to produce a negative contrast *in vitro* was demonstrated by imaging U-87 MG cells after 8 h incubation. As shown in Fig. 5b, the MRI signal detected in cancer cells treated with Zn-SPIONs at a low iron concentration (0.1 mM) was significantly different from that in the control sample. In addition, an *in vitro* MH was performed to evaluate the efficiency of these Zn-SPIONs as heat mediators. The images highlighted a more pronounced cell death effect when the cells incubated with polymer-coated Zn-SPIONs were subjected to an

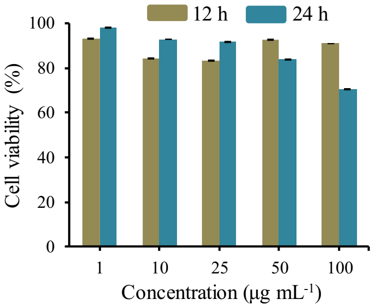

Fig. 4. Cell viability of U-87 MG cancer cells after treatment with polymer-coated Zn-SPIONs at concentrations of 1–100 μg mL^{-1} for 12 and 24 h using standard MTS colorimetric assay.

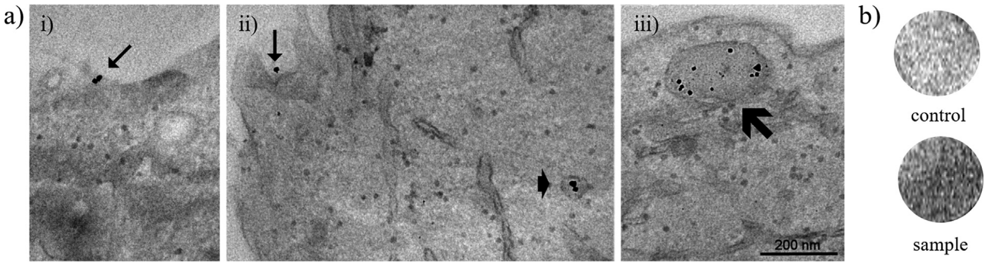

Fig. 5. (a) Transmission electron micrographs of U-87 MG cells incubated for 24 h with polymer-coated Zn-SPIONs. i) Two nanoparticles are adhering to the cell surface (arrow). ii) A nanoparticle occurs into a cell surface invagination (arrow), while two nanoparticles are enclosed in a small endosome (arrowhead). iii) A large vacuole (thick arrow), probably a secondary lysosome, contains many nanoparticles. (b) T_2-weighted magnetic resonance images of untreated U-87 MG cells (control) and U-87 MG cells treated with polymer-coated Zn-SPIONs (sample) after 8 h incubation at a concentration of 0.1 mM of iron.

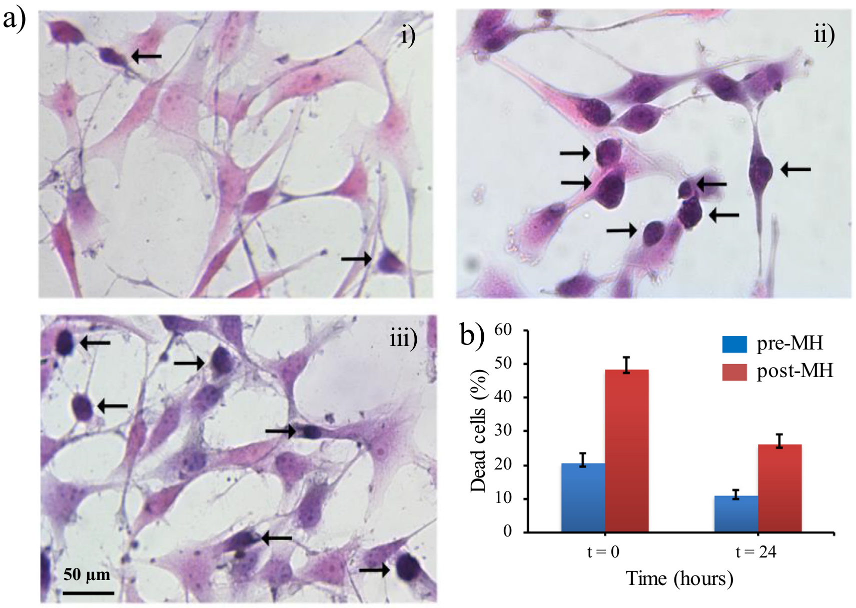

Fig. 6. (a) Light microscopy micrographs of U-87 MG cells before and after magnetic hyperthermia therapy. i) Cells incubated for 2 h with polymer-coated Zn-SPIONs and then placed in the induction coil without undergoing hyperthermia treatment (control). ii, iii) Cells incubated for 2 h with polymer-coated Zn-SPIONs, submitted to hyperthermia and observed immediately (i.e., t = 0) (ii) or after 24 h (i.e., t = 24) (iii) from the treatment. Arrows show dead cells. (b) Quantitative evaluation of dead cells in samples shown in (a). Samples (a, ii) and (a, iii) show a significantly higher values in comparison to sample (a, i) (P less than 0.001 for both).

alternating magnetic field below the biological safe level of 5×10^9 Am^{-1} s^{-1} as shown in Fig. 6a (ii and iii) in comparison with the unexposed sample as represented in Fig. 6a (i). Fig. 6b demonstrates that the percentage of dead cells was significantly higher in samples submitted to nanoparticles treatment and subsequent hyperthermia in comparison to the samples undergoing nanoparticles internalisation without hyperthermic treatment.

Taken together, the efficient cellular internalization as well as the maintenance of heating and contrast enhancement capabilities demonstrated the suitability of Zn-SPIONs for theranostic purposes. Furthermore, the improved magnetic properties of these biocompatible polymer-coated Zn-SPIONs are expected to substantially lower the dosage required for the identification and treatment of glioblastoma and thus their side-effects. Therefore, in comparison to other previously reported doped iron oxide nanoparticles utilized for MRI and MH applications, our polymer-coated Zn-SPIONs should be an efficient theranostic agent for cancer diagnosis and treatment (Table S2). In addition, the efficiency and selectivity of these unique nanoparticles can be further improved by exploiting exposed carboxyl groups to decorate the nanoparticles surface with several biomolecules (such as peptides and antibodies).

4. Conclusions

In summary, we successfully prepared highly crystalline and non-spherical Zn-SPIONs with an average core diameter of 15 nm and narrow size distribution *via* high-temperature thermal decomposition method. These hydrophobic Zn-SPIONs were then coated with an amphiphilic polymer to make highly colloidal stable water dispersible nanoparticles. The superparamagnetic character of these polymer-coated Zn-SPIONs of 24 nm average hydrodynamic size was further investigated: in particular, a high T_2 relaxivity of 471 mM^{-1} s^{-1} and a SAR value up to 743.8 W g^{-1} demonstrated the superior physical properties of Zn-SPIONs in comparison to most previously reported SPIONs [4,6,34,36] and thus the potential of these nanoparticles as an efficient MRI contrast agent and heating mediator in MH. This contrast enhancer was able to generate darker T_2-weighted images of glioblastoma U-87 MG cells even at low iron concentration, supporting their potential to improve the sensitivity of MRI analysis in future *in vivo* application. In addition, the produced heat from Zn-SPIONs-labeled U-87 MG cells efficiently killed cancer cells when exposed to an alternating magnetic field in the biological safe range. In conclusion, this nanosystem could be proposed as a valid tool for cancer theranostics, especially for glioblastoma. The coating polymer confers the additional advantage of allowing straightforward functionalization with targeting ligands and drug conjugation, which could allow combination therapy. Future directions will explore the impact of the bioconjugation with active targeting ligands on the nanoparticle performance.

CRediT authorship contribution statement

Pradip Das: Data curation, Formal analysis, Investigation, Methodology, Writing - original draft, Writing - review & editing. **Lucia Salvioni:** Data curation, Writing - review & editing. **Manuela Malatesta:** Formal analysis, Investigation, Visualization. **Federica Vurro:** Formal analysis, Investigation, Validation. **Silvia Mannucci:** Formal analysis, Investigation. **Marco Gerosa:** Formal analysis, Investigation. **Maria Antonietta Rizzuto:** Data curation, Formal analysis, Validation. **Chiara Tullio:** Data curation, Formal analysis. **Anna Degrassi:** Data curation, Formal analysis, Validation, Writing - original draft. **Miriam Colombo:** Conceptualization, Supervision, Validation, Funding acquisition. **Anna M. Ferretti:** Data curation, Investigation. **Alessandro Ponti:** Conceptualization, Supervision, Methodology, Validation, Writing - original draft, Writing - review & editing, Funding acquisition. **Laura Calderan:** Conceptualization, Supervision, Methodology, Validation, Writing - original draft. **Davide Prosperi:** Conceptualization, Funding acquisition, Methodology, Project administration, Resources, Supervision, Writing - original draft, Writing - review & editing.

Declaration of Competing Interest

The authors declare that they have no known competing financial interests or personal relationships that could have appeared to influence the work reported in this paper.

Acknowledgements

This work was supported by Direzione Generale Ricerca, Innovazione, Università, Export e Internazionalizzazione of the Regione Lombardia. Financial support from the Italian Ministry of University and Research (MIUR) through grant "Dipartimenti di Eccellenza-2017" is gratefully acknowledged. This activity has received funding from the European Institute of Innovation and Technology (EIT). This body of the European Union receives support from the European Union's Horizon 2020 research and innovation programme. (KIC Magnetometry Network, Project Agreement n. 16207).

Appendix A. Supplementary data

Supplementary data to this article can be found online at https://doi.org/10.1016/j.jcis.2020.05.119.

References

[1] W. Wu, C.Z. Jiang, V.A.L. Roy, Designed synthesis and surface engineering strategies of magnetic iron oxide nanoparticles for biomedical applications, Nanoscale 8 (2016) 19421–19474.

[2] J. Kudr, Y. Haddad, L. Richtera, Z. Heger, M. Cernak, V. Adam, O. Zitka, Magnetic nanoparticles: From design and synthesis to real world applications, Nanomaterials 7 (2017) 243.

[3] N. Lee, D. Yoo, D. Ling, M.H. Cho, T. Hyeon, J. Cheon, Iron oxide based nanoparticles for multimodal imaging and magnetoresponsive therapy, Chem. Rev. 115 (2015) 10637–10689.

[4] P. Das, M. Colombo, D. Prosperi, Recent advances in magnetic fluid hyperthermia for cancer therapy, Colloids Surf, B 174 (2019) 42–55.

[5] B.T. Mai, S. Fernandes, P.B. Balakrishnan, T. Pellegrino, Nanosystems based on magnetic nanoparticles and thermo- or pH responsive polymers: An update and future perspectives, Acc. Chem. Res. 51 (2018) 999–1013.

[6] Z. Shen, A. Wu, X. Chen, Iron oxide nanoparticle based contrast agents for magnetic resonance imaging, Mol. Pharmaceutics 14 (2017) 1352–1364.

[7] M.J. Sands, A. Levitin, Basics of magnetic resonance imaging, Semin. Vasc. Surg. 17 (2004) 66–82.

[8] V.P.B. Grover, J.M. Tognarelli, M.M.E. Crossey, I.J. Cox, S.D. Taylor-Robinson, M.J. W. McPhail, Magnetic resonance imaging: Principles and techniques: Lessons for clinicians, J. Clin. Exp. Hepatol. 5 (2015) 246–255.

[9] H. Shokrollahi, Contrast agents for MRI, Mater. Sci. Eng. C 33 (2013) 4485–4497.

[10] Y.X.J. Wang, Current status of superparamagnetic iron oxide contrast agents for liver magnetic resonance imaging, World J. Gastroenterol. 21 (2015) 13400–13402.

[11] N. Lee, H. Kim, S.H. Choi, M. Park, D. Kim, H.C. Kim, Y. Choi, S. Lin, B.H. Kim, H.S. Jung, H. Kim, K.S. Park, W.K. Moon, T. Hyeon, Magnetosome-like ferrimagnetic iron oxide nanocubes for highly sensitive MRI of single cells and transplanted pancreatic islets, Proc. Natl. Acad. Sci. U. S. A. 108 (2011) 2662–2667.

[12] A. Hervault, N.T.K. Thanh, Magnetic nanoparticle-based therapeutic agents for thermo-chemotherapy treatment of cancer, Nanoscale 6 (2014) 11553–11573.

[13] Q. Zhang, I. Castellanos-Rubio, R. Munshi, I. Orue, B. Pelaz, K.I. Gries, W.J. Parak, P.D. Pino, A. Pralle, Model driven optimization of magnetic anisotropy of exchange-coupled core-shell ferrite nanoparticles for maximal hysteretic loss, Chem. Mater. 27 (2015) 7380–7387.

[14] K. Mahmoudi, A. Bouras, D. Bozec, R. Ivkov, C. Hadjipanayis, Magnetic hyperthermia therapy for the treatment of glioblastoma: A review of the therapy's history, efficacy and application in humans, Int. J. Hyperthermia 34 (2018) 1316–1328.

[15] D. Chang, M. Lim, J.A.C.M. Goos, R. Qiao, Y.Y. Ng, F.M. Mansfeld, M. Jackson, T.P. Davis, M. Kavallaris, Biologically targeted magnetic hyperthermia: Potential and limitations, Front. Pharmacol. 9 (2018) 831.

[16] C. Guibert, V. Dupuis, V. Peyre, J. Fresnais, Hyperthermia of magnetic nanoparticles: Experimental study of the role of aggregation, J. Phys. Chem. C 119 (2015) 28148–28154.

[17] M. Albino, E. Fantechi, C. Innocenti, A. López-Ortega, V. Bonanni, G. Campo, F. Pineider, M. Gurioli, P. Arosio, T. Orlando, G. Bertoni, C. de Julián Fernández, A. Lascialfari, C. Sangregorio, Role of Zn^{2+} substitution on the magnetic, hyperthermic, and relaxometric properties of cobalt ferrite nanoparticles, J. Phys. Chem. C 123 (2019) 6148–6157.

[18] V. Mameli, A. Musinu, A. Ardu, G. Ennas, D. Peddis, D. Niznansky, C. Sangregorio, C. Innocenti, N.T.K. Thanh, C. Cannas, Studying the effect of Zn-substitution on the magnetic and hyperthermic properties of cobalt ferrite nanoparticles, Nanoscale 8 (2016) 10124–10137.

[19] S. Noh, S.H. Moon, T.H. Shin, Y. Lim, J. Cheon, Recent advances of magneto-thermal capabilities of nanoparticles: From design principles to biomedical applications, Nano Today 13 (2017) 61–76.

[20] E.C. Abenojar, S. Wickramasinghe, J. Bas-Concepcion, A.C.S. Samia, Structural effects on the magnetic hyperthermia properties of iron oxide nanoparticles, Prog. Nat. Sci. : Mater. Int. 26 (2016) 440–448.

[21] J. Jang, H. Nah, J.H. Lee, S.H. Moon, M.G. Kim, J. Cheon, Critical enhancements of MRI contrast and hyperthermic effects by dopant-controlled magnetic nanoparticles, Angew. Chem., Int. Ed. 48 (2009) 1234–1238.

[22] C.A.J. Lin, R.A. Sperling, J.K. Li, T.Y. Yang, P.Y. Li, M. Zanella, W.H. Chang, W.J. Parak, Design of an amphiphilic polymer for nanoparticle coating and functionalization, Small 4 (2008) 334–341.

[23] L. Fiandra, S. Mazzucchelli, C.D. Palma, M. Colombo, R. Allevi, S. Sommaruga, E. Clementi, M. Bellini, D. Prosperi, F. Corsi, Assessing the in vivo targeting efficiency of multifunctional nanoconstructs bearing antibody-derived ligands, ACS Nano 7 (2013) 6092–6102.

[24] M. Costanzo, M. Malatesta, Embedding cell monolayers to investigate nanoparticle-plasmalemma interactions at transmission electron microscopy, Eur. J. Histochem. 63 (2019) 3026.

[25] S. Noh, W. Na, J. Jang, J.H. Lee, E.J. Lee, S.H. Moon, Y. Lim, J.S. Shin, J. Cheon, Nanoscale magnetism control via surface and exchange anisotropy for optimized ferrimagnetic hysteresis, Nano Lett. 12 (2012) 3716–3721.

[26] J. Liu, Y. Bin, M. Matsuo, Magnetic behavior of Zn-doped Fe_3O_4 nanoparticles estimated in terms of crystal domain size, J. Phys. Chem. C 116 (2012) 134–143.

[27] W. Li, S.S. Lee, J. Wu, C.H. Hinton, J.D. Fortner, Shape and size controlled synthesis of uniform iron oxide nanocrystals through new non-hydrolytic routes, Nanotechnology 27 (2016) 324002.

[28] J.M. Byrne, V.S. Coker, E. Cespedes, P.L. Wincott, D.J. Vaughan, R.A.D. Pattrick, G. van der Laan, E. Arenholz, F. Tuna, M. Bencsik, J.R. Lloyd, N.D. Telling, Biosynthesis of zinc substituted magnetite nanoparticles with enhanced magnetic properties, Adv. Funct. Mater. 24 (2014) 2518–2529.

[29] M. Khalkhali, K. Rostamizadeh, S. Sadighian, F. Khoeini, M. Naghibi, M. Hamidi, The impact of polymer coatings on magnetite nanoparticles performance as MRI contrast agents: a comparative study, DARU J. Pharm. Sci. 23 (2015) 45.

[30] N. Lee, T. Hyeon, Designed synthesis of uniformly sized iron oxide nanoparticles for efficient magnetic resonance imaging contrast agents, Chem. Soc. Rev. 41 (2012) 2575–2589.

[31] G. Huang, H. Li, J. Chen, Z. Zhao, L. Yang, X. Chi, Z. Chen, X. Wang, J. Gao, Tunable $_T1$ and $_T2$ contrast abilities of manganese-engineered iron oxide nanoparticles through size control, Nanoscale 6 (2014) 10404–10412.

[32] J.C. Park, G.T. Lee, H.K. Kim, B. Sung, Y. Lee, M. Kim, Y. Chang, J.H. Seo, Surface design of Eu-doped iron oxide nanoparticles for tuning the magnetic relaxivity, ACS Appl. Mater. Interfaces 10 (2018) 25080–25089.

[33] U.I. Tromsdorf, N.C. Bigall, M.G. Kaul, O.T. Bruns, M.S. Nikolic, B. Mollwitz, R.A. Sperling, R. Reimer, H. Hohenberg, W.J. Parak, S. Fo1rster, U. Beisiegel, G. Adam, H. Weller, Size and surface effects on the MRI relaxivity of manganese ferrite nanoparticle contrast agents, Nano Lett. 7 (2007) 2422–2427.

[34] M.R. Marinozzi, L. Pandolfi, M. Malatesta, M. Colombo, V. Collico, P.M.J. Lievens, S. Tambalo, C. Lasconi, F. Vurro, F. Boschi, S. Mannucci, A. Sbarbati, D. Prosperi, L. Calderan, Innovative approach to safely induce controlled lipolysis by superparamagnetic iron oxide nanoparticles-mediated hyperthermic treatment, Int. J. Biochem. Cell Biol. 93 (2017) 62–73.

[35] M. Singh, R. Ramanathan, E.L.H. Mayes, S. Masková, P. Svoboda, V. Bansal, One-pot synthesis of maghemite nanocrystals across aqueous and organic solvents for magnetic hyperthermia, Appl. Mater. Today 12 (2018) 250–259.

[36] Z. Li, X. Ma, Y. Xia, K. Qian, O.U. Akakuru, L. Luo, J. Zheng, P. Cui, Z. Shen, A. Wu, A pH-sensitive polymer based precise tumor targeting strategy with reduced uptake of nanoparticles by non-cancerous cells, J. Mater. Chem. B 7 (2019) 5983–5991.

nanomaterials

MDPI

Article

Porous Si Microparticles Infiltrated with Magnetic Nanospheres

Elena Chistè [1], Gloria Ischia [2], Marco Gerosa [3], Pasquina Marzola [3], Marina Scarpa [4] and Nicola Daldosso [1,*]

[1] Department of Computer Science, Fluorescence Laboratory, University of Verona, 37134 Verona, Italy; elena.chiste@univr.it
[2] Department of Industrial Engineering, University of Trento, 38123 Trento, Italy; gloria.ischia@unitn.it;
[3] Department of Morphological-Biomedical Sciences, Section of Anatomy and Histology, University of Verona, 37134 Verona, Italy; marco.gerosa@univr.it (M.G.); pasquina.marzola@univr.it (P.M.)
[4] Department of Physics, Laboratory of Nanoscience, University of Trento, 38123 Trento, Italy; marina.scarpa@unitn.it
* Correspondence: nicola.daldosso@univr.it

Received: 29 February 2020; Accepted: 3 March 2020; Published: 4 March 2020

Abstract: Porous silicon (pSi) microparticles obtained by porosification of crystalline silicon wafers have unique optical properties that, together with biodegradability, biocompatibility and absence of immunogenicity, are fundamental characteristics to candidate them as tracers in optical imaging techniques and as drug carriers. In this work, we focus on the possibility to track down the pSi microparticles also by MRI (magnetic resonance imaging), thus realizing a comprehensive tool for theranostic applications, i.e., the combination of therapy and diagnostics. We have developed and tested an easy, quick and low-cost protocol to infiltrate the COOH-functionalized pSi microparticles pores (tens of nanometers about) with magnetic nanospheres (SPIONs—Super Paramagnetic Iron Oxide Nanoparticles, about 5–7 nm) and allow an electrostatic interaction. The structural properties and the elemental composition were investigated by electron microscopy techniques coupled to elemental analysis to demonstrate the effective attachment of the SPIONs along the pores' surface of the pSi microparticles. The magnetic properties were investigated under an external magnetic field to determine the relaxivity properties of the material and resulting in an alteration of the relaxivity of water due to the SPIONs presence, clearly demonstrating the effectiveness of the easy functionalization protocol proposed.

Keywords: porous silicon microparticles; Super Paramagnetic Iron Oxide Nanoparticles (SPIONs); electron microscopy; MRI; theranostics

1. Introduction

Porous silicon (pSi) is a sponge-like material photoluminescent at room temperature. [1] Its distinctive properties make this material a promising tool for theranostics, i.e., the union of therapy and diagnostics. [2] In fact, it is biocompatible: [3] it degrades into silicic acids that kidneys are able to secrete, and it is neither toxic for the cells nor activator of the immune system. It could be exploited as bioimaging tracer in-vitro and in-vivo, due to its photoluminescence, [4,5] as carrier for drug loading and release, due to its porosity with large surface to volume ratio, [6,7] or as PTT (photothermal therapy) [8] or PDT (photodynamic therapy) [9] agent. Porous silicon is produced from crystalline silicon by a cheap and simple fabrication process, i.e., electrochemical etching in acid solution, resulting in pSi microparticles with photoluminescence (PL) in the orange-red portion of the visible spectrum [10,11] due to the quantum confinement effect. [12] The electrochemical etching produces pores on the silicon wafer surface, whose dimensions are adjustable with the etching parameters: in our optimized procedure, the pores are around 20–30 nm. [13] A hydrosilylation procedure (leading to a surface terminated with carboxyl-groups, which are negatively charged at pH > 4) is sufficient to stabilize the pSi microparticles for years in ethanol. [13] To homogenize the microparticles dimension and to reduce and manage their average size, we recently established a simple post-synthesis procedure, based on ultrasounds, without affecting the optical properties. [14]

One of the main concerns about the acceptance of this material in theranostics was the fast PL quenching in biological media. To overcome this issue, the pSi microparticles surface has been coated either with organic polymer (e.g., PEG or chitosan) by covalent attachment [15] or with inorganic atomic layer deposition (ALD) of TiO_2 resulting in a shell with tunable thickness. [16] This allows the stabilization of the material and of its optical properties for several months. The functionalized microparticles were shown to be effective carriers of model drugs. [15]

The aim of the present work is to investigate the possibility of adding magnetic properties to the pSi microparticles to be traced by MRI (magnetic resonance imaging). MRI is a versatile and informative diagnostic technique, since the contrast in MRI is multifactorial, depending not only on proton density but also on T_1 and T_2 relaxation rates and flow. [17] Nanoparticles (NPs) with magnetic properties are widely used to further increase this contrast and therefore improve the biomedical diagnosis. [18,19] For magnetic NPs exploitation in theranostics, the magnetic remanence should vanish once the external magnetic field is switched off: that is one of the main reasons because, among all the magnetic NPs employed in MRI, SPIONs (SuperParamagnetic Iron Oxide Nanoparticles) are the most promising. [20,21] In fact, they are able to substantially modify the relaxation time of the interacting water molecules and are therefore used as contrast agents. [22,23] In particular, they belong to the class of negative contrast agents, meaning that they affect preferentially the transversal relaxation time T_2 and consequently darken the MR image thus increasing the contrast between tissues. Furthermore, SPIONs biocompatibility [17] and the toxicity testing in animals [24] supports their use in biomedical applications.

Within this paper, we explored the possibility to fill the pores and decorate the pSi microparticles porous surface by magnetite (Fe_3O_4) nanoparticles with a dimension of few nm, with the goal of easily infiltrating the porous structure and favoring electrostatic attachment at the pSi surface.

Few studies were previously reported about SPIONs infiltrated within the pores of porous silicon [25] or mesoporous silica nanoparticles. [26] In the former, the pSi microparticles were placed in an aqueous solution of magnetic NPs, which were infused inside the porous structure and embedded by a thermal oxidation/dehydration procedure, which is anyway long and requires special ovens. The magnetic pSi microparticles are drug loaded and delivered under the guidance of a magnetic field. In the latter, the magnetite NPs were anchored on the mesoporous silica nanoparticles by a boronate esters linker, to produce a pH-responsive tool for targeted delivery to low pH tissues.

The structural and magnetic results of this experimental work clearly show that, by means of an easy (just chemical mixing in a simple bucket), fast (only few minutes) and cheap (very inexpensive reagents: less than 80 euro-cents per mg) chemical protocol, based on the use of cyclohexane diamine (a small molecule that bears two positively charged groups) without the need of any oxidation steps, it is possible to get luminescent pSi microparticles infiltrated with SPIONs, which could be loaded in large quantity and electrostatically attached to the surface of the functionalized pSi pores. The absence of covalent binding enables a possible separation of the magnetic nanoparticles from the porous matrix for further MRI applications. Moreover, contrary to other procedures, it avoids the embedding of the SPIONs within a coating layer on the Si surface, thus opening the possibility of further molecular targeting. The use of the porous silicon matrix as a carrier for the SPIONs prevent the need of polymer's shielding, [27] in perspective of in-vivo tests, and protect them from being cleaved in the circulation. In addition to that, in our approach, the photoluminescence of the functionalized pSi infiltrate with SPIONs is completely maintained.

2. Materials and Methods

Porous silicon samples have been fabricated according to the procedure already assessed in our laboratory, [13] which is briefly summarized in the following.

2.1. pSi Fabrication and Carboxyl Functionalization

The porosification of boron-doped p-type Si wafers (<100> oriented, 10–20 Ω·cm resistivity, University wafers, Boston, MA, USA) was obtained by electrochemical etching at constant current (80 mA·cm^{-2}) in ethanol: HF (16%) solution in a PTFE cell for 15 minutes. The pSi layer was removed from the wafer, dispersed in toluene and was fragmented into microparticles by 20 min sonication in a thermal bath. At the end of this procedure, microparticles with pore size about 20–30 nm, bearing Si-H groups on the surface are produced. [28] Light-driven hydrosilylation by acrylic acid in toluene at 50 °C under mild stirring (two hours) has been performed to introduce COOH groups at the porous surface. The obtained solution was washed (10 min centrifugation and removal of the supernatant) several times in ethanol and stored in this solvent. After this step, the microparticles bear COOH groups on the external surface and inside the pores, as previously proved by titled angle XPS. [29] However, some oxidation occurs and some SiO_x groups are present as shown by FTIR spectra. [28]

SPIONs (Super Paramagnetic Iron Oxide—Fe_3O_4—Nanoparticles) were purchased from Sigma-Aldrich, St. Louis, MO, USA (concentration: 5 mg·mL^{-1} in water, magnetization > 25 emu·g^{-1} at 4500 Oe, average particle size: 5–7 nm) and diluted in PBS to perform the experiments. We chose phosphate-buffered saline (PBS, pH 7.4) as a solvent in perspective of in-vitro tests. For the SPIONs functionalization (see in the following), the (±)-trans-1,2-Diaminocyclohexane (8.3 M) was purchased from Sigma-Aldrich (St. Louis, MO, USA).

2.2. Samples Characterization

The structural and magnetic properties of the samples were studied by DLS (Dynamic Light Scattering), S/TEM (Scanning/Transmission Electron Microscopy) coupled to EDS (Energy Dispersive X-ray Spectroscopy) and MRI (Magnetic Resonance Imaging) measurements.

The surface charge (ζ-potential) of SPIONs and their size distribution, before and after diamine addition, was determined by Zetasizer Nano-SZ (Malvern) instrument, by dynamic light scattering (DLS) with a 633 nm laser beam. The measurements were performed at 25 °C after the dispersion of the SPIONs in PBS, pH 7.4, and 5 min of sonication in a thermal bath.

TEM (Transmission electron microscopy) analysis was performed with an S/TEM ThermoFisher Talos F200S operating at 200 kV. The microscope is equipped with an integrated EDS (Energy Dispersive X-rays Spectroscopy) system with two windowless silicon drift detectors (SDD). The samples were observed in both TEM and STEM mode in order to investigate the SPIONs average size and the possible interaction between the magnetic nanoparticles and the pSi microparticles. Moreover, the STEM mode allows evaluating the actual elemental distribution in the sample collecting EDS maps. To support the samples during the observation, a 50 mL drop of this solution (in PBS and then water) was deposited on TEM copper support grids covered by a holey amorphous carbon film.

The magnetic properties were investigated by using a Pharmascan system operating at 7 T (Bruker, Germany). The longitudinal, T_1, and transversal, T_2, relaxation times were measured by acquiring an MSME (multi-spin multi-echo) pulse sequence. It consists of a 90° excitation RF pulse, followed by repeated 180° refocusing pulses, separated by a constant interval or echo-time. The signals coming from each point of the images were mediated to obtain the relaxation curve decays, that were fitted with an exponential decay function to obtain the T_1 and T_2 values. Afterwards, the longitudinal and transversal relaxivities r_1 and r_2 were determined by varying the sample concentration. The values obtained for the pSi-SPIONs sample were compared to the relaxivity of SPIONs and that of pSi-COOH microparticles alone.

2.3. SPIONs Infiltration within the pSi-COOH Microparticles

The key step of the sample preparation was the decoration of pSi-COOH microparticles with the purchased iron oxide nanoparticles (SPIONs). We infiltrated them into the pores and covered the pSi surface with the NPs by electrostatic interaction. Since both the materials are negatively charged, we functionalized the SPIONs surface with a molecule bearing positively charged groups to favor the attachment of the nanoparticles onto the porous surface of the microparticles. The scheme of the sample preparation is reported in Figure S1, in the ESI.

We chose a diamine ((±)-trans-1,2-Diaminocyclohexane) to functionalize the iron oxide nanoparticles to let them become positively charged. The diamine was protonated by the addition of HCl to let the terminal amino group (NH_2) become positive (NH_3^+). Then, the cyclohexane diamine was added to the magnetic nanospheres (0.2 $mg\cdot mL^{-1}$) in PBS and the NPs dimension and surface charge were adjusted by varying the diamine concentration from 0.3 M to 2 M. Thus, the diamine-functionalized SPIONs were incubated with 0.6 $mg\cdot mL^{-1}$ pSi-COOH microparticles. SPIONs decorated pSi microparticles (labelled as pSi-SPIONs microparticles) were re-dispersed in water: the sample was centrifuged, the surnatant was removed and then refilled with fresh water several times. This step was also important to assess if the nanoparticles were or not attached to the pSi microparticles.

3. Results and Discussion

3.1. SPIONs Characterization and Functionalization

The structural properties of magnetite nanoparticles (SPIONs) were analyzed by TEM and DLS techniques to obtain the real average size and the size distribution. Figure 1a shows a characteristic TEM image of the SPIONs in water and Figure 1b the comparison between the size distributions obtained by TEM and DLS techniques.

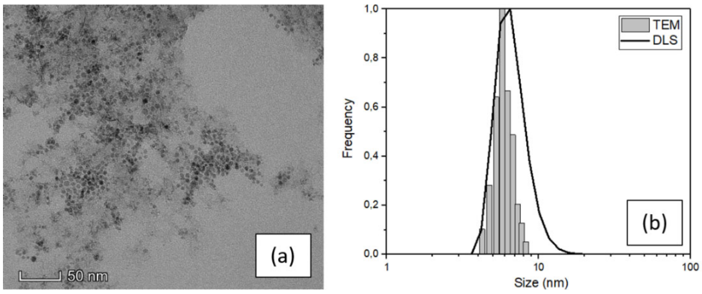

Figure 1. (**a**) TEM image and (**b**) size distribution of SPIONs dispersed in water obtained by TEM and DLS.

The SPIONs particles showed in the TEM image (Figure 1) feature spherical shape and narrow distribution of dimension highly less than 10 nm in diameter. A high-resolution image of a single particle is reported in the ESI (Figure S2a) with the diffraction pattern relative to the agglomerate of Figure 1a, which demonstrates that the nanoparticles are composed of magnetite. [30] An evaluation of their dimension was carried out using ImageJ software and processing a fair number of TEM images. The result of this analysis leads to an average value of (6 ± 2) nm (see the histogram in Figure 1b) which is consistent with the nominal value of the purchased NPs and confirm the narrow size distribution. The average SPIONs size was also investigated by DLS, with an average value of (7 ± 3) nm which is consistent with the TEM result, although slightly overestimated because the DLS measurement is performed in liquid and gives an estimation of the hydrodynamic diameter. [31]

Then, the surface charge (i.e., ζ-potential value) was determined by DLS measurement and the surface charge distribution of the purchased SPIONs was found to be very broad and peaked at about −25–30 mV (see Figure S3a in ESI), in contrast with the declared neutral charge of the purchased magnetic nanospheres. Since the pSi microparticles are negatively charged too, they would repulse the SPIONs. Hence, we studied and validated a simple chemical procedure to make them positive: a functionalization with cyclohexane diamine molecules as described in detail in the experimental section. We investigated the effect of different cyclohexane diamine concentration on the ζ-potential value (see Figure S3 in ESI) and on the average size distribution (Figure 2) of the functionalized SPIONs (namely sample SPIONs_A, SPIONs_B and SPIONs_C) as the cyclohexane diamine is 0.3 M, 1 M and 2 M, respectively.

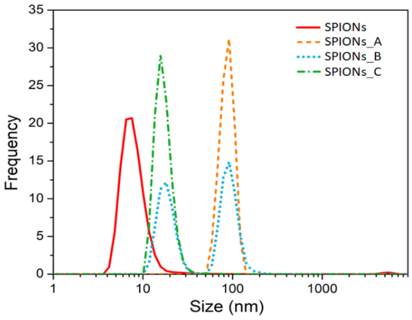

Figure 2. Size distribution obtained by DLS technique of diluted SPIONs and after the functionalization with increasing cyclohexane diamine concentration. Each distribution is the average of three measurements.

After the addition of the protonated cyclohexane diamine to SPIONs, we realized that the size distribution (orange dashed line of Figure 2) was surprisingly centered at about 100 nm. This is due to the agglomeration of the SPIONs because of an almost equal amount of both positive and negative charged SPIONs. In fact, a broad and peaked charge distribution has been found (see Figure S3 in the ESI) suggesting that only a partial functionalization was achieved for such a concentration of cyclohexane diamine.

To avoid the agglomeration and to increase the amount of positively charged SPIONs, we increased the ratio between protonated cyclohexane diamines and SPIONs, first by a factor three (sample SPIONs_B) and we obtained a size distribution with two populations (see blue dotted line in Figure 2): one peak is still centered at about 100 nm and it is related to the agglomerated particles, the other peak is at about 20 nm and it is related to the positively charged SPIONs. Thus, we further increase the ratio of cyclohexane diamine to SPIONs up to 10 mmol/mg (see green line in Figure 2) thus decreasing the average size distribution up to (18 ± 3) nm.

These results are in line with the ζ–potential results that clearly show that SPIONs_C has a positive surface charge (see panel (c) of Figure S3 in the ESI).

With these experimental findings, we set up a protocol to get positively charged SPIONs to the pSi-COOH microparticles, whose morphology and porosity have been carefully characterized in previously published works. [14,28] The resulting sample (namely pSi-SPIONs microparticles) was dispersed in PBS.

3.2. pSi-SPIONs Structural Properties

To verify that functionalized SPIONs were effectively infiltrated onto the pSi microparticles, we performed TEM analysis: the results are reported in Figure 3.

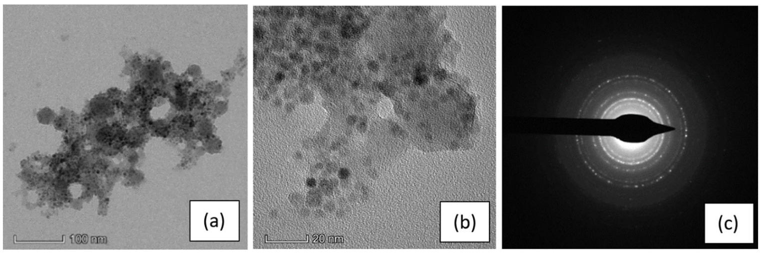

Figure 3. TEM images of a pSi microparticle after SPIONs infiltration at: (**a**) 100 nm scale and (**b**) 20 nm scale; (**c**) the SAED (selected area electron diffraction) pattern indexed as magnetite (PDF card 82–1533).

Figure 3a shows a pSi microparticle, with its porous structure and a size of about 400 nm, whose surface is covered by SPIONs (dark dots in the picture), clearly on the porous structure. Their presence is even more evident in the magnified image (panel b) and evidenced by the diffraction pattern generated from the SPIONs (panel c). The ring pattern is consistent with the SPIONs dimensions and indicates a random orientation of the Fe_3O_4 nanocrystal. It is worth noting that the diffraction pattern of Si crystallites, produced from electrochemical etching, is hardly detectable, due to their random orientation and their very small dimension, with a large amount of voids. [32]

The presence of the SPIONs onto the pSi microparticles was also confirmed by EDS elemental analysis (see Figure S4 in the ESI) performed on the microparticle showed in panel (a) of Figure 3, indeed, the EDS spectrum exhibit the peaks relative to the characteristic elements of SPIONs and pSi microparticles.

The TEM observations were repeated after the re-dispersion in water and a comparison between the two solvents, PBS and water, is reported in Figure 4.

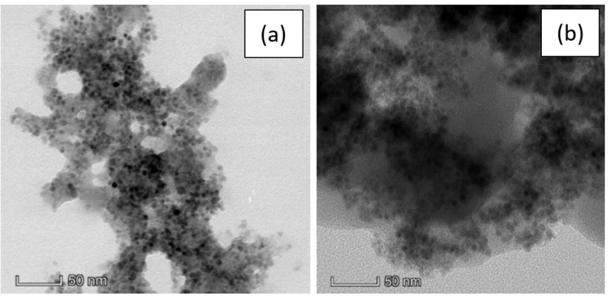

Figure 4. TEM images of a pSi microparticle after SPIONs decoration at 50 nm scale in: (**a**) PBS; (**b**) water.

Here we can observe no substantial difference between the pSi-SPIONs microparticles in PBS (Figure 4a) or water (Figure 4b). The morphology is not modified by the re-dispersion, but the PBS buffer gives more contrast to the image and, consequently, the SPIONs are more visible.

The surnatant obtained from the washing to re-disperse the sample in water was collected and probed by TEM and no SPIONs have been observed at all similarly to DLS investigation of the surnatant. This suggests that almost the totality of the functionalized SPIONs is infiltrated and electrostatically attached to the porous surface meaning even after several centrifugations and washing cycles (see Figure 5a). Besides the structural and morphological analysis, we also performed the EDS characterization of the supernatant without observing any peaks related to neither Fe_3O_4 nor porous silicon (see Figure 5b).

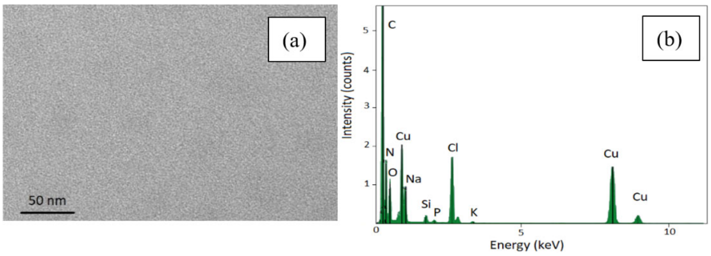

Figure 5. TEM image of the supernatant removed after centrifugation (panel **a**) and its EDS spectrum (panel **b**).

The sample was observed also in STEM mode, in which a focalized electron beam is scanned on the sample surface allowing to combine morphological investigation with EDS mapping. It is a powerful technique to investigate the actual elemental distribution inside the material with high spatial resolution. The results of STEM analysis are reported in Figure 6e and Figure 7.

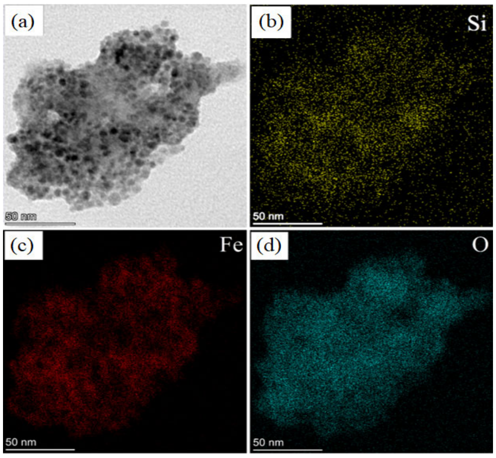

Figure 6. STEM (BF) images of: (**a**) a pSi microparticle after SPIONs decoration at 50 nm scale; elemental mapping of: (**b**) Si; (**c**) Fe; (**d**) O.

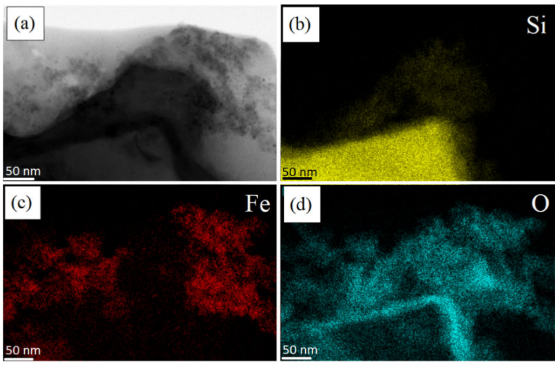

Figure 7. STEM images of: (**a**) a non-porous pSi microparticle after SPIONs decoration at 50 nm scale; elemental mapping of: (**b**) Si; (**c**) Fe; (**d**) O.

Figure 6 shows the comparison between STEM Bright Field (BF) image (panel a) and elemental maps of Si (panel b), Fe (panel c) and O (panel d). This is very convenient to understand if the SPIONs are on the porous surface: we observed a quite perfect overlap between the distribution of Si (panel b), Fe (panel c) and O atoms (panel d).

On the other hand, we performed STEM maps on a fragment of non-porous silicon, see the portion of the triangle at the bottom of Figure 7a: it shows a flat surface and homogeneous intensity. The small piece of crystalline silicon is characterized by a more compact structure (see the Si "yellow dots" in panel b with respect to those of Figure 6b) and its border is covered by a SiO_2 layer, i.e., the cyan line clearly visible in panel (d).

As it can be observed, in this case, the SPIONs do not attach onto silicon, due to the absence of porosity and proper surface functionalization due to previous surface oxidation. In fact, the positions of Fe atoms (panel c) and Si atoms (panel b) are not superimposable, meaning that the binding between nonporous silicon and SPIONs was not possible. In this case, a cloud of SPIONs (Fe and O atoms) are accumulated at the right top of the images, not at the non-porous Si surface.

3.3. pSi-SPIONs Magnetic Properties

After having proved the effectiveness of the functionalization protocol and of the infiltration procedure, we looked at the magnetic properties of the "new" system. As first evidence, Figure 8 shows the proof that magnetic properties were added to the pSi microparticles by SPIONs decoration: the SPIONs decorated pSi microparticles are attracted by a magnet, differently from pSi-COOH microparticles.

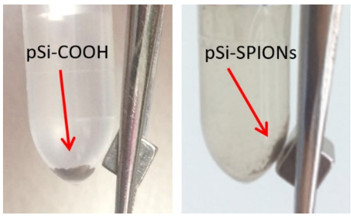

Figure 8. Evidence of the pSi-SPIONs microparticles, highlighted by an arrow, magnetic properties, differently from pSi-COOH microparticles, not attracted by the magnet.

It is worth reminding here that the diagnostic application of pSi microparticles infiltrate with SPIONs in MRI relies on their capability to affect the water relaxation times. The relaxivities of pSi microparticles decorated with SPIONs were therefore investigated by MRI technique. Both longitudinal (spin-lattice) relaxivity r_1 and transversal (spin-spin) relaxivity r_2 were determined. [33] The relaxivity is obtained by measuring the relaxation time of the sample at different NPs concentration and then extrapolated via linear fit by using the formula: $1/T_i = 1/T_{i,0} + r_i \cdot c$.

First the longitudinal and transversal relaxivity of SPIONs in water were measured. The relaxation rates ($1/T_i$) as a function of the iron concentration are shown in Figure 9a. Values of about 5.5 and 1.1 $(\text{mmol})^{-1}\text{s}^{-1}$ are obtained for r_2 and r_1, respectively. These values are compatible with the literature and, as expected, the value of longitudinal relaxivity is substantially lower than that of transversal relaxivity [34]: $r_2/r_1 \approx 5$. In fact, SPIONs are usually employed as negative contrast agents and act primarily on T_2 relaxation time.

In a second stage, we measured the relaxation efficacy of pSi-SPIONs and pSi microparticles in water (panel b); in this case, the relaxation rates have been reported as a function of the pSi concentration expressed in $\text{mg}\cdot\text{mL}^{-1}$ and therefore the obtained relaxivities are expressed in $(\text{mL}\cdot\text{mg}^{-1})$ s^{-1}. Concerning the pSi microparticles (Figure 9b), we did not observe, within the experimental error, any variation of T_1 and T_2 as a function of the microparticles concentration. Nevertheless, a slight difference was found with respect to the relaxation times of pure water ($T_1 \approx 3100$ ms, $T_2 \approx 600$ ms), due to the interaction of water with the pSi-COOH microparticles. When pSi-SPIONs microparticles (Figure 9b) were added to water, transversal relaxivity was altered, while the effect on longitudinal relaxivity was negligible since T_1 was found almost not to be concentration-dependent. The observed alteration in transversal relaxation deserves further investigations and paves the way for diagnostic applications of pSi-SPIONs in MRI.

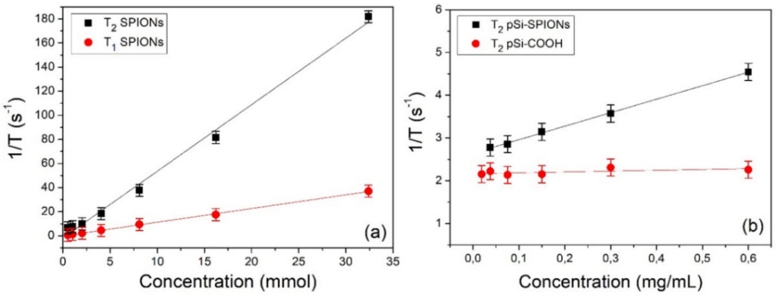

Figure 9. Relaxivity determination: (**a**) $1/T_1$ and $1/T_2$ relaxation rates of SPIONs as a function of the iron concentration; (**b**) $1/T_2$ relaxation rate of pSi-SPIONs and pSi-COOH microparticles as a function of the microparticles concentration.

4. Conclusions

In this paper, we demonstrated the possibility to combine magnetic properties to the well-known properties of functionalized pSi microparticles, by infiltrating and decorating the pores with iron oxide nanoparticles (SPIONs). Thanks to an easy and fast chemical protocol based on the functionalization with cyclohexane diamine molecules, positively charged SPIONs are obtained, in a very short time and with a little cost. Furthermore, this new protocol enables a possible separation of the magnetic nanoparticles for further MRI applications and, contrary to other procedures, it avoids the embedding of the SPIONs within a coating layer on the Si surface. They can easily enter the pores (about 20 nm in size) because of their small dimension (about 6 nm) and attach to the functionalized porous silicon surface by electrostatic interactions. By TEM and STEM images analysis, we proved the magnetic nanospheres to be attached to the pSi surface. On the other hand, no attachment was observed in the case of non-porous functionalized surfaces (i.e., the small crystalline silicon portion). As first evidence of magnetic properties, we verified that the pSi microparticles decorated with SPIONs are effectively attracted by a magnet and that variations in the transversal relaxivity were observed, in comparison with "naked" pSi microparticles. Further studies will be carried out to optimize the relaxivity of the material by using other SPIONs and to quantitatively compare the relaxivity of pSi-SPIONs with that of other nanomaterials.

These encouraging new results pave the way to the exploitation of functionalized pSi microparticles infiltrated with magnetic nanospheres in the wide field of theranostics.

Supplementary Materials: The following are available online at www.mdpi.com/xxx/s1: Figure S1: Functionalized porous Si microparticles infiltration scheme; Figure S2: HR-TEM image and diffraction pattern of a SPION nanoparticle; Figure S3: ζ-potential distribution of functionalized SPIONs; Figure S4: EDS spectrum of pSi-SPIONs microparticles

Author Contributions: Conceptualization, M.S. and N.D.; investigation, E.C.; TEM investigation G.I.; MRI measurements M.G. and P.M.; writing—original draft preparation, E.C., N.D. and M.S.; writing—review and editing, P.M., M.S. and N.D. All authors have read and agreed to the published version of the manuscript.

Funding: This research received no external funding

Acknowledgments: The authors acknowledge the CPT (Technological Platform Center) of the University of Verona for the access to the instrumentation for the magnetic measurements (Pharmascan system operating at 7 T).

Conflicts of Interest: The authors declare no conflict of interest

References

1. Canham, L.T. Silicon quantum wire array fabrication by electrochemical and chemical dissolution of wafers. *Appl. Phys. Lett.* **1990**, *57*, 1046–1048.
2. Savage, D.J.; Liu, X.; Curley, S.A.; Ferrari, M.; Serda, R.E. Porous silicon advances in drug delivery and immunotherapy. *Curr. Opin. Pharmacol.* **2013**, *13*, 834–841.
3. Slowing, I.I.; Vivero-Escoto, J.L.; Wu, C.-W.; Lin, V.S.-Y. Mesoporous silica nanoparticles as controlled release drug delivery and gene transfection carriers. *Adv. Drug Deliv. Rev.* **2008**, *60*, 1278–1288.
4. Secret, E.; Maynadier, M.; Gallud, A.; Chaix, A.; Bouffard, E.; Gary-Bobo, M.; Marcotte, N.; Mongin, O.; Cheikh, K.E.; Hugues, V.; et al. Two-Photon Excitation of Porphyrin-Functionalized Porous Silicon Nanoparticles for Photodynamic Therapy. *Adv. Mater.* **2014**, *26*, 7643–7648.
5. Park, J.-H.; Gu, L.; von Maltzahn, G.; Ruoslahti, E.; Bhatia, S.N.; Sailor, M.J. Biodegradable luminescent porous silicon nanoparticles for in vivo applications. *Nat. Mater.* **2009**, *8*, 331–336.
6. Wang, C.-F.; Sarparanta, M.P.; Mäkilä, E.M.; Hyvönen, M.L.K.; Laakkonen, P.M.; Salonen, J.J.; Hirvonen, J.T.; Airaksinen, A.J.; Santos, H.A. Multifunctional porous silicon nanoparticles for cancer theranostics. *Biomaterials* **2015**, *48*, 108–118.
7. Martín-Palma, R.J.; Hernández-Montelongo, J.; Torres-Costa, V.; Manso-Silván, M.; Muñoz-Noval, Á. Nanostructured porous silicon-mediated drug delivery. *Expert Opin. Drug Deliv.* **2014**, *11*, 1273–1283.
8. Hong, C.; Lee, J.; Zheng, H.; Hong, S.-S.; Lee, C. Porous silicon nanoparticles for cancer photothermotherapy. *Nanoscale Res. Lett.* **2011**, *6*, 321.
9. Xiao, L.; Gu, L.; Howell, S.B.; Sailor, M.J. Porous Silicon Nanoparticle Photosensitizers for Singlet Oxygen and Their Phototoxicity against Cancer Cells. *ACS Nano* **2011**, *5*, 3651–3659.
10. Henstock, J.R.; Canham, L.T.; Anderson, S.I. Silicon: The evolution of its use in biomaterials. *Acta Biomater.* **2015**, *11*, 17–26.
11. Parkhutik, V. Porous silicon—mechanisms of growth and applications. *Solid State Electron.* **1999**, *43*, 1121–1141.
12. Nash, K.J.; Calcott, P.D.J.; Canham, L.T.; Kane, M.J.; Brumhead, D. The origin of efficient luminescence in highly porous silicon. *J. Lumin.* **1994**, *60–61*, 297–301.
13. Ghafarinazzari, A.; Paterlini, V.; Cortelletti, P.; Bettotti, P.; Scarpa, M.; Daldosso, N. Optical Study of Diamine Coupling on Carboxyl-Functionalized Mesoporous Silicon. *J. Nanosci. Nanotechnol.* **2017**, *17*, 1240–1246.
14. Chistè, E.; Ischia, G.; Scarpa, M.; Daldosso, N. Ultrasonication effect on size distribution of functionalized porous silicon microparticles. *Mater. Res. Express* **2019**, *6*, 075006.
15. Ghafarinazari, A.; Scarpa, M.; Zoccatelli, G.; Franchini, M.C.; Locatelli, E.; Daldosso, N. Hybrid luminescent porous silicon for efficient drug loading and release. *RSC Adv.* **2017**, *7*, 6724–6734.
16. Chistè, E.; Ghafarinazari, A.; Donini, M.; Cremers, V.; Dendooven, J.; Detavernier, C.; Benati, D.; Scarpa, M.; Dusi, S.; Daldosso, N. TiO2-coated luminescent porous silicon micro-particles as a promising system for nanomedicine. *J. Mater. Chem. B* **2018**, *6*, 1815–1824.
17. Stephen, Z.R.; Kievit, F.M.; Zhang, M. Magnetite nanoparticles for medical MR imaging. *Mater. Today* **2011**, *14*, 330–338.
18. McCarthy, J.R.; Weissleder, R. Multifunctional magnetic nanoparticles for targeted imaging and therapy. *Adv. Drug Deliv. Rev.* **2008**, *60*, 1241–1251.
19. Mornet, S.; Vasseur, S.; Grasset, F.; Duguet, E. Magnetic nanoparticle design for medical diagnosis and therapy. *J. Mater. Chem.* **2004**, *14*, 2161–2175.
20. Serda, R.E.; Adolphi, N.L.; Bisoffi, M.; Sillerud, L.O. Targeting and cellular trafficking of magnetic nanoparticles for prostate cancer imaging. *Mol. Imaging* **2007**, *6*, 277–288.
21. Weissleder, R.; Hahn, P.F.; Stark, D.D.; Rummeny, E.; Saini, S.; Wittenberg, J.; Ferrucci, J.T. MR imaging of splenic metastases: Ferrite-enhanced detection in rats. *AJR Am. J. Roentgenol* **1987**, *149*, 723–726.
22. Kandasamy, G.; Maity, D. Recent advances in superparamagnetic iron oxide nanoparticles (SPIONs) for in vitro and in vivo cancer nanotheranostics. *Int J. Pharm.* **2015**, *496*, 191–218.

23. Roch, A.; Muller, R.N.; Gillis, P. Theory of proton relaxation induced by superparamagnetic particles. *J. Chem. Phys.* **1999**, *110*, 5403–5411.
24. Bacon, B.R.; Stark, D.D.; Park, C.H.; Saini, S.; Groman, E.V.; Hahn, P.F.; Compton, C.C.; Ferrucci, J.T. Ferrite particles: A new magnetic resonance imaging contrast agent. Lack of acute or chronic hepatotoxicity after intravenous administration. *J. Lab. Clin. Med.* **1987**, *110*, 164–171.
25. Gu, L.; Park, J.-H.; Duong, K.H.; Ruoslahti, E.; Sailor, M.J. Magnetic luminescent porous silicon microparticles for localized delivery of molecular drug payloads. *Small* **2010**, *6*, 2546–2552.
26. Gan, Q.; Lu, X.; Yuan, Y.; Qian, J.; Zhou, H.; Lu, X.; Shi, J.; Liu, C. A magnetic, reversible pH-responsive nanogated ensemble based on Fe3O4 nanoparticles-capped mesoporous silica. *Biomaterials* **2011**, *32*, 1932–1942.
27. Gabizon, A.; Shmeeda, H.; Horowitz, A.T.; Zalipsky, S. Tumor cell targeting of liposome-entrapped drugs with phospholipid-anchored folic acid-PEG conjugates. *Adv. Drug Deliv. Rev.* **2004**, *56*, 1177–1192.
28. Daldosso, N.; Ghafarinazari, A.; Cortelletti, P.; Marongiu, L.; Donini, M.; Paterlini, V.; Bettotti, P.; Guider, R.; Froner, E.; Dusi, S.; et al. Orange and blue luminescence emission to track functionalized porous silicon microparticles inside the cells of the human immune system. *J. Mater. Chem. B* **2014**, *2*, 6345–6353.
29. Lion, A.; Laidani, N.; Bettotti, P.; Piotto, C.; Pepponi, G.; Barozzi, M.; Scarpa, M. Angle resolved XPS for selective characterization of internal and external surface of porous silicon. *Appl. Surf. Sci.* **2017**, *406*, 144–149.
30. Joseph, J.; Mishra, N.; Mehto, V.R.; Banerjee, A.; Pandey, R.K. Structural, optical and magnetic characterisation of bifunctional core shell nanostructure of Fe3O4/CdS synthesised using a room temperature aqueous route. *J. Exp. Nanosci.* **2014**, *9*, 807–817.
31. Souza, T.G.F.; Ciminelli, V.S.T.; Mohallem, N.D.S. A comparison of TEM and DLS methods to characterize size distribution of ceramic nanoparticles. *J. Phys. Conf. Ser.* **2016**, *733*, 012039.
32. Canham, L. (Ed.) *Handbook of Porous Silicon*; Springer International Publishing Switzerland: 2014; ISBN 978-3-319-05744-6.
33. Rohrer, M.; Bauer, H.; Mintorovitch, J.; Requardt, M.; Weinmann, H.-J. Comparison of Magnetic Properties of MRI Contrast Media Solutions at Different Magnetic Field Strengths. *Investig. Radiol.* **2005**, *40*, 715–724.
34. Xiao, W.; Legros, P.; Chevallier, P.; Lagueux, J.; Oh, J.K.; Fortin, M.-A. Superparamagnetic Iron Oxide Nanoparticles Stabilized with Multidentate Block Copolymers for Optimal Vascular Contrast in T1-Weighted Magnetic Resonance Imaging. *ACS Appl. Nano Mater.* **2018**, *1*, 894–907.

nanomaterials

Article

Improving the Cellular Uptake of Biomimetic Magnetic Nanoparticles

Federica Vurro [1], Ylenia Jabalera [2], Silvia Mannucci [1], Giulia Glorani [3], Alberto Sola-Leyva [4,5], Marco Gerosa [1], Alessandro Romeo [6], Maria Grazia Romanelli [1], Manuela Malatesta [1], Laura Calderan [1], Guillermo R. Iglesias [7], María P. Carrasco-Jiménez [4], Concepcion Jimenez-Lopez [2,*] and Massimiliano Perduca [3,*]

[1] Department of Neurosciences, Biomedicine and Movement Sciences, University of Verona, 37134 Verona, Italy; federica.vurro@univr.it (F.V.); silvia.mannucci@univr.it (S.M.); marco.gerosa@univr.it (M.G.); mariagrazia.romanelli@univr.it (M.G.R.); manuela.malatesta@univr.it (M.M.); laura.calderan@univr.it (L.C.)
[2] Department of Microbiology, Faculty of Sciences, University of Granada, 18071 Granada, Spain; yjabalera@ugr.es
[3] Department of Biotechnology, University of Verona, Strada Le Grazie 15, 37134 Verona, Italy; gglorani@zedat.fu-berlin.de
[4] Department of Biochemistry and Molecular Biology I, University of Granada, 18071 Granada, Spain; albertosola@ugr.es (A.S.-L.); mpazcj@ugr.es (M.P.C.-J.)
[5] Instituto de Investigación Biosanitaria ibs.GRANADA, 18014 Granada, Spain
[6] Department of Computer Science, University of Verona, Strada Le Grazie 15, 37134 Verona, Italy; alessandro.romeo@univr.it
[7] Department of Applied Physic, Faculty of Sciences, University of Granada, 18071 Granada, Spain; iglesias@ugr.es
* Correspondence: cjl@ugr.es (C.J.-L.); massimiliano.perduca@univr.it (M.P.); Tel.: +34-958-249-833 (C.J.-L.); +39-045-802-7984 (M.P.)

check for updates

Citation: Vurro, F.; Jabalera, Y.; Mannucci, S.; Glorani, G.; Sola-Leyva, A.; Gerosa, M.; Romeo, A.; Romanelli, M.G.; Malatesta, M.; Calderan, L.; et al. Improving the Cellular Uptake of Biomimetic Magnetic Nanoparticles. *Nanomaterials* **2021**, *11*, 766. https://doi.org/10.3390/nano11030766

Academic Editor: Abdelhamid Elaissari

Received: 5 February 2021
Accepted: 15 March 2021
Published: 18 March 2021

Abstract: *Magnetococcus marinus* magnetosome-associated protein MamC, expressed as recombinant, has been proven to mediate the formation of novel biomimetic magnetic nanoparticles (BMNPs) that are successful drug nanocarriers for targeted chemotherapy and hyperthermia agents. These BMNPs present several advantages over inorganic magnetic nanoparticles, such as larger sizes that allow the former to have larger magnetic moment per particle, and an isoelectric point at acidic pH values, which allows both the stable functionalization of BMNPs at physiological pH value and the molecule release at acidic (tumor) environments, simply based on electrostatic interactions. However, difficulties for BMNPs cell internalization still hold back the efficiency of these nanoparticles as drug nanocarriers and hyperthermia agents. In the present study we explore the enhanced BMNPs internalization following upon their encapsulation by poly (lactic-co-glycolic) acid (PLGA), a Food and Drug Administration (FDA) approved molecule. Internalization is further optimized by the functionalization of the nanoformulation with the cell-penetrating TAT peptide (TATp). Our results evidence that cells treated with the nanoformulation [TAT-PLGA(BMNPs)] show up to 80% more iron internalized (after 72 h) compared to that of cells treated with BMNPs (40%), without any significant decrease in cell viability. This nanoformulation showing optimal internalization is further characterized. In particular, the present manuscript demonstrates that neither its magnetic properties nor its performance as a hyperthermia agent are significantly altered due to the encapsulation. In vitro experiments demonstrate that, following upon the application of an alternating magnetic field on U87MG cells treated with BMNPs and TAT-PLGA(BMNPs), the cytotoxic effect of BMNPs was not affected by the TAT-PLGA enveloping. Based on that, difficulties shown in previous studies related to poor cell uptake of BMNPs can be overcome by the novel nanoassembly described here.

Keywords: biomimetic magnetic nanoparticles; poly (lactic-co-glycolic) acid; PLGA; penetrating TAT peptide; nanoparticles; magnetic hyperthermia; cellular uptake

1. Introduction

Directed chemotherapy has emerged as a promising alternative to systematic treatments, allowing the selective delivery of the therapeutic agent to the target, thus reducing undesirable secondary effects. In some cases, the directed chemotherapy also allows the localized in situ combination of several therapeutic treatments [1]. In this scenario, choosing an optimal carrier becomes crucial. Within the broad range of nanocarriers so far studied, magnetic nanoparticles have become attractive candidates. On one hand, their nano scale size makes them display a larger surface area that allows them to carry relatively large amounts of the relevant molecule. On the other hand, their magnetic properties allow an external guidance and/or concentration at the target site plus the combination of therapies, such as targeted drug delivery and magnetic hyperthermia [2–5].

Although there is a wide range of magnetic nanoparticles already available on the market, they are generally produced by methods that present some drawbacks, mainly associated to the use of high temperatures, organic solvents, poor solubility in water and relatively small size (generally around 10–20 nm) [6]. Moreover, for a number of applications, including clinics, such a small size of the nanoparticles becomes a problem because it may result in a small magnetic moment per particle [7] that compromises their optimal response to an external magnetic field used for guidance/concentration or to induce magnetic hyperthermia. For clinical applications the magnetic nanoparticles should be superparamagnetic, that is, they should behave as non-magnetic in the absence of an external magnetic field (to avoid undesired nanoparticle aggregation prompted by magnetic dipole interactions), but, once a magnetic field is applied, they should respond as efficiently as possible to allow the guidance/concentration at the target [8]. Such a magnetic response depends on the magnetic moment per particle, which is strongly related to the size of superparamagnetic crystalline stoichiometric magnetite nanoparticles (MNPs) [7]. Therefore, in the context of the existing synthetic magnetic nanoparticles, an increase in their size above 20 nm (but keeping it below ~120 nm) [7] would represent a great advantage for most applications, especially related to drug delivery and magnetic hyperthermia [9].

While obtaining larger synthetic magnetic nanoparticles by using eco-friendly protocols is challenging, many of these drawbacks affecting synthetic magnetic nanoparticles are overcome in biomimetic ones (BMNPs). These are produced by taking inspiration from nature, that is, by using magnetosome membrane associated proteins, expressed as recombinant, to in vitro control the nucleation and growth process of magnetic nanoparticles synthesized from aqueous solutions. Moreover, the production of those BMNPs is eco-friendly and cost-effective [10]. MamC-mediated BMNPs have raised special interest, as they have shown in vitro to be effective drug nanocarriers and magnetic hyperthermia agents, both uncoated and coated by liposomes [4,5,11–13]. These BMNPs are larger than most commercial SPION and/or other biomimetic magnetites. The increased size makes them to be single magnetic domain and to have larger magnetic moment per particle than other synthetic magnetic nanoparticles or even biomimetic (Mms6-mediated) magnetic nanoparticles [10]. Moreover, BMNPs contain up to 4.5 wt% of MamC, giving them novel surface properties and providing functional groups for further functionalization [14]. In particular, it is noticeable the change in the isoelectric point (iep) of BMNPs (pH 4.4) compared to that of the inorganic magnetic nanoparticles (pH ~7.0), which allows the electrostatic bonding between the BMNPs and the relevant molecule at physiological pH values, and the spontaneous release of such a molecule at acidic pH values [14]. This is particularly interesting in the context of cancer, as it is well known the acidic environment related to tumors.

Additionally, these BMNPs have proven to be effective hyperthermia agents under the application of an alternate magnetic field (AMF) [4,5,12,14]. Temperature variations could interfere with basal metabolisms and homeostasis processes. In fact, Park et al. [15] reported that the increase of 1–2 °C from physiological temperature represents a mild heat shock for the cells, while higher temperatures lead to severe heat shock due to changes in the viscosity of membrane lipids and the transduction of a signal that induce cell heat shock responses. Cancer cells are especially sensitive to these temperature increases [16]. However, an important challenge in therapy is to combine heating effect on tumor cells avoiding damages on the surrounding healthy cells. In fact, temperatures within the range 42–46 °C result in an extremely selective thermal ablation of tumor. This effect is due to heat generation by magnetic energy dissipation from the single-domain particles caused by internal Néel fluctuations of the nanoparticle magnetic moment and external Brownian fluctuations following the application of an AMF [17]. Therefore, the use of magnetic nanoparticles able to be directed to the target and, once there, to locally increase the temperature is a promising alternative to treat cancer, being the optimum results when magnetic hyperthermia is combined with directed chemotherapy by using the magnetic nanoparticles as nanocarriers [5].

Nevertheless, to maximize the effects of the directed chemotherapy and/or magnetic hyperthermia, it is important to facilitate the cellular uptake of the BMNPs [4,5]. While placing a magnet at the target site has been shown to facilitate internalization [3,5], other strategies need to be developed to further optimize BMNPs cellular uptake. Encapsulation of BMNPs becomes an attractive candidate to improve, not only internalization, but also biocompatibility and to prevent aggregation and oxidation. Liposomes have been used to encapsulate BMNPs and such encapsulation has been proven to be effective for drug delivery [3] and to combine directed chemotherapy and magnetic hyperthermia [13]. However, such an encapsulation may not be stable when BMNPs are functionalized with drugs whose target are cell membranes, since they may disrupt the liposomes by similar mechanisms to those that disrupt/alter cell membranes. Therefore, another encapsulation strategy needs to be developed.

In this context, different natural or synthetic polymers have been used for the encapsulation of magnetic nanoparticles, such as polyethylene glycol (PEG), [18] dextran, [19] zwitterionic linear polyamidoamine, [20] hexadecantiol [21] or carbon nanomaterials [22] and cationic peptides [23,24]. However, the use of FDA-approved molecules for encapsulation, such as poly (lactic-co-glycolic) acid, commonly known as PLGA, is becoming a priority [25]. PLGA is a copolymer of the ester family, widely used to prepare nano and microparticles [26,27], when biocompatibility and biodegradability are required, such as in clinics and, specifically, for drug delivery [28,29]. PLGA has been approved for human therapies by the FDA and the European Medicines Agency (EMA) [29–31]. The biocompatibility of this copolymer for human cells is the result of its spontaneous hydrolysis, which leads to the release of lactic and glycolic acid monomers that can be easily metabolized by cells through the Krebs cycle.

Interestingly, encapsulations of nanoparticles that display different properties can be obtained by changing the ratio between the lactic and the glycolic acid used during the PLGA polymerization process, which allows a great versatility of the nanoformulations [32]. Moreover, due to the presence of carboxyl groups, PLGA copolymers allow further functionalization, for instance with signaling molecules that allows the target recognition and/or the internalization of the nanoformulation. Some examples are the sequence arginine-glycine-aspartate (RGD) used to recognize tumoral cells expressing integrin $\alpha_v\beta_3$ on their surface [33], the apolipoprotein E modified peptide (pep-apoE), and the peptide of lipocalin-type prostaglandin-d-synthase (L-PGDS) that allow PLGA nanoparticles to cross the blood-brain barrier (BBB) [34] or the phage peptide Pep-1, which show great affinity for the interleukin 13 receptor $\alpha2$ (a glioblastoma multiforme-associated plasma membrane receptor) [35]. In this scenario, TAT peptide (TATp) has been the first cationic peptide characterized as cell-penetrating peptides (CPPs) and it has been used for cancer therapy applications due to its low cytotoxicity and high tumor-penetrating ability [36,37]. Moreover, TATp-modified nanoparticles have been demonstrated to be able to cross the BBB and translocate in the nucleus of neurons in vitro and in vivo [38–40]. TATp is derived from the transcriptional activator protein TAT encoded by human immunodeficiency virus type 1 (HIV-1) exhibiting a positive charge in its transduction domain (RKKRRQRRR) that confers the property of rapid translocation through the plasma membrane [41]. TATp, as well as other cationic CPPs, have been widely used to deliver different cargoes, including nanoparticles into cells in vitro and in vivo [42–45].

Although this is the first study to attempt PLGA encapsulation of BMNPs, that of MNPs has already been explored by a number of authors [35,46,47]. The purpose of these studies was to produce nanocomposite that could be used as drug nanocarriers and hyperthermia agents and/or for theranostic purposes. Nevertheless, since BMNPs show differences in terms of size, magnetic properties, stability and surface properties compared to that of MNPs, as detailed above, PLGA encapsulation of BMNPs is not straightforward, and new protocols need to be set to be able to produce this novel nanocomposite.

In the context of improving PLGA(BMNPs) nanocomposites by decoration with TAT peptides, this strategy has already been used in PLGA(MNPs) nanocomposites, but there are no studies on TAT-PLGA(BMNPs). The existing studies of TAT-PLGA(MNPs) have proven efficient to bring hesperidin, naringin, and glutathione through the BBB, so effective local doses can be reached in mice brain cells bEnd.3 [48]. Developing protocols to produce novel TAT-PLGA(BMNPs) is important, since it may result in an improved efficiency of drug delivery therapies based on magnetic nanoparticles, due to the better performance, in this context, of BMNPs compared to MNPs.

However, one of the drawbacks of the encapsulation of magnetic nanoparticles is the potential shielding of the magnetic core, thus potentially compromising both the magnetic guidance of the nanoformulation as well as the ability of inducing magnetic hyperthermia. In the present study, a new nanoformulation (PLGA enveloping BMNPs) has been formulated and characterized to avoid significant shielding of the magnetic properties of the BMNPs and the ability to induce magnetic hyperthermia. How this nanoformulation increase the BMNPs cell uptake and the cytocompatibility of the nanoformulation is also investigated. The nanoformulation was further functionalized with TAT peptide to optimize cell uptake without decreasing the magnetic hyperthermia efficiency.

2. Materials and Methods

2.1. Materials

PLGA (poly[DL-lactide-co-glycolide],50:50 lactide-glycolide ratio, molecular weight 7,000–17,000, PDI 2.3, CAS 26780-50-7), ethanol ($\geq$99% purity, CAS 64-17-5), PVA (poly[vinyl alcohol], molecular weight 30,000–70,000, and degree of alcoholysis 87–90%, CAS 9002-89-5), EDC (1-ethyl-3-(3-dimethylaminopropyl)carbodiimide, CAS 25952-53-8), NHS (N-hydroxysuccinimide, 98% purity, CAS 6066-82-6), glycine ($\geq$99% purity, CAS 56-40-6), acetone ($\geq$99% purity, 1.00013.) were purchased from Merck KGaA (Darmstadt, Germany). TAT peptide (Transactivator of Transcription of human immunodeficiency virus (GRKKR-RQRRRPQ)) was purchased from CRIBI-Biotechnology Centre, University of Padua (Padua, Italy). Foetal bovine serum (FBS), L-glutamine, penicillin and streptomycin were obtained from Biowest (Nuaillé, France). Cell Proliferation Reagent WST-1 was acquired from Roche Diagnostic (Mannheim, Germany). *Escherichia coli* TOP10 and the plasmid pTrcHis-TOPO were purchased from Life Technologies: Invitrogen, Grand Island, NY, USA. Isopropyl-1-thio-β-D-galactopyranoside (IPTG), Na_2CO_3, $NaHCO_3$, $Fe(ClO_4)_2$, $FeCl_3$, $K_4Fe(CN)_6$, urea and HEPES were purchased from Sigma-Aldrich. Glutaraldehyde, Paraformaldehyde, OsO_4 and Epon resin were purchased from Electron Microscopy Sciences, Hatfield, PA, USA. The U87MG cell line was purchased by ATCC Manassas, VA, USA. Eagle's minimum essential medium (EMEM) and Dulbecco's modified Eagle's medium were purchased from Sigma-Aldrich. Amphotericin b (AmpB) and trypsin were purchased from Gibco, Life Technologies Inc., Grand Island, NY, USA.

2.2. Biomimetic Magnetic Nanoparticles Synthesis

The BMNPs used in this study were also used in a previous one [14]. Since an extensive characterization of these particles was done in this work, only basic mineral characterization is included in the present manuscript, as powder X-ray diffraction (XRD) analyses, transmission electron microscopy (TEM) and hysteresis cycle at 5K and 300K. As shaker (Ika KS 260 Control—2000 rpm) at 20 °C overnight under nitrogen atmosphere to evaporate the organic phase. The preparation was pelleted using a magnet and the pellet was washed three times with sterile filtered PBS solution pH 7.4. The final pellet was re-suspended in 1 mL of sterile PBS buffer and stored at 4 °C.

To functionalize the PLGA surface of the nanoparticles with the TAT peptide, 5 mg of the previously prepared NPs were re-suspended in 1 mL of 50 mM MES, pH 5.8 and subsequently activated with 0.1 M EDC and 0.7 M NHS for 1 h a 20 °C; subsequently the NPs were recovered with a magnet and washed three times with PBS. A total of 250 µg of TAT peptide was added to the suspension and incubated overnight at 20 °C under shaking. The reaction was stopped adding glycine (20 mg/mL) and leaving the reaction at room temperature for 1 h; NPs were subsequently washed twice with PBS and the final pellet was re-suspended in 1 mL of sterile PBS buffer and stored at 4 °C.

2.5. Dynamic Light Scattering and Zeta Potential

Size and ζ-potential of the empty PLGA and the nanoformulations were estimated by dynamic light scattering (DLS) (Nano Zeta Sizer ZS, ZEN3600, Malvern Instruments, Malvern, Worcestershire, UK). For the size measurements, each sample was re-suspended in PBS to a final concentration between 0.1 and 1 mg/mL, being used as a stock suspension. Aliquots from this stock were withdrawn, resuspended in 10 mM $NaClO_4$ and the pH was adjusted to 7.5 using 0.1M NaOH for ζ-potential measurements. All samples were measured in triplicate with the sample cell temperature fixed at 25 °C. Data were collected and analyzed by the ZetaSizer 7.10 software (Malvern, Worcestershire, UK).

2.6. Atomic Force Microscopy

The empty PLGA and nanoformulations were prepared for the Atomic Force Microscopy (AFM) experiments with a final concentration of 5 mg/mL. 20 µL drops of each suspension were deposited on 20 mm diameter mica discs sprayed with argon to avoid excess conglomeration of the NPs and the excess solvent was allowed to evaporate at room temperature. A NT-MDT Solver Pro microscope (Moscow, Russia), with single crystal silicon-antimony doped probe and a gold-coated tip (NSG-01 from NT-MDT) was used to collect images. The microscope was calibrated by a calibration grating (TGQ1 from NT-MDT) in order to reduce nonlinearity and hysteresis in the measurements. Scanning was performed in intermittent mode, with a frequency of 3 to 1 Hz. and the resolution of all the images acquired was 15 nm. The images were processed with the program Gwyddion and a statistical analysis over on the diameters of 30 different nanoparticles of each type was conducted to compare results to DLS data.

2.7. Hysteresis Cycle at 5 and 300 K and Magnetic Hyperthermia

Magnetization measurements were carried out by using a quantum design superconducting quantum interference device 5T magnetic properties measurement system (MPMS-XL SQUID magnetometer, Quantum Design, San Diego, CA, USA). Hysteresis cycles were run at 5 and 300 K.

Magnetic hyperthermia was evaluated by using a Nanotherics MagneTherm system (Warrington, UK). The alternate magnetic field apparatus is characterized by a water-cooled solenoid constituted by 17 turns and yields a magnetic field intensity of 23.133 kA/m (≈29 mT) associated with a multichannel thermometer equipped with optical fiber probes (FOTEMP4, Optocon AG, Dresden, Germany) used to assess temperature variation within the sample every 10.0 s. The nanoparticles [BMNPs, PLGA(BMNPs) and TAT-PLGA(BMNPs)] were resuspended in 1 mL water solvent with a Fe concentration of 0.5 mg/mL. Thermograms were acquired through a time window of 20 min that was chosen considering human application of the MFH and the characteristics of nanoparticles adopted. In order to maintain the samples under adiabatic conditions during the whole procedure, we set up a homemade device constituted by a thermostated closed box in which we fluxed the air stream at 37 °C.

stated in the work above mentioned, the BMNPs used in the present study contain up to 5 wt% of MamC, show an isoelectric point of 4.4 and specific surface area of 90 m^2/g.

A summary of how BMNPs were synthesized is here provided. MamC expression and purification were performed as previously described by Valverde-Tercedor et al. [10]. *E. coli* TOP10 was transformed with the plasmid pTrcHis-TOPO used as a vector of the MamC protein-coding gene (Mmc1_2265) coupled to a hexahistidine tag coding sequence at its 5′ terminus. These cells were grown at 37 °C and MamC overproduction was induced by adding IPTG. Once expressed, the purification of the protein was carried out under denaturing conditions by fast protein liquid chromatography (FPLC, GE Healthcare) by using immobilized metal affinity chromatography (IMAC, GE Healthcare, Chicago, IL, USA). Lastly, dialysis was performed for a gradual removal of urea, which allowed MamC to refold progressively and the purity was evaluated by SDS-PAGE electrophoresis.

The synthesis of BMNPs was carried out at 25 °C and 1 atm total pressure from oxygen-free solutions (protocol described in Perez-Gonzalez et al. 2010 [49] and Valverde-Tercedor et al. 2015 [10]) containing 3.5 mM Na_2CO_3, 3.5 mM $NaHCO_3$, 2.78 mM $Fe(ClO_4)_2$, 5.56 mM $FeCl_3$,and 10 μg/mL recombinant MamC, at a pH value of 9. All experiments were done under anaerobic conditions inside an anaerobic Coy chamber (96% N_2/4% H_2, Coy Laboratory Products, Grass Lake, MI, USA). Samples were incubated for 30 days and then the solids were magnetically concentrated, washed three times with deoxygenated Milli-Q water, and stored in HEPES buffer (pH 7.4) inside the Coy Chamber at 25 °C. Samples were autoclaved before their use.

Powder X-ray diffraction analysis was carried out with an Xpert Pro X-ray diffractometer (PANalytical) using the Cu Kα radiation, 20 to 60° in 2θ (0.01°/step; 3 s per step). Precipitates were identified by XPowderX software v. 2021 (Granada, Spain) [35]. TEM analyses of the BMNPs were performed with a STEM Philips Model CM20 microscope, after embedding in Embed 812 resin and ultrathin sections (50–70 nm) preparation with a Reichert Ultracut S microtome (Leica Microsystems GmbH, Wetzlar, Germany). Crystal size was measured on 1000 nanoparticles per experiment using ImageJ 1.47.

2.3. PLGA Empty Nanoparticles Synthesis

The protocol used for the production of both the empty and BMNPs-embedded PLGA nanoparticles is based on the single emulsion-evaporation method [29,50] and all operations have been carried under sterile conditions The preparation of the empty NPs was the following: 10 mg of the PLGA copolymer were dissolved in 1 mL of organic solution (85% acetone and 15% ethanol). To better allow the homogenization of solvent and polymer, the preparation was sonicated for 30 s (power 8 RMS for 10 s with rest 5 s/cycle), and subsequently dripped in to 10 mL of a solution of PVA 1% in milliQ water, previously filtered with a 0.2 μM filter, maintaining a constant intensity of sonication at room temperature. The reaction mixture was stirred (2000 rpm) *overnight* at 20 °C, to evaporate the organic solvent. The preparation was pelleted at 11,000 g at 4 °C for 10′ (Eppendorf Centrifuge 5804R) and the pellet was washed three times with sterile filtered PBS solution pH 7.4. The final pellet was re-suspended in 1 mL of sterile PBS buffer and stored at 4 °C.

2.4. PLGA Encapsulation of BMNPs and TAT Peptide Functionalization

The encapsulation protocol for the BMNPs is based on the single emulsion-evaporation one used to prepare the empty PLGA NPs above described (Figure S1). To prevent the oxidation of the magnetic particles, all buffers and aqueous solutions were degassed under vacuum.

A total of 10 mg of the PLGA copolymer were dissolved in 1 mL of organic solution (85% acetone and 15% ethanol), together with the magnetic nanoparticles, to obtain a concentration of 0.5 mg/mL of BMNPs in the final reaction volume. The mixture was dripped in 10 mL of sterile PVA (1%) in a sonication bath, keeping the sonication intensity constant. The suspension was then left under sonication for 5′ and then kept on a flat

The heat dissipation value depends on the frequency and amplitude of the applied AMF by means of two parameters, specific absorption rate (SAR) and intrinsic loss power (ILP). In particular, the transformation of magnetic energy into thermal energy mediated by magnetic nanoparticles in presence of an external AMF is quantified from the value of SAR. The SAR value of nanoparticles in solution is calculated by using the following equation:

$$\mathrm{SAR} = \frac{dT}{dt}\frac{C_V}{m_{Fe}},$$

where C_V is the specific heat capacity of the solvent per g, $\frac{dT}{dt}$ is the temperature variation in time and m_{Fe} is the mass of iron per g in the compound [51,52].

ILP was defined to evaluate the magnetothermal performance of a given suspension in order to perform a comparison between different materials without the eventual interference of the setup or the specific device used. ILP was calculated using the following equation:

$$\mathrm{ILP} = \frac{\mathrm{SAR}}{fH^2}.$$

For the magnetic hyperthermia characterization of the three samples, all the available frequencies (ranging from 111 to 970 kHz) of the Magnetherm device were tested. Finally, SAR and ILP were evaluated on the 111 kHz frequency, the most performant among all the possible setups and the closest to clinical applications.

2.8. Transmission Electron Microscopy Analysis

The U87MG cell line was cultured in EMEM with 10% (v/v) FBS, 1% (w/v) L-glutamine, 0.5% (v/v) AmpB, 100 units/mL of penicillin streptomycin (P/S), at 37 °C in a 5% CO_2 humidified atmosphere. Cells were trypsinized when subconfluent (about 80%) and seeded on glass coverslips in 24-multiwell microplates. Cells were treated with 50 µg/mL of BMNPs, PLGA(BMNPs) and TAT-PLGA(BMNPs) for 24 h at 37 °C. In order to visualize the uptake mechanisms, cells were processed for TEM as monolayers [53]: they were fixed with 2.5% (v/v) glutaraldehyde and 2% (v/v) paraformaldehyde in 0.1 M phosphate buffer, pH 7.4, at 4 °C for 1 h, post-fixed with 1% OsO_4 and 1.5% $K_4Fe(CN)_6$ in H_2O for 1 h, dehydrated with acetone and embedded in Epon resin. Ultrathin sections were observed in a Philips Morgagni transmission electron microscope (FEI Company Italia Srl, Milan, Italy) operating at 80 kV and equipped with a Megaview II camera for digital image acquisition.

2.9. Quantitative Analysis of Nanoparticle Internalization

U87MG cells (300,000 cells per well) were seeded in 12-well plates. Then, cells were treated with BMNPs, PLGA(BMNPs) or TAT-PLGA(BMNPs) at 300 µg/mL. After 48 and 72 h of incubation, cells were washed with PBS, trypsinized, transferred to 2 mL tubes and centrifuged at 1000 rpm during 5 min. Then, 37% HCl/10% H_2O_2 was used to dissolve the cell pellets, and incubated at room temperature for 20 min. Subsequently 1 mL of 1% potassium thiocyanate in Milli-Q water was added and the absorbance at 490 nm was measured. A standard curve was used to obtain the endogenous iron of the cells.

2.10. Cell Proliferation Assay

The U87MG cell line was cultured in EMEM with 10% (v/v) FBS, 1% (w/v) Gln, 0.5% (v/v) AmpB, 100 units/mL of PS, at 37 °C in a 5% CO_2 humidified atmosphere. Cells were trypsinized when subconfluent (about 80%) and seeded on 96-well plate for cell viability evaluation. U87MG cells were seeded (10,000 cells per well) in a 96-well plate and grown for 24 h in a humidified incubator at 37 °C with 5% CO_2. Then, the medium was replaced with fresh medium containing different amounts of the BMNPs, PLGA, PLGA-TAT and nanoassemblies. A modified tetrazolium-based cytotoxic assay [54], the WST-1 assay was used to evaluate the cytotoxicity of the samples after 48 and 72 h. Once the time of treatment was reached, the media was replaced with 100 µL of WST solution (10%). The plate was incubated at 37 °C for 30 min and then was shaken for 10 min. Finally, the absorbance was read at a wavelength of 480 nm using a microplate reader (HTX Microplate Reader BioTek Instruments, Winooski, VT, USA). A one-way ANOVA was done with post hoc comparisons by Bonferroni test. $p < 0.05$ is considered statistically significant.

2.11. In Vitro Cytotoxicity of the Nanoformulation

Hyperthermia assay were performed as previously reported in [3]. Briefly, U87MG cells were seeded on 96-well plates and treated with BMNPs and the nanoassembly TAT-PLGA(BMNPs), both at a concentration of 300 µg/mL. After 48 h of incubation, cells were exposed to alternating magnetic field (frequency = 110 kHz, H = 30 kA/m) during 2 h. Finally, the viability was assessed by WST colorimetric assay, as described above. Three replicates were run to ensure reproducibility.

3. Results and Discussion

3.1. Synthesis and Characterization of Biomimetic Magnetic Nanoparticles (BMNPs) and the Nanoformulations of PLGA (BMNPs) and TAT-PLGA(BMNPs)

According to powder XRD analysis (Figure S2), MamC-mediated BMNPs were composed of >95% magnetite. TEM images revealed nanoparticles displaying well-developed crystal faces with rhombic, rectangular, and square two-dimensional morphologies (Figure S3A). Particle size distribution was 36 ± 12 nm (Figure S3B).

In order to obtain both the empty PLGA and BMNP-embedded PLGA [PLGA(BMNPS)] nanoformulations, the single emulsion-evaporation method [29,50] (Figure S1) was used. The first dimensional characterization was performed by DLS, and AFM was used to further characterize their surface (Figure S4) and dimensional properties (Table S1). Empty PLGA nanoformulations exhibit an average size close to 183 nm, both by DLS and AFM measurements, a polydispersity index (PDI) of 0.054 ± 0.007 and a ζ-potential of −3.4 ± 2.1 mV (at pH = 7.5). These nanoformulations can be easily re-suspended despite the low superficial charge and remain in suspension enough time to perform the cell experiments without significant aggregation.

PLGA nanoparticle-embedding BMNPs (PLGA(BMNPs)) exhibit larger dimensions: DLS value for the non-functionalized ones is close to 222 nm, with a PDI of 0.191 ± 0.013; the diameter is confirmed by AFM analysis (218 nm). Instead, TAT functionalized PLGA(BMNPs) (namely TAT-PLGA(BMNPs)) are even larger with a size close to 238 nm (PDI 0.194 ± 0.019) and an AFM-size of 220 nm. The lower size measured in all cases by AFM compared to that from DLS measurements is related to the techniques used: DLS measures the hydrodynamic radius, instead AFM samples have been dehydrated during the preparation to the experiment. Measurements of the ζ-potential of PLGA(BMNPs) and TAT-PLGA(BMNPs) at pH 7.5 are −15.0 ± 9.3 and −12.6 ± 5.1 mV, respectively, which is consistent with the better colloidal stability observed in the nanoformulations compared to that of the empty PLGA. The increase of the negative ζ-potential for PLGA(BMNPs), if compared to empty PLGA nanoparticles, can be attributed to the further contribution of carboxylic groups, made by the increased number of PLGA monomers participating in the nanoassemblies. This contribution is partially neutralized in the TAT-PLGA(BMNPs) by their involvement into the covalent reaction with the TAT peptide, as it is evident from the decreased negative value. All the nanoparticles analyzed by AFM exhibit a spherical shape.

3.2. Magnetic Saturation and Magnetic Hyperthermia of the Nanoformulations

The hysteresis cycles at 5 and 300 K (Figure 1) show the ferromagnetic behavior at 5 K and the superparamagnetic behavior at 300 K [7]. At 5 K, the samples present a remnant magnetization in the absence of an external magnetic field while at 300 K, the samples showed zero magnetic coercivity. This characteristic is important, since at temperatures higher than 300 K, this sample will behave as paramagnetic (non-magnetic) in the absence of an external magnetic field, thus preventing aggregation [7,10]. However, when an external magnetic field is applied, the sample will respond efficiently, allowing magnetic guidance and/or concentration at the target site. Magnetization saturation (Ms) measurements show that the embedding of BMNPs within PLGA does not shield the magnetism of the former due to the non-magnetic coating, since the Ms for both BMNPs and TAT-PLGA(BMNPs) at 300 K is ~56 emu/g.

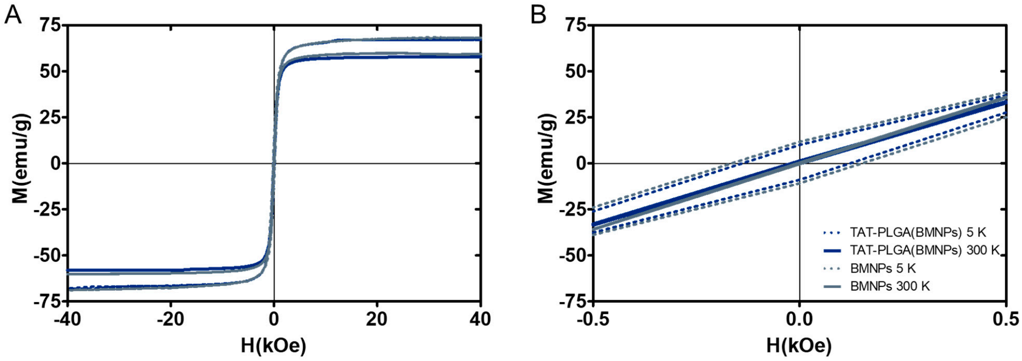

Figure 1. Hysteresis cycles of TAT-PLGA(BMNPs) and BMNPs. (**A**) Magnetization cycles of TAT-PLGA(BMNPs) and bare BMNPs at 5 and 300 K, showing the ferromagnetic and the superparamagnetic behavior. (**B**) Magnifications of the low-field region.

Magnetic hyperthermia data show that BMNPs, PLGA(BMNPs) and TAT-PLGA(BMNPs) are able to transform magnetic energy into thermal energy in presence of external AMF. Measurements of the temperature rise over time were achieved with a frequency ranging from 111 to 970 kHz were tested (Figure 2). Faster temperature rises occurred at 111 kHz. The hyperthermic efficiency is quantified by the value of SAR and ILP (Table S2). The SAR and ILP values extrapolated are comparable with them reported in literature and used in clinical trials [55].

3.3. Enhanced Cellular Uptake of the Nanoformulations versus BMNPs

Ultrastructural analysis showed that BMNPs and the nanoformulations PLGA(BMNPs) and TAT-PLGA(BMNPs) enter inside the cells by endocytosis and phagocytosis, in the case of large clusters (Figure 3A,B). Once in the cytoplasm, all the BMNPs and nanoformulations are enclosed in a cytoplasmic vacuole (Figure 3D). As expected, TAT-PLGA(BMNPs) enter the cells in larger amounts in comparison to PLGA(BMNPs). This enhanced uptake is supported by data acquired by a quantitative analysis of nanoparticle internalization. Previous studies have shown that BMNPs are internalized via endocytosis when they are incubated with cells [4]. Cell internalization in the present experiments was indirectly determined by measuring the intracellular iron of the different nanoformulations [BMNPs, PLGA(BMNPs) and TAT-PLGA(BMNPs)]. As it can be seen in Figure 4, statistically significant differences were observed in iron internalized when comparing BMNPs to both PLGA(BMNPs) and TAT-PLGA(BMNPs). After 48 h, an internalization of 50% of PLGA(BMNPs) and 65% of TAT-PLGA(BMNPs) compared to 40% of BMNPs was observed. After 72 h, there is an increment in iron internalization for PLGA(BMNPs) (67%) and TAT-PLGA(BMNPs) (84%) nanoassemblies. In all cases, the internalization of TAT-PLGA(BMNPs) was always greater, up to 80% more iron internalized, demonstrating the ability of that moiety to ease or induce the internalization of the nanoformulation in the cells. In fact, TAT peptide is known as a cell-penetrating peptide and has been used to overcome the lipophilic barrier of the cellular membranes and deliver large molecules and even small particles inside the cell for biological actions [38–40].

3.4. Cytocompatibility of PLGA(BMNPs)

As shown in Figure 5A, PLGA, TAT-PLGA, BMNPs, PLGA (BMNPs) and TAT-PLGA(BMNPs) did not exert significant toxicity on cells after 48 h, demonstrating the high cytocompatibility of the samples. In fact, no sample showed significant cell viability reduction compared to control at all doses tested. These results are in agreement with previous studies that have demonstrated the cytocompatibility of nanoassemblies comprising BMNPs [4,12].

On the contrary, after 72 h (Figure 5B), the highest doses of PLGA(BMNPs) and TAT-PLGA(BMNPs) showed a low decrease in cell viability, >60% and >70%, respectively. This increase in cell death rate could be explained by the fact that PLGA and TAT-PLGA would promote the BMNPs internalization, compared to BMNPs control, increasing the toxicity on cells as consequence of high iron concentrations [12].

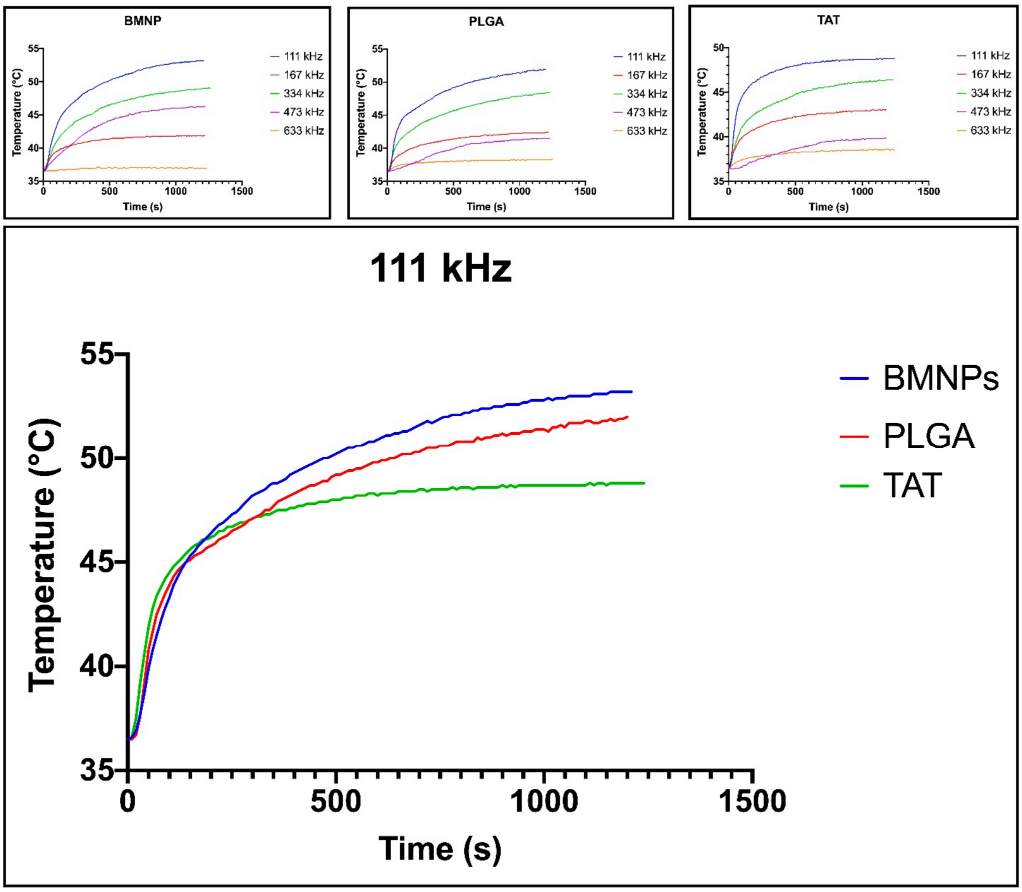

Figure 2. Magnetic hyperthermia data of BMNPs, PLGA(BMNPs) and TAT-PLGA(BMNPs). Hyperthermia efficiency of BMNPs, PLGA-BMNPs and TAT-PLGA-BMNPs on different frequencies (upper part of the figure) and comparison between the different nanoformulation efficiency on the 111 kHz frequency, evaluated using a Nanotherics MagneTherm system.

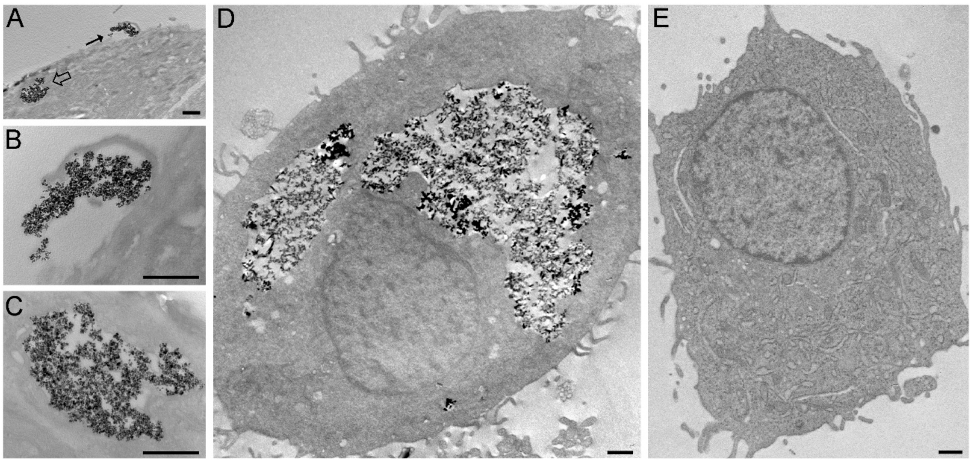

Figure 3. Transmission electron micrographs of cells treated for 24 h with TAT-PLGA-BMNPs (**A**–**D**) and the untreated (control) cell (**E**). (**A**) Clusters of NPs occur both at the surface (arrow) and inside (open arrow) the cell. (**B**) High magnification of the NPs at the cell surface (arrow in A): Note the cell protrusion indicating a phagocytic process. (**C**) High magnification of nanoparticles enclosed in a cytoplasmic vacuole (open arrow in **A**). (**D**) The internalized nanoparticles are stored inside large vacuoles. Bars = 1000 nm (**A**,**D**,**E**), 500 nm (**B**,**C**).

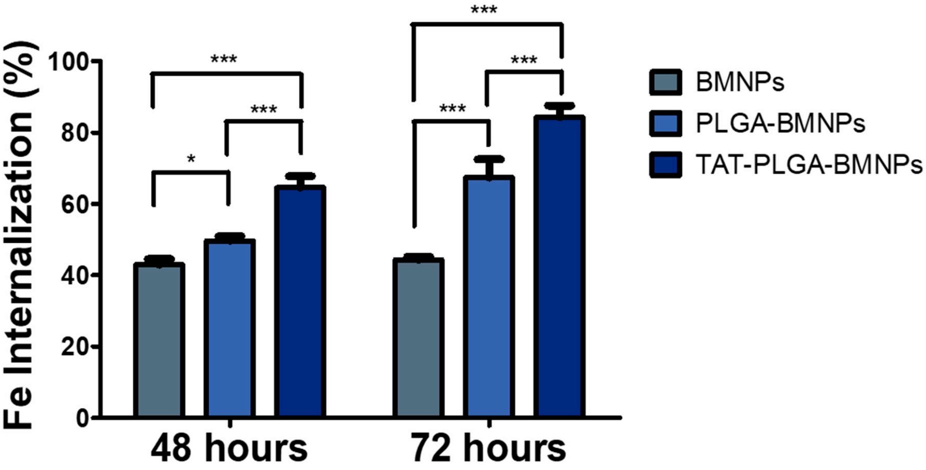

Figure 4. Quantitative analyses of BMNPs internalization in U87MG. Experiments were conducted twice in triplicates. Statistical differences between the treatments were considered significant when p values were $p < 0.05$ (*), $p < 0.001$ (***).

3.5. Cytotoxicity of PLGA(BMNPs)

Results show that, under the conditions studied, both BMNPs and the nanoassembly reduced cell viability by ~30%, being such a reduction statistically significant when compared with that of the untreated cells (Figure 6). Variations in the cytotoxic effect within the two treatment were negligible. This result demonstrates that the enveloping of the BMNPs nanoparticles in PLGA, while greatly improving BMNPs uptake by cells, does not interfere with their cytotoxic effect following upon application of an alternating magnetic field.

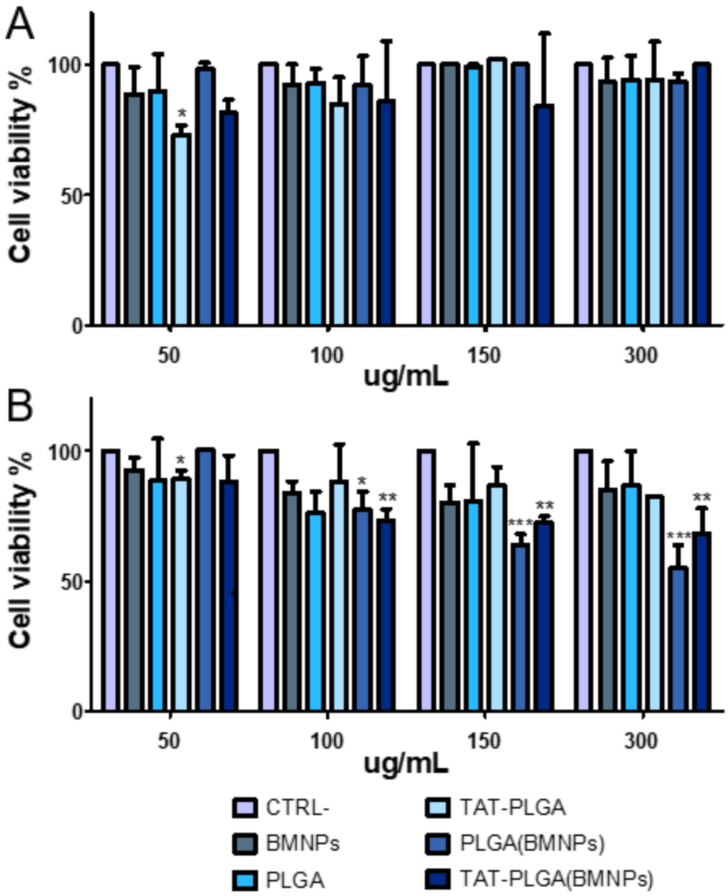

Figure 5. Cell proliferation assay of U87MG. U87MG cells were treated with the different samples after 48 (**A**) and 72 (**B**) hours. Statistical differences between the treatments were considered significant when p values were $p \leq 0.05$ (*), $p \leq 0.01$ (**), $p \leq 0.001$ (***).

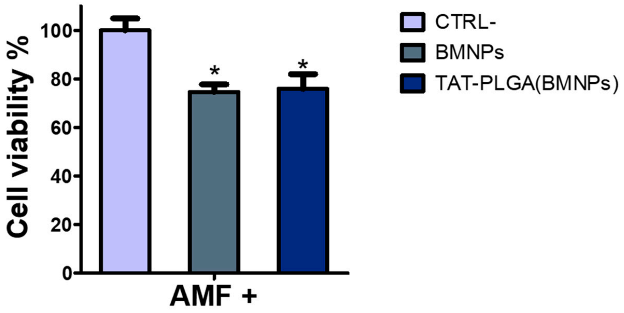

Figure 6. Cytotoxicity on U87MG of the nanoassembly combined with the application of an alternating magnetic field (AMF). U87MG cells were treated with BMNPs and TAT-PLGA(BMNPs) and exposed to an alternating magnetic field for 2 h. Statistical differences between the treatments were considered significant when p values were $p \leq 0.05$ (*).

4. Conclusions

The embedding of biomimetic magnetic nanoparticles in PLGA functionalized with TAT peptide enhances the BMNPs cellular uptake with no modification of the BMNPs' magnetic properties and/or their in vitro performance as hyperthermia agents, paving the way to the use of these nanocarriers in combined antitumoral therapy. This is the first study where a novel technology to produce PLGA-embedding BMNPs has been developed. Moreover, this technology opens the possibility of using PLGA(BMNPs) nanoformulations in different cell types by simply changing the specific targeting moiety bound to the nanoformulation surface.

Supplementary Materials: The following are available online at https://www.mdpi.com/2079-4991/11/3/766/s1, Table S1. Size (nm) and Z-potential (mV) of PLGA nanoassemblies, empty or embedding BMNPs. Table S2. SAR and ILP values evaluated on the 111 kHz frequency. Figure S1. Representation of the PLGA(BMNPs) synthesis. Figure S2. X-ray powder diffractogram for BMNPs. Figure S3. Characterization of biomimetic magnetic nanoparticles. Figure S4. Atomic force microscopy observation of PLGA(BMNPs) and PLGA NPs.

Author Contributions: Conceptualization, M.P., C.J.-L., L.C., M.P.C.-J. and G.R.I.; data curation, A.R., Y.J., A.S.-L. and Y.J.; investigation, F.V., Y.J., S.M., G.G., A.S.-L., M.G., G.R.I. and A.R.; methodology, M.P., C.J.-L., M.G.R., M.M., G.R.I. and M.P.C.-J.; supervision, C.J.-L. and M.P.; writing—original draft, M.P., C.J.-L., M.G.R., L.C. and M.P.C.-J.; writing—review and editing, C.J.-L. and M.P. with contributions from the rest of authors. All authors have read and agreed to the published version of the manuscript.

Funding: This research was funded by the FUR (Fondo Unico della Ricerca—University of Verona) of M. Perduca. C.J.-L. acknowledges funding from projects CGL2016-76723 from the Ministerio de Economía y Competitividad from Spain and Fondo Europeo de Desarrollo Regional (FEDER) and Programa Operativo FEDER 2014–2020 (A-BIO-376-UGR18) Junta de Andalucia. M.P.C.-J. acknowledges funding from projects PID2019-109294RB-100 from the Ministerio de Ciencia e Innovación from Spain.

Data Availability Statement: No new data were created or analyzed in this study. Data sharing is not applicable to this article.

Acknowledgments: We are grateful to the "Centro Piattaforme Tecnologiche" of the University of Verona for giving access to DLS equipment. CJL acknowledges. the Unidad Científica de Excelencia UCE PP 2016.05 (U. Granada) and Instituto de Biotecnología. Y.J. wants to acknowledge a FPU2016 grant (ref. FPU16_04580) from the Ministerio de Educación, Ciencia y Deporte y Competitividad (Spain). AS-L is funded by the Spanish Ministry of Science, Innovation and Universities: Formación de Doctores 2018 (ref. PRE2018-0854409). Thanks go to the Scientific Instrumentation Center (CIC) personnel of the University of Granada for technical assistance with the TEM. We also thank Salvatore Calogero Gaglio for his help in preparing Figure S4.

Conflicts of Interest: The authors declare no conflict of interest.

Abbreviations

BMNPs, biomimetic magnetic nanoparticles; MNPs, magnetite nanoparticles; PLGA, poly (lactic-co-glycolic) acid; FDA, Food and Drug Administration; TATp, TAT peptide; iep, isoelectric point; TAT-PLGA(BMNPs), TAT functionalized PLGA(BMNPs); TAT-PLGA, PLGA nanoparticles functionalized with TAT; AMF, alternate magnetic field; PEG, polyethylene glycol; EMA, European Medicines Agency; RGD, arginine-glycine-aspartate; pep-apoE, apolipoprotein E modified peptide; L-PGDS, lipocalin-type prostaglandin-d-synthase; BBB, blood–brain barrier; CPPs, cell-penetrating peptides; HIV-1, human immunodeficiency virus type 1; MNPs, magnetic nanoparticles; TAT-PLGA(MNPs), TAT functionalized PLGA containing MNPs; PVA, polyvinyl alcohol; EDC, 1-ethyl-3-(3-dimethylaminopropyl)carbodiimide; NHS, N-hydroxysuccinimide; IPTG, isopropyl-1-thio-β-D-galactopyranoside; EMEM; Eagle's minimum essential medium; AmpB, amphotericin b; XRD; X-ray diffraction; TEM, transmission electron microscopy; FPLC, fast protein liquid chromatography; DLS, dynamic light scattering; AFM, atomic force microscopy; SAR, specific absorption rate; ILP, intrinsic loss power.

References

1. Glasgow, M.D.K.; Chougule, M.B. Recent Developments in Active Tumor Targeted Multifunctional Nanoparticles for Combination Chemotherapy in Cancer Treatment and Imaging. *J. Biomed. Nanotechnol.* **2015**, *11*, 1859–1898. [CrossRef]
2. Jabalera, Y.; Oltolina, F.; Peigneux, A.; Sola-Leyva, A.; Carrasco-Jiménez, M.P.; Prat, M.; Jimenez-Lopez, C.; Iglesias, G.R. Nanoformulation Design Including MamC-Mediated Biomimetic Nanoparticles Allows the Simultaneous Application of Targeted Drug Delivery and Magnetic Hyperthermia. *Polymers* **2020**, *12*, 1832. [CrossRef] [PubMed]
3. Garcia-Pinel, B.; Jabalera, Y.; Ortiz, R.; Cabeza, L.; Jimenez-Lopez, C.; Melguizo, C.; Prados, J. Biomimetic Magnetoliposomes as Oxaliplatin Nanocarriers: In Vitro Study for Potential Application in Colon Cancer. *Pharmaceutics* **2020**, *12*, 589. [CrossRef]
4. Jabalera, Y.; Sola-Leyva, A.; Peigneux, A.; Vurro, F.; Iglesias, G.R.; Vilchez-Garcia, J.; Pérez-Prieto, I.; Aguilar-Troyano, F.J.; López-Cara, L.C.; Carrasco-Jiménez, M.P.; et al. Biomimetic Magnetic Nanocarriers Drive Choline Kinase Alpha Inhibitor inside Cancer Cells for Combined Chemo-Hyperthermia Therapy. *Pharmaceutics* **2019**, *11*, 408. [CrossRef]
5. Oltolina, F.; Peigneux, A.; Colangelo, D.; Clemente, N.; D'Urso, A.; Valente, G.; Iglesias, G.R.; Jiménez-Lopez, C.; Prat, M. Biomimetic Magnetite Nanoparticles as Targeted Drug Nanocarriers and Mediators of Hyperthermia in an Experimental Cancer Model. *Cancers* **2020**, *12*, 2564. [CrossRef]
6. El-Boubbou, K. Magnetic Iron Oxide Nanoparticles as Drug Carriers: Preparation, Conjugation and Delivery. *Nanomedicine* **2018**, *13*, 929–952. [CrossRef]
7. Prozorov, T.; Bazylinski, D.A.; Mallapragada, S.K.; Prozorov, R. Novel Magnetic Nanomaterials Inspired by Magnetotactic Bacteria: Topical Review. *Mater. Sci. Eng. R Rep.* **2013**, *74*, 133–172. [CrossRef]
8. Dobson, J. Magnetic Micro- and Nano-Particle-Based Targeting for Drug and Gene Delivery. *Nanomedicine* **2006**, *1*, 31–37. [CrossRef] [PubMed]
9. Li, Q.; Kartikowati, C.W.; Horie, S.; Ogi, T.; Iwaki, T.; Okuyama, K. Correlation between Particle Size/Domain Structure and Magnetic Properties of Highly Crystalline Fe_3O_4 Nanoparticles. *Sci. Rep.* **2017**, *7*, 9894. [CrossRef] [PubMed]
10. Valverde-Tercedor, C.; Montalbán-López, M.; Perez-Gonzalez, T.; Sanchez-Quesada, M.S.; Prozorov, T.; Pineda-Molina, E.; Fernandez-Vivas, M.A.; Rodriguez-Navarro, A.B.; Trubitsyn, D.; Bazylinski, D.A.; et al. Size Control of in Vitro Synthesized Magnetite Crystals by the MamC Protein of Magnetococcus Marinus Strain MC-1. *Appl. Microbiol. Biotechnol.* **2015**, *99*, 5109–5121. [CrossRef]
11. Peigneux, A.; Jabalera, Y.; Vivas, M.A.F.; Casares, S.; Azuaga, A.I.; Jimenez-Lopez, C. Tuning Properties of Biomimetic Magnetic Nanoparticles by Combining Magnetosome Associated Proteins. *Sci. Rep.* **2019**, *9*, 8804. [CrossRef] [PubMed]
12. Jabalera, Y.; Garcia-Pinel, B.; Ortiz, R.; Iglesias, G.; Cabeza, L.; Prados, J.; Jimenez-Lopez, C.; Melguizo, C. Oxaliplatin–Biomimetic Magnetic Nanoparticle Assemblies for Colon Cancer-Targeted Chemotherapy: An In Vitro Study. *Pharmaceutics* **2019**, *11*, 395. [CrossRef]
13. Jabalera, Y.; Fernández-Vivas, A.; Iglesias, G.R.; Delgado, Á.V.; Jimenez-Lopez, C. Magnetoliposomes of Mixed Biomimetic and Inorganic Magnetic Nanoparticles as Enhanced Hyperthermia Agents. *Colloids Surf. B Biointerfaces* **2019**, *183*, 110435. [CrossRef] [PubMed]
14. García Rubia, G.; Peigneux, A.; Jabalera, Y.; Puerma, J.; Oltolina, F.; Elert, K.; Colangelo, D.; Gómez Morales, J.; Prat, M.; Jimenez-Lopez, C. PH-Dependent Adsorption Release of Doxorubicin on MamC-Biomimetic Magnetite Nanoparticles. *Langmuir* **2018**, *34*, 13713–13724. [CrossRef] [PubMed]
15. Park, H.G.; Han, S.I.; Oh, S.Y.; Kang, H.S. Cellular Responses to Mild Heat Stress. *CMLS Cell. Mol. Life Sci.* **2005**, *62*, 10–23. [CrossRef] [PubMed]
16. Bettaieb, A.; Wrzal, K.P.; Averill-Bates, A.D. Hyperthermia: Cancer Treatment and Beyond. In *Cancer Treatment—Conventional and Innovative Approaches*; Rangel, L., Ed.; InTech Open: London, UK, 2013; ISBN 978-953-51-1098-9.
17. Das, P.; Colombo, M.; Prosperi, D. Recent Advances in Magnetic Fluid Hyperthermia for Cancer Therapy. *Colloids Surf. B Biointerfaces* **2019**, *174*, 42–55. [CrossRef]
18. Yallapu, M.M.; Foy, S.P.; Jain, T.K.; Labhasetwar, V. PEG-Functionalized Magnetic Nanoparticles for Drug Delivery and Magnetic Resonance Imaging Applications. *Pharm. Res.* **2010**, *27*, 2283–2295. [CrossRef]
19. Laurent, S.; Forge, D.; Port, M.; Roch, A.; Robic, C.; Vander Elst, L.; Muller, R.N. Magnetic Iron Oxide Nanoparticles: Synthesis, Stabilization, Vectorization, Physicochemical Characterizations, and Biological Applications. *Chem. Rev.* **2010**, *110*, 2574. [CrossRef]
20. Galli, M.; Rossotti, B.; Arosio, P.; Ferretti, A.M.; Panigati, M.; Ranucci, E.; Ferruti, P.; Salvati, A.; Maggioni, D. A New Catechol-Functionalized Polyamidoamine as an Effective SPION Stabilizer. *Colloids Surf. B Biointerfaces* **2019**, *174*, 260–269. [CrossRef]
21. Lee, D.-W.; Yu, J.-H.; Jang, T.; Kim, B.-K. Enhanced Oxidation Resistance of Iron Nanoparticles via Surface Modification in Chemical Vapor Condensation Process. *J. Mater. Sci. Technol.* **2010**, *26*, 367–370. [CrossRef]
22. Wu, S.; Ladani, R.B.; Zhang, J.; Kinloch, A.J.; Zhao, Z.; Ma, J.; Zhang, X.; Mouritz, A.P.; Ghorbani, K.; Wang, C.H. Epoxy Nanocomposites Containing Magnetite-Carbon Nanofibers Aligned Using a Weak Magnetic Field. *Polymer* **2015**, *68*, 25–34. [CrossRef]
23. Shin, M.C.; Zhang, J.; Min, K.A.; Lee, K.; Byun, Y.; David, A.E.; He, H.; Yang, V.C. Cell-Penetrating Peptides: Achievements and Challenges in Application for Cancer Treatment: Cell-Penetrating Peptides. *J. Biomed. Mater. Res.* **2014**, *102*, 575–587. [CrossRef] [PubMed]

24. Derakhshankhah, H.; Jafari, S. Cell Penetrating Peptides: A Concise Review with Emphasis on Biomedical Applications. *Biomed. Pharmacother.* **2018**, *108*, 1090–1096. [CrossRef]
25. Mosafer, J.; Teymouri, M. Comparative Study of Superparamagnetic Iron Oxide/Doxorubicin Co-Loaded Poly (Lactic-Co-Glycolic Acid) Nanospheres Prepared by Different Emulsion Solvent Evaporation Methods. *Artif. Cells Nanomed. Biotechnol.* **2018**, *46*, 1146–1155. [CrossRef] [PubMed]
26. Hirano, S.; Bovi, M.; Romeo, A.; Guzzo, F.; Chiamulera, C.; Perduca, M. Ketamine Nano-Delivery Based on Poly-Lactic-Co-Glycolic Acid (PLGA) Nanoparticles. *Appl. Nanosci.* **2018**, *8*, 655–663. [CrossRef]
27. Cherubin, A.; Destefanis, L.; Bovi, M.; Perozeni, F.; Bargigia, I.; de la Cruz Valbuena, G.; D'Andrea, C.; Romeo, A.; Ballottari, M.; Perduca, M. Encapsulation of Photosystem I in Organic Microparticles Increases Its Photochemical Activity and Stability for Ex Vivo Photocatalysis. *ACS Sustain. Chem. Eng.* **2019**, *7*, 10435–10444. [CrossRef]
28. Kumari, A.; Yadav, S.K.; Yadav, S.C. Biodegradable Polymeric Nanoparticles Based Drug Delivery Systems. *Colloids Surf. B Biointerfaces* **2010**, *75*, 1–18. [CrossRef]
29. Makadia, H.K.; Siegel, S.J. Poly Lactic-Co-Glycolic Acid (PLGA) as Biodegradable Controlled Drug Delivery Carrier. *Polymers* **2011**, *3*, 1377–1397. [CrossRef]
30. Danhier, F.; Ansorena, E.; Silva, J.M.; Coco, R.; Le Breton, A.; Préat, V. PLGA-Based Nanoparticles: An Overview of Biomedical Applications. *J. Control. Release* **2012**, *161*, 505–522. [CrossRef]
31. Lü, J.-M.; Wang, X.; Marin-Muller, C.; Wang, H.; Lin, P.H.; Yao, Q.; Chen, C. Current Advances in Research and Clinical Applications of PLGA-Based Nanotechnology. *Expert Rev. Mol. Diagn.* **2009**, *9*, 325–341. [CrossRef]
32. Hines, D.J.; Kaplan, D.L. Poly(Lactic-Co-Glycolic) Acid-Controlled-Release Systems: Experimental and Modeling Insights. *Crit. Rev. Ther. Drug Carr. Syst.* **2013**, *30*, 257–276. [CrossRef]
33. Danhier, F.; Pourcelle, V.; Marchand-Brynaert, J.; Jérôme, C.; Feron, O.; Préat, V. Targeting of Tumor Endothelium by RGD-Grafted PLGA-Nanoparticles. *Meth. Enzymol.* **2012**, *508*, 157–175. [CrossRef]
34. Portioli, C.; Bovi, M.; Benati, D.; Donini, M.; Perduca, M.; Romeo, A.; Dusi, S.; Monaco, H.L.; Bentivoglio, M. Novel Functionalization Strategies of Polymeric Nanoparticles as Carriers for Brain Medications: Peptidic Moieties Enable BBB Traversal of the NPs. *J. Biomed. Mater. Res.* **2017**, *105*, 847–858. [CrossRef] [PubMed]
35. Wang, B.; Wu, W.; Lu, H.; Wang, Z.; Xin, H. Enhanced Anti-Tumor of Pep-1 Modified Superparamagnetic Iron Oxide/PTX Loaded Polymer Nanoparticles. *Front. Pharmacol.* **2019**, *9*, 1556. [CrossRef] [PubMed]
36. Cantelmo, A.R.; Cammarota, R.; Noonan, D.M.; Focaccetti, C.; Comoglio, P.M.; Prat, M.; Albini, A. Cell Delivery of Met Docking Site Peptides Inhibit Angiogenesis and Vascular Tumor Growth. *Oncogene* **2010**, *29*, 5286–5298. [CrossRef] [PubMed]
37. Lee, J.-Y.; Choi, Y.-S.; Suh, J.-S.; Kwon, Y.-M.; Yang, V.C.; Lee, S.-J.; Chung, C.-P.; Park, Y.-J. Cell-Penetrating Chitosan/Doxorubicin/TAT Conjugates for Efficient Cancer Therapy: Cell-Penetrating Conjugates for Cancer Therapy. *Int. J. Cancer* **2011**, *128*, 2470–2480. [CrossRef]
38. Santra, S.; Yang, H.; Stanley, J.T.; Holloway, P.H.; Moudgil, B.M.; Walter, G.; Mericle, R.A. Rapid and Effective Labeling of Brain Tissue Using TAT-Conjugated CdS: Mn/ZnS Quantum Dots. *Chem. Commun.* **2005**, 3144. [CrossRef] [PubMed]
39. Liu, L.; Venkatraman, S.S.; Yang, Y.-Y.; Guo, K.; Lu, J.; He, B.; Moochhala, S.; Kan, L. Polymeric Micelles Anchored with TAT for Delivery of Antibiotics across the Blood-Brain Barrier. *Biopolymers* **2008**, *90*, 617–623. [CrossRef]
40. Wang, H.; Xu, K.; Liu, L.; Tan, J.P.K.; Chen, Y.; Li, Y.; Fan, W.; Wei, Z.; Sheng, J.; Yang, Y.-Y.; et al. The Efficacy of Self-Assembled Cationic Antimicrobial Peptide Nanoparticles against Cryptococcus Neoformans for the Treatment of Meningitis. *Biomaterials* **2010**, *31*, 2874–2881. [CrossRef]
41. Schwarze, S.R.; Hruska, K.A.; Dowdy, S.F. Protein Transduction: Unrestricted Delivery into All Cells? *Trends Cell Biol.* **2000**, *10*, 290–295. [CrossRef]
42. Kaplan, I.M.; Wadia, J.S.; Dowdy, S.F. Cationic TAT Peptide Transduction Domain Enters Cells by Macropinocytosis. *J. Control. Release* **2005**, *102*, 247–253. [CrossRef] [PubMed]
43. Brooks, H.; Lebleu, B.; Vives, E. Tat Peptide-Mediated Cellular Delivery: Back to Basics. *Adv. Drug Deliv. Rev.* **2005**, *57*, 559–577. [CrossRef]
44. Wadia, J.S.; Stan, R.V.; Dowdy, S.F. Transducible TAT-HA Fusogenic Peptide Enhances Escape of TAT-Fusion Proteins after Lipid Raft Macropinocytosis. *Nat. Med.* **2004**, *10*, 310–315. [CrossRef]
45. Wadia, J.; Dowdy, S. Transmembrane Delivery of Protein and Peptide Drugs by TAT-Mediated Transduction in the Treatment of Cancer. *Adv. Drug Deliv. Rev.* **2005**, *57*, 579–596. [CrossRef]
46. Peng, S.-L.; Lai, C.-H.; Chu, P.-Y.; Hsieh, J.-T.; Tseng, Y.-C.; Chiu, S.-C.; Lin, Y.-H. Nanotheranostics With the Combination of Improved Targeting, Therapeutic Effects, and Molecular Imaging. *Front. Bioeng. Biotechnol.* **2020**, *8*, 570490. [CrossRef] [PubMed]
47. Park, J.; Park, J.; Castanares, M.A.; Collins, D.S.; Yeo, Y. Magnetophoretic Delivery of a Tumor-Priming Agent for Chemotherapy of Metastatic Murine Breast Cancer. *Mol. Pharm.* **2019**, *16*, 1864–1873. [CrossRef]
48. Wen, X.; Wang, K.; Zhao, Z.; Zhang, Y.; Sun, T.; Zhang, F.; Wu, J.; Fu, Y.; Du, Y.; Zhang, L.; et al. Brain-Targeted Delivery of Trans-Activating Transcriptor-Conjugated Magnetic PLGA/Lipid Nanoparticles. *PLoS ONE* **2014**, *9*, e106652. [CrossRef] [PubMed]
49. Perez-Gonzalez, T.; Jimenez-Lopez, C.; Neal, A.L.; Rull-Perez, F.; Rodriguez-Navarro, A.; Fernandez-Vivas, A.; Iañez-Pareja, E. Magnetite Biomineralization Induced by Shewanella Oneidensis. *Geochim. Cosmochim. Acta* **2010**, *74*, 967–979. [CrossRef]

50. Gaglio, S.C.; De Rosa, C.; Piccinelli, F.; Romeo, A.; Perduca, M. Complexes of Rare Earth Ions Embedded in Poly(Lactic-Co-Glycolic Acid) (PLGA) Nanoparticles: Characterization and Spectroscopic Study. *Opt. Mater.* **2019**, *94*, 249–256. [CrossRef]
51. Predescu, A.M.; Matei, E.; Berbecaru, A.C.; Pantilimon, C.; Drăgan, C.; Vidu, R.; Predescu, C.; Kuncser, V. Synthesis and Characterization of Dextran-Coated Iron Oxide Nanoparticles. *R. Soc. Open Sci.* **2018**, *5*, 171525. [CrossRef]
52. Cotin, G.; Blanco-Andujar, C.; Nguyen, D.-V.; Affolter, C.; Boutry, S.; Boos, A.; Ronot, P.; Uring-Lambert, B.; Choquet, P.; Zorn, P.E.; et al. Dendron Based Antifouling, MRI and Magnetic Hyperthermia Properties of Different Shaped Iron Oxide Nanoparticles. *Nanotechnology* **2019**, *30*, 374002. [CrossRef]
53. Costanzo, M.; Malatesta, M. Embedding Cell Monolayers to Investigate Nanoparticle-Plasmalemma Interactions at Transmission Electron Microscopy. *Eur. J. Histochem.* **2019**, *63*. [CrossRef] [PubMed]
54. Park, E.; Gong, E.-Y.; Romanelli, M.G.; Lee, K. Suppression of Estrogen Receptor-Alpha Transactivation by Thyroid Transcription Factor-2 in Breast Cancer Cells. *Biochem. Biophys. Res. Commun.* **2012**, *421*, 532–537. [CrossRef] [PubMed]
55. Gneveckow, U.; Jordan, A.; Scholz, R.; Brüß, V.; Waldöfner, N.; Ricke, J.; Feussner, A.; Hildebrandt, B.; Rau, B.; Wust, P. Description and Characterization of the Novel Hyperthermia- and Thermoablation-System MFH®300F for Clinical Magnetic Fluid Hyperthermia. *Med. Phys.* **2004**, *31*, 1444–1451. [CrossRef] [PubMed]

Journal of Colloid and Interface Science 596 (2021) 332–341

Contents lists available at ScienceDirect

Journal of Colloid and Interface Science

journal homepage: www.elsevier.com/locate/jcis

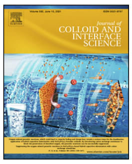

Regular Article

Polymer-coated silver-iron nanoparticles as efficient and biodegradable MRI contrast agents

Vincenzo Amendola [a,*], Andrea Guadagnini [a], Stefano Agnoli [a], Denis Badocco [a], Paolo Pastore [a], Giulio Fracasso [b], Marco Gerosa [c], Federica Vurro [c], Alice Busato [c], Pasquina Marzola [c,*]

[a] *Department of Chemical Sciences, University of Padova, Padova I-35131, Italy*
[b] *Department of Medicine, University of Verona, Verona, Italy*
[c] *Department of Computer Science, University of Verona, Verona 37134, Italy*

GRAPHICAL ABSTRACT

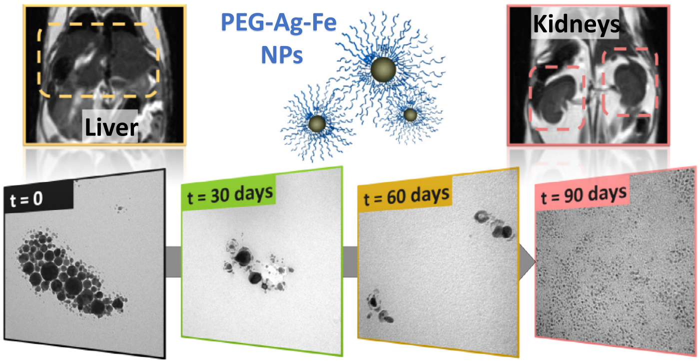

ARTICLE INFO

Article history:
Received 16 January 2021
Revised 24 February 2021
Accepted 15 March 2021
Available online 19 March 2021

Keywords:
Silver nanoparticles
Bimetallic nanoparticles
Laser ablation
MRI, biodegradation

ABSTRACT

Bimetallic nanoparticles allow new and synergistic properties compared to the monometallic equivalents, often leading to unexpected results. Here we present on silver-iron nanoparticles coated with polyethylene glycol, which exhibit a high transverse relaxivity (316 ± 13 mM^{-1}s^{-1}, > 3 times that of the most common clinical benchmark based on iron oxide), excellent colloidal stability and biocompatibility *in vivo*. Ag-Fe nanoparticles are obtained through a one-step, low-cost laser-assisted synthesis, which makes surface functionalization with the desired biomolecules very easy. Besides, Ag-Fe nanoparticles show biodegradation over a few months, as indicated by incubation in the physiological environment. This is crucial for nanomaterials removal from the living organism and, in fact, *in vivo* biodistribution studies evidenced that Ag-Fe nanoparticles tend to be cleared from liver over a period in which the benchmark iron oxide contrast agent persisted. Therefore, the Ag-Fe NPs offer positive prospects for solving the problems of biopersistence, contrast efficiency, difficulties of synthesis and surface functionalization usually encountered in nanoparticulate contrast agents.

---

* Corresponding authors.
E-mail addresses: vincenzo.amendola@unipd.it (V. Amendola), pasquina.marzola@univr.it (P. Marzola).

https://doi.org/10.1016/j.jcis.2021.03.096
0021-9797/

1. Introduction

Bimetallic nanoparticles (NPs) are appreciated for the range of original and synergistic properties compared to single element analogues, as well as for providing fundamental information on how different elements of the periodic table grow and arrange at the nanoscale, in each specific conditions [1–2]. Structural motifs in nonequilibrium noble metal alloy clusters offer new ways for controlling atomic arrangement into complex shapes and structures [3]. Iron-gold core–shell nanoparticles were studied as model systems for element segregation and thermodynamics of nanoalloys during the out-of-equilibrium synthesis of nanoparticles by laser ablation in liquid [4]. Au-Pd NPs are studied as a green technology for water remediation by simultaneous photocatalytic oxidation of phenol and reduction of hexavalent chromium [5]. Bimetallic copper-silver nanoparticles have been studied as model systems for the mechanism of antimicrobial killing [6]. Polymer coated Au-Pd nanoparticles have bimodal cancer therapy activity by combining radiosensitization and photothermal therapy [7], while Au-Ag NPs enabled dual-modal imaging by X-ray computed tomography (CT) and dual-energy mammography [8].

In the field of contrast agents for magnetic resonance imaging (MRI), several multicomponent NPs have been proposed as contrast agents (CA) with appealing properties [9]. Ag-Gd nanoparticles were developed for multimodal imaging and pH-responsive doxorubicin release [10]. MRI, CT and luminescent imaging was possible with the same Eu(III)-doped core–shell NPs [11]. Au-Fe nanoalloys showed a range of composition-dependent properties such as trimodal imaging ability (MRI, CT and Raman) at low iron content (~11 at%) [12], or bimodal MRI/CT contrast ability and a 4-D behaviour with spontaneous degradation *in vivo* at higher iron content (>30 at%) [13]. Nickel [14] or gadolinium [15] doped ferrites can be designed to obtain superior properties for simultaneous use in magnetic resonance imaging and magnetic fluid hyperthermia. MRI-guided photodynamic therapy was demonstrated with manganese ferrite NPs loaded with organic photosensitizers [16].

Compared to molecular CA based on Gd(III) chelates, nanometric CA have also other advantages due to the longer circulation time, instead of immediate renal clogging, thus with a facilitated accumulation in the imaged lesions or tumors by the enhanced permeation and retention effect [9,17]. By avoiding massive and quick renal accumulation, allergic reactions up to anaphylactic shock, renal toxicity and specific reactions such as the nephrogenic systemic fibrosis induced by Gd(III) chelates are prevented. Besides, the total dose of CA can be much lower, with the advantages of higher drug tolerability, shorter administration time and lower risk of accumulation of metals in the brain, as observed again with Gd(III) chelates [9,17–18]. In fact, it is important to reduce the problems of the transmetallation of Gd(III) complexes since calcium, zinc or iron ions can displace Gd from chelates increasing its toxicity by accumulation in the tissues [19].

Nonetheless, the biopersistence of nanomaterials in living organisms is a major issue [18], even when dealing with NPs of biocompatible elements such as the chemically inert noble metals or elements with a well-defined role in human metabolism like iron [20–23]. This is the dilemma of nanomedicine: [13] dose and biodistribution are optimal in a size range that is not compatible with the clearance of nanomaterials, hence the ideal nanomedicines should evolve their size over time [13,24]. For this reason, there is a growing interest in the development of biodegradable nanomedicines with organic [25–26], inorganic [13,27–28] or hybrid [29–31] composition.

Other frequent issues of the nano-medicines are the surface functionalization with the desired biomolecules, not easy when coating agents are indispensable for the synthesis of NPs, and the need to avoid expensive, multistep and not-scalable synthetic procedures often sought for accessing to multielement nanostructures [9,17–18].

Here we describe silver-iron nanoparticles coated with polyethylene glycol (PEG), that exhibit a transverse relaxivity (r_2) > 3 times that of the most common clinical benchmark based on iron oxide (Feridex/Endorem), in addition to excellent colloidal stability and biocompatibility *in vivo*. Importantly, the Ag-Fe nanoparticles show biodegradation over a few months in the physiological environment at lysosomal pH. The *in vivo* biodistribution in mice evidenced the massive clearance from liver over 30 days, a period after which the benchmark iron oxide CA persisted without relevant changes.

The Ag-Fe NPs are obtained by a one-step synthetic approach based on laser ablation in liquid (LAL). LAL relies on a relatively simple and self-standing set-up, that can be controlled also remotely with a PC or a smartphone [32–33]. This method proved to be versatile and successful for the preparation of a library of single and multi-element colloidal nanoparticles, also with metastable phases [12,34–35]. The procedure is usually low-cost and environmentally friendly [33,36–38]. Another advantage of Ag-Fe nanoparticles obtained by LAL is that they can be surface functionalized with the desired biomolecules very easily [39–40].

Therefore, the Ag-Fe NPs offer positive prospects for the crucial problem of nanomaterials removal from the living organism, while offering at the same time efficient contrast, easy synthesis and straightforward surface functionalization. This further demonstrates that bimetallic nanocrystals provide useful and innovative behaviours of great interest for nanotechnological applications.

2. Experimental methods

2.1. Synthesis

Ag-Fe NPs were obtained by LAL, using 1064 nm (6 ns, 50 Hz) pulses of a Nd-YAG laser focused with an f 100 mm lens up to a fluence of 20 J/cm^2 on a bimetallic target composed of 25 at% Ag and 75 at% Fe (from Mateck GmbH) and placed at the bottom of a cell containing pure ethanol (HPLC grade, from Sigma-Aldrich). The ablated target area was set to 5 mm × 5 mm in 300 s, by mounting the cell on a motorized XY scanning stage (Standa) managed with a 2-axis stepper and a DC motor controller.

The so-obtained Fe-Ag NPs colloid was concentrated with a rotavapor at 30 °C, then mixed 1:1 v/v with an aqueous solution containing ethylenediaminetetraacetic acid disodium salt dihydrate (disodium EDTA, Sigma-Aldrich, 3 mg/mL) and 0.1 mg/mL of thiolated polyethylene glycol (PEG-SH, 6000 Da, Sigma-Aldrich) or 0.1 mg/mL of bovine serum albumin (BSA, Sigma-Aldrich). The mixture was kept for 60 min at 30 °C, then washed with distilled water using dialysis concentration membranes (Sartorius, 10 kDa) until redispersion in distilled water. Then, the Ag-Fe NPs were centrifuged at 40 rcf for 1 h in 1.5 mL tubes to discard the heavy sediment, and at 700 rcf for 1 h to collect the heavy fraction while discarding the supernatant. The sediment of the 700 rcf centrifugation run was redispersed in distilled water and identified as the PEG-Fe-Ag NPs (or BSA-Fe-Ag NPs) sample.

2.2. Characterization

UV–visible spectra were recorded with a JASCO V770 spectrophotometer using quartz cells with a 2 mm optical path. Fourier transformed infrared (FTIR) spectroscopy was performed with a Perkin Elmer 1720X FTIR spectrophotometer, depositing the dried samples on a KBr window. Dynamic light scattering (DLS) was performed with a Malvern Zetasizer Nano ZS in DTS1070 cells. Transmission electron microscopy (TEM) analysis was performed with a FEI Tecnai G2 12 transmission electron microscope operating at 100 kV and equipped with a TVIPS CCD camera. The samples for TEM analysis were prepared by evaporating NP suspensions on a copper grid coated with an amorphous carbon holey film. For the ageing experiment, the PEG-Ag-Fe NPs were dispersed at 0.05 mg/mL concentration in 20% v/v foetal calf serum (FCS, Sigma-Aldrich) at pH 4.5 (by adding acetate buffer), then incubated at 37 °C and analyzed at different time points (0, 30, 60 and 90 days). Each time, a drop of the solution was deposed on a copper grid coated with an amorphous carbon film. ImageJ software was used to measure the geometrical (Feret) size distributions. Statistics considered more than n = 500 NPs for each sample. The average Feret size and standard deviation were obtained from these statistics. Energy dispersive X-ray (EDX) microanalysis was performed with an environmental scanning electron microscope model FEI Quanta 200 on a sample of PEG-Ag-Fe NPs drop cast on a glassy carbon substrate, without further metallization. EDX analysis on isolated Ag-Fe NPs was performed by drop casting a diluted colloid on a crystalline Si substrate.

Inductively coupled plasma-assisted mass spectroscopy (ICP-MS) measurements were performed with ICP-MS Agilent 7700x (Agilent Technologies), equipped with an octupole collision cell operating in kinetic energy discrimination mode for the removal of polyatomic interferences and argon-based interferences. Standard Ag and Fe solutions for the instrumental calibration, were purchased from Multistandard IV-ICPMS-71A (Inorganic-Ventures). For sample digestion, the solutions were accurately weighed and digested with 14 vol% of HNO_3 69% at 100 °C for 2 h. The resulting solution was diluted with the same solvent used for calibrations.

Carbon and hydrogen content was measured in lyophilized Ag-Fe NPs with an Organic Elemental Analyzer FLASH 2000 Thermo Scientific.

X-ray diffraction (XRD) analysis was performed with a Panalytical XPert 3 Powder diffractometer equipped with a Cu tube (40 kV, 40 mA), a BBHD mirror, a spinner and a PIXcel detector. The samples were deposed on Si zero-background substrates by drop-casting and drying at room temperature. Crystalline phase identification was executed with the Panalytical High Score Plus 4 software and Panalytical ICSD, PDF2 and COD databases.

X-ray photoelectron spectroscopy (XPS) analysis was performed at room temperature using normal emission geometry with a modified VG ESCALAB MKII (Vacuum generators, Hastings, England) equipped with a Mg anode X-ray source (K_α radiation at 1253.6 eV), a sputter gun, and a hemispherical electrostatic analyzer with a five-channel detector. The sample was obtained by dropwise deposition of a Ag-Fe NPs dispersion on a Cu sample holder and drying at room temperature.

2.3. Citotoxicity

RAW264.7 and 4 T1 cells, supplied by ATCC (American Type Culture Collection, Manassas, VA, US) were seeded one day before the experiment in a 96 well plate. The day after cells were treated with PEG-Ag-Fe NPs or BSA-Ag-Fe NPs at various dilution (5.4, 10.8, 21.6, 32.3, 43.1, 53.9 mg/ml of total mass of metal Ag + Fe) for 24 h. The maximum concentration of NPs corresponds to a Fe concentration comparable to the peak serum concentration of Fe in Endorem in the conventional human dosage. At the end of the experiment, cell viability was detected following the XTT assay instruction. Cell viability was calculated analyzing the ratio between the absorbance of treated samples and mock treated samples.

2.4. MRI analysis

Magnetic resonance images were acquired with a Bruker system operating at 7 T (Bruker Biospin, Ettlingen, Germany). The samples were dispersed in water by serial dilution starting from a solution with Fe concentration of 0.44 mM. The transversal relaxation times (r_2 value) was calculated from the slopes of the best fit lines of relaxation rates ($1/T_2$) versus iron concentration. The T_2 map in phantoms were acquired using a Multi Slice Multi Echo (MSME) sequence with the following parameters: TR = 2000 ms, TE from 6.5 to 170.43 ms, FOV = 55 × 55 mm, matrix size = 128 × 128, slice thickness = 1 mm, number of echoes = 25.

In vivo experiments were performed with Balb/c male mice (6–8 weeks old, Envigo). Mice were intravenously injected with PEG-Ag-Fe or Endorem (Guerbet) NPs at a dosage of 5 mg_Fe/kg. For MRI acquisitions, animals were anaesthetized with a mixture of O_2 and air containing 1–1.5% of isoflurane, placed in a heated animal bed and inserted in a 7.2 cm internal diameter bird-cage coil. T_2-weighted images of the mice body were acquired using a Rapid Acquisition with Relaxation Enhancement (RARE) sequence with the following parameters: FOV = 60 × 40 mm, MTX = 256 × 256, slice thickness = 1 mm, TE = 19 ms and TR = 2.500 ms. The images were acquired before (t = 0) and 1, 6, 24, 48 h, 5, 14 and 30 days after NPs injection. T_2 signal intensity was calculated by Region of Interest (ROI) and normalized by the ROI defined on the white signal produced from the fat tissue. Before each MRI acquisition, an automatic calibration procedure was applied to prevent the saturation of digitizer. Thanks to this calibration, the tomograph sets the receiver gain on the maximum of the signal avoiding the saturation of the digitizer. T_2 map images were acquired using a multi slice multi echo (MSME) sequence with following parameters: TR = 3000 ms; TE = from 6.8 to 68 ms; FOV = 40 × 35 mm; MTX = 128 × 128; slice thickness = 1 mm; n-slice = 20). *In vivo* experiments were carried out with the authorization of the Italian Ministry of Health and the Committee for Research on Laboratory Animals of the University of Verona.

2.5. Histopathology analysis

After 30 days from NPs injection, mice were sacrificed and organs dissected out for histopathology analysis. The organs were washed with phosphate-buffered saline (PBS) 0.1 M and fixed in 10% formalin for 4 h. Tissues were embedded in paraffin and cut in 5 μm thick sections with a microtome and dried at 37 °C for 24 h. To evaluate the presence of Fe in the tissue, prussian blue (PB) staining (Iron staining) was performed on liver and kidney: sections were incubated with PB solution (5% hydrochloric acid and 5% potassium ferrocyanide) for 40 min and counterstained with nuclear fast red (Bio-Optica) for 10 min. To morphologically evaluate tissue damage, sections of liver and kidney were also stained with Hematoxylin-Eosin (HE, Bio-Optica). Sections were examined under a light microscope (Olympus BXS1) equipped with a charge-coupled device camera and, subsequently, analysed also with the ESEM after removal of the top cover glass by dipping in xylene for 2 h.

3. Results and discussion.

Ag-Fe NPs were obtained by LAL in ethanol, starting from a bimetallic Ag-Fe target irradiated with 1064 nm (6 ns) laser pulses at a fluence of 20 mJ/cm^2 (Fig. 1A, left) following a previously established procedure [39–40]. These experimental conditions avoid the complete oxidation of iron or the segregation of the two components [39–40], despite the thermodynamic phase diagram of the Ag-Fe alloy does not contemplate miscibility beyond

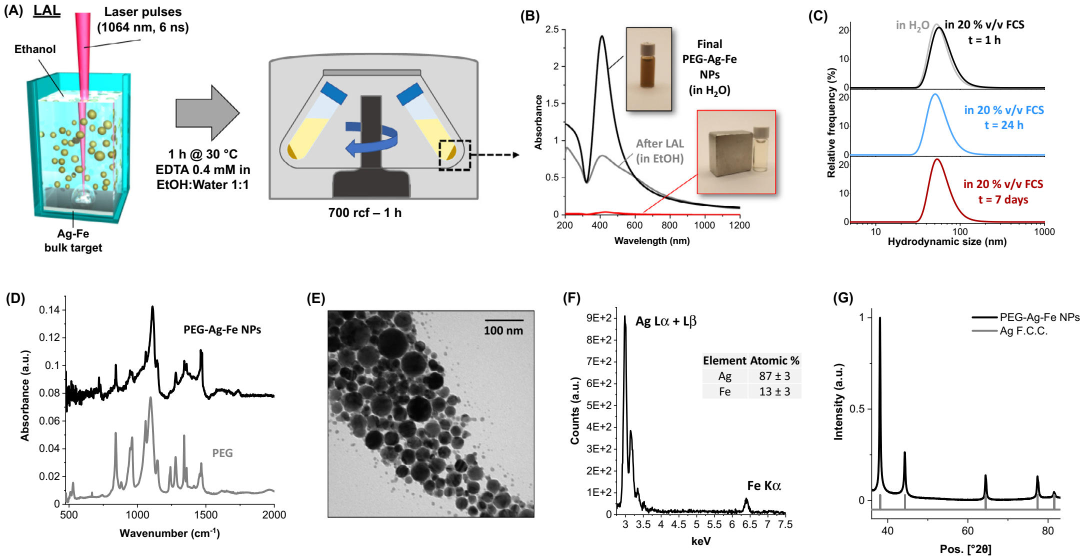

Fig. 1. (A) Sketch of the synthesis procedure: Ag-Fe NPs are produced by LAL, dialysed with water after 1 h in EDTA/PEG solution and centrifuged to collect the heavy fraction, that is redispersed in distilled water. (B) UV–vis spectra of final PEG-Ag-Fe NPs in water (black line) and of Ag-Fe NPs as obtained from LAL in pure ethanol (grey line). The spectrum of the solution after migration of the PEG-Ag-Fe NPs in proximity of a permanent NdFeB magnet (shown in the inset) is also reported (red line). (C) Hydrodynamic size distribution measured by DLS on PEG-Ag-Fe NPs dispersed in water (grey line) or after 1 h (black line), 24 h (blue line) and 7 days (wine-red line) in 20% v/v FCS. (D) FTIR spectra of PEG-Ag-Fe NPs (black line) and a reference PEG powder (grey line). (E) Representative TEM image of PEG-Ag-Fe NPs. (F) EDX analysis of PEG-Ag-Fe NPs. (G) Powder XRD pattern of PEG-Ag-Fe NPs (black) and expected reflections of the Ag F.C.C. structure (grey). (For interpretation of the references to colour in this figure legend, the reader is referred to the web version of this article.)

traces of one element in the other [41]. Nonetheless, some iron by-products form during LAL, even in ethanol that is a less oxidising environment compared to other solvents like water. The iron compounds present as synthesis by-products are effectively removed by a purification procedure consisting in the addition of a 1:1 v/v disodium EDTA aqueous solution (0.8 mM) and mixing for 1 h at 30 °C. Simultaneously, the desired thiolated compounds can be added to the solution, in order to bind particles surface by a metal-sulphur chemical bond with the Ag atoms, that are free from any other chemical capping agent. In this case, thiolated PEG (6000 Da) was used as an effective and biocompatible stabilizer for the NPs. Thus, the colloidally stable Ag-Fe NPs are cleaned from the other undesired or colloidally unstable compounds by dialysis (10 kDa cut off) and transferred in distilled water. Since the size and composition of the Ag-Fe NPs cannot be controlled by acting on LAL parameters such as the laser power, a last cleaning step consisting in centrifugation of the colloid at 70 rcf for 1 h, to remove the sediment, and at 700 rcf for 1 h to collect the heavy fraction (Fig. 1A, right) is performed, to remove very large and ultra-small NPs. The final PEG-Ag-Fe NPs sample is analysed by UV–visible spectroscopy (Fig. 1B). The absorption spectrum (black line in Fig. 1B) is indicative of Ag nanostructures, because of the intense peak at 408 nm due to the surface plasmon resonance (SPR) [39–40,42]. Compared to the absorption spectrum of the colloid just obtained after LAL (grey line in Fig. 1B), the PEG-Ag-Fe NPs have a much sharper SPR band, that is an indication of effective dispersion and de-aggregation of the particles after the treatment with EDTA/PEG and the purification procedure. The bimetallic composition of the Ag-Fe NPs is easily verified by observing their magnetophoretic accumulation in proximity of a permanent NdFeB magnet, that is complete after 3 days (see red line and insets of Fig. 1B). The process required several days because of the efficacy of PEG coating for particles colloidal stability, that is renowned even at very high nanomaterials concentration [43–45]. This was further assessed by DLS (Fig. 1C), where similar average hydrodynamic sizes of 60 ± 19 nm and 65 ± 23 nm are measured in, respectively, pure water and in a solution of FCS 20% v/v. The hydrodynamic size range is equivalent to that of Endorem iron oxide NPs (50 – 190 nm), that can be considered as the benchmark of nanoparticulate contrast agents [46–47]. Importantly for the effective biodistribution of nanoparticles *in vivo*, the hydrodynamic size of the PEG-Ag-Fe NPs did not undergo significant changes after 24 h (58 ± 20 nm) and 7 days (62 ± 21 nm) of incubation at 37 °C in the same 20% v/v FCS solution (respectively, blue and wine-red lines in Fig. 1C). Indeed, serum proteins may contribute to stabilize the NPs and it was evidenced that PEG-SH can be released from NPs at 37 °C and in physiological environment [48], therefore we repeated the DLS analysis on PEG-Ag-Fe NPs incubated 1/1 v/v with PBS (pH 7.4) or acetate buffer (pH 4.5, same as in cell lysosomes). The results (Figure S1 in S.I.) show that the colloidal stability persisted without changes in PBS also after 6 days. Even in acetate buffer the colloidal stability persisted, although smaller nanoparticles appeared after 24 h, that is promising for a desirable NPs degradation in lysosomes as discussed later.

The coating of Ag-Fe NPs with PEG was verified also by FTIR spectroscopy (Fig. 1D), where the vibrational fingerprint of the polyethylene glycol backbone, such as the intense C—O—C stretching at 1100 cm^{-1} and the vibrational progression in the 800–1500 cm^{-1} range, are clearly identified in the NPs like in the pure PEG reference. According to organic elemental analysis, the PEG mass fraction in the PEG-Ag-Fe NPs is 27 ± 1 w%. Using the average Feret size measured by TEM (20 ± 14 nm, Fig. 1E), it can be estimated a density of ca. 1 PEG chain per nm^2 of nanoparticle surface. Although the organic PEG shell is not detected by electron microscopy without appropriate staining, TEM indicates that the metal cores in the PEG-Ag-Fe NPs have a spherical shape (Fig. 1E). The average size is compatible with the DLS result considering that the 6000 Da PEG shell is expected to increase the hydrodynamic size of the metal core of several tens of nm (~40 nm according to ref. [49–50]. EDX spectroscopy clearly shows the Ag L_α and L_β series at 2.98 – 3.15 keV and the Fe K_α peak at 6.40 keV in the PEG-Ag-Fe NPs (Fig. 1F), with a quantitative composition of 87 at% of Ag and 13 at% of Fe. The simultaneous presence of the Ag L series and the Fe K peak was verified also in isolated Ag-Fe NPs (Figure S2 in S.I.), in agreement with single particle analysis previously reported [39–40]. The elemental composition was confirmed with higher accuracy by ICP-MS, that also measured 87 at% of Ag and 13 at% of Fe.

It has been previously assessed that the Ag-Fe NPs obtained by LAL in ethanol have a face-centred cubic (F.C.C.) structure with same cell parameter as in pure Ag, due to the high mixing enthalpy of the two elements and consequent segregation of the minority constituent into defective and disordered domains [39–40,51]. This is confirmed by the powder XRD pattern reported in Fig. 1G, that features the same reflections of F.C.C. Ag.

The ability of the PEG-Ag-Fe NPs to shorten the transverse relaxation time (T_2) of nearby water protons during MRI was measured in phantoms obtained by serial dilution of a solution with 0.44 mM concentration in Fe atoms (the magnetic centers). The results (Fig. 2A) evidenced a remarkable CA ability, with a transverse relaxivity r_2 of 316 ± 13 $mM(Fe)^{-1}\ s^{-1}$ in the linear portion of the plot of $1/T_2$ versus iron concentration. This value is > 3 times that of the benchmark clinical CA based on dextran-coated iron oxides (Endorem/Feridex) [12,52–53]. The inverse of the relaxation time grows monotonously in the whole range of concentrations tested in the experiment, which is of more than two orders of magnitude (0.0034 – 0.44 mM(Fe)). This is qualitatively appreciable also from the T_2-weighted cross-sectional images of phantoms reported in Fig. 2B.

Given the promising MRI CA features in terms of relaxivity and colloidal stability, a preliminary test of PEG-Ag-Fe NPs biocompatibility was performed *in vitro*. Cell viability was evaluated with XTT assay by incubating for 24 h the PEG-Ag-Fe NPs at a variable concentration up to 53.9 mg/mL of total metal mass with mouse mammary tumor cells (4 T1, Fig. 2C) and monocyte/macrophage like mouse cells (RAW264.7, Fig. 2D). The two cell types were selected in order to have different uptake and NPs dissolution abilities. In all cases, no changes in cell viability were detected. Also, BSA-coated Ag-Fe NPs (BSA-Ag-Fe NPs) were tested, since nanoparticles in living organisms may undergo to coating with serum proteins over time (i.e. protein corona), that may significantly change their interaction with cells compared to the stealth PEG coating [52,54–55].

The observed biocompatibility was expected from the LAL synthetic protocol [13,34,38] which starts from pure metal targets in pure ethanol and prosecute through basic purification steps to obtain nanostructures in the absence of undesired or toxic chemicals. On the other hand, it has been reported that biocompatibility of Ag-based NPs is obtained by slowing down the release of Ag^+ ions to the environment [8,10,56], according to the most general pharmaceutical principle “the dose makes the poison” [22,57]. This can be achieved by a dense surface coating with a biocompatible organic shell [10,56] and by mixing Ag with other metals like Au [8], Cu [6] or a “sacrificial” transition metal [58]. Thus, the cytocompatibility results reported in Fig. 2C,D points to the effectiveness of the PEG coating and the composition of the Ag-Fe NPs in avoiding the quick release of toxic ions in the physiological environment. The possible sacrificial redox role of Fe in the Ag-Fe NPs was assessed by XPS analysis (Fig. 2E,F). The photoemission line of Ag ($3d_{5/2}$ peak, Fig. 2E) is centered at a binding energy (BE) of 368 eV, which is the typical Ag(0) value expected for plasmonic Ag. The Fe photoemission spectrum, reported in Fig. 2F, is constituted by several components with a complex multiplet structure, well fitted with Fe(III) oxides and hydroxides (709–714 eV) and a minoritary component at values of metal Fe (707 eV). According to previous XPS analysis reported in literature for these Ag-Fe NPs [39], the metal component is ascribable to iron inside the particles, while the Fe(III) component dominates the surface, as expected in the aqueous environment. Thus, XPS confirms that Fe undergoes to oxidation while Ag in the Ag-Fe NPs is still in the metallic state.

Since the oxidation of Ag is expected in the aqueous solution, especially in conditions mimicking *in vivo* biological environments [59], we performed ICP-MS analysis of Ag and Fe released from the PEG-Ag-Fe NPs (0.051 mg/mL of total metal mass) incubated at

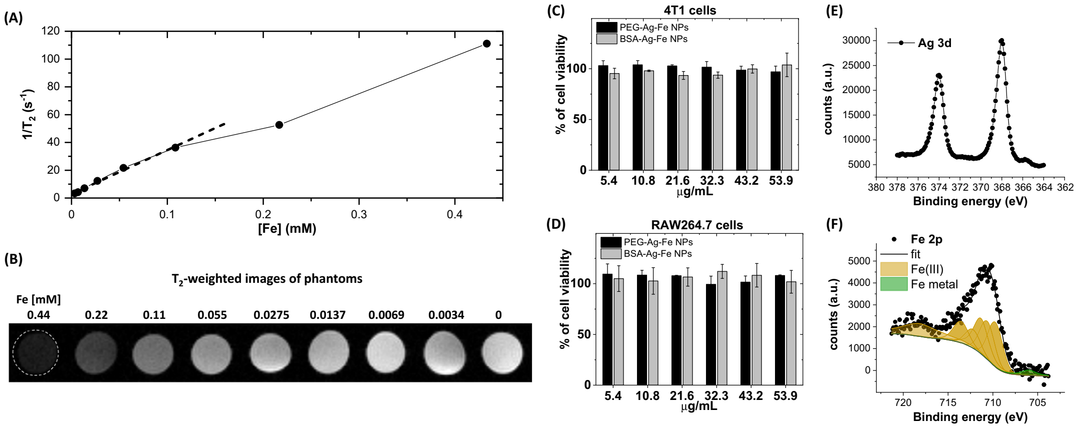

Fig. 2. (A) Transverse relaxivity ($r_2 = 1/T_2$) versus Fe concentration from PEG-Ag-Fe NPs. (B) T_2-weighted images of PEG-Ag-Fe NPs phantoms. (C-D) Cell viability of 4 T1 (C) and RAW264.7 (D) cells incubated for 24 h with PEG-Ag-Fe NPs or BSA-Ag-Fe NPs at concentrations ranging from 5.4 to 53.9 µg/mL of total metal mass. (E) XPS Ag 3d peak. (F) XPS Fe 2p peak. The experimental results (black circles) are fitted (black line) with the Fe(III) multiplet (light brown) and the metal Fe component (green). (For interpretation of the references to colour in this figure legend, the reader is referred to the web version of this article.)

37 °C in 1/1 v/v PBS (pH 7.4) and acetate buffer (AB, pH 4.5) for 6 days. In this experiment, the NPs were collected by centrifugation for 20′ at 10,000 rcf, while the supernatant was collected and analysed with ICP-MS. In the PBS solution, there is no clear evidence of the release of Ag, while Fe content increases with time, in the order of 0.1 w% (Figure S3 in S.I.). In AB, after 6 days the release of Ag and Fe are in the order of, respectively, 0.2 and 0.1 w% of the NPs mass, thus confirming that iron dissolution takes place at least simultaneously to Ag and that the release of silver is slow, in agreement with the cell viability experiments.

Then, the biodistribution and MRI CA ability were investigated *in vivo* in healthy mice, at different time-points up to 30 days. PEG-Ag-Fe NPs were administered at a concentration of 5 mg (Fe)/kg(mouse), after dispersion in PBS. T_2-weighted contrast (i.e. the change in the T_2 signal) increased in liver 1 h after NPs administration (top of Fig. 3A) but is not appreciable in the images collected after 30 days. Conversely, the contrast in kidneys slowly increased, as indicated by the images collected after 14 and 30 days (bottom of Fig. 3A). This suggests that the NPs fluxed from the liver to the kidneys, where they can take the clearance pathway of urines. A more precise indication on NPs biodistribution is shown in the plot of T_2 signal change (measured as the T_2 signal intensity decrease in %) in liver, spleen and kidneys (Fig. 3B). The plot confirms that the T_2 signal change is maximum in liver at 1 h after injection of NPs (26 ± 2%), and continuously changed until almost complete recovery after 30 days (2 ± 1%). The trend in spleen and kidneys is opposite, with a negligible change 1 h after NPs injection (respectively, 2 ± 1% and 0%), followed by a continuous T_2 signal intensity decrease up to, respectively, 26 ± 4% and 22 ± 6%. Noticeably, the signal changes earlier in the spleen than in kidneys, with a difference of a few days. This trend was confirmed also by quantitative T_2 map measurements (see Figure S4 in S.I.). Finally, the T_2 signal intensity decrease (%) in muscle (a tissue rich in blood vessels which reflects the presence of contrast agents in the bloodstream) was also reported in Fig. 3B (grey triangles). The T_2 signal intensity in the muscle decreased by 22% 1 h after Ag-Fe NPs injection but returned to its background level ca. 100 h after administration of the NPs. This trend is in agreement with the T_2 signal dynamics observed in the other organs, pointing to the optimal biodistribution of the Ag-Fe NPs, that are not accumulated immediately in liver, spleen or kidneys.

To better understand the *in vivo* results of PEG-Ag-Fe NPs, the biodistribution of a benchmark CA like the dextran-coated iron oxides (Endorem) NPs was also measured in the same conditions (i.e. healthy mice with a dose of 5 mg(Fe)/kg(mouse)). In this case, the plot of T_2 signal intensity decrease (%) has a different evolution in time (Fig. 3C and Figure S5 in S.I.), because the signal changes abruptly 1 h after administration in all three organs considered (liver, spleen and kidneys). Subsequently, the T_2 signal intensity decrease (%) underwent a much slower change over the 30 days of the experiment. In particular, the percentage of signal intensity decrease in liver, spleen and kidneys at 30 days (respectively, 45 ± 5%, 54 ± 4% and 27 ± 2%) are similar to those after 1 h (respectively, 77 ± 4%, 40 ± 2% and 42 ± 6%). The T_2 signal intensity decrease (%) in muscle resulted of only 5% 1 h after Endorem injection and remained almost constant over 30 days, further confirming the long-term accumulation of Endorem iron oxide NPs in the other organs.

Overall, the *in vivo* MRI results suggest that PEG-Ag-Fe NPs have longer circulation time than Endorem, with low accumulation in liver and absence of high accumulation in spleen and kidneys in the first days after administration. This feature of the PEG-Ag-Fe NPs is useful for biodegradation, that is slower when NPs aggregate and massively accumulate in cells, as recently reported for iron oxides [60]. According to the plot in Fig. 3B, on a timescale of days to weeks, the Ag-Fe NPs takes the way of renal clearance through the spleen, where macrophages bring the payload of bodies phagocyted, to complete the dissolution at acidic pH inside their lysosomes and release the waste in the kidneys through the circulatory system [61]. This process allowed the massive clearance of nanoparticles from liver and suggests that Ag-Fe NPs underwent size reduction over time. Conversely, the results for Endorem are indicative of accumulation in liver and spleen with a limited dissolution of the iron oxide nanoparticles into small fragments, corresponding to a limited clearance through urines.

The histological examination of the liver and kidneys (Fig. 4) added further information to the outcomes of MRI biodistribution measurements. Prussian blue staining (iron staining) was used to detect the presence of iron in the tissue by deposition of blue crys-

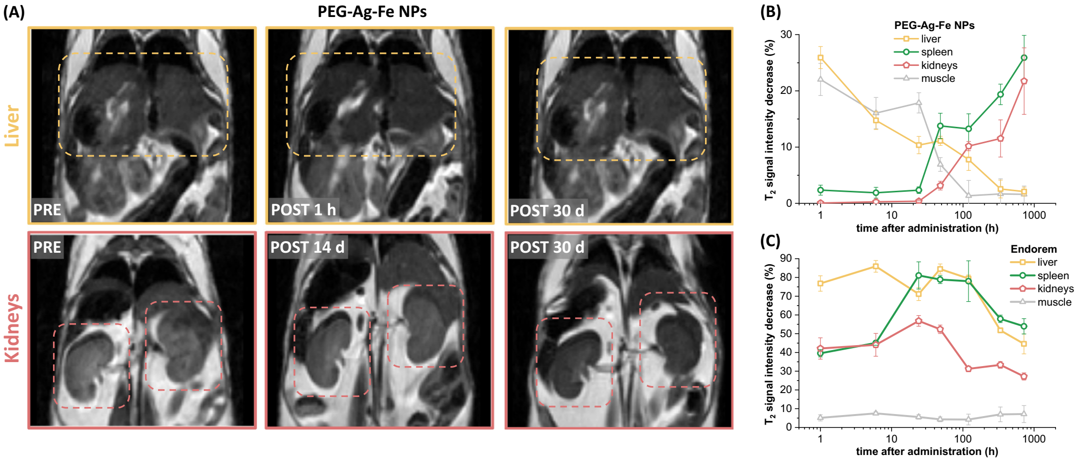

Fig. 3. (A) T_2-weighted images of liver (top) and kidneys (bottom) of mice treated with PEG-Ag-Fe NPs at different timepoints. (B) Plot of T_2 signal change, expressed as signal intensity decrease (%), in liver, spleen, kidneys and muscle at different time points up to 30 days after administration of PEG-Ag-Fe NPs. (C) T_2 signal change, expressed as signal intensity decrease (%) in liver, spleen, kidneys and muscle of mice treated with iron oxide NPs (Endorem).

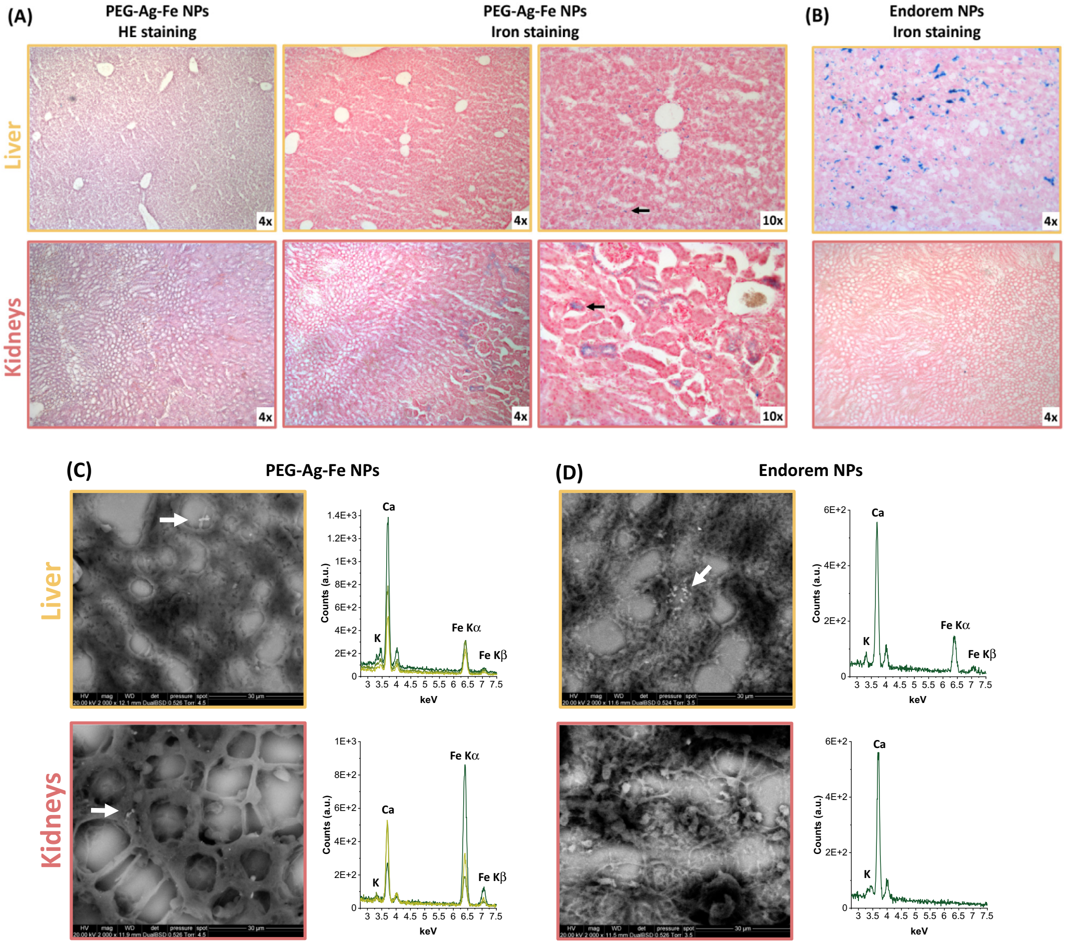

Fig. 4. (A) Histological analysis of liver and kidney from animals treated with PEG-Ag-Fe NPs (30 days after administration). HE (magnification 10x) and iron staining (magnification 4x and 10x) are reported. Black arrows indicate representative blue spots corresponding to iron deposits in the tissues treated with the iron staining. (B) Histological analysis of iron-stained liver and kidney from animals treated with iron oxide (Endorem) NPs (30 days after administration, magnification 4x). (C) ESEM images (left) and EDS analysis on selected NPs (right) of liver and kidney tissues of mice treated with Ag-Fe NPs. (D) ESEM images (left) and EDS analysis on selected NPs (right) of liver and kidney tissues of mice treated with Endorem iron oxide NPs. White arrows indicate some NPs. The tissues are the same used for histological analysis. (For interpretation of the references to colour in this figure legend, the reader is referred to the web version of this article.)

tals. In the liver 30 days after PEG-Ag-Fe NPs injection, homogeneously distributed blue spots with limited extension are found (top of Fig. 4A). The blue deposits indicative of iron are detected on a much larger area and density in the kidney (bottom of Fig. 4A, prevalently in the cortical region), in agreement with the relaxivity measured *in vivo* 30 days after NPs administration.

The detection of some iron deposits in the liver (top of Fig. 4A), despite the almost complete recovery of T_2 signal (Fig. 3B) is compatible with the storage of a fraction of iron coming from the degradation of the PEG-Ag-Fe NPs in ferritin (a protein abundant in the liver) and its remineralization into insoluble iron oxides, as reported in other cases of loss of magnetic signal after the dissolution of iron oxide NPs [62]. Biodegradation and clearance is an important positive feature for the PEG-Ag-Fe NPs, because NPs accumulation in the liver is associated to three main drawbacks that are: the formation of gaps between tightly packed cells, resulting permeable to toxins or metastasizing cells; Kupfer cells activation and release of pro-inflammatory signals; loss of cell functions such as xenobiotic detoxification; induction of fibrosis on the long term [22].

From the histology of animals treated with the benchmark iron oxide NPs (Endorem), iron can be massively detected in liver (top of Fig. 4B), whereas low spot density is observed in kidneys (bottom of Fig. 4B). In association with the large T_2 signal still observed in liver after 1 month (Fig. 3C), these results suggest that the iron oxide NPs have not yet started a process of massive degradation and clearance through urines.

The histological analysis also provides the evidence of PEG-Ag-Fe NPs biocompatibility after a relatively long time of 30 days *in vivo*. No relevant structural alterations and a good preservation of cellular morphology were observed with HE staining of the liver and kidneys (Fig. 4A). The central vein and surrounding hepatocytes in liver show normal hepatic architecture as well as kidney sections show a normal parenchymal structure in both medulla and cortex region. Moreover, during the *in vivo* MRI observation period, the weight of the animals was measured, and no weight loss was observed.

To obtain additional information on the localization and composition of the NPs *in vivo*, environmental scanning electron microscopy (ESEM) images and EDS analysis were performed on liver and kidney samples of the histological analysis. In animals treated with the Ag-Fe NPs, NPs are detected prevalently in kidneys and, with much lower density, in liver (white arrows in Fig. 4C). Noteworthy, no Ag peaks were detected in the EDS spectra collected in all the NPs analysed in kidney or liver, whereas the iron signals were always present (right of Fig. 4C). This is clearly compatible with biodegradation of the Ag-Fe NPs after 30 days, followed by release and clearance of Ag with urines, given the higher abundance of residual iron NPs in kidneys. As stated above, accumulation of iron in ferritin and even its remineralization in insoluble iron oxide nanocrystals has been observed several times in cells treated with iron NPs [62]. ESEM analysis of liver and kidneys of animals treated with Endorem confirmed the extended localization of NPs in the liver (top of Fig. 4D), as well as the iron-based composition (left of Fig. 4D), while no NPs were detected in kidney (bottom of Fig. 4D). Overall, the ESEM analysis fully confirmed the results of *in vivo* MRI and of histological analysis, with the additional information that Ag has been cleared from the organs already after 30 days, leaving only some nanometric iron NPs.

To further assess the long-term size and structural evolution in a biological environment, the PEG-Ag-Fe NPs were dispersed in 20% v/v FCS at lysosomal pH (4.5) at a final concentration of 0.05 mg/mL, incubated at 37 °C and the size distribution measured by TEM after 30, 60 and 90 days (Fig. 5). The results after 30 days already show the morphological evidence of NPs corrosion (Fig. 5A), such as nano-crescents, nano-donuts and hollow nanospheres accompanying volume contraction and particles fragmentation [13,63–65]. This is reflected by a fractional increase below 20 nm in the size histogram (Fig. 5B), although the average size and standard deviation (19 ± 16 nm) are comparable to the initial values (20 ± 14 nm, Fig. 5C). The trend becomes more pronounced after 60 days, especially for what concerns the almost complete disappearance of the largest particles (>50 nm) and consequent reduction of average size (11 ± 9 nm). NPs size reduction is complete after 90 days (2 ± 1 nm). NPs in this size range are easily excreted through kidneys because smaller than the average glomerular pore size, which is of the order of 5–10 nm [66–67]. It is reasonable to hypothesize that NPs degradation can be faster *in vivo* for the higher complexity of the chemical and biological environment, especially due to the action of cells belonging to the mononuclear phagocytic system [61].

4. Conclusions

In summary, we showed another example of how bimetallic nanoparticles allow new, unexpected and synergistic properties compared to the monometallic equivalents. In fact, we demonstrated that silver-iron nanoparticles coated with polyethylene glycol are efficient and biodegradable MRI contrast agents. These NPs exhibit a transverse relaxivity r_2 of 316 ± 13 $mM^{-1}s^{-1}$, that is 3 times that of the most common clinical benchmark based on iron oxide NPs. The PEG coating ensured excellent colloidal stability and biocompatibility *in vivo*. These bimetallic Ag-Fe nanoparticles were obtained in one-step by a low-cost LAL synthesis that allows total flexibility and easy functionalization of particles surface with the desired biomolecules. Importantly, TEM analysis showed that Ag-Fe NPs undergo size reduction over a few months in the physiological environment at lysosomal pH (4.5). *In vivo* biodistribution studies further evidenced that PEG-Ag-Fe NPs leave the liver over 30 days, while taking the way of renal clearance. In the same period, the benchmark iron oxide contrast agent showed high biopersistence in the liver. The biodegradation behaviour of Ag-Fe NPs is crucial in the frame of nanomaterials removal from the living organism. Hence, these Ag-Fe NPs offer positive prospects for the problems of biopersistence, contrast efficiency, difficulties of synthesis and surface functionalization usually encountered in nanoparticulate contrast agents.

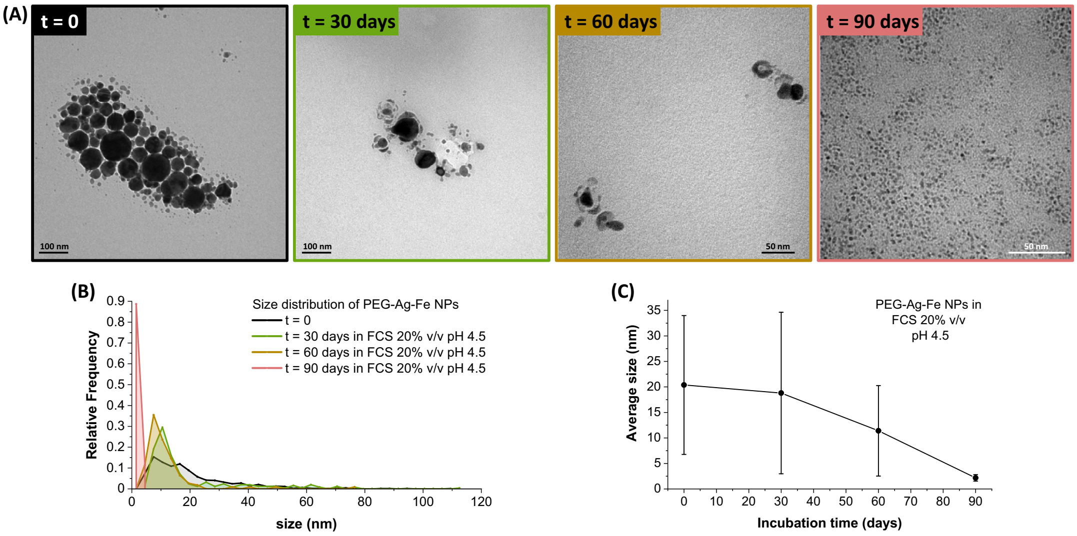

Fig. 5. Representative TEM images (A), size histograms (B) and average size and standard deviation (C) at different time-points (0, 30, 60 and 90 days) of PEG-Ag-Fe NPs incubated at 37 °C and pH 4.5 with FCS 20% v/v.

CRediT authorship contribution statement

Vincenzo Amendola: Conceptualization, Validation, Formal analysis, Data curation, Writing - review & editing, Visualization, Supervision, Project administration, Funding acquisition. **Andrea Guadagnini:** Methodology, Validation, Formal analysis, Investigation, Data curation, Visualization. **Stefano Agnoli:** Validation, Formal analysis, Investigation, Resources, Data curation. **Denis Badocco:** Validation, Formal analysis, Investigation, Resources, Data curation. **Paolo Pastore:** Validation, Formal analysis, Resources, Data curation. **Giulio Fracasso:** Methodology, Validation, Formal analysis, Investigation, Resources, Data curation. **Marco Gerosa:** Methodology, Validation, Formal analysis, Investigation, Resources, Data curation. **Federica Vurro:** Methodology, Validation, Formal analysis, Investigation, Resources, Data curation. **Alice Busato:** Methodology, Validation, Formal analysis, Investigation, Resources, Data curation. **Pasquina Marzola:** Methodology, Validation, Formal analysis, Resources, Data curation, Writing - review & editing, Supervision.

Declaration of Competing Interest

The authors declare that they have no known competing financial interests or personal relationships that could have appeared to influence the work reported in this paper.

Acknowledgments

This research was funded by the University of Padova STARS grant "4NANOMED", P-DiSC project "DYNAMO" and the Italian Ministry of Foreign Affairs and International Cooperation "Great relevance project" with protocol number 0191594. MRI experiments were performed at Centro Piattaforme Tecnologiche (CPT, University of Verona) which is gratefully acknowledged.

Appendix A. Supplementary material

Supplementary data to this article can be found online at https://doi.org/10.1016/j.jcis.2021.03.096. DLS analysis on Ag-Fe NPs incubated in PBS and AB; EDS analysis on isolated Ag-Fe NPs; Ag and Fe release in PBS or AB solutions; quantitative T_2 Map measurements; MRI images of liver and kidney of mice treated with Endorem NPs.

References

[1] K. Loza, M. Heggen, M. Epple, Adv. Funct. Mater. 30 (2020) 1909260.
[2] K.D. Gilroy, A. Ruditskiy, H.C. Peng, D. Qin, Y. Xia, Chem. Rev. 116 (2016) 10414–10472.
[3] F. Calvo, Phys. Chem. Chem. Phys. 17 (2015) 27922–27939.
[4] A. Tymoczko, M. Kamp, C. Rehbock, L. Kienle, E. Cattaruzza, S. Barcikowski, V. Amendola, Nanoscale Horizons 4 (2019) 1326–1332.
[5] S. Patnaik, D.P. Sahoo, K.M. Parida, J. Colloid Interf. Sci. 560 (2020) 519–535.
[6] O. Długosz, M. Sochocka, M. Ochnik, M. Banach, J. Colloid Interf. Sci. 586 (2021) 807–818.
[7] Y. Xiang, X. Peng, X. Kong, Z. Tang, H. Quan, Colloids Surf. A Physicochem. Eng. Asp. 594 (2020) 124652.
[8] P.C. Naha, K.C. Lau, J.C. Hsu, M. Hajfathalian, S. Mian, P. Chhour, L. Uppuluri, E.S. McDonald, A.D.A. Maidment, D.P. Cormode, Nanoscale 8 (2016) 13740–13754.
[9] X. Han, K. Xu, O. Taratula, K. Farsad, Nanoscale 11 (2019) 799–819.
[10] S.K. Mishra, S. Kannan, A.C.S. Biomater, Sci. Eng. 3 (2017) 3607–3619.
[11] D. González-Mancebo, A.I. Becerro, A. Corral, S. García-Embid, M. Balcerzyk, M. L. Garcia-Martin, J.M. de la Fuente, M. Ocaña, J. Colloid Interf. Sci. 573 (2020) 278–286.
[12] V. Amendola, S. Scaramuzza, L. Litti, M. Meneghetti, G. Zuccolotto, A. Rosato, E. Nicolato, P. Marzola, G. Fracasso, C. Anselmi, M. Pinto, M. Colombatti, Small 10 (2014) 2476–2486.
[13] V. Torresan, D. Forrer, A. Guadagnini, D. Badocco, P. Pastore, M. Casarin, A. Selloni, D. Coral, M. Ceolin, M.B. Fernández van Raap, A. Busato, P. Marzola, A.E. Spinelli, V. Amendola, ACS Nano 14 (2020) 12840–12853.
[14] E. Umut, M. Coşkun, F. Pineider, D. Berti, H. Güngüneş, J. Colloid Interf. Sci. 550 (2019) 199–209.
[15] S.V. Jadhav, P.S. Shewale, B.C. Shin, M.P. Patil, G.D. Kim, A.A. Rokade, S.S. Park, R.A. Bohara, Y.S. Yu, J. Colloid Interf. Sci. 541 (2019) 192–203.
[16] D. García-Soriano, R. Amaro, N. Lafuente-Gómez, P. Milán-Rois, Á. Somoza, C. Navío, F. Herranz, L. Gutiérrez, G. Salas, J. Colloid Interf. Sci. 578 (2020) 510–521.
[17] D. Kim, J. Kim, Y. Il Park, N. Lee, T. Hyeon, ACS Cent. Sci. 4 (2018) 324–336.
[18] G. Yang, S.Z.F. Phua, A.K. Bindra, Y. Zhao, Adv. Mater. 31 (2019) 1805730.
[19] L. Pasquini, A. Napolitano, E. Visconti, D. Longo, A. Romano, P. Tomà, M.C.R. Espagnet, CNS Drugs 32 (2018) 229–240.
[20] J. Volatron, F. Carn, J. Kolosnjaj-Tabi, Y. Javed, Q. L. Vuong, Y. Gossuin, C. Ménager, N. Luciani, G. Charron and M. Hémadi, Small.
[21] J. Kolosnjaj-Tabi, L. Lartigue, Y. Javed, N. Luciani, T. Pellegrino, C. Wilhelm, D. Alloyeau, F. Gazeau, Nano Today 11 (2016) 280–284.
[22] A. Boey, H.K. Ho, Small 16 (2020) 2000153.
[23] F. Perton, M. Tasso, G. A. Muñoz Medina, M. Ménard, C. Blanco-Andujar, E. Portiansky, M. B. F. van Raap, D. Bégin, F. Meyer, S. Begin-Colin and D. Mertz, Appl. Mater. Today, 2019, 16, 301–314.
[24] Q. Hu, Q. Chen, Z. Gu, Biomaterials 178 (2018) 546–558.
[25] J.D. Wolf, M. Kurpiers, R.A. Baus, R.X. Götz, J. Griesser, B. Matuszczak, A. Bernkop-Schnürch, J. Colloid Interf. Sci. 566 (2020) 234–241.
[26] A.K. Biswal, S. Saha, J. Colloid Interf. Sci. 566 (2020) 120–134.
[27] Y. Liu, Y. Tang, J. Wu, J. Sun, X. Liao, Z. Teng, G. Lu, J. Colloid Interf. Sci. 570 (2020) 402–410.
[28] V. Torresan, A. Guadagnini, D. Badocco, P. Pastore, G. A. Muñoz Medina, M. B. Fernàndez van Raap, I. Postuma, S. Bortolussi, M. Bekić, M. Čolić, M. Gerosa, A. Busato, P. Marzola and V. Amendola, Adv. Healthc. Mater., 2020, 2001632.
[29] S. Khan, J. McCabe, K. Hill, P.A. Beales, J. Colloid Interf. Sci. 562 (2020) 418–428.
[30] S. Rutkowski, T. Si, M. Gai, M. Sun, J. Frueh, Q. He, J. Colloid Interf. Sci. 541 (2019) 407–417.
[31] O. Koshkina, P.B. White, A.H.J. Staal, R. Schweins, E. Swider, I. Tirotta, P. Tinnemans, R. Fokkink, A. Veltien, N.K. van Riessen, E.R.H. van Eck, A. Heerschap, P. Metrangolo, F. Baldelli Bombelli, M. Srinivas, J. Colloid Interf. Sci. 565 (2020) 278–287.
[32] S. Crivellaro, A. Guadagnini, D.M.D.M. Arboleda, D. Schinca, V. Amendola, Rev. Sci. Instrum. 90 (2019) 033902.
[33] V. Amendola, D. Amans, Y. Ishikawa, N. Koshizaki, S. Scirè, G. Compagnini, S. Reichenberger, S. Barcikowski, Chem. - A Eur. J. 26 (2020) 9206–9242.
[34] B. Pang, Y. Ma, Z. Tian, J. Liu, S. Wu, D. Teng, P. Li, C. Liang, J. Colloid Interf. Sci. 585 (2020) 452–458.
[35] V. Amendola, S. Scaramuzza, F. Carraro, E. Cattaruzza, J. Colloid Interf. Sci. 489 (2017) 18–27.
[36] K.I. Saitow, Y. Okamoto, H. Suemori, ACS Omega 4 (2019) 14307–14311.
[37] F. Davodi, E. Mühlhausen, D. Settipani, E.L. Rautama, A.P. Honkanen, S. Huotari, G. Marzun, P. Taskinen, T. Kallio, J. Colloid Interf. Sci. 556 (2019) 180–192.
[38] J. Zhang, M. Chaker, D. Ma, J. Colloid Interf. Sci. 489 (2017) 138–149.
[39] V. Amendola, S. Scaramuzza, S. Agnoli, G. Granozzi, M. Meneghetti, G. Campo, V. Bonanni, F. Pineider, C. Sangregorio, P. Ghigna, S. Fiameni, L. Nodari, S. Polizzi, P. Riello, S. Fiameni, L. Nodari, Nano Res. 8 (2015) 4007–4023.
[40] S. Scaramuzza, S. Polizzi, V. Amendola, Nanoscale Adv. 1 (2019) 2681–2689.
[41] H. Okamoto, Desk Handbook: Phase Diagrams for Binary Alloys, ASM International, Ohio, 2000.
[42] V. Amendola, O.M.M. Bakr, F. Stellacci, Plasmonics 5 (2010) 85–97.
[43] A. Hodaei, O. Akhlaghi, N. Khani, T. Aytas, D. Sezer, B. Tatli, Y.Z. Menceloglu, B. Koc, O. Akbulut, A.C.S. Appl, Mater. Interfaces 10 (2018) 9873–9881.
[44] B. Godin, J. Gu, R.E. Serda, R. Bhavane, E. Tasciotti, C. Chiappini, X. Liu, T. Tanaka, P. Decuzzi, M. Ferrari, J. Biomed. Mater. Res. Part A 94 (2010) 1236–1243.
[45] A.M. King, C. Bray, S.C.L. Hall, J.C. Bear, L.K. Bogart, S. Perrier, G.L. Davies, J. Colloid Interf. Sci. 579 (2020) 401–411.
[46] M. Visscher, J.J. Pouw, J. Van Baarlen, J.M. Klaase, B. Ten Haken, IEEE Trans. Biomed. Eng. 60 (2013) 2594–2602.
[47] Y.X.J. Wang, S.M. Hussain, G.P. Krestin, Eur. Radiol. 11 (2001) 2319–2331.
[48] M. Borzenkov, G. Chirico, L. D'Alfonso, L. Sironi, M. Collini, E. Cabrini, G. Dacarro, C. Milanese, P. Pallavicini, A. Taglietti, C. Bernhard, F. Denat, Langmuir 31 (2015) 8081–8091.
[49] T.L. Doane, C.H. Chuang, R.J. Hill, C. Burda, Acc. Chem. Res. 45 (2011) 317–326.
[50] C. Biver, R. Hariharan, J. Mays, W.B. Russel, Macromolecules 30 (1997) 1787–1792.
[51] A. Guadagnini, S. Agnoli, D. Badocco, P. Pastore, D. Coral, M.B. Fernandez van Raap, D. Forrer, V. Amendola, J. Colloid Interf. Sci. 585 (2021) 267–275.
[52] M. Rohrer, H. Bauer, J. Mintorovitch, M. Requardt, H.-J. Weinmann, Invest. Radiol. 40 (2005) 715–724.
[53] Y.-X.J. Wang, Quant. Imaging Med. Surg. 1 (2011) 35–40.
[54] L. Ding, C. Yao, X. Yin, C. Li, Y. Huang, M. Wu, B. Wang, X. Guo, Y. Wang, M. Wu, Small 14 (2018) 1801451.
[55] G. Glorani, R. Marin, P. Canton, M. Pinto, G. Conti, G. Fracasso, P. Riello, J. Nanoparticle Res. 19 (2017) 1–14.
[56] T.J. Miesen, A.M. Engstrom, D.C. Frost, R. Ajjarapu, R. Ajjarapu, C.N. Lira, M.R. Mackiewicz, RSC Adv. 10 (2020) 15677–15693.
[57] S. Liu, T. Xia, Small 16 (2020) 2000603.
[58] R. Sachan, V. Ramos, A. Malasi, S. Yadavali, B. Bartley, H. Garcia, G. Duscher, R. Kalyanaraman, Adv. Mater. 25 (2013) 2045–2050.
[59] P. Pallavicini, L. Preti, L. De Vita, G. Dacarro, Y.A. Diaz Fernandez, D. Merli, S. Rossi, A. Taglietti, B. Vigani, J. Colloid Interf. Sci. 563 (2020) 177–188.

[60] A. Plan Sangnier, A.B. Van De Walle, A. Curcio, R. Le Borgne, L. Motte, Y. Lalatonne, C. Wilhelm, Nanoscale 11 (2019) 16488–16498.
[61] A.S. Arbab, L.B. Wilson, P. Ashari, E.K. Jordan, B.K. Lewis, J.A. Frank, NMR Biomed. 18 (2005) 383–389.
[62] A. Curcio, A. Van De Walle, A. Serrano, S. Preveral, C. Péchoux, D. Pignol, N. Menguy, C.T. Lefevre, A. Espinosa, C. Wilhelm, ACS Nano 14 (2020) 1406–1417.
[63] P. Liu, Q. Chen, Y. Ito, J. Han, S. Chu, X. Wang, K.M. Reddy, S. Song, A. Hirata, M. Chen, Nano Lett. 20 (2020) 1944–1951.
[64] X. Li, Q. Chen, I. McCue, J. Snyder, P. Crozier, J. Erlebacher, K. Sieradzki, Nano Lett. 14 (2014) 2569–2577.
[65] L. Chen, A. Leonardi, J. Chen, M. Cao, N. Li, D. Su, Q. Zhang, M. Engel, X. Ye, Nat. Commun. 11 (2020) 3041.
[66] S. Tang, Y. Huang, J. Zheng, Angew. Chem. 132 (2020) 20066–20070.
[67] A.M. Ferretti, S. Usseglio, S. Mondini, C. Drago, R. La Mattina, B. Chini, C. Verderio, M. Leonzino, C. Cagnoli, P. Joshi, D. Boraschi, P. Italiani, Y. Li, B.J. Swartzwelter, L. Sironi, P. Gelosa, L. Castiglioni, U. Guerrini, A. Ponti, J. Colloid Interf. Sci. 582 (2021) 678–700.

Bibliography

- Accardo A, Mannucci S, Nicolato E, et al. Easy formulation of liposomal doxorubicin modified with a bombesin peptide analogue for selective targeting of GRP receptors overexpressed by cancer cells. Drug Deliv Transl Res. 2019; 9(1): 215-226.
- Acharya S. and Sahoo S. K.. Effects of Sonication Processing on the Behavior of the Synthesis Human Serum Albumin-SPIONs Loaded PLGA Nanoparticles. Advanced Drug Delivery Rev. (2011), 63, 170–183.
- Ahrens E.T., Bulte J.W.. Tracking immune cells in vivo using magnetic resonance im- aging, Nat Rev Immunol 13 (2013) 755–763.
- Angelakeris M. Magnetic nanoparticles: A multifunctional vehicle for modern theranostics. Biochim Biophys Acta Gen Subj. 2017 Jun;1861(6):1642-1651.
- Arora A. Optical and electric field control of magnetism, Thesis Dissertation, 2018
- Bañobre-López M, García-Hevia L, Cerqueira MF, et al. Tunable Performance of Manganese Oxide Nanostructures as MRI Contrast Agents. Chemistry. 2018 Jan 26;24(6):1295-1303.
- Barbic M, Dodd SJ, Morris HD, et al. Magnetocaloric materials as switchable high contrast ratio MRI labels. Magn Reson Med. 2019; 81(4): 2238-2246.
- Barnabucci U, Basiricò L, Morera P, et al. Heat shock modulates adipokines expression in 3T3-L1 adipocyres. J Mol Endocrinol. 2009; 42(2):139-147.
- Beuf O. High-resolution MRI techniques for studies in small-animal models. Methods Mol Med. 2004;101:219-29.
- Bhardwaj A, Parekh K, Jain N. In vitro hyperthermic effect of magnetic fluid on cervical and breast cancer cells. Sci Rep. 2020 Sep 17;10(1):15249. doi: 10.1038/s41598-020-71552-3.
- Binnemars-Postma K, Storm G, Prakash J. Nanomedicine Strategies to Target Tumor-Associated Macrophages. Int J Mol Sci. 2017 May 4;18(5):979.
- Bogdanov A Jr, Mazzanti ML. Molecular magnetic resonance contrast agents for the detection of cancer: past and present. *Semin Oncol*. 2011;38(1):42-54.

- Brero F, Albino M, Antoccia A, et al. Hadron Therapy, Magnetic Nanoparticles and Hyperthermia: A promising Combined Tool for Pancreatic Cancer Treatment. Nanomaterials. 2000; 10(10): 1919.
- Bulte JW, Kraitchman DL. Iron oxide MR contrast agents for molecular and cellular imaging. NMR Biomed. 2004 Nov;17(7):484-99.
- Calcagno V, Vecchione R, Quagliariello V, et al. Oil Core-PEG Shell Nanocarriers for In Vivo MRI Imaging. Adv Healthc Mater. 2019; 8(3): e1801313.
- Calderwood SK, Asea A. Targeting HSP70-induced thermotolerance for design of thermal sensitizers. Int J Hyperthermia. 2002; 18(6): 597-608.
- Calvo MB, Figueroa A, Pulido EG, et al. Potential role of sugar transporters in cancer and their relationship with anticancer therapy. Int J Endocrinol. 2010.
- Caravan P, Ellison JJ, McMurry TJ, et al. Gadolinium(III) Chelates as MRI Contrast Agents: Structure, Dynamics, and Applications. Chem Rev. 1999 Sep 8;99(9):2293-352.
- Cassim S, Giustini A, Petryk A, Strawbridge R, Hoopes P. Iron Oxide Hyperthermia And Radiation Cancer Treatment. Proc SPIE Int Soc Opt Eng. 2009 Feb 23;7181:71810.
- Cazares-Cortes E, Espinosa A, Guigner JM, et al. Doxorubicin Intracellular Remote Release from Biocompatible Oligo(ethylene glycol) Methyl Ether Methacrylate-Based Magnetic Nanogels Triggered by Magnetic Hyperthermia. ACS Appl Mater Interfaces. 2017 Aug 9;9(31):25775-25788.
- Chandrasekharan P, Tay ZW, Hensley D, et al. Using magnetic particle imaging systems to localize and guide magnetic hyperthermia treatment: tracers, hardware, and future medical applications. Theranostics. 2020 Feb 10;10(7):2965-2981.
- Chang D, Lim M, Goos JACM, et al. Biologically Targeted Magnetic Hyperthermia: Potential and Limitations. Front Pharmacol. 2018 Aug 2;9:831.
- Cherukuri P, Glazer ES, Curley SA. Targeted hyperthermia using metal nanoparticles. Adv Drug Deliv Rev. 2010 Mar 8;62(3):339-45.
- Cornell RM, Schwertmann U, The Iron Oxides: Structure, Properties, Reactions, Occurrences and Uses. Wiley-VCH. 2003.

- Cortelletti P, Facciotti C, Cantarelli IX, et al. Nd^{3+} activated CaF_2 NPs as colloidal nanothermometers in the biological window. Optical materials. 2017; 68: 29-34.
- Cotin G, Blanco-Andujar C, Nguyen DV, et al. Dendron based antifouling, MRI and magnetic hyperthermia properties of different shaped iron oxide nanoparticles. Nanotechnology. 2019; 30(37): 374002.
- Court KA, Hatakeyama H, Wu SY, et al. Inhibition Synergistically Enhances the Effects of Magnetic Fluid Hyperthermia in Ovarian Cancer. Mol Cancer Ther. 2017; 16(5): 966-976.
- Dadfar SM, Roemhild K, Drude NI, et al. Iron oxide nanoparticles: Diagnostic, therapeutic and theranostic applications. Adv Drug Deliv Rev. 2019 Jan 1;138:302-325.
- Das P, Colombo M, Prosperi D, Recent advances in magnetic fluid hyperthermia for cancer therapy. Colloids Surf B Biointerfaces. 2019; 174: 42-55.
- Di Corato R, Béalle G, Kolosnjaj-Tabi J, et al. Combining magnetic hyperthermia and photodynamic therapy for tumor ablation with photoresponsive magnetic liposomes. ACS Nano. 2015 Mar 24;9(3):2904-16.
- Dragar Č, Kralj S, Kocbek P. Bioevaluation methods for iron-oxide-based magnetic nanoparticles. Int J Pharm. 2021 Mar 15;597:120348.
- Du Y, Liu X, Liang Q, Liang XJ, Tian J. Optimization and Design of Magnetic Ferrite Nanoparticles with Uniform Tumor Distribution for Highly Sensitive MRI/MPI Performance and Improved Magnetic Hyperthermia Therapy. Nano Lett. 2019 Jun 12;19(6):3618-3626.
- Egea-Benavente D, Ovejero JG, Morales MDP, et al. Understanding MNPs Behaviour in Response to AMF in Biological Milieus and the Effects at the Cellular Level: Implications for a Rational Design That Drives Magnetic Hyperthermia Therapy toward Clinical Implementation. Cancers (Basel). 2021 Sep 12;13(18):4583.
- Etemadi H, Buchanan JK, Kandile NG, et al. Iron Oxide Nanoparticles: Physicochemical Characteristics and Historical Developments to Commercialization for Potential Technological Applications. ACS Biomater Sci Eng. 2021 Dec 13;7(12):5432-5450.

- Fang K, Song L, Gu Z, et al. Magnetic field activated drug release system based on magnetic PLGA microspheres for chemo-thermal therapy. Colloids Surf B Biointerfaces. 2015 Dec 1;136:712-20.
- Fantechi E, Innocenti C, Zanardelli M, et al. A smart platform for hyperthermia application in cancer treatment: cobalt-doped ferrite nanoparticles mineralized in human ferritin cages. ACS Nano. 2014; 8(5): 4705-19.
- Ferguson R.M.,Khandhar A.P.,Kemp S.J, et al. Magnetic particle imaging with tailored iron oxide nanoparticle tracers, IEEE Trans. Med. Im- aging 34 (2015) 1077–1084.
- Fontes de Paula Aguiar M., Bustamante Mamami, Javier K. F., et al. "Magnetic targeting with superparamagnetic iron oxide nanoparticles for *in vivo* glioma" Nanotechnology Reviews, vol. 6, no. 5, 2017, pp. 449-472.
- Fortin J. P., Gazeau F. and Wilhelm C., Intracellular heating of living cells through Néel relaxation of magnetic nanoparticles. European biophysics Journal. (2008), 37, 223–228
- Gerosa M, Grande MD, Busato A, et al. Nanoparticles exhibiting self-regulating temperature as innovative agents for Magnetic Fluid Hyperthermia. Nanotheranostics. 2021 Mar 15;5(3):333-347.
- Gleich B, Weizenecker J. Tomographic imaging using the nonlinear response of magnetic particles. Nature. 2005 Jun 30;435(7046):1214-7.
- Gneveckow U, Jordan A, Scholz R, et al. Description and characterization of the novel hyperthermia- and thermoablation-system MFH 300F for clinical magnetic fluid hyperthermia. Med Phys. 2004 Jun;31(6):1444-51.
- Goldstein LS, Dewhirst MW, Repacholi M, et al. Summary, conclusions and recommendations: adverse temperature levels in the human body. Int J Hyperthermia. 2003; 19(3): 373-84.
- Golstein P.and Kroemer G., Trends Biochem. Cell death by necrosis: towards a molecular definition, Sci., (2007), 32, 37–43.
- Goodwill PW, Conolly SM. The X-space formulation of the magnetic particle imaging process: 1-D signal, resolution, bandwidth, SNR, SAR, and magnetostimulation. IEEE Trans Med Imaging. 2010 Nov;29(11):1851-9.

- Goodwill PW, Saritas EU, Croft LR, et al. X-space MPI: magnetic nanoparticles for safe medical imaging. Adv Mater. 2012 Jul 24;24(28):3870-7.
- Graeser M., Knopp T., Szwargulski P., et al. Towards Picogram Detection of Superparamagnetic Iron-Oxide Particles using a Gradiometric Receive Coil, Sci. Rep. 7 (2017) 6872.
- Guardia P, Di Corato R, Lartigue L, Wilhelm C, Espinosa A, Garcia-Hernandez M, Gazeau F, Manna L, Pellegrino T. Water-soluble iron oxide nanocubes with high values of specific absorption rate for cancer cell hyperthermia treatment. ACS Nano. 2012 Apr 24;6(4):3080-91.
- Hall EJ, Roizin-Towle L. Biological effects of heat. Cancer Res 44 (10 Suppl). 1984; 4708s-4713s.
- Harisinghani MG, Barentsz J, Hahn PF, Deserno WM, Tabatabaei S, van de Kaa CH, de la Rosette J, Weissleder R. Noninvasive detection of clinically occult lymph-node metastases in prostate cancer. N Engl J Med. 2003 Jun 19;348(25):2491-9.
- Hartshorn CM, Bradbury MS, et al. Nanotechnology Strategies To Advance Outcomes in Clinical Cancer Care. ACS Nano. 2018 Jan 23;12(1):24-43.
- Harvell-Smith S, Tung LD, Thanh NTK. Magnetic particle imaging: tracer development and the biomedical applications of a radiation-free, sensitive, and quantitative imaging modality. Nanoscale. 2022 Jan 26.
- Hegyi G, Szasz O, Szasz A. Oncothermia: a new paradigm and promising method in cancer therapies. Acupunct Electrother Res. 2013;38(3-4):161-97.
- Hemery G, Keyes AC Jr, Garaio E, Rodrigo I, Garcia JA, Plazaola F, Garanger E, Sandre O. Tuning Sizes, Morphologies, and Magnetic Properties of Monocore Versus Multicore Iron Oxide Nanoparticles through the Controlled Addition of Water in the Polyol Synthesis. Inorg Chem. 2017 Jul 17;56(14):8232-8243.
- Hendrick RE, Haacke EM. Basic physics of MR contrast agents and maximization of image contrast. J Magn Reson Imaging. 1993 Jan-Feb;3(1):137-48.
- Hergt and Dutz S., J, Magnetic particle hyperthermia—biophysical limitations of a visionary tumour therapy. Journal of Magnetism and Magnetic Materials. (2007), 311, 187– 192.

- Hergt R, Dutz S, Müller R, et al. Magnetic Particle Hyperthermia: Nanoparticle Magnetism and Materials Development for Cancer Therapy. Journal of Physics: Condensed Matter. 2006; 18, S2919-S2934.
- Hervault A, Thanh NT. Magnetic nanoparticle-based therapeutic agents for thermo-chemotherapy treatment of cancer. Nanoscale. 2014; 6(20): 11553-73.
- Hildebrandt B, Wust P, Ahlers O, et al. The cellular and molecular basis of hyperthermia. Crit Rev Oncol Hematol. 2002; 43(1): 33-56.
- Hilger I, Andrä W, Hergt R, et al. Electromagnetic heating of breast tumors in interventional radiology: in vitro and in vivo studies in human cadavers and mice. Radiology. 2001 Feb;218(2):570-5.
- Hofmann-Amtenbrink M, Hofmann H, Montet X. Superparamagnetic nanoparticles - a tool for early diagnostics. Swiss Med Wkly. 2010 Sep 17;140:w13081.
- Huang H. S. and Hainfeld J. F.. Intravenous magnetic nanoparticle cancer hyperthermia. Interantional Journal of Nanomedicine. (2013), 8, 2521–2532.
- Huang J, Chan PS, Lok V, et al. Global incidence and mortality of breast cancer: a trend analysis. Aging (Albany NY). 2021 Feb 11;13(4):5748-5803
- Ito A, Matsuoka F, Honda H, et al. Heat shock protein 70 gene therapy combined with hyperthermia using magnetic nanoparticles. Cancer Gene Ther. 2003; 10(12): 918-25.
- Ito A, Shinkai M, Honda H, et al. Medical application of functionalized magnetic nanoparticles. J Biosci Bioeng. 2005; 100(1): 1-11.
- Jang J., Nah H., H J.. Lee, Moon S. H., Kim M. G. and Cheon J.. Critical enhancements of MRI contrast and hyperthermic effects by dopant-controlled magnetic nanoparticles. Angewandte Chemie. (2009), 48, 1234-1238.
- Jang JT, Lee J, Seon J, et al. Giant Magnetic Heat Induction of Magnesium-Doped γ-$Fe_2 O_3$ Superparamagnetic Nanoparticles for Completely Killing Tumors. Adv Mater. 2018 Feb;30(6).
- Jia G, Han Y, An Y, et al. NRP-1 targeted and cargo-loaded exosomes facilitate simultaneous imaging and therapy of glioma in vitro and in vivo. Biomaterials. 2018; 178: 302-316.

- Jin R, Lin B, Li D, Ai H. Superparamagnetic iron oxide nanoparticles for MR imaging and therapy: design considerations and clinical applications. Curr Opin Pharmacol. 2014 Oct;18:18-27.
- Johannsen M, Thiesen B, Wust P, et al. Magnetic nanoparticle hyperthermia for prostate cancer, Int J Hyperthermia. 2010; 26(8): 790-5.
- Jordan A, Wust P., Scholz R., et al. Magnetic fluid hyperthermia (MFH): Cancer treatment with AC magnetic field induced excitation of biocompatible superparamagnetic nanoparticles. Journal of Magnetism and Magnetic Materials. (1997),978-1-4757-6482-6.
- Jun YW, Choi JS, Cheon J. Heterostructured magnetic nanoparticles: their versatility and high performance capabilities. Chem Commun (Camb). 2007 Mar 28;(12):1203-14.
- Kallumadil M., Tada M., Nakagawa T., et al. Suitability of commercial colloids for magnetic hyperthermia. Journal of Magnetism and Magnetic Materials. 2009;321(10):1509–1513.
- Kandasamy G, Sudame A, Luthra T, et al. Functionalized Hydrophilic Superparamagnetic Iron Oxide Nanoparticles for Magnetic Fluid Hyperthermia Application in Liver Cancer Treatment. ACS Omega. 2018; 3(4):3991-4005.
- Kekalo K, Baker I, Meyers R, et al. Magnetic Nanoparticles with High Specific Absorption Rate at Low Alternating Magnetic Field. Nano Life. 2015; 5(2).
- Kerr J. F. R., Winterford C. M. and Harmon B. V.. Apoptosis, its significance in cancer therapy, Cancer. (1994), 73, 2013–2026.
- Kharisov BI, Dias Rasika HV, Kharissova OV, et al. Solubilization, dispersion and stabilization of magnetic nanoparticles in water and non acqueous solvents: recent trends. RSC Advances. 2014; 85.
- Khoei S, Goliaei B, Neshasteh-Riz A, et al. The role of heat shock protein 70 in the thermoresistance of prostate cancer cell line spheroids. FEBS Lett. 2004; 561(1-3): 144-8.
- Kiani, A., Nabiyouni, G., Masoumi, S., et al. A novel magnetic MgFe2O4–MgTiO3 perovskite nanocomposite: Rapid photo-degradation of toxic dyes under visible irradiation. Composites Part B: Engineering, 175(July), 2019 107080.

- Kita E, Oda T, Kayano T, et al. Ferromagnetic Nanoparticles for magnetic hyperthermia and thermoablation therapy. Journal of Physics D. 2010; 43, 474011.
- Kobayashi T. Cancer hyperthermia using magnetic nanoparticles. Biotechnol J. 2011; 6(11): 1342-7.
- Kok HP, van der Zee J, Guirado FN, et al. Treatment planning facilitates clinical decision making for hyperthermia treatments. Int J Hyperthermia. 2021 Jan 1;38(1):532-551.
- Kotitz R., Weitschies W., Trahms L. et al. Investigation of Brownian and Neel relaxation in magnetic fluids. Journal of Magnetism and magnetic materials. (1999), 201, 102–104.
- Kovár D, Malá A, Mlčochová J, et al. Preparation and Characterization of Highly Stable Iron Oxide Nanoparticles for Magnetic Resonance Imaging. Journal of Nanomaterials. 2017.
- Kozissnik B, Bohorquez AC, Dobson J, et al. Magnetic fluid hyperthermia: advances, challenges, and opportunity. Int J Hyperthermia. 2013 Dec;29(8):706-14.
- Kregel K. C.. Heat shock proteins: modifying factors in physiological stress responses and acquired thermotolerance. Journal of applied physiology. (2002), 92(5):2177-86.
- Krishnan KM. Biomedical Nanomagnetics: A Spin Through Possibilities in Imaging, Diagnostics, and Therapy. IEEE Trans Magn. 2010 Jul 1;46(7):2523-2558.
- Kumar C.S.S.R. , Mohammad F., “Magnetic nanomaterials for hyperthermia-based therapy and controlled drug delivery”, Adv. Drug Deliv. Rev. (2011), 63(9): 789–808.
- Lacroix LM, Ho D, Sun S. Magnetic nanoparticles as both imaging probes and therapeutic agents. Curr Top Med Chem. 2010;10(12):1184-97.
- Laszlo, “The effects of hyperthermia on mammalian cell structure and function”, Cell proliferation. (1992), 25(2):59-87.
- Laurent S, Boutry S, Mahieu I, et al. Iron oxide based MR contrast agents: from chemistry to cell labeling. Curr Med Chem. 2009;16(35):4712-27.

- Laurent S, Dutz S, Häfeli UO, et al. Magnetic fluid hyperthermia: focus on superparamagnetic iron oxide nanoparticles. Adv Colloid Interface Sci. 2011; 166(1-2): 8-23.
- Lee C.T., Mace T., and Repasky E.A., "Hypoxia-driven immunosuppression: a new reason to use thermal therapy in the treatment of cancer", International journal of hyperthermia. (2010), 26(3):232-246.
- Levy M., Wilhelm C., Siaugue J.-M., Horner O., Bacri J.-C. and Gazeau F., "Magnetically induced hyperthermia: size-dependent heating power of γ-Fe_2O_3 nanoparticles"Journal of Physics.: Condensed. Matter. (2008), 20, 204133.
- Lewinski N, Colvin V, Drezek R. Cytotoxicity of nanoparticles. Small. 2008 Jan;4(1):26-49.
- Liu XL, Ng CT, Chandrasekharan P, Yang HT, Zhao LY, Peng E, Lv YB, Xiao W, Fang J, Yi JB, Zhang H, Chuang KH, Bay BH, Ding J, Fan HM. Synthesis of Ferromagnetic Fe0.6 Mn0.4 O Nanoflowers as a New Class of Magnetic Theranostic Platform for In Vivo T1 -T2 Dual-Mode Magnetic Resonance Imaging and Magnetic Hyperthermia Therapy. Adv Healthc Mater. 2016 Aug;5(16):2092-104.
- Liu X, Zhang Y, Wang Y, et al. Comprehensive understanding of magnetic hyperthermia for improving antitumor therapeutic efficacy. Theranostics. 2020 Feb 19;10(8):3793-3815.
- Liu X.L., Fan H.M., Yi J.B., Yang Y., Choo E.S.G., Xue J.M., Fan D. D. and Ding J. Optimization of surface coating on Fe_3O_4 nanoparticles for high performance magnetic hyperthermia agents. Journal of Material Chemistry (2012), 22, 8235
- Liu S, Shi D, Chen L, et al. Paclitaxel-loaded magnetic nanocrystals for tumor neovascular-targeted theranostics: an amplifying synergistic therapy combining magnetic hyperthermia with chemotherapy. Nanoscale. 2021 Feb 14;13(6):3613-3626.
- Lu K, Goodwill PW, Saritas EU, et al. Linearity and shift invariance for quantitative magnetic particle imaging. IEEE Trans Med Imaging. 2013 Sep;32(9):1565-75.

- Lu Q, Dai X, Zhang P, et al. Fe_3O_4@Au composite magnetic nanoparticles modified with cetuximab for targeted magneto-photothermal therapy of glioma cells. Int J Nanomedicine. 2018; 13: 2491-2505.
- Lu Y, Rivera-Rodriguez A, Tay ZW, et al. Combining magnetic particle imaging and magnetic fluid hyperthermia for localized and image-guided treatment. Int J Hyperthermia. 2020 Dec;37(3):141-154.
- Ludewig P, Gdaniec N, Sedlacik J, et al. Magnetic Particle Imaging for Real-Time Perfusion Imaging in Acute Stroke. ACS Nano. 2017 Oct 24;11(10):10480-10488.
- Mailänder V, Lorenz MR, Holzapfel V, et al. Carboxylated superparamagnetic iron oxide particles label cells intracellularly without transfection agents. Mol Imaging Biol. 2008 May-Jun;10(3):138-46.
- Majid A, Ahmed W, Patil-Sen Y, et al., Micro and Nanomanufacturing Volume II, Synthesis and Characterisation of Magnetic Nanoparticles in Medicine, 2018.
- Mannucci S, Ghin L, Conti G, et al. Magnetic nanoparticles from Magnetospirillum gryphiswaldense increase the efficacy of thermotherapy in a model of colon carcinoma. PLoS One. 2014; 9(10): e108959.
- Mannucci S, Tambalo S, Conti G, et al. Magnetosomes Extracted from Magnetospirillum gryphiswaldense as theranostic agents in experimental model of glioblastoma. Contrast Media Mol Imaging. 2018; 2198703.
- Martinez-Boubeta C, Simeonidis K, Makridis A, et al. Learning from nature to improve the heat generation of iron-oxide nanoparticles for magnetic hyperthermia applications. Sci Rep. 2013;3:1652.
- Matteazzi P, Gherlinzoni F, Gottardi M. Method for the production of sub-micrometric particles and their theranostic use in oncology with specific apparatus. European Patent EP 2961429B1 Pr. 28.02.2014.
- Matteazzi P. Mechanomaking of nanophased materials, Interface Controlled Materials. 2000. Volume 9.
- McHenry M, Laughlin D, Theory of Magnetic Phase Transition, Characterization of Materials, 2002

- Miaskowski A, Subramanian M. Numerical Model for Magnetic Fluid Hyperthermia in a Realistic Breast Phantom: Calorimetric Calibration and Treatment Planning. Int J Mol Sci. 2019; 20(18).
- Mieszawska AJ, Kim Y, Gianella A, et al. Synthesis of polymer-lipid nanoparticles for image-guided delivery of dual modality therapy. Bioconjug Chem. 2013 Sep 18;24(9):1429-34.
- Mondal S, Manivasagan P, Bharathiraja S, et al. Hydroxyapatite Coated Iron Oxide Nanoparticles: A Promising Nanomaterial for Magnetic Hyperthermia Cancer Treatment. Nanomaterials (Basel). 2017; 7(12).
- Moya X, Kar-Narayan S, Mathur ND. Caloric materials near ferroic phase transitions. Nat Mater. 2014 May;13(5):439-50.
- Moyer H.R. and Delman K.A., “the role of hyperthermia in optimizing tumor response to regional therapy”, Internation journal of hyperthermia. (2008), 24:3, 251-261.
- Muela A, Munoz D, Rodriguez RM, et al. Optimal Parameters for Hyperthermia Treatment Using Biomineralized Magnetite Nanoparticles: Theoretical and Experimental Approach. Journal of Physical Chemistry C. 2016; 120, 42, 24437-24448.
- Na H.B, Song I.C., Hyeon T.. Inorganic Nanoparticles for MRI contrast agents. Advanced Materials. 2009; 21, 21, 2133-2148.
- Namdeo M, Saxena S, Tankhiwale R, et al. Magnetic nanoparticles for drug delivery applications. J Nanosci Nanotechnol. 2008 Jul;8(7):3247-71.
- Natividad E, Castro M and Mediano A, “Accurate measurement of the specific absorption rate using a suitable adiabatic magnetothermal setup”, Applied Physics Letter. (2008), 92, 093116.
- Nunn AD, Linder KE, Tweedle MF. Can receptors be imaged with MRI agents? Q J Nucl Med. 1997 Jun;41(2):155-62.
- Obaidat MI, Issa B, Haik Y, Magnetic Properties of Magnetic Nanoparticles for Efficient Hyperthermia. Nanomaterials. 2015; 5(1): 63-89.
- Panagiotopoulos N, Duschka RL, Ahlborg M, Bringout G, Debbeler C, Graeser M, Kaethner C, Lüdtke-Buzug K, Medimagh H, Stelzner J, Buzug TM, Barkhausen J, Vogt FM, Haegele J. Magnetic particle imaging: current

developments and future directions. Int J Nanomedicine. 2015 Apr 22;10:3097-114.

- Pankhurst Q. A., Connolly J.,. Jones S. K, et al. “Applications of magnetic nanoparticles in biomedicine”, journal of physics. (2003), 36, R167-R181.
- Pankhurst, Q. A.; Thanh, N. K. T.; Jones, S. K.; et al. . Progress in Applications of Magnetic Nanoparticles in Biomedicine. J. Phys. D: Appl. Phys. 2009, 42, 224001.
- Pelaz B, Alexiou C, Alvarez-Puebla RA, et al. Diverse Applications of Nanomedicine. ACS Nano. 2017; 11(3): 2313-2381.
- Predescu AM, Matei E, Berbecaru AC, et al. Synthesis and characterization of dextran- coated iron oxide nanoparticles. R Soc Open Sci. 2018; 5(3): 171525.
- Rana S, Jadhav NV, Barick KC, et al. Polyaniline shell cross-linked Fe3O4 magnetic nanoparticles for heat activated killing of cancer cells. Dalton Trans. 2014 Aug 28;43(32):12263-71.
- Romanus E., Hückel M., Groß C., et al. Magnetic nanoparticle relaxation measurement as a novel tool for in vivo diagnostics, Journal of Magnetism and Magnetic Materials. Volume 252, 2002, Pages 387-389.
- Rubia-Rodríguez I, Santana-Otero A, Spassov S, et al. Whither Magnetic Hyperthermia? A Tentative Roadmap. Materials (Basel). 2021 Feb 3;14(4):706.
- Santos-Marques MJ, Carvalho F, Sousa C, et al. Cytotoxicity and cell signaling induced by continuous mild hyperthermia in freshly isolated mouse hepatocytes. Toxicology. 2006; 224(3): 210-8.
- Sapareto SA, Dewey WC. Thermal dose determination in cancer therapy. Int J Radiat Oncol Biol Phys. 1984; 10(6): 787-800.
- Saritas EU, Goodwill PW, Croft LR, et al. Magnetic particle imaging (MPI) for NMR and MRI researchers. J Magn Reson. 2013 Apr;229:116-26.
- Senpan A, Caruthers SD, Rhee I, et al. Conquering the dark side: colloidal iron oxide nanoparticles. ACS Nano. 2009 Dec 22;3(12):3917-26.
- Shapiro EM, Skrtic S, Sharer K, et al. MRI detection of single particles for cellular imaging. Proc Natl Acad Sci U S A. 2004 Jul 27;101(30):10901-6.

- Sharifi, H., Shokrollahi and S. Amiri, “Ferrite-Based Magnetic Nanofluids Used in Hyperthermia Applications”, Journal of Magnetism and magnetic materials. (2012), 324, 903–915.
- Shokrollahi H. Contrast agents for MRI. Mater Sci Eng C Mater Biol Appl. 2013 Dec 1;33(8):4485-97.
- Siemann W., The Unique Characteristics of Tumor Vasculature and Preclinical Evidence for its Selective Disruption by Tumor-Vascular Disrupting Agents”, Cancer Treat. Rev. (2011), 37, 63–74.
- Silverstein, Robert M, Francis X. Webster, and David J. Kiemle. Spectrometric Identification of Organic Compounds. Hoboken, NJ: John Wiley & Sons, 2005.
- Song W, Effect of local hyperthermia on blood flow and microenvironment: a review, Cancer Research. (1984), 44, 4721s–4730s.
- Song W, Park H. and Griffin R. J., Improvement of tumor oxygenation by mild hyperthermia. Radiat. Res. (2001), 155, 515–528.
- Song CW, Park HJ, Lee CK, et al. Implications of increased tumor blood flow and oxygenation caused by mild temperature hyperthermia in tumor treatment. Int J Hyperthermia. 2005 Dec;21(8):761-7.
- Sosnovik D, Weissleder R. Magnetic resonance and fluorescence based molecular imaging technologies. Prog Drug Res. 2005;62:83-115.
- Soto K, Garza KM, Murr LE. Cytotoxic effects of aggregated nanomaterials. Acta Biomater. 2007 May;3(3):351-8.
- Strijkers GJ, Mulder WJ, van Tilborg GA, et al. MRI contrast agents: current status and future perspectives. Anticancer Agents Med Chem. 2007 May;7(3):291-305.
- Suto M., Hirota Y., Mamiya H., Fujita A., Kasuya R., Tohji K. and Jeyadevan B., Heat dissipation mechanism of magnetite nanoparticles in magnetic fluid hyperthermia. Journal of Magnetism and Magnetic Materials. (2009), 321, 1493–1496
- Suto R, Srivastava PK. A mechanism for the specific immunogenicity of heat shock protein-chaperoned peptides. Science. 1995; 269(5230): 1585-8.

- Tay ZW, Chandrasekharan P, Chiu-Lam A, et al. Magnetic Particle Imaging-Guided Heating in Vivo Using Gradient Fields for Arbitrary Localization of Magnetic Hyperthermia Therapy. ACS Nano. 2018 Apr 24;12(4):3699-3713.
- Thiesen B, Jordan A. Clinical applications of magnetic nanoparticles for hyperthermia. Int J Hyperthermia. 2008 Sep;24(6):467-74.
- Valero E, Fiorini S, Tambalo S, et al. In vivo long-term magnetic resonance imaging activity of ferritin-based magnetic nanoparticles versus a standard contrast agent. J Med Chem. 2014; 57(13): 5686-92.
- Wáng YX, Idée JM. A comprehensive literatures update of clinical researches of superparamagnetic resonance iron oxide nanoparticles for magnetic resonance imaging. Quant Imaging Med Surg. 2017 Feb;7(1):88-122.
- Weizenecker J., Gleich B., Rahmer J., et al. Three-dimensional real- time in vivo magnetic particle imaging. Phys. Med. Biol. 54 (2009) L1–L10.
- Wust P., Hildebrandt B., Sreenivasa G., Rau B., Gellermann J., Riess H., Felix R.and Schlag P. M.. Hyperthermia in combined treatment of cancer. Lancet Oncol. (2002), 3, 487–497.
- Yang and Zhang. Tumor associated macrophages: from basic research to clinical application, Journal of Hematology and Oncology, 10:58, 2017.
- Yao Y, Zhou Y, Liu L, et al. Nanoparticle-Based Drug Delivery in Cancer Therapy and Its Role in Overcoming Drug Resistance. Front Mol Biosci. 2020 Aug 20;7:193.
- Yu E.Y., Bishop M., Zheng B., et al. Magnetic Particle Imaging: a Novel in Vivo Imaging Platform for Cancer Detection, Nano Lett. 17 (2017) 1648–1654.
- Yu E.Y., Chandrasekharan P., Berzon R., et al. Magnetic Particle Imaging for Highly Sensitive, Quantitative, and Safe in Vivo Gut Bleed Detection in a Murine Model, ACS Nano 11 (2017) 12067–12076.
- Zagar TM, Oleson JR, Vujaskovic Z, et al. Hyperthermia for locally advanced breast cancer. Int J Hyperthermia. 2010;26(7):618-624.
- Zhang Y, Li M, Gao X, Chen Y, et al. Nanotechnology in cancer diagnosis: progress, challenges and opportunities. J Hematol Oncol. 2019 Dec 17;12(1):137.

- Zheng B., Vazin T., Goodwill P.W. et al. Magnetic Particle Imaging tracks the long term fate of in vivo neural cell implants with high image contrast. Scientific Report, 5, 14055, 2015.